# Filamentary plasma eruptions in tokamaks

Sophia Ingeborg Amalie Henneberg

**Doctor of Philosophy**

**University of York**

**Physics**

**June 2016**

# Abstract

The nonlinear MHD ballooning model [1–3] is exploited for two distinct studies: firstly, the interaction of multiple filamentary eruptions in magnetised plasmas in a slab geometry is investigated and secondly, this model is examined quantitatively against experimental observations of ELMs in MAST and JET-like geometries.

The model consists of two differential equations which characterise the spatial and temporal evolution of the displacement: the first differential equation describes the displacement along the field line, the second differential equation is a two-dimensional nonlinear ballooning-like equation which is often second order in time, but can involve a fractional derivative in a tokamak geometry.

Filaments always evolve independently in the linear regime and equally sized filaments evolve independently in the nonlinear regime. However, we find that filaments with varying heights interact with each other in the nonlinear regime: Smaller filaments are slowed down and eventually are completely suppressed by the larger filaments which grow faster due to the interaction. This mechanism is explained by the down-draft caused by the nonlinear drive of the larger filaments which pushes the smaller filaments downwards.

To employ the second differential equation for a specific geometry one has to evaluate the coefficients of the equation which is non-trivial in a tokamak geometry as it involves field line averaging of slowly converging functions.

The coefficients of a Type I ELMy equilibrium from MAST and a Type II ELMy JET-like equilibrium have been determined. In both cases the two coefficients of the nonlinear terms are negative which would imply imploding rather than exploding filaments. By changing the equilibrium the signs of these coefficients can be inverted. This suggests that either the nonlinear Ballooning model does not capture the behaviour of Type I and Type II ELMs, or that the calculation of the coefficients are too sensitive to a given equilibrium.

# Contents

# List of Figures

# List of Tables

# Acknowledgement

I would like to thank my supervisor Prof. Howard Wilson for giving me the opportunity to undertake this PhD under his supervision, for the profound mathematical and physical insight, for all the interesting discussions, for his patience, and for the continuous motivation throughout the years. Additionally I would like to thank Prof. Steve Cowley for collaborating with me, for the inspiring discussions and the honest feedback on my work.
Part of this work is funded by the German National Academic Foundation (Studienstiftung des deutschen Volkes), the German Academic Exchange Service (DAAD - Stipendium für Doktoranden), and the York WW Smith Fund for all of which I am deeply thankful.
I would also like to mention that this work has been carried out within the framework of the EUROfusion Consortium and has received funding from the Euratom research and training programme 2014-2018 under grant agreement No 633053 and from the RCUK Energy Programme (grant number EP/I501045). The views and opinions expressed herein do not necessarily reflect those of the European Commission.
I would like to acknowledge Dr. Samuli Saarelma for providing me with the equilibria used in this thesis; Dr. Ben Dudson and Dr. David Dickinson for always having time to answer questions; Jarrod Leddy, for the helpful discussions, for introducing me to Deton8 at the beginning of my PhD, and for proofreading my PhD thesis; Andy West for all the technical advice which made it much easier to write my PhD thesis.
I would also like to thank the YPI in general for the welcoming and inspiring atmosphere and all the other PhD students in the YPI since they made the last couple of years even more enjoyable. There are too many to name all of them, but I would particularly like to thank Peshwaz Abdoul, David Blackman, Arka Bokshi, Chris Bowman, Andrew Gibson, Amelia Lunniss, Sandra Schröter, Brendan Shanahan, Ellie Tubman and Hannah Willett.
Furthermore, I would like to thank my family for their continuous support and patience through all my years as a student. In particular I would like to thank my parents Prof. Dr. Alexandra Henneberg and Hans-Joachim Henneberg for all the years of financial, intellectual and emotional support and my twin brother Julius for being such a supportive and understanding brother.
Finally, I would like to thank my amazing husband, Brendan, for all the patience and support, in particular for proofreading my thesis, listening and discussing physics whenever(!) something came to my mind, constantly encouraging, motivating and calming me but also distracting me from work whenever necessary.

# Declaration

I, Sophia Ingeborg Amalie Henneberg, declare that the work presented in this thesis is my own except where otherwise stated. This work has not previously been submitted for a degree at the University of York or any other university.
Some parts of the work presented in Chapter 4 have been published in:

1. S.C. Cowley, B. Cowley, S.A. Henneberg, and H.R. Wilson, "Explosive instability and erupting flux tubes in a magnetized plasma", Proc. Roy. Soc. A, A 471, 2180, (2015) , [4]

2. S.A. Henneberg, S.C. Cowley, H.R. Wilson, "Interacting filamentary eruptions in magnetised plasmas", Plasma Physics and Controlled Fusion, 57, (2015), [5]

Furthermore work from Chapters 4 and 5 have been presented during talks and posters at several conferences and can be found in the following conference proceedings:

1. S.A. Henneberg, S.C. Cowley, H.R. Wilson, "Explosive Ballooning Mode Instability in Tokamaks: Modelling the ELM Cycle", 41$^{\text{st}}$ EPS Conference on Plasma Physics, 2014, [6]

2. S.A. Henneberg, S.C. Cowley, H.R. Wilson, "Interaction of explosive multiple filaments in magnetised plasmas", 42$^{\text{nd}}$ EPS Conference on Plasma Physics, 2015, [7]

The following codes were provided by Prof. H.R. Wilson:

- The code Deton8, which I modified for the simulations in Chapters 4 and 5,
- the first version of the coefficient code, which I improved and extended including to calculate the inertial coefficients (including the fractional derivative coefficient), the field line stability term (also known as $1/n$-correction term coefficient) and the quasilinear nonlinearity coefficient (see Chapter 5),
- and the self-consistent equilibrium code SCENE [8] which we extended to create up-down symmetric equilibria.

Additionally the equilibria from MAST and JET used in Chapter 5 were provided by Dr. S. Saarelma who produced it in collaboration with R. Scannell, M. Beurskens, I. Nunes, the MAST team, and JET contributors.

# 1. Introduction

## 1.1. Motivation: $CO_2$, climate change and energy demand

The carbon dioxide ($CO_2$) concentration in the atmosphere has reached its highest historical level since the Industrial Revolution, see Fig. 1.1. The global temperature has also increased, which is a symptom of climate change, also called global warming, see Fig. 1.2. It is very likely that the major cause for the increase in temperature is carbon dioxide and

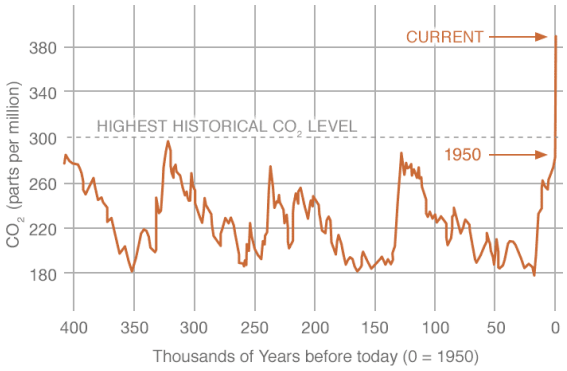


(a) *The data presented are reconstruction from ice cores. Shown are the ice age cycles in $CO_2$. The minima indicate ice ages. see [9] and [10].*

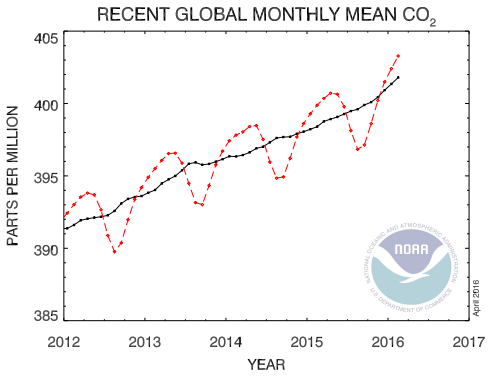


(b) *The monthly mean $CO_2$ which is globally averaged over marine surfaces sites is displayed, see [10]*

Figure 1.1.: *Global mean $CO_2$ development in the atmosphere.*

other greenhouse gas emissions [13]. This change in temperature and therefore the climate has ramifications such as extreme weather conditions, therefore it must be a priority for the world to decrease $CO_2$ emissions. The high increase of carbon dioxide concentration is mainly due to burning fossil fuels such as coal, oil and natural gas for energy production and transportation [14]. Additionally, the world's energy demand is quickly rising, and could increase by 33% by 2040 [15]. Therefore, it is necessary to develop energy sources which have reduced or no $CO_2$ emissions. Solutions could involve an increased use of fission

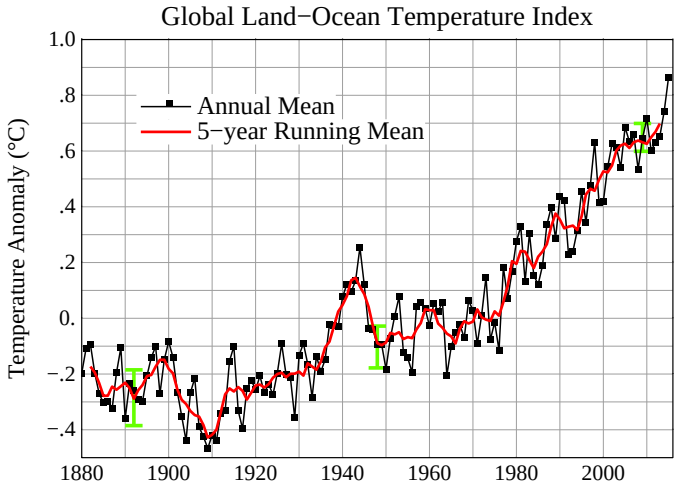


Figure 1.2.: *Increase of the global mean temperature over the last 130 years, see [11] and [12].*

power and renewable energy sources, since they do not produce $CO_2$. However, both of these have disadvantages.

LLLLL LLL LLL Renewable energy sources depend highly on the weather (solar panels need sun, wind turbines need the right wind speed, etc) and hence they do not always deliver a steady supply of energy. This intermittency means renewables are insufficient to meet the energy demand without the development of energy storage or the use of supplementary energy sources. Additionally there are debates on whether exclusively renewable energy sources can deliver enough energy for the human demand [16, 17]. The main disadvantages of fission power stations are the long lived radioactive waste they produce and the potential safety risk (e.g. melt down).

Since both renewable energy and fission have drawbacks, it is advisable to explore other options. Fusion as an energy source has very good features: it has no $CO_2$ emissions and the readily available fuel would be sufficient to provide energy for thousands of years. Additionally it has the advantage over fission power that it could only produce short lived radioactive waste, and with the current power plant designs it is not vulnerable to human failure or natural disasters [18].

## 1.2. Nuclear fusion

The mass of an atomic nucleus is less than the sum of the masses of its isolated nucleons (protons and neutrons). The mass $m$ is related to the energy $E$ by $E = mc^2$ where $c$ is the speed of light, and the difference in mass measured when forming an atom corresponds to the binding energy $E_B$ which would be needed to separate the nucleons. The experimental observed relation between the binding energy per nucleon and the number of nucleons $A$ in an atom is presented in Fig. 1.3. The element iron ($A = 56$) represents the maximum

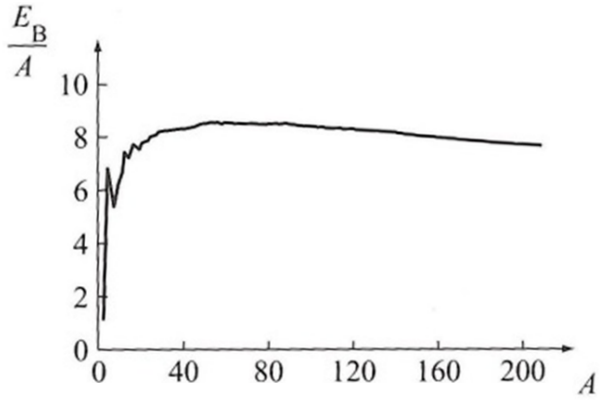


Figure 1.3.: *Binding energy $E_B$ per nucleon versus number of nucleons in an atom A [19].*

of this curve, which means that its nucleus is the most tightly bound. With this plot one can understand why fusion and fission can provide energy. If one splits atoms which are heavier than iron into two elements, one moves from the far right of the plot towards iron. The difference in energy is the energy release per nucleon one gains during this process which is called fission. On the other side, if one fuses two elements which are lighter than iron, the difference in the binding energy is released and therefore one can also gain energy. With this figure it also becomes clear why the energy release per nucleon for fusion is larger than for fission since there are larger differences in the binding energy.

The fusion reactions with high cross sections $\sigma$ (which means they are more likely to happen

than other reactions) are as follows:

$$\begin{aligned} \mathrm{D} + \mathrm{D} \quad &\longrightarrow \begin{cases} {}^3\mathrm{He} + \mathrm{n} & +3.3\mathrm{MeV}(50\%) \\ \mathrm{T} + \mathrm{p} & +4\mathrm{MeV}(50\%) \end{cases} \\ \mathrm{D} + {}^3\mathrm{He} \quad &\longrightarrow {}^4\mathrm{He} + \mathrm{p} + 18.4\mathrm{MeV} \\ \mathrm{D} + \mathrm{T} \quad &\longrightarrow {}^4\mathrm{He} + \mathrm{n} + 17.6\mathrm{MeV} \end{aligned}$$

where D stands for deuterium, a hydrogen isotope with one additional neutron, T denotes tritium, the hydrogen isotope with two additional neutrons, n indicates neutrons, p stands for protons and the numbers next to the He (Helium) indicate how many nucleons there are in the helium isotope. The energy displayed after the reaction is the released energy. We understand now why we can gain energy through fusion, but why does it not happen frequently if it causes a more optimised state of energy? The reason is the repulsive Coulomb force between protons, see Fig. 1.4. This force has to be overcome first before

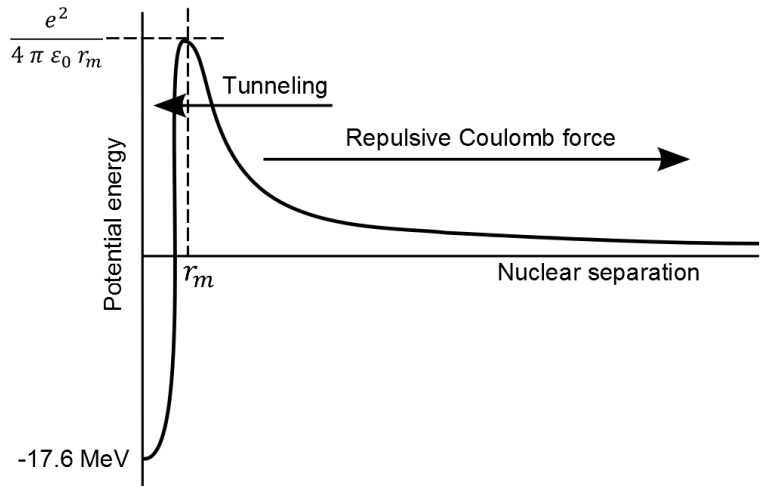


Figure 1.4.: *A sketch of potential energy for deuterium - tritium.*

nucleons fuse together, which means that the nuclei must come very close to each other. It is not necessary to actually overcome the barrier as the particles can tunnel through it if they have high enough energy, which is a quantum effect. The probability of tunneling is proportional to $\exp\left(-\frac{2\pi Z_1 Z_2 e^2}{\hbar v}\right)$ where $Z_i$ is the charge of the reacting particle and $v$ is the relative velocity [20]. Therefore the tunnelling, and with it fusion, can be achieved

at high enough temperatures.

The reaction rate of fusion, which indicates the likelihood of a reaction, is proportional to $\langle\sigma\nu\rangle$, which is displayed in Fig. 1.5. It is clear from Fig. 1.5 that the D-T reaction is more likely than the others at the considered temperatures. Additionally it produces the second

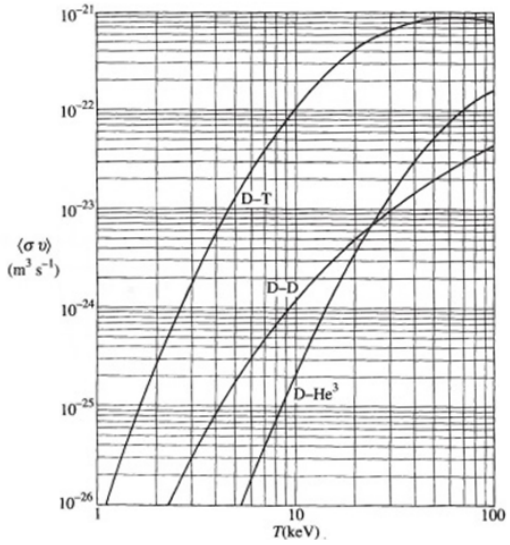


Figure 1.5.: $\langle\sigma\nu\rangle$ *versus temperature for D-T, D-D and D-*$^3$*He [21]*

highest amount of energy per reaction compared to the other reactions presented before. This makes the D-T reaction a promising candidate for fusion devices. Another important feature is how available and lasting the fuel is. Deuterium can be easily extracted from ocean water, however, tritium is rarer as it is radioactive with a half life of 12.26 years with the following decay process:

$$\mathrm{T} \longrightarrow {}^3\mathrm{He} + \mathrm{e}^- + \overline{\nu}_e$$

where $\overline{\nu}_e$ is an electron antineutrino. During the D-T reaction a fast neutron is created with 14.1 MeV kinetic energy and a He-atom with 3.5 MeV. This fast neutron can be used in combination with lithium to breed tritium:

$$\mathrm{n(slow)} + {}^6\mathrm{Li} \longrightarrow {}^4\mathrm{He} + \mathrm{T} + 4.8\mathrm{MeV}$$
$$\mathrm{n(fast)} + {}^7\mathrm{Li} \longrightarrow {}^4\mathrm{He} + \mathrm{T} + \mathrm{n} - 2.5\mathrm{MeV}$$

Natural lithium consists of 7.4% $^6$Li and 92.6% $^7$Li [19]. However, the $^7$Li reaction needs energy to be initiated and one finds that the $^6$Li reaction is the dominant reaction in fusion relevant conditions [19]. With this in mind one can build a fusion power plant with a lithium coated wall to provide the required tritium and with that the fuel for D-T reactions would last for thousands of years.

The state of matter we are interested in to achieve fusion is plasma which is an ionised gas and will be described further in Sect. 1.3. The energy $W$ in the plasma is roughly given by

$$W = \int 3nT\mathrm{d}V$$

where $n$ is the density, $T$ is the temperature and $V$ the volume of the plasma. We denote the energy lost from the plasma as $P_L$, the energy used for external heating as $P_H$ and the energy gained from the $\alpha$ particle produced during the D-T reaction as $P_\alpha = \int \frac{1}{4} n^2 \langle \sigma v \rangle E_\alpha \mathrm{d}V$ where $E_\alpha$ is the energy of an $\alpha$ particle. One can define the confinement time, which is a parameter describing how well the plasma is confined, as:

$$\tau_E = \frac{W}{P_L}$$

The power balance for a steady state plasma is:

$$P_L = P_H + P_\alpha$$

The point when no external heating is needed is called ignition. This means $P_H = 0$ and we obtain:

$$\int \frac{1}{4} n^2 \langle \sigma v \rangle E_\alpha \mathrm{d}V = \frac{\int 3nT\mathrm{d}V}{\tau_E}$$

Estimating the density and temperature to be constant we obtain the ignition condition [22]:

$$n\tau_E > \frac{12T}{\langle \sigma v \rangle E_\alpha}$$

where the dependency of $\langle \sigma v \rangle$ on the temperature is presented in Fig. 1.5. One can approximate this behaviour in the range of $10 - 20keV$:

$$\langle \sigma v \rangle \approx 1.1 \times 10^{-24} T^2 m^3 s^{-1}.$$

where the temperature $T$ is measured in keV. With $E_\alpha = 3.5MeV$ we obtain the ignition condition for temperatures in the range of $10 - 20keV$:

$$nT\tau_E > 3 \times 10^{21} m^{-3} keV s$$

With this condition it becomes clear that the triple product of density, temperature and confinement time must be large. This allows some freedom to achieve fusion; for example one can choose a very high density and short confinement time (used in inertially confined fusion) or a very high confinement time but low density (used in magnetically confined fusion).

A common measure of the energy produced in a plasma is the parameter $Q$ defined as $Q = \frac{P_{fus}}{P_H}$ where $P_{fus}$ is the thermonuclear power produced in the plasma. $P_{fus}$ is five times higher than $P_\alpha$. Therefore we can write

$$Q = \frac{5P_\alpha}{P_H}.$$

There are several important values of $Q$ representing important plasma conditions. Ignition is equivalent to $Q \to \infty$. Another important value of $Q$ is $Q = 1$ which indicates the state when the heating power is the same than the thermonuclear power produced due to fusion. This is called break-even.

## 1.3. Plasma physics

Sustainable fusion requires the fuel to be in a state of matter called plasma to obtain the required triple product. A plasma is an ionised gas with some additional characteristics. It has to be quasi-neutral which means that there are approximately as many positively as negatively particles in a volume element. Furthermore charge exchange, which is the process when a neutral particle and a charged one collide and become charged and neutralised

respectively, is not too frequent. This just means that the particles remain charged for long enough to behave significantly different than a gas [23].

It is very useful to consider a single charged particle first to understand the behaviour of plasmas. The force acting on a charged particle in a given magnetic field $\boldsymbol{B}$ and electric field $\boldsymbol{E}$ is the Lorentz force $\boldsymbol{F}$:

$$\boldsymbol{F} = q\left(\boldsymbol{E} + \boldsymbol{v} \times \boldsymbol{B}\right)$$

where $q$ is the charge of the particle and $\boldsymbol{v}$ is its velocity. Ignoring the electric field and assuming that the magnetic field has only one component pointing in the $z$ direction ($\boldsymbol{B}$=B$\boldsymbol{z}$) one obtains an orbit around the magnetic field lines for the particle (see Fig. 1.6):

$$\boldsymbol{v} = v_{\perp}\left(\sin(\Omega t)\boldsymbol{x} + \cos(\Omega t)\boldsymbol{y}\right) + v_{\parallel}\boldsymbol{z}$$

where $v_{\perp} = \sqrt{v_x^2 + v_y^2}$ is constant in an homogeneous magnetic field and $\Omega$ is the cyclotron or (gyro-) frequency given by:

$$\Omega = \frac{qB}{m}$$

where $m$ is the mass of the particle. The parallel component of the velocity $v_{\parallel}$ is never

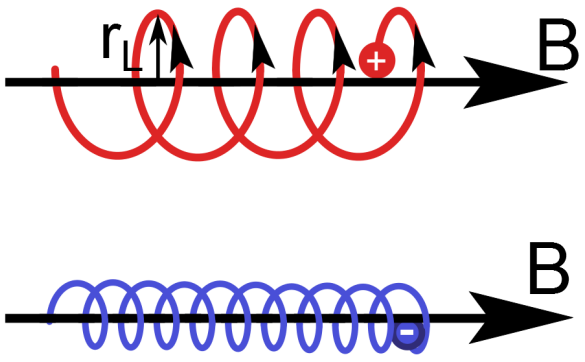


Figure 1.6.: *Orbital path of positive and negative charges. For electrons the Larmor radius is much smaller than for protons. Additionally they rotate in opposite directions around the magnetic field line because $\Omega$ depends on the charge.*

affected by a homogeneous magnetic field as its force only influences the perpendicular components. The radius of the particle orbit around the magnetic field lines is called

Larmor radius $r_L$:

$$r_L = \frac{v_\perp}{\Omega}$$

In a homogeneous, straight magnetic field without electric fields, a particle simply follows the magnetic field line. However, there are effects which lead to a change of direction, or drift of particles.

The most common particle drifts are:

$$E \times B\text{-drift:} \qquad \boldsymbol{v}_{E\times B} = \frac{\boldsymbol{E} \times \boldsymbol{B}}{B^2} \tag{1.1}$$

$$\text{curvature drift:} \qquad \boldsymbol{v}_c = \frac{m v_\parallel^2}{qB^2} \frac{\boldsymbol{R}_c \times \boldsymbol{B}}{R_c} \tag{1.2}$$

$$\nabla B\text{-drift:} \qquad \boldsymbol{v}_{\nabla B} = \frac{1}{2} r_L v_\perp \frac{\boldsymbol{B} \times \nabla B}{B^2} \tag{1.3}$$

where $\boldsymbol{R}_c$ is the radius of curvature vector which points away from the centre of curvature and $R_c$ is its magnitude. The sign of the curvature and $\nabla B$ drifts depend on the sign of the charge which therefore can cause charge separation. However, the $E \times B$-drift is the same for both positive and negative charged particles.

### 1.3.1. Magnetic confinement

Magnetic confinement fusion (MCF) is the approach to obtain fusion through the use of magnetic coils to achieve good confinement of plasma at fusion relevant temperatures and densities.

Two useful quantities to understand MCF are the magnetic moment $\mu$ and the total energy $\mathcal{E}$ since both quantities are conserved. The magnetic moment is given by

$$\mu = \frac{m v_\perp^2}{2B}$$

and the total energy is:

$$\mathcal{E} = \frac{1}{2} m v^2 + q\phi$$

where $\phi$ is the electrostatic potential and $v^2 = v_\perp^2 + v_\parallel^2$. With these two expressions we can obtain a condition for the turning point of charged particles in a magnetic field with spatially varying magnetic field strength. We begin by neglecting the electric field and

assuming a particle moves in the $z$-direction with a starting velocity $\boldsymbol{v}_0$ in a region where the magnetic field is initially $B_0$ towards a stronger magnetic field $B$. Exploiting the expressions for the magnetic moment leads to:

$$v_\perp^2 = \frac{B}{B_0} v_{\perp 0}^2$$

and from the energy conservation neglecting $\phi$ we obtain:

$$v_\parallel^2 = v_0^2 \left(1 - \frac{B}{B_0} \frac{v_{\perp 0}^2}{v_0^2}\right)$$

When $v_\parallel^2$ changes sign the particle turns around since the velocity cannot be imaginary. This turning point is at a magnetic field strength given by:

$$B = \frac{B_0 \, v_0^2}{v_{\perp 0}^2}$$

This process of reflecting particles due to a stronger magnetic field is called a magnetic mirror. This effect can be used to confine the plasma, which has been done before in linear mirror devices, see Fig. 1.7 which shows a sketch of a simple linear mirror. However, we

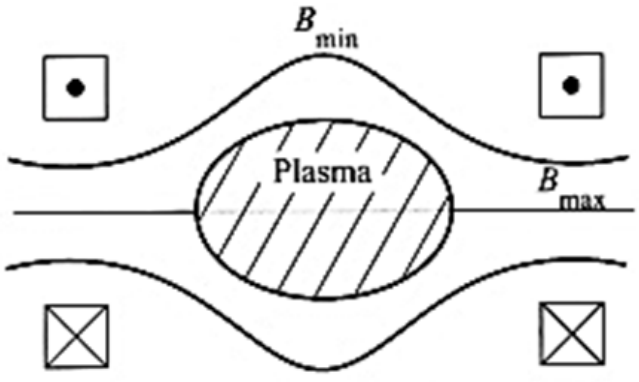


Figure 1.7.: *A mirror with two sets of coils such that the plasma is confined in between [19].*

can determine the maximum magnetic field strength $B_{max}$ such that all particles with

$$\frac{v_{\perp 0}^2}{v_0^2} < \frac{B_0}{B_{max}}$$

are lost since the magnetic field is not strong enough to reflect them. Due to collisions there will always be particles which have a small enough speed ratio $\frac{v_{\perp 0}^2}{v_0^2}$ to escape and therefore there will always be lost from the plasma. The basic solution to losing particles at the ends is to connect the ends of a magnetic mirror which leads to a toroidal magnetic confinement device. One such kind of toroidal confinement device is called the Tokamak.

## 1.4. The tokamak

Tokamak (a Russian acronym meaning "Toroidal chamber in magnetic coils") is a toroidal magnetic fusion device with helical magnetic field lines which are located on nested flux surfaces. To understand why tokamaks need helical fields, one can investigate the particle drifts introduced before. Let us assume a purely toroidal field (see Fig. 1.8 for the definitions of toroidal and poloidal direction). This purely toroidal field has a gradient in the magnetic

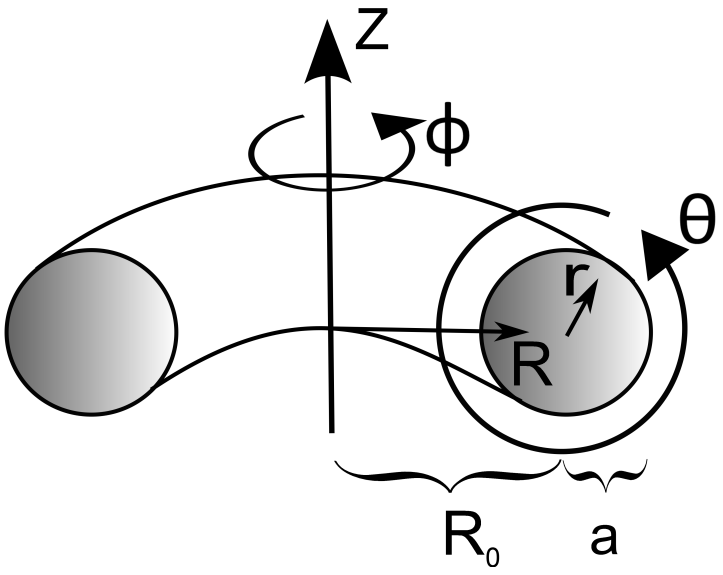


Figure 1.8.: *A sketch of a tokamak. a denotes the minor radius and $R_0$ denotes the major radius. In a cylindrical coordinate system with the conventionally used variables $\phi$, $R$ and $Z$, the toroidal direction points in the $\phi$-direction and the poloidal is the $\theta$-direction. The poloidal cross section is described by a radius $r$ and the angle $\theta$.*

field strength since its magnetic field is stronger for smaller radii $R$. This gradient causes a $\nabla B$-drift, see equation (1.3), which causes a charge separation. If the magnetic field points in the direction of the cylindrical coordinate $\phi$, see Fig. 1.8, positive particles drift vertically up and negative particles drift downwards. This charge separation causes an $E \times B$ drift, which for both types of charged particles points outwards, see Fig. 1.9b.

Therefore particles are not very well confined. If we consider positively charged particles

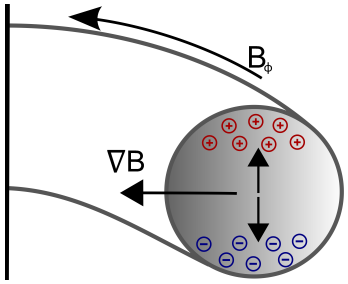


(a) *The magnetic field strength is stronger at the inside of the tokamak than on the outside because it decays like* $\sim \frac{1}{R}$. *Charge separation is generated through* $\nabla B$ *drift.*

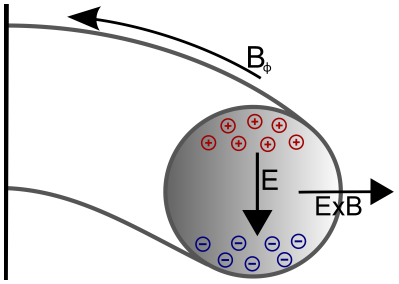


(b) *The created electrical field and the toroidal magnetic field causes a* $E \times B$ *drift outwards for both positive and negative particles.*

Figure 1.9.: *The particle loss due to a purely toroidal field.*

in a helical field instead, the $\nabla B$ force still exists and it still points upwards, but it shifts the positive particle onto another flux surface. If it is on the top half it will drift onto a flux surfaces with a larger radius, and if it is on the bottom half it will drift onto a flux surfaces with a smaller radius. Therefore the net-drift of such a particle averages to zero. The same is valid for a negative particle but with opposite drift-directions.

To characterise tokamaks one uses the aspect ratio which is defined as:

$$\text{aspect ratio} = \frac{R_0}{a}$$

where $R_0$ is the major radius and $a$ is the minor radius, see Fig. 1.8. Tokamaks with a tight aspect ratio (1.2-1.5) are called spherical tokamaks. Tokamaks with larger aspect ratios (2.5-3.5) are considered conventional tokamaks.

### 1.4.1. High confinement mode (H-mode)

Two main operational regimes exist in a tokamak fusion device: the low-confinement mode (L-mode) and the high-confinement mode (H-mode) which has an improved energy confinement time compared to the L-mode. This improvement is due to altered transport processes which also changes the appearance of the edge, see Fig. 1.10. Fusion devices aim to operate in H-mode because the improved confinement increases the performance. The L-mode was achieved first, then the H-mode was unexpectedly detected for the first time

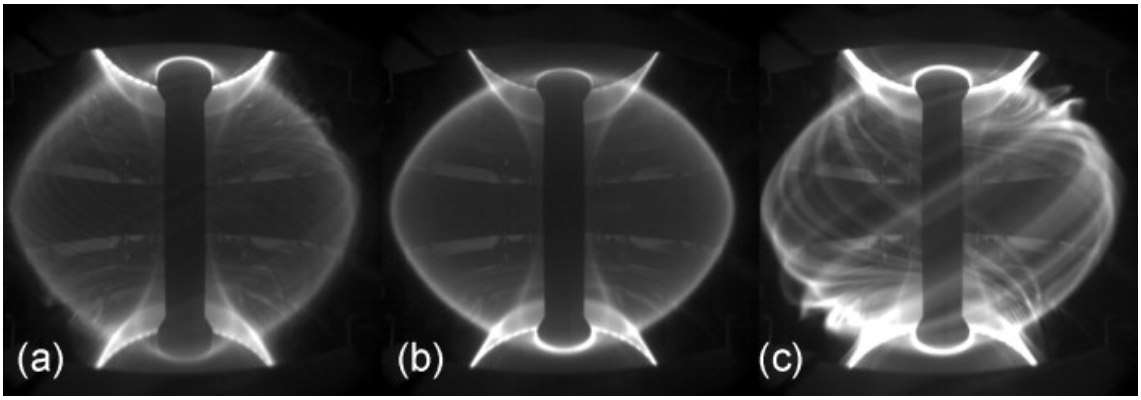


Figure 1.10.: *Image of MAST plasma during (a) L-mode (b) H-mode (c) ELM [24]. The visible plasma edge differs in all three cases due to diverse transport processes.*

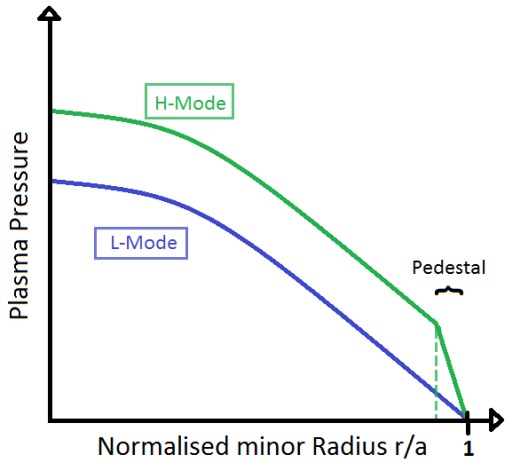


Figure 1.11.: *Schematic pressure profile for L- and H-mode.*

on the ASDEX experiment in Garching in 1982, [25]. The transition from L- to H-mode occurs when a power threshold is reached [26], although it is not fully understood why this transition exists [27]. The main difference between these regimes is a steep edge pressure gradient region caused by an edge transport barrier in the H-mode, called the pedestal (Fig. 1.11). The transport is reduced due to a sheared perpendicular rotation caused by a radial electric field $E_r$ ($E_r \times B$ rotation) [28]. Because of the shear the large, turbulent eddies are suppressed and therefore the turbulent transport is reduced as well [29]. Though an improvement in confinement is desirable, there are negative side effects of the H-mode. The steep pressure gradient can drive instabilities such as Edge Localised Modes which can damage the device‘ but can also help to control density and impurities, [30].

#### Edge Localised Modes

Edge Localised Modes (ELMs) are quasi-periodic instabilities which have a filamentary structure and grow very rapidly, see Fig. 1.10. They release a large amount of energy and particles which decreases the confinement of the plasma and can erode plasma facing components on future fusion devices, such as ITER [31]. Therefore it is very important to understand the nature of ELMs and how they can be controlled.
We will discuss the latest understanding and research relevant to ELMs in Sect. 2.4.

ELMs are an ubiquitous phenomenon and have been observed in many tokamaks such as ASDEX-Upgrade in Germany [32, 33], DIII-D [34] and NSTX (National Spherical Torus Experiment) in the USA [35, 36] , and MAST [37] and JET [38] in the UK. Next we discuss MAST and the EU device JET in more detail since we investigate data from these experiments in Chapter 5.

### 1.4.2. MAST

MAST (Mega Amp Spherical Tokamak) is a UK spherical tokamak based at CCFE (Culham Centre for Fusion Energy) in the UK [39–41]. MAST is currently being upgraded [42]

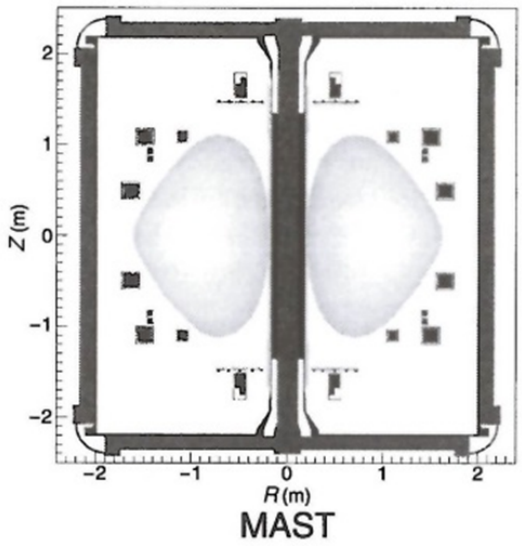


Figure 1.12.: *MAST (Mega Amp Spherical Tokamak) plasma and its dimensions [21]. The results from this configuration are used in this thesis.*

| MAST | |
|---|---|
| Major radius | 0.85 m |
| Minor radius | 0.65m |
| Aspect ratio | $\geq 1.3$ |
| Plasma current | 2 MA |
| Toroidal field | 0.52 T |

Table 1.1.: Parameters of the spherical tokamak MAST [41]

and any references to MAST in this thesis will refer to the older version which is shown in Fig. 1.12. MAST has a high speed, wide angle camera which captures pictures of the entire plasma including ELMs, as shown later in Fig. 2.7.

MAST and NSTX [43, 44] at the Princeton Plasma Physics Laboratory are the two largest spherical tokamaks in the world. MAST itself has an aspect ratio of 1.3, see Table 1.1. This and the large vacuum vessel are why it is possible for MAST to have a wide angle camera which can show the entire plasma cross section [41, 45].

### 1.4.3. JET

The JET (Joint European Torus) is the largest tokamak currently in operation worldwide and it is a joint research device between 16 European countries [46]. It has an aspect ratio of about 2.96 and therefore it is a conventional tokamak, see Fig. 1.13 and Table 1.2. The

| JET | |
|---|---|
| Major radius | $\sim 2.96$ m |
| Minor radius | $\sim$ 1m |
| Aspect ratio | $\sim 2.96$ |
| Plasma current | $\sim 7$ MA |
| Toroidal field | $\sim 3.8$ T |

Table 1.2.: Ballpark parameters of the original JET design [21]

first plasma in JET was produced in 1983 [47], the first operation with D-T in 1991 [48], and it achieved the world's record peak fusion power of 16MW in 1997 [49, 50].

JET has undergone several upgrades such as implementing different types of divertors [51], and changing the plasma facing components from carbon (mainly carbon fibre-reinforced carbon composite (CFC)) to an ITER-like wall (tungsten and beryllium) [52]. These changes were made to examine the consequences of the design of the next generation

tokamak ITER which is currently being built in the south of France [53]. ITER is designed to achieve $Q \approx 10$ in order to prove that tokamaks can be viable fusion power plants which will attempt to produce even higher fusion gain ($Q \sim 30$).

The data used in this thesis were obtained with the carbon wall and with the MKII-HD divertor which allows a quasi-double-null configuration (which is approximately an up-down-symmetric configuration) to be produced [54].

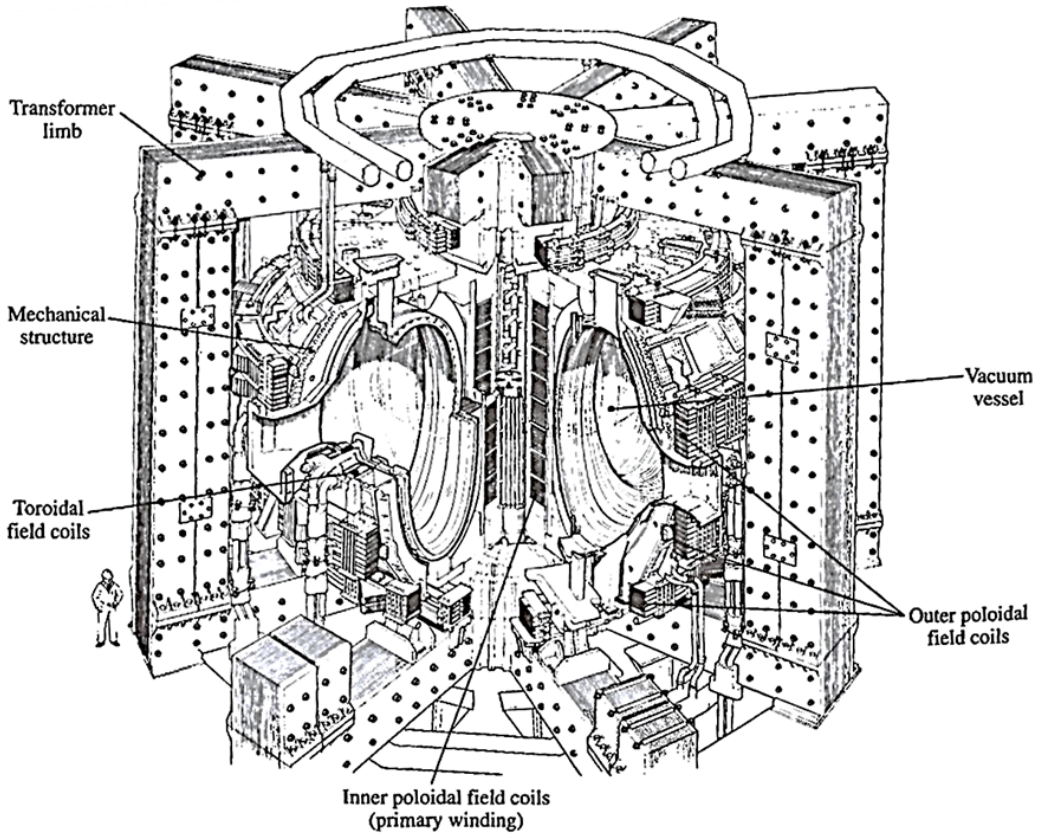


Figure 1.13.: *Original JET (Joint European Torus) [21].*

## 1.5. Outline of the dissertation

This thesis uses an analytical model to simulate the nonlinear dynamics of ballooning instabilities and attempts to apply this model in realistic tokamak geometries to compare it with experimental observations of ELMs. Chapter 2 provides the background material for this thesis. It starts with a description and overview of coordinate systems used in tokamaks (Section 2.1). Then a short introduction to magnetohydrodynamics is presented (Section 2.2) as this model is the starting point of the derivation provided in Chapter 3.
Chapter 3 presents the derivation of the nonlinear ballooning model for tokamak geometries. This model was derived by Cowley and Wilson [2] from ideal MHD. However, a detailed description of the derivation for tokamak geometry has not been published previously and therefore it will be provided in this thesis.
Chapter 4 presents results for how filaments with different sizes interact. These calculations have been done in slab geometry for which the nonlinear ballooning model has been derived separately.
The last research chapter (Chapter 5) starts with an outline of how the coefficients, needed for the nonlinear ballooning model in tokamaks, are determined. The results of simulations in both MAST (Type I ELMs) and JET (Type II ELMs) geometries are presented.
Chapter 6 contains the conclusion of this thesis and an outlook for future work.

# 2. Background

## 2.1. Common coordinate systems in tokamaks

Several coordinate systems and basis vectors for tokamak geometries are used in this thesis. To make it easier for the reader to follow which variable names correspond to a certain coordinate system, an overview of all coordinate systems is presented here. A more detailed description of the coordinate systems can be found in [55].

### 2.1.1. Clebsch coordinate system ($\psi$, $\alpha$ and $l$)

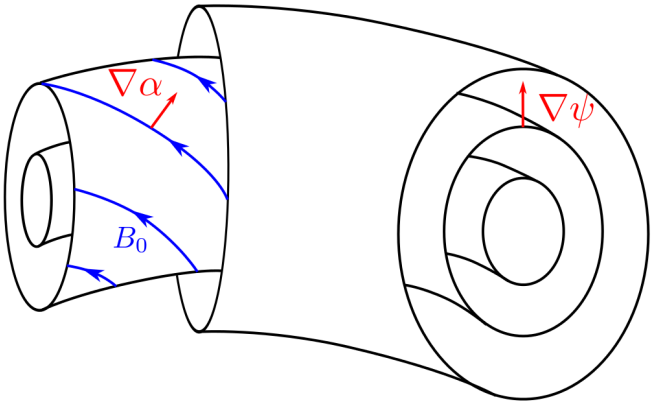


Figure 2.1.: *Spatial components of the coordinate system where* $B_0 = \nabla\psi \times \nabla\alpha$. *(Thanks to Brendan Shanahan for producing the Figure.)*

In the Clebsch coordinate system the magnetic field is written as [55]:

$$\boldsymbol{B}_0 = \nabla\psi \times \nabla\alpha \tag{2.1}$$

where $\alpha$ labels the magnetic field lines on a certain flux surface $\psi$, see Fig. 2.1. $\alpha$ is chosen

to be:

$$\alpha = q(\psi)\theta - \phi \tag{2.2}$$

where $\phi$ is the toroidal angle, $\theta$ is the poloidal angle in straight field line coordinates and $q$ is the safety factor which describes how many times a certain magnetic field line goes around the torus for one poloidal revolution. It is defined as:

$$q \equiv \frac{1}{2\pi} \oint \mathrm{d}\theta \frac{rB_\phi}{RB_\theta} \tag{2.3}$$

where $B_\phi$ is the magnetic field component in the toroidal direction and $B_\theta$ is the component in the poloidal direction.

So far we have only chosen two variables for the Clebsch coordinates: $\psi$ and $\alpha$. The third one can be chosen freely. Here we choose it as $l$ which measures the distance along a magnetic field line. Later, in Sect. 2.1.2, we will define another variable .

The Jacobian in this coordinate system is given by:

$$\begin{aligned} J &= \frac{1}{\nabla\psi \cdot \nabla\alpha \times \nabla l} \\ &= \frac{1}{B_0} \end{aligned}$$

Therefore the operator $\boldsymbol{B}_0 \cdot \boldsymbol{\nabla}$ is:

$$\boldsymbol{B}_0 \cdot \boldsymbol{\nabla} = \frac{1}{B_0} \left.\frac{\partial}{\partial l}\right|_{\psi,\alpha} .$$

#### Contravariant coordinate system of $\psi$, $\alpha$ and $l$

The contravariant basis vectors are given by:

$$\boldsymbol{e}^\alpha = \nabla\alpha \qquad \boldsymbol{e}^\psi = \nabla\psi \qquad \boldsymbol{e}^l = \nabla l$$

Contravariant basis vectors are perpendicular to the surfaces on which the corresponding coordinate is constant. In this system one can represent the nabla operator $\nabla$ as:

$$\nabla = \nabla\alpha \left.\frac{\partial}{\partial\alpha}\right|_{\psi,l} + \nabla\psi \left.\frac{\partial}{\partial\psi}\right|_{\alpha,l} + \nabla l \left.\frac{\partial}{\partial l}\right|_{\alpha,\psi} \tag{2.4}$$

A more detailed explanation can be found in reference [55].

#### $\boldsymbol{e}_\perp$, $\boldsymbol{e}_\wedge$ and $\boldsymbol{B}_0$

We generate new basis vectors: $\boldsymbol{e}_\perp$, $\boldsymbol{e}_\wedge$ and $\boldsymbol{B}_0$ to decompose the quantities into perpendicular and parallel components relative to the magnetic field line. The first two vectors are defined as:

$$\boldsymbol{e}_\perp \equiv \frac{\nabla\alpha \times \boldsymbol{B}_0}{B_0}$$
$$\boldsymbol{e}_\wedge \equiv \frac{\boldsymbol{B}_0 \times \nabla\psi}{B_0}$$

$\boldsymbol{e}_\perp$ and $\boldsymbol{e}_\wedge$ are vectors perpendicular to the equilibrium magnetic field lines $\boldsymbol{B}_0$ whose components are along the magnetic field lines. One can show that (see Appendix A):

$$|\boldsymbol{e}_\perp|^2 = |\nabla\alpha|^2$$
$$|\boldsymbol{e}_\wedge|^2 = |\nabla\psi|^2$$

To determine what $\boldsymbol{e}_\perp \cdot \nabla$ and $\boldsymbol{e}_\wedge \cdot \nabla$ are we can use equation (2.4) and equation (2.1) to obtain the useful relations:

$$\begin{aligned}
\boldsymbol{e}_\perp \cdot \boldsymbol{\nabla} &= B_0 \left.\frac{\partial}{\partial\psi}\right|_{\alpha,l} - \frac{\boldsymbol{e}_\psi \cdot \boldsymbol{B}_0}{B_0^2} (\boldsymbol{B}_0 \cdot \boldsymbol{\nabla}) \\
\boldsymbol{e}_\wedge \cdot \boldsymbol{\nabla} &= B_0 \left.\frac{\partial}{\partial\alpha}\right|_{\psi,l} - \frac{\boldsymbol{e}_\alpha \cdot \boldsymbol{B}_0}{B_0^2} (\boldsymbol{B}_0 \cdot \boldsymbol{\nabla}) \\
\boldsymbol{B}_0 \cdot \boldsymbol{\nabla} &= B_0 \left.\frac{\partial}{\partial l}\right|_{\alpha,\psi}
\end{aligned} \tag{2.5}$$

where we have defined two new vectors:

$$\boldsymbol{e}_\alpha \equiv \nabla l \times \nabla\psi \qquad\qquad \boldsymbol{e}_\psi \equiv \nabla\alpha \times \nabla l$$

### 2.1.2. The $\psi$-$\chi$-$\phi$ coordinate system

Lets replace $l$ by the variable $\chi$ where $\chi$ is a poloidal angle which increases by $2\pi$ every time a field line goes around poloidally. It is chosen such that $\nabla\chi$ is orthogonal to $\nabla\psi$ and $\nabla\phi$. All equilibrium quantities are periodic with respect to $\chi$. In this coordinate system,

the $(\boldsymbol{B}_0 \cdot \boldsymbol{\nabla})$-operator becomes:

$$\boldsymbol{B}_0 \cdot \boldsymbol{\nabla} = \frac{1}{\hat{J}} \left.\frac{\partial}{\partial \chi}\right|_{\psi,\alpha}$$

where $\hat{J}$ is given by

$$\hat{J} = \frac{1}{\nabla\psi \cdot \nabla\chi \times \nabla\phi}$$

and the representation of the nabla operator is:

$$\nabla = \nabla\chi \left.\frac{\partial}{\partial \chi}\right|_{\phi,\psi} + \nabla\phi \left.\frac{\partial}{\partial \phi}\right|_{\chi,\psi} + \nabla\psi \left.\frac{\partial}{\partial \psi}\right|_{\chi,\phi} \tag{2.6}$$

The absolute values of the contravariant basis vectors are:

$$|\nabla\chi| = \frac{1}{\hat{J} B_p} \tag{2.7}$$

$$|\nabla\phi| = \frac{1}{R} \tag{2.8}$$

$$|\nabla\psi| = R B_p \tag{2.9}$$

where $B_p$ is the poloidal component of the magnetic field. The variable $\alpha$ can be written as:

$$\alpha = q(\chi - \chi_0) + Y - \phi \tag{2.10}$$

where $\chi_0$ is a constant and the periodic function $Y$ is defined as:

$$Y \equiv \int_0^{\chi} \nu d\chi - q(\chi - \chi_0)$$

with $\nu$ defined as $\nu = \dfrac{fJ}{R^2}$ with $f = B_\phi R$. $\nu$ is related to the safety factor defined in Eq. (2.3) by the relation: $q = \dfrac{1}{2\pi} \oint \nu \mathrm{d}\chi$ (see [56]).
With these quantities we can rewrite $\boldsymbol{e}_\perp$ and $\boldsymbol{e}_\wedge$ as:

$$\boldsymbol{e}_\perp \equiv \frac{\nabla\alpha \times \mathbf{B_0}}{B_0} = \frac{B_0}{|\nabla\psi|^2}\nabla\psi - \frac{\Lambda}{B_0}\boldsymbol{B}_0 \times \nabla\psi \tag{2.11}$$

$$\boldsymbol{e}_\wedge \equiv \frac{\boldsymbol{B}_0 \times \nabla\psi}{B_0} = \frac{f(\psi)}{B_0}\boldsymbol{B}_0 - R^2 B_0 \nabla\phi \tag{2.12}$$

where the quantity $\Lambda$ is given by $\Lambda = q'\chi + Y'$ with the prime denoting a derivative with respect to $\psi$. And we can show (see Appendix A):

$$\begin{aligned} |\boldsymbol{e}_\perp|^2 &= |\nabla\alpha|^2 \\ &= \frac{B_0^2}{R^2 B_p^2} + \Lambda^2 R^2 B_p^2 \\ |\boldsymbol{e}_\wedge|^2 &= |\nabla\psi|^2 \\ &= R^2 B_p^2 \end{aligned} \tag{2.13}$$

### 2.1.3. Straight field-line (or toroidal flux) coordinates system ($\psi$, $\theta$ and $\phi$)

One can construct toroidal flux coordinates in which the magnetic field is straight. In axisymmetric devices one can choose the flux surface label $\psi$, the toroidal angle $\phi$ and a poloidal-like angle $\theta$ which was mentioned in the definition of $\alpha$ (Eq. (2.2)). Exploiting the Clebsch representation of the magnetic field (2.1), we can see that magnetic field lines are described by constant $\alpha$ and $\psi$ surfaces. Using equation (2.2) we obtain the following equation for a magnetic field line on a given flux surface:

$$\alpha = \text{constant} = q(\psi)\theta - \phi.$$

This equation describes a straight line. This means that the coordinate system consisting of $\psi$, $\theta$ and $\phi$ is a straight field line system. Using again equation (2.1) we obtain for the magnetic field:

$$\boldsymbol{B}_0 = q(\psi)\nabla\psi \times \nabla\theta + \nabla\phi \times \nabla\psi$$

with

$$|\nabla\psi| = B_p R \qquad |\nabla\phi| = \frac{1}{R} \qquad |\nabla\theta| = \frac{1}{JB_p}$$

where $B_p$ is the poloidal component of the magnetic field, $R$ is the radial component of a cylindrical coordinate system, where the origin is at the axis of the toroidal symmetry and

$J$ is the Jacobian determinant of this coordinate system:

$$J = \frac{1}{\nabla\phi \cdot \nabla\psi \times \nabla\theta} \tag{2.14}$$

Because of axisymmetry the following equations are valid:

$$\nabla\psi \cdot \nabla\phi = 0 \qquad\qquad \nabla\phi \cdot \nabla\theta = 0$$

However, it is generally not true that $\nabla\psi$ is perpendicular to $\nabla\theta$. Therefore this coordinate system is not an orthogonal one. Since $\nabla\psi$ and $\nabla\theta$ are both orthogonal to $\nabla\phi$, the vector given by $\nabla\theta \times \nabla\psi$ is parallel to $\nabla\phi$ and can therefore be written as: $\nabla\psi \times \nabla\theta = s\nabla\phi$. By using the equation of the Jacobian determinant (2.14), we can obtain an equation for $s$:

$$s = \frac{R^2}{J}$$

With that the representation of the magnetic field becomes

$$\boldsymbol{B}_0 = f\nabla\phi + \nabla\phi \times \nabla\psi \tag{2.15}$$

with $f = f(\psi)$ defined as $f \equiv \frac{qR^2}{J}$ and $B_\phi = \frac{f}{R}$.

## 2.2. Magnetohydrodynamics

In Sect. 1.3, we analysed the plasma behaviour with a particle picture. A more realistic treatment would take into account the interaction of the particles with each other and the electromagnetic fields. The inclusion of these interactions greatly increases the complexity. Because of this we exploit a reduced model which is called magnetohydrodynamic (MHD). In this section we summarise the most important aspects of the MHD description of plasmas. This model describes plasma as a single fluid, which means it combines the electrons and ions. Furthermore ideal MHD neglects all dissipative effects such as resistivity and viscosity. It is commonly used to determine the stability of a plasma with respect to small perturbations. Detailed reviews of MHD can be found in [57–59]

### 2.2.1. Eulerian MHD

Kinetic theory describes the position $\boldsymbol{x}$ and velocity $\boldsymbol{v}$ of each particle in a fluid with a distribution function $f_j(\boldsymbol{x}, \boldsymbol{v}, t)$. $f_j(\boldsymbol{x}, \boldsymbol{v}, t)$ gives the number of particles per unit volume in a phase space where $j$ stands for electrons "e" or ions "i". The density $n_j$, the flow velocity $\boldsymbol{u}_j$ and the pressure tensor $\underline{\underline{P}}_j$ are defined by the zeroth, first and second moments of the distribution function in the following way:

$$
\begin{aligned}
n_j(\boldsymbol{r}) &= \int f_j(\boldsymbol{r}, \boldsymbol{v}, t) \mathrm{d}\boldsymbol{v} \\
\boldsymbol{u}_j &= \frac{1}{n_j} \int \boldsymbol{v} f_j(\boldsymbol{r}, \boldsymbol{v}, t) \mathrm{d}\boldsymbol{v} \\
\left(\underline{\underline{P}}_j\right)_{l,m} &= m_j \int f_j(\boldsymbol{r}, \boldsymbol{v}, t) \left[ (\boldsymbol{v})_l (\boldsymbol{v})_m - (\boldsymbol{u}_j)_l (\boldsymbol{u}_j)_m \right] \mathrm{d}\boldsymbol{v}
\end{aligned}
$$

The distribution function can be changed by sinks, sources or collisions. If there are no sources or sinks, $f$ can be described by:

$$
\frac{\mathrm{d}f_j}{\mathrm{d}t} = C_j(f_j)
$$

where $C$ is the collision operator. Without collisions the RHS is zero and one can derive the so called Vlasov equation (or collisionless Boltzmann equation):

$$
\frac{\partial f_j}{\partial t} + (\boldsymbol{v} \cdot \boldsymbol{\nabla}) f_j + \frac{1}{m_j} (\boldsymbol{F} \cdot \boldsymbol{\nabla}_v) f_j = 0
$$

where $\boldsymbol{F}$ is a force and the total derivative has been expanded into inertial and advective components.

If one integrates the Vlasov equation over the velocity space (which is equivalent to taking the zeroth moment) one obtains the continuity equation:

$$
\frac{\partial n_j}{\partial t} + \nabla \cdot (n_j \boldsymbol{u_j}) = 0
$$

If one multiplies the Vlasov equation by $m_j \boldsymbol{v}$ and then integrates over the velocity space (or taking the first moment) one can obtain the force balance (or momentum) equation:

$$m_j n_j \left[ \frac{\partial \boldsymbol{u}_j}{\partial t} + (\boldsymbol{u}_j \cdot \boldsymbol{\nabla}) \boldsymbol{u}_j \right] = -\boldsymbol{\nabla} p_j + n_j q_j (\boldsymbol{E} + \boldsymbol{u}_j \times \boldsymbol{B})$$

where the Maxwellian distribution was assumed to reduce the pressure tensor to a scalar with $p_j = n_j k_B T_j$. To obtain an expression for the pressure $p_j$ one could take the next moment of the Vlasov equation. Instead we assume an adiabatic behaviour which is given by $p_j V^\Gamma = \text{constant} = C$ where $V$ is the volume and $\Gamma$ is the ratio of the specific heats. The pressure is then given by:

$$p_j = C n_j^\Gamma$$

To obtain the MHD model from a two-fluid model (with electrons and ions) one must use the following approximations:

$$n_i \approx n_e = n$$

$$m_e u_e \ll m_i u_i$$

$$m_e \ll m_i$$

and one can use the following definitions:

$$\rho \boldsymbol{v} \equiv n (m_e \boldsymbol{u}_e + m_i \boldsymbol{u}_i)$$

$$\rho \approx n m_i$$

$$\boldsymbol{v} \approx \boldsymbol{u}_i$$

$$p = p_e + p_i$$

where $\rho$ is the mass density of a fluid element. With these definitions and approximations and Maxwell's equation, one obtains the MHD equations:

$$\begin{aligned}
&\text{Conservation of mass:} && \frac{\partial \rho}{\partial t} + \nabla \cdot (\rho \boldsymbol{v}) = 0 && \\
&\text{Momentum equation:} && \rho \frac{d\boldsymbol{v}}{dt} = \boldsymbol{J} \times \boldsymbol{B} - \nabla p && \\
&\text{Energy equation:} && \frac{d}{dt}\left(\frac{p}{\rho^{\Gamma}}\right) = 0 && (2.16) \\
&\text{Ohm's law:} && \boldsymbol{E} + \boldsymbol{v} \times \boldsymbol{B} = 0 && (2.17) \\
&\text{Maxwell's equations:} && && \\
&\text{(Maxwell-Faraday equation)} && \nabla \times \boldsymbol{E} = -\frac{\partial \boldsymbol{B}}{\partial t} && (2.18) \\
&\text{(Ampère's law)} && \nabla \times \boldsymbol{B} = \boldsymbol{J} && \\
&\text{(Gauss's law for magnetism)} && \nabla \cdot \boldsymbol{B} = 0 &&
\end{aligned}$$

where $\rho$ is the mass density, $\boldsymbol{v}$ is the fluid velocity, $\boldsymbol{J}$ is the current density, $p$ is the pressure, $\Gamma$ is the ratio of specific heats and $\boldsymbol{E}$ is the electric field. The convective derivative $\frac{d}{dt}$ can be written as: $\frac{d}{dt} = \frac{\partial}{\partial t} + \boldsymbol{v} \cdot \boldsymbol{\nabla}$. Additionally one can use Ampère's law to replace the current density $\boldsymbol{J}$ in the expression $\boldsymbol{J} \times \boldsymbol{B} = \boldsymbol{B} \cdot \boldsymbol{\nabla} \boldsymbol{B} - \boldsymbol{\nabla} \frac{B^2}{2}$. Therefore the momentum equation can be written as:

$$\rho \left( \frac{\partial \boldsymbol{v}}{\partial t} + \boldsymbol{v} \cdot \boldsymbol{\nabla} \boldsymbol{v} \right) = -\boldsymbol{\nabla} \left( p + \frac{B^2}{2} \right) + \boldsymbol{B} \cdot \boldsymbol{\nabla} \boldsymbol{B}. \tag{2.19}$$

With an additional kinematic, scalar viscosity term that is included to provide simple viscous dissipation [60] the momentum equation becomes:

$$\rho \left( \frac{\partial \boldsymbol{v}}{\partial t} + \boldsymbol{v} \cdot \boldsymbol{\nabla} \boldsymbol{v} \right) = -\boldsymbol{\nabla} \left( p + \frac{B^2}{2} \right) + \boldsymbol{B} \cdot \boldsymbol{\nabla} \boldsymbol{B} + \nu \rho \triangle \boldsymbol{v}.$$

where the Laplace operator $\Delta$ is defined as $\Delta \equiv \boldsymbol{\nabla}^2$ and $\boldsymbol{v} = \frac{\partial \boldsymbol{r}}{\partial t}$ is the velocity and $\nu$ is the scalar viscosity.

### 2.2.2. Lagrangian MHD

We choose to perform the calculation later in this thesis in Lagrangian variables. In this approach all quantities can be expressed in terms of the displacement $\boldsymbol{\xi}$ of a fluid element. The position vector of a fluid element, $\boldsymbol{r}(t)$, is related to its initial position vector, $\boldsymbol{r}_0$, through $\boldsymbol{r}(t) = \boldsymbol{r}_0 + \boldsymbol{\xi}(\boldsymbol{r}_0, t)$ (see Fig. 2.2), so that the components of the Jacobian matrix

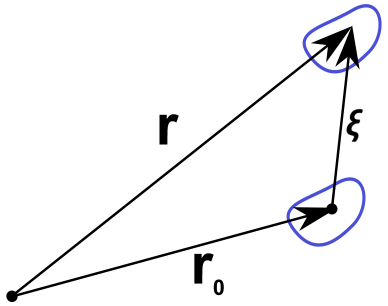


Figure 2.2.: *The movement of a fluid element with its starting position $\boldsymbol{r}_0$, its position $\boldsymbol{r}$ at time $t$ and the vector connecting the two position vectors: $\boldsymbol{\xi}$, which is the displacement vector.*

$J_{ij}$ are

$$J_{ij} = (\boldsymbol{\nabla}_0 \boldsymbol{r})_{ij} = \delta_{ij} + \frac{\partial \xi_j}{\partial x_{0i}},$$

where $x_{0i}$ are the components of $\boldsymbol{r}_0$ and $i, j$ run from 1 to 3 to label $x$, $y$ and $z$ coordinates of a Cartesian system. The operator $\nabla_0$ is defined as derivatives with respect to $x_0$, $y_0$ and $z_0$ and in general the subscript "0" indicates an equilibrium quantity when we use the Lagrangian description. The Jacobian $J$ is the determinant of the Jacobian matrix $J_{ij}$.

$$J = 1 + \boldsymbol{\nabla}_0 \cdot \xi + \frac{1}{2}\left[(\boldsymbol{\nabla}_0 \cdot \boldsymbol{\xi})^2 + (\boldsymbol{\xi} \cdot \boldsymbol{\nabla}_0)(\boldsymbol{\nabla}_0 \cdot \boldsymbol{\xi}) - \boldsymbol{\nabla}_0 \cdot (\boldsymbol{\xi} \cdot \boldsymbol{\nabla}_0 \boldsymbol{\xi})\right] + \mathcal{O}(\boldsymbol{\xi}^3) \qquad (2.20)$$

A unit volume at $\boldsymbol{r}$ is given by: $\mathrm{d}\boldsymbol{r} = J\mathrm{d}\boldsymbol{r}_0$. Conservation of mass is equivalent to: $\rho_0 \mathrm{d}\boldsymbol{r}_0 = \rho(\boldsymbol{r}, t) J \mathrm{d}\boldsymbol{r}_0$ where the density at position $\boldsymbol{r}$ at time $t$ is $\rho(\boldsymbol{r}, t)$ and the equilibrium density at $\boldsymbol{r}_0$ is $\rho_0(x_0)$. This yields

$$\rho(\boldsymbol{r}, t) = \frac{\rho_0(\boldsymbol{r}_0)}{J}.$$

Exploiting Eq. (2.16) and the expression for $\rho(\boldsymbol{r},t)$ we obtain:

$$p(\boldsymbol{r},t)=\frac{p_0(\boldsymbol{r}_0)}{J^\Gamma}$$

The conservation of magnetic flux yields (using equations (2.17) and (2.18)):

$$\boldsymbol{B}(\boldsymbol{r},t)=\frac{\boldsymbol{B}_0(\boldsymbol{r}_0)\cdot\boldsymbol{\nabla}_0\boldsymbol{r}}{J}.$$

With these results the ideal MHD momentum equation in the Lagrangian description is:

$$\begin{aligned}\frac{\rho_0}{J}(\boldsymbol{\nabla}_0\boldsymbol{r})\cdot\frac{\partial^2\boldsymbol{\xi}}{\partial t^2}=&-\boldsymbol{\nabla}_0\left[\frac{p_0}{J^\Gamma}+\frac{|(\boldsymbol{B}_0\cdot\boldsymbol{\nabla}_0\boldsymbol{r})|^2}{2J^2}\right]\\&+(\boldsymbol{\nabla}_0\boldsymbol{r})\cdot\left[\frac{1}{J}(\boldsymbol{B}_0\cdot\boldsymbol{\nabla}_0)\left(\frac{1}{J}(\boldsymbol{B}_0\cdot\boldsymbol{\nabla}_0\boldsymbol{r})\right)\right].\end{aligned}\tag{2.21}$$

A complete derivation of the Lagrangian MHD can be found in [61].

### 2.2.3. Equilibrium

At this point it is useful to discuss the equilibrium case as it will be used later. The equilibrium is characterised by $\frac{\partial}{\partial t}\approx 0$ in Eq. (2.19). This leads to:

$$\boldsymbol{\nabla}\left(p+\frac{B^2}{2}\right)=\boldsymbol{B}\cdot\boldsymbol{\nabla}\boldsymbol{B}\tag{2.22}$$

or

$$\boldsymbol{\nabla}p=\boldsymbol{J}\times\boldsymbol{B}\tag{2.23}$$

The right hand side of Eq. (2.22) defines the so called magnetic curvature $\boldsymbol{\kappa}$:

$$\begin{aligned}\boldsymbol{\kappa}&\equiv\boldsymbol{B}\cdot\boldsymbol{\nabla}\boldsymbol{B}\\&=\boldsymbol{\nabla}\left(p+\frac{B^2}{2}\right)\end{aligned}\tag{2.24}$$

That the curvature is equal a gradient of plasma pressure and magnetic pressure is used many times in the nonlinear analysis later in this thesis.

#### Flux surfaces

Using Eq. (2.23) one can easily see that magnetic field lines lie on constant pressure surfaces since:

$$\boldsymbol{B} \cdot \boldsymbol{\nabla} p = 0$$

The same is valid for the current $\boldsymbol{J}$ as:

$$\boldsymbol{J} \cdot \boldsymbol{\nabla} p = 0$$

These surfaces on which the currents and magnetic field lines lie are called flux surfaces and they are usually labelled with $\psi$:

$$\boldsymbol{B} \cdot \nabla \psi = 0$$

$$\boldsymbol{J} \cdot \nabla \psi = 0$$

In axisymmetric equilibria these flux surfaces can be closed and nested. However, this is not always the case in non-axisymmetric scenarios. Several quantities are so called flux quantities since they only depend on $\psi$ like the pressure $p = p(\psi)$ or the quantity $f$ defined in 2.1 $f = f(\psi)$.

#### Grad-Shafranov equation

A very important equation which describes equilibrium in an axisymmetric plasma is the Grad-Shafranov equation [62]. It is given by:

$$\Delta^* \psi \equiv R^2 \nabla \cdot \left( \frac{\nabla \psi}{R^2} \right) = -R^2 p'(\psi) - f f'(\psi) \tag{2.25}$$

where the primes denote a derivative with respect to the flux variable $\psi$.

### 2.2.4. Energy principle

One can calculate the change of potential energy $\delta W$ caused by perturbation to determine the stability of the plasma [63]. If $\delta W$ is negative it means that the plasma has lost potential energy, converting it to kinetic energy and therefore it is unstable. If $\delta W$ for any

possible perturbation is positive the plasma is stable and if it is equal to 0, it is considered marginally stable, see Fig. 2.3. The plasma contribution to the energy in the intuitive form

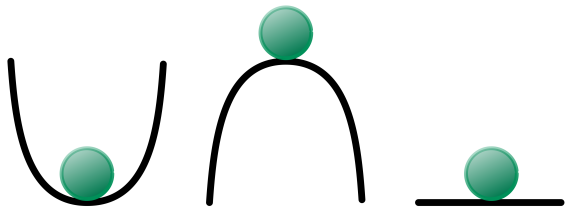

Figure 2.3.: *Mechanical analogues for a stable, an unstable and a marginal stable case.*

is given by [57]:

$$\delta W = \frac{1}{2}\int \mathrm{d}V \Bigg\{ \begin{aligned} &|\boldsymbol{B}_1|^2 && \text{Field-line bending} \geq 0 \\ &+ B^2|\nabla\cdot\boldsymbol{\xi}_\perp + 2\boldsymbol{\xi}_\perp\cdot\boldsymbol{\kappa}|^2 && \text{Magnetic compression} \geq 0 \\ &+ \Gamma p_0|\nabla\cdot\boldsymbol{\xi}|^2 && \text{Plasma compression} \geq 0 \\ &- 2\left(\boldsymbol{\xi}_\perp\cdot\nabla p\right)\left(\tilde{\boldsymbol{\kappa}}\cdot\boldsymbol{\xi}_\perp^*\right) && \text{Pressure gradient} + \text{ or } - \\ &- \boldsymbol{B}_1\cdot\left(\boldsymbol{\xi}_\perp\times\boldsymbol{b}\right) j_\parallel \Bigg\} && \text{Parallel current drive} + \text{ or } - \end{aligned} \tag{2.26}$$

where $\boldsymbol{B}_1 = \boldsymbol{\nabla}\times(\boldsymbol{\xi}\times\boldsymbol{B}_0)$, the $^*$ indicates a complex conjugated vector, and $\tilde{\boldsymbol{\kappa}} \equiv \boldsymbol{b}\cdot\boldsymbol{\nabla}\boldsymbol{b}$ with $\boldsymbol{b} \equiv \dfrac{\boldsymbol{B}}{|\boldsymbol{B}|}$ and $\tilde{\boldsymbol{\kappa}} = -\dfrac{\boldsymbol{R}_c}{R_c^2}$ [57]. The first three terms can only be stabilising since they are always positive. The last two terms can be either stabilising or destabilising.

## 2.3. Ballooning instability

### 2.3.1. Ballooning modes

Ballooning modes are pressure driven MHD instabilities which appear in toroidal devices. They are driven by a combination of the pressure gradient and field line curvature and typically have high mode numbers. Additionally they set a limit on the maximum stable

$\beta$ which is defined as:

$$\beta = \frac{2p}{B^2}.$$

$\beta$ is therefore a measure of how strong the magnetic field pressure $\frac{B^2}{2}$ is compared to the plasma pressure $p$. The geometry of ballooning modes is caused by good and bad curvature and typically takes the form shown in Fig. 2.4 [64], which is the reason for their name.

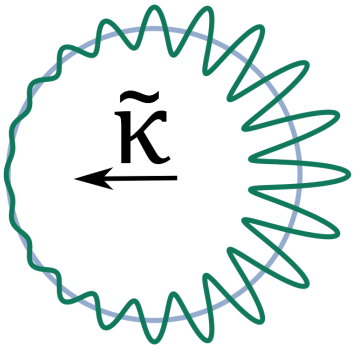


Figure 2.4.: *Ballooning structure at a poloidal cross section. The instability is smaller at the inboard side (good curvature) and larger at the outboard side (bad curvature).*

#### Good and bad curvature

If one assumes a perturbation on the plasma edge with the pressure gradient $\nabla p$ pointing in the same direction as the curvature $\tilde{\boldsymbol{\kappa}}$, one obtains a charge separation by the curvature drift (equation (1.2)), which then leads to a destabilising $E \times B$ drift (equation (1.1)), see Fig. 2.5. This is called bad curvature. However, if one assumes the pressure gradient $\nabla p$ to point in the opposite direction relative to the curvature $\tilde{\boldsymbol{\kappa}}$, one obtains a stabilising $E \times B$ drift (Fig. 2.5). This combination of pressure gradient and curvature is called good curvature.

The same can be observed when investigating the pressure gradient term in the energy equation (see Eq. (2.26)). If the vector of the pressure gradient and the curvature vector have the same sign the entire term is negative and therefore destabilising. However, if they point in different directions, this term becomes positive and therefore stabilising. In a tokamak the bad curvature normally lies on the low field side and the good curvature normally lies on the high field side, see Fig. 2.6. This explains why the ballooning modes are mainly found at the outboard side of a tokamak, as shown in Fig. 2.4.

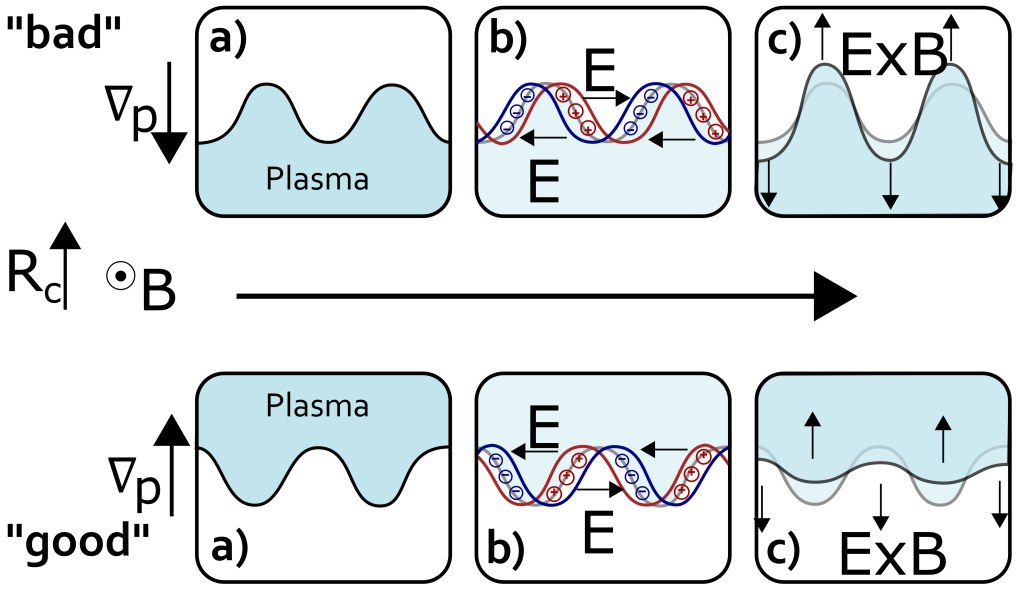


Figure 2.5.: *A sketch for an intuitive picture of bad (top) and good (bottom) curvature. a) a small perturbation; b) the radius of curvature crossed with the magnetic field creates a curvature drive (see Eq. (1.2)) in opposite directions for positive and negative charges which leads to an electric field; c) Bad curvature (top): the $E \times B$ drift reinforces the perturbation because of the pressure gradient; Good curvature (bottom): the $E \times B$ drift reduces the perturbation because of the pressure gradient.*

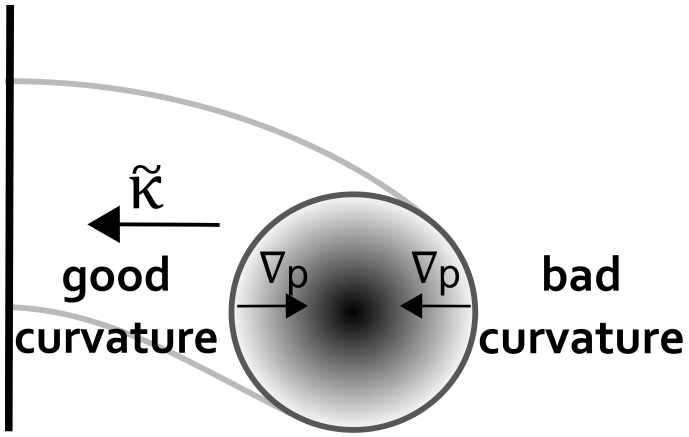


Figure 2.6.: *Good and bad curvature in a circular cross section tokamak.*

### 2.3.2. Ballooning stability

With the MHD energy principle one can determine if a plasma is unstable to certain instabilities. The so called Mercier criterion is a necessary but not sufficient local condition

for interchange stability in tokamaks [65] which was derived from the energy principle (similar to the Suydam criterion [66] which is the cylindrical limit of the Mercier criterion). The Mercier criterion is:

$$D_M < \frac{1}{4}$$

where $D_M$ is the Mercier coefficient[1] [65] which only depends on equilibrium quantities [57]. One has to test each flux surface for Mercier stability. If a plasma is Mercier stable (which means none of the flux surfaces are Mercier unstable), then the linear ballooning mode differential equation is applicable to test ballooning stability. This equation is of the following form:

$$(\boldsymbol{B}_0 \cdot \boldsymbol{\nabla}_0) \left[ \frac{|\boldsymbol{e}_\perp|^2}{B_0^2} (\boldsymbol{B}_0 \cdot \boldsymbol{\nabla}_0) X \right] + \frac{2\mu}{B_0^4} \left( \boldsymbol{e}_\perp \cdot \boldsymbol{\kappa}_0 \right) \left( \boldsymbol{e}_\perp \cdot \boldsymbol{\nabla}_0 p_0 \right) X = 0 \tag{2.27}$$

where $X$ describes the leading order radial displacement[2] and $\mu(\psi)$ is the so called ballooning eigenvalue which has to be determined. If $1 - \mu$ is positive the plasma is ballooning unstable, if it is negative the plasma is stable and if it is equal to zero, the plasma is marginally stable [57].

### 2.3.3. Nonlinear ballooning theory

In this subsection an overview of the development of the nonlinear ballooning model is outlined. But since there is an entire Chapter which describes the derivation of the nonlinear ballooning model in tokamak geometries (Chapter 3) and an Appendix deriving the nonlinear ballooning model in slab geometries (Appendix D), this subsection is relatively concise.

Cowley et al.[1, 67] used nonlinear calculations to determine a mechanism for the behaviour of a plasma detonation (such as solar flares or precursors of tokamak disruptions), exploiting a Rayleigh-Taylor instability in a line tied equilibrium. After this, Hurricane et al.[3] described the filamentary eruptions with the nonlinear ballooning approach, but for generalised magnetic field geometries. Fong et al. [68, 69] investigated how a finite Larmor radius affects the evolution of the filaments. In 2003 the nonlinear envelope equation for

[1] See Eq. (3.9) for more detail.

[2] The leading order radial displacement can be separated into two function $\hat{\chi}$ and $X$ where only $X$ depends on the field aligned variable, see Eq. (3.30) for more detail.

some toroidal cases was derived by Cowley et al. [70], which mentioned the potential application for ELMs. Wilson and Cowley [2] continued these calculations for a more complete tokamak geometry and therefore presented the nonlinear ballooning differential equations for tokamaks. In [4] (or for more details [71]) there is a more detailed description of how filaments behave in plasmas including the nonlinear ballooning model with an additional scalar viscosity term. The investigation of the viscosity and how it changes the evolution is presented in more detail in Section 4.2 of Chapter 4. Additionally how filaments with different initial sizes interact with each other has been investigated [5], and is presented in Chapter 4.

The nonlinear ballooning model has been derived by using the momentum equation (4.2). To solve the incompatibility problem of shear and periodicity[3], we assume that the investigated filament lies on a non-rational magnetic field line or that the filament decays sufficiently fast along the field line so that there is no problem of overlapping.

This model is not just used to determine stability, but to predict the early evolution of filaments with their explosive growth. Some indications that this model describes ELMs are that it can explain why the inter-ELM times are long compared to explosive growth of the ELMs, why the ELMs have filamentary structures, and why the spacing between ELM filaments are larger than the ELM filament width.

To allow, however, a quantitative comparison between this nonlinear ballooning theory and experiments (e.g. ELMs) one must evaluate the coefficients of the nonlinear ballooning equation for tokamak geometries. Previously only one of the coefficients has been evaluated for a model JET-like equilibrium [73]. A full study of all relevant coefficients has now been done and is presented in Chapter 5.

## 2.4. Current knowledge of ELMs

ELMs are quasi-periodic instabilities which grow very rapidly and have a filamentary structure [37, 45, 74], see Fig. 2.7, which was correctly predicted by the nonlinear ballooning model [75]. They release a large amount of energy (e.g. approximately 15% of stored energy during Type I ELMs in JET [77]) which is still tolerable in current tokamaks but

[3]This problem is usually solved with the so called ballooning formalism [56, 72]. However, we analyse nonlinear terms, for which the ballooning mode formalism is not applicable.

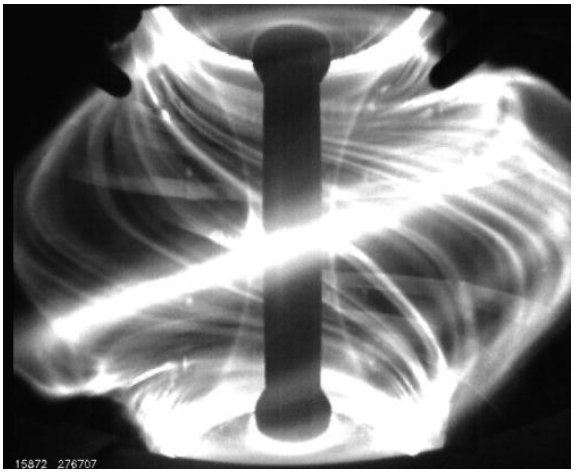


Figure 2.7.: *High speed camera image of an ELM in MAST [76]. Filamentary structure of the ELM is evident.*

is a potential issue for future tokamak devices such as ITER [31]. However, there are also advantages to ELMs since they do not only release energy but also flush out impurities [78]. This is needed because the high $Z$ impurities radiate energy from the core decreasing the energy confinement.

#### Types of ELMs and ELM mitigation

There are different kinds of ELMs including Type I or large ELMs (e.g. in MAST and ASDEX Upgrade [45, 74]), Type II or grassy ELMs (e.g. in JET [79, 80]; in ASDEX Upgrade [54]), Type III or small ELMs (e.g. in JET [81]), and small Type V ELMs at NSTX [82]. They are characterized by the dependence of the repetition frequency on heating power and by different kinds of ancillary effects, [83, 84]. For example Type I ELMs are large and less frequent, and Type III ELMs are smaller and more frequent. Additionally, each of these types has a preferred operating regime [76, 85, 86].

Ideally Type I ELMs should be suppressed because they are the most harmful ones. Other mechanisms to decrease the impurities should instead be identified, such as smaller ELMs. There are several approaches to mitigating Type I ELMs [87]. One of them is to trigger the smaller ELMs via pellet injection in the regime of the Type I ELMs [88]. These pellets could be used to inject the fuel needed in future fusion power plants. Therefore, it is possible to maximize the confinement without having the large ELMs. Another approach is magnetic triggering or vertical kicks which uses a vertical movement of the plasma to change the

plasma conditions such that a less harmful type of ELM is triggered [89, 90]. One method which can not only mitigate but also suppress ELMs is resonant magnetic perturbations (RMPs) which create a stochastic magnetic boundary to suppress the ELMs [91–93].

### 2.4.1. ELM theory and simulation

#### Theory

The leading theory for the Type I ELMs is the peeling-ballooning model [94–96]. It com-

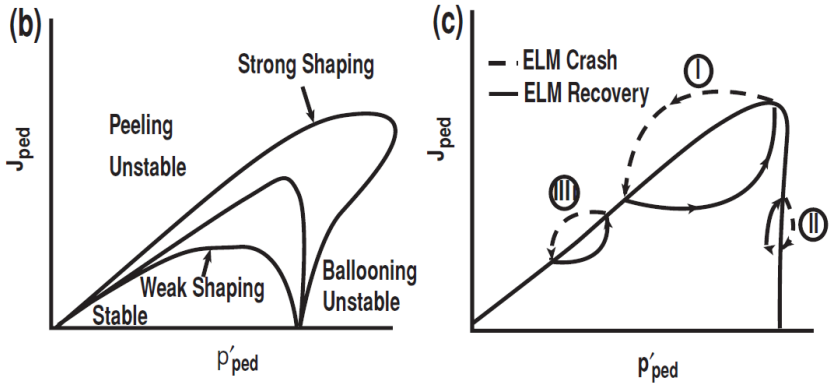


Figure 2.8.: *Left: Sketch of peeling-ballooning stability limits for different shaping. The peeling limit is reached by increasing the pedestal current (y-axis) and the ballooning limit is reached by exceeding certain pressure gradients (x-axis). Right: A model of ELM cycles of Type I, II and III is shown. Type I ELMs appear at a peeling-ballooning limit, Type II ELMs appear at the ballooning limit, and Type III ELMs are caused by the peeling limit [96].*

bines the boundaries of two instabilities: ballooning instability and the peeling instability, [30, 94], see Fig. 2.8. These modes are driven by different sources of free energy. The ballooning instability was discussed before in Sect. 2.3. In H-mode a large edge current (Bootstrap current) exists which can drive peeling modes that are typically driven by the edge current density and stabilized by the edge pressure gradient. Peeling modes have rather small toroidal mode number (8-10). The peeling-ballooning model can also provide an ELM cycle model for the other types of ELMs, see Fig. 2.8. The MHD stability code ELITE can evaluate at which stability boundary an equilibrium is located [97] and there has been good agreement of the peeling-ballooning model with experiments [96, 98].
Furthermore the nonlinear ballooning theory describes the early nonlinear evolution of ELMs, see Sect. 2.3.3 for more details.

#### Simulations

There are many simulations of ELMs with less reduced models than the nonlinear ballooning model for example: there have been ELM simulations with BOUT++[99–101]; BOUT [102] which produces qualitatively the same results as analytic nonlinear ballooning theory predicts [73]; with JOREK [103] and with NIMROD [104]. However, it seems that to reach the point where ELMs self-consistently develop in the simulations one must change the plasma parameters in such a way that the plasma is beyond the peeling-ballooning boundary. The initial growth depends on how far beyond the stability boundary the parameters where chosen. Therefore these simulations cannot be used to predict ELM sizes with certainty at this stage [105].

## 2.5. Computational background

For the research presented within this thesis, enhancements have been made primarily to two different codes. In this section, some of the fundamental methods used in these codes are described.

### 2.5.1. Deton8

Deton8 was written in Fortran90 to investigate one of the two differential equations of the nonlinear ballooning model [2] and edited and benchmarked [106]. Deton8 evaluates the ballooning envelope equation for up-down symmetric equilibria of the following form:

$$D_0\kappa\frac{\partial^\lambda}{\partial t^\lambda}\xi = \left(D_1 - \frac{(\psi-\psi_0)^2}{\Delta^2}\right)\xi - D_2\frac{\partial^2 u}{\partial\psi^2} + D_3\left(\xi^2 - \overline{\xi^2}\right) + D_4\xi\frac{\partial^2\overline{\xi^2}}{\partial\psi^2} \tag{2.28}$$

where $\xi$ is the displacement which depends on the spatial variables $\alpha$, $\psi$ (see Sect. 2.1.1), the time $t$, and the quantity $\lambda$ which can only be between 1 and 2 in this model [2]. The variable $u$ is defined by $u = \frac{\partial^2\xi}{\partial\alpha^2}$, the overbar is indicating an average over the $\alpha$ variable, the $\Delta$-term originates from a Taylor expansion of the eigenvalue $\mu$ and therefore $\Delta$ has to be determined from equilibrium quantities, and $\kappa = \Gamma(2-\lambda)$ is the complete gamma

function. The fractional derivative in the LHS of Eq. (2.28) is given by:

$$\frac{\partial^\lambda}{\partial t^\lambda} f(t) = \frac{1}{\Gamma(2-\lambda)} \frac{\partial^2}{\partial t^2} \int_0^t \mathrm{d}t' \frac{f(t')}{(t-t')^{(\lambda-1)}}$$

Each of the coefficients $D_i$ in Eq. (2.28) depends on the equilibrium. However, one can modify the variables $\alpha$, $\psi$, $t$ and the displacement $\xi$ in a way such that all the coefficients disappear. Then the equation is a generic equation with the exception of the parameter $\Delta$. The code itself can compute this generic ballooning envelope equation by simply setting all coefficients equal 1.

#### Predictor-corrector method

The code exploits a finite difference method for solving this partial differential equation. More precisely this method is an iterative predictor-corrector algorithm [107]. This numerical method is a combination of an explicit and implicit method. In our case, Euler's method is the first step which is explicit and is used to solve problems of the following form:

$$\frac{dy(t)}{dt} = f(t, y(t)) \tag{2.29}$$

with an initial condition: $y(t_0) = y_0$ and the time $t_{n+1} = t_n + \Delta t$ with $n$ being the label for the time steps with size $\Delta t$.

The first guess for the solution at the next time step with Euler's method is:

$$y_{n+1}^{(1)} = y_n + \Delta t \cdot f(t_n, y_n)$$

where the (1) labels that it is the first iteration value for $y_{n+1}$. This subsequent correction is an implicit method of the following form:

$$y_{n+1}^{(i)} = y_n + \frac{1}{2}\Delta t \left[ f(t_n, y_n) + f\left(t_{n+1}, y_{n+1}^{(i-1)}\right) \right]$$

where $i$ labels the iteration step and starts with 2.

This expression is an average of the right hand side of equation (2.29) for the previous time step ($n$) and the $n+1$ time step of the previous iteration multiplied by the time difference

$\Delta t$. This implicit method is called the trapezoidal rule.

Deton8 solves a set of two first order differential equations of the form (2.29) with this predictor corrector method. For $\lambda = 2$ the set of differential equations is:

$$\frac{\mathrm{d}y}{\mathrm{d}t} = \left(D_1 - \frac{(\psi - \psi_0)^2}{\Delta^2}\right)\xi - D_2\frac{\partial^2 u}{\partial \psi^2} + D_3\left(\xi^2 - \overline{\xi^2}\right) + D_4\xi\frac{\partial^2\overline{\xi^2}}{\partial\psi^2}$$
$$\frac{\mathrm{d}\xi}{\mathrm{d}t} = y$$

For $\lambda = 1$ the second equation changes to: $\xi = y$ and therefore Deton8 only solves one differential equation in that case.

### 2.5.2. Mercier-Luc formalism

The Mercier-Luc formalism [108] is a technique to provide equilibrium quantities of adjoining flux-surfaces by expanding the Grad-Shafranov equation (2.25) locally near to the reference flux surface, which enables one to calculate radial derivatives. These are required to determine the coefficients of the ballooning mode envelope equation for tokamak geometries (Chapter. 5), in particular the second order expansion is needed. The original Mercier-Luc formalism uses only a first-order expansion of the flux-surface [108, 109], however, the results of the second order expansion are derived in [97] since the code ELITE requires the second order derivatives.

The Mercier-Luc coordinate system is introduced to expand the Grad-Shafranov equation (2.25). This orthogonal coordinate system consists of $\rho$, $l$ and the toroidal angle $\phi$, see Fig. 2.9. $\rho$ is the radial distance from the reference flux surface $\psi_0$ and $l$ labels the poloidal position on the flux surface $\psi_0$ (Fig. 2.9). The tangent vector of the reference flux surface $\psi_0$ on the poloidal cross section, which is labelled by $R_s(l)$ and $Z_s(l)$, is given by $\boldsymbol{T} = \left(\frac{dR_s(l)}{dl}, \frac{dZ_s(l)}{dl}\right)$ where the subscript $s$ indicates the reference flux surface. The angle $u$ which is introduced to make the calculation clearer can be defined such that $\boldsymbol{T} = (-\sin(u), \cos(u))$. Therefore $\frac{dR_s(l)}{dl} = -\sin(u)$ and $\frac{dZ_s(l)}{dl} = \cos(u)$. It follows that $\frac{\partial u}{\partial l} = -\frac{1}{R_c}$ since the derivative of a tangent vector with respect to $l$ is inversely proportional to the radius of the curvature $R_c$. The Jacobian of the Mercier-Luc coordinate system with respect to the Cartesian coordinate system is given by $J = \left|\frac{\partial(x,y,z)}{\partial(\rho,l,\phi)}\right| = R\left(1 - \frac{\rho}{R_c}\right)$. The approach to obtain analytic expressions for the adjoining flux surfaces is to expand $\psi$ with

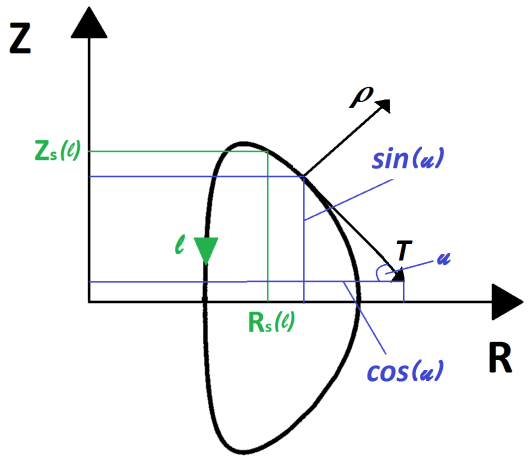


Figure 2.9.: *Mercier-Luc coordinate system.*

respect to $\rho$:

$$\psi = \psi_0 + \rho\psi_1 + \rho^2\psi_2 + \rho^3\psi_3 + \dots$$

The magnetic field is described by $\boldsymbol{B} = \boldsymbol{\nabla}\phi \times \boldsymbol{\nabla}\psi + f(\psi)\boldsymbol{\nabla}\phi$ (see equation (2.15)). Therefore the poloidal component $B_p$ can be expressed as:

$$\begin{aligned} \boldsymbol{B}_p &= \boldsymbol{\nabla}\phi \times \boldsymbol{\nabla}\psi \\ &= \frac{\hat{\mathrm{I}}}{R}\left[\psi_1 + 2\psi_2\rho + 3\psi_3\rho^2\right] - \frac{\hat{\rho}}{R}\left[\frac{\partial\psi_1}{\partial l}\rho + \frac{\partial\psi_2}{\partial l}\rho^2\right] + \mathcal{O}(\rho^3) \end{aligned}$$

The lowest order of this equation determines $\psi_1$:

$$\psi_1 = R_s(l)B_{ps}(l)$$

The Grad-Shafranov equation (2.25) is expanded up to the second order in $\rho$ to obtain $\psi_2$ and $\psi_3$:

$$\begin{aligned}
\psi_2(l) &= \frac{1}{2}\left[\left(\frac{R_s}{R_c}+\sin(u)\right)B_{ps} - R_s^2 p'(\psi_0) - f f'(\psi_0)\right] \\
\psi_3(l) &= \frac{1}{6}\Bigg[ -2B_{ps}\sin(u)\left(\frac{\sin(u)}{R_s}+\frac{1}{R_c}\right) + 4\psi_2\left(\frac{\sin(u)}{R_s}+\frac{1}{R_c}\right) \\
&\quad -R_s\frac{\partial}{\partial l}\left(\frac{1}{R_s}\frac{\partial\psi_1}{\partial l}\right) - R_s^2 p'(\psi_0)\left(\frac{\sin(u)}{R_s}-\frac{1}{R_c}\right) \\
&\quad +f f'(\psi_0)\left(\frac{\sin(u)}{R_s}+\frac{1}{R_c}\right) - R_s B_{ps}(R_s^2 p''(\psi_0) + (f f')'|_{\psi=\psi_0}\Bigg]
\end{aligned}$$

### 2.5.3. Algorithm for determining the ballooning eigenvalue $\mu$

In this section we present an algorithm to determine numerically the ballooning eigenvalue $\mu$ and the function $X$, which describes the radial displacement (see Eq. (3.30)) and is determined by Eq. (2.27). The differential equation and $\lambda_S$ depend on the eigenvalue. For the first iteration $n = 1$ we set the first two eigenvalues to one and just below one: $\mu_0 = 1$ and $\mu_1 = 0.999$. We start the algorithm by determining $X$ for $\chi > 0$.

#### Shooting method for $\chi > 0$

The Runge-Kutta-Nyström method (e.g. [110]) is used to solve the linear ballooning equation (2.27) which is a second order differential equation for the shape of the displacement along the magnetic field line. This method is an initial value solver, however, the boundary values are given for the displacement instead. This is why the shooting method is exploited, as it can convert a boundary value problem to an initial value problem, [111]. Starting with a second order differential equation:

$$X'' = pX' + qX + r \tag{2.33}$$

with the boundary conditions: $X(0) = 1$ and $X'(\chi_a) = D$ where $D \approx -\lambda_S X(\chi_a)/\chi_a$ is determined in Chapter 3 via an asymptotic treatment of the derivative of $X$ with respect to $\chi$, which is the field aligned variable. $\chi_a$ is the largest value of $\chi$ in the numerical

calculation and $\lambda_S$ is defined as:

$$\lambda_S = \frac{1}{2} + \sqrt{\frac{1}{4} - D_M}.$$

The function $X$ can be split up into two functions: $X = X_1 + c\,X_2$ with the following properties of $X_1$ and $X_2$:

$$X_1'' = p\,X_1' + q\,X_1 + r$$
$$X_2'' = p\,X_2' + q\,X_1$$

and the boundary conditions:

$$\begin{aligned} X_1(0) &= 1,\ X_1'(0) = 0 \\ X_2(0) &= 0,\ X_2'(0) = 1 \end{aligned} \tag{2.34}$$

The sum of $X_1$ and $cX_2$ satisfies (2.33) which can be easily seen by substituting $X = X_1 + c\,X_2$ into equation (2.33). The boundary conditions (2.34) are exploited to determine the scaling factor $c$. The boundary condition of the original function is

$$X'(\chi_a) = D \approx -\lambda_S\,X(\chi_a)/\chi_a \tag{2.35}$$

Now $X = X_1 + c\,X_2$ is substituted into equation (2.35):

$$\begin{aligned} X_1'(\chi_a) + c\,X_2(\chi_a)' &= -\lambda_S\,X_1(\chi_a)/\chi_a - c\lambda_S\,X_2(\chi_a)/\chi_a \\ \Rightarrow c &= -\frac{\lambda_S\,X_1(\chi_a) + \chi_a\,X_1'(\chi_a)}{\chi_a\,X_2(\chi_a) + \lambda_S\,X_2(\chi_a)} \end{aligned} \tag{2.36}$$

The numerical procedure to find the solution of the linear ballooning equation for $\chi > 0$ is to determine the functions $X_1$ and $X_2$ with the Runge-Kutta-Nyström method, then calculate the scaling factor $c$ with equation (2.36). The solution of this iteration $n$ of the linear ballooning equation for $\chi > 0$ is then given by $X_+^n = X_1 + cX_2$ where the $+$ indicates that the function $X$ is calculated along the positive $\chi$ range.

#### Secant method for $\chi < 0$

For negative $\chi$ ones solves the differential equation (2.33) again with the Runge-Kutta-Nyström method with the boundary condition $X_-^n(0) = X_+^n(0)$ where the $-$ indicates the negative $\chi$ range and ${X'_-}^n(0) = {X'_+}^n(0)$. Analytically we know that $X'_- = \frac{\lambda_S X}{\chi}$ for $\chi \ll -1$. Therefore we define a function $\Delta$:

$$\Delta(\mu_n) \equiv -\chi_a X_-^n(-\chi_a) + \lambda_s {X'_-}^n(-\chi_a)$$

With the correct eigenvalue $\mu$ this function $\Delta$ is zero. We use the secant method to find the root of $\Delta$ [110]:

$$\mu_{n+1} = \mu_n - \Delta(\mu_n)\frac{\mu_n - \mu_{n-1}}{\Delta(\mu_n) - \Delta(\mu_{n-1})}$$

After updating the eigenvalue $\mu$ we must re-apply all of what was presented: re-calculating $X_+$ and then $X_-$. This entire routine is iterated until the correct eigenvalue $\mu$ is obtained for which $\Delta(\mu) = 0$.

## 2.6. Summary

We have now provided a technical background: of the coordinate systems used in this thesis and of the MHD description which is needed to derive the nonlinear ballooning model. A physical description has been given of the ballooning instability which is described by the nonlinear ballooning model, and the current experimental knowledge of ELMs since we will examine whether the nonlinear ballooning model can describe ELMs quantitatively. Furthermore we provided some background on the computational methods used.
In the next chapter the nonlinear ballooning model for tokamak geometries is derived.

# 3. Derivation of the nonlinear ballooning model for tokamak geometries

The derivation of the nonlinear ideal MHD ballooning model for tokamak geometries is outlined in this chapter. This theory is originally derived by Wilson and Cowley [2] and builds on previous work [1, 3, 70]. However, a detailed description of the derivation for tokamak geometry has not been published yet and therefore it will be provided here for the convenience of the reader.

The result of the derivation is two differential equations: the linear ballooning equation which describes the displacement of the filaments along the field lines and the nonlinear ballooning mode envelope equation, which is a two-dimensional, nonlinear differential equation which can involve fractional temporal-derivatives but is often second-order in time and space.

This chapter starts with the ordering and boundary condition used for the derivation (Sect 3.1). One of the basic ideas of the derivation is to divide the magnetic field line into segments where different physical mechanisms are dominant (shown in Section 3.2 and Fig. 3.1): the nonlinear region is discussed in Subsection 3.2.3, the inertial region in Subsection 3.2.1 and the matching region of inertial and nonlinear solutions is discussed in 3.2.2, 3.2.4 and 3.2.5. In the final section, where the matching of the two main regions is described, the final ballooning envelope equation is derived.

The following Chapter 4 applies the ballooning envelope equation to investigate the interaction between these filaments. The coefficients of this equation are field-line averaged quantities and depend strongly on the geometry. To get quantitative results we must determine these coefficients, which will be described in Section 5.1 of Chapter 5 for tokamak geometries and then used in the following sections.

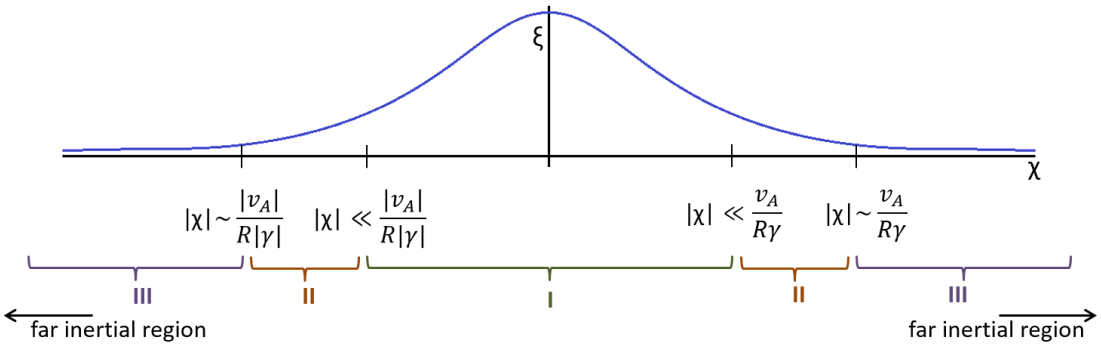


Figure 3.1.: *Regions along a magnetic field line. Region I: nonlinear region(Section 3.2.3); Region II: matching region (Sections 3.2.2, 3.2.4 and 3.2.5) and Region III: inertial region (Section 3.2.1).*

In this chapter all the coordinate systems presented in Section 2.1 are used.

## 3.1. Ballooning ordering and boundary conditions

In this section we introduce the common ordering of ballooning modes and the boundary conditions which will be used in the entire chapter.

### 3.1.1. Ordering

A dummy small parameter $\epsilon$ (which is related to $n$ of Chapter 4 by $n \sim \epsilon^{-2}$) is commonly used in ballooning theory to simplify the MHD momentum equation, in our case the Lagrangian momentum Eq. (2.21). This parameter $\epsilon$ exploits the geometry of the linear ballooning mode, as the ballooning instability varies slowly along the magnetic field, moderately radially outwards and rapidly in the remaining spatial direction perpendicular to the field lines. This can be expressed by ordering the spatial derivatives as well as the order of the Lagrangian displacement [56]:

$$\frac{\partial}{\partial\psi} \sim \mathcal{O}(\epsilon^{-1}) \qquad \frac{\partial}{\partial\alpha} \sim \mathcal{O}(\epsilon^{-2}) \qquad \frac{\partial}{\partial l} \sim \mathcal{O}(1)\,.$$

where the coordinate system with $\psi$, $\alpha$ and $l$ is described in Sect. 2.1.1 and their derivatives are given by equations (2.5) where they are related to the basis vectors $\boldsymbol{e}_\perp$, $\boldsymbol{e}_\wedge$ and $\boldsymbol{B}_0$ (see Equations (2.11) and (2.12)).

With Lagrangian variables all quantities can be expressed in terms of the displacement

$\boldsymbol{\xi}$ of a fluid element. The position vector of a fluid element, $\boldsymbol{r}(t)$, is related to its initial position vector, $\boldsymbol{r}_0$, through $\boldsymbol{r}(t) = \boldsymbol{r}_0 + \boldsymbol{\xi}(\boldsymbol{r}_0, t)$, so that the components of the Jacobian matrix $J_{ij}$ are $J_{ij} = (\boldsymbol{\nabla}_0 \boldsymbol{r})_{ij}$ where $i, j$ run from 1 to 3 to label $x$,$y$ and $z$ coordinates of a Cartesian system. The Jacobian $J$ is the determinant of the Jacobian matrix $J_{ij}$.
Expanding the components of the displacement $\boldsymbol{\xi} = \xi_\psi \boldsymbol{e}_\perp + \xi_\parallel \boldsymbol{B}_0 + \xi_\wedge \boldsymbol{e}_\wedge$ and the Jacobian $J$ in powers of $\epsilon$ we anticipate:

$$\xi_\psi = \sum_{i=2}^{\infty} \epsilon^i \xi_\psi^{(i)} \qquad \xi_\parallel = \sum_{i=2}^{\infty} \epsilon^i \xi_\parallel^{(i)} \qquad \xi_\wedge = \sum_{i=3}^{\infty} \epsilon^i \xi_\wedge^{(i)} \qquad J = 1 + \sum_{i=1}^{\infty} \epsilon^i J^{(i)}.$$

If we only have one region because the displacement is decaying fast enough along the magnetic field line, then we describe the inertia as a perturbation. The growth rate $\gamma$ of the most unstable position is of order $\epsilon$ since the ballooning instability initially grows slowly as we assume the plasma to be close to marginally stable. Thus

$$\frac{\partial}{\partial t} \sim \mathcal{O}(\epsilon).$$

in case of a perturbed inertia.
If, however, the displacement decays slower, then we use the three regions as in Fig. 3.1. The inertia must only be considered in the inertial region and is of order:

$$\frac{\partial}{\partial t} \sim \mathcal{O}(\epsilon^0)$$

To derive both possible solutions we will include a perturbed inertia in the nonlinear region. However, this only needs to be considered for a fast decaying displacement along the magnetic field line, where the terms arising from the inertial region can be neglected.

### 3.1.2. Assumptions and boundary conditions

We use the geometry of the ballooning instability to determine the boundary conditions (needed to solve the two differential equations derived in this chapter). The ballooning instability is assumed to be highly localised in the radial direction which is motivated by the filamentary geometry, (see Section 1.4.1) which is equivalent to the following boundary

condition:

$$\lim_{|\psi-\psi_{fil}|\to\infty} \xi = 0 \tag{3.1}$$

where $\psi_{fil}$ is the flux surface, labelling the initial position of the filament. It is not possible to apply the Ballooning Transformation (see [56]) to a nonlinear equation. To avoid the problem of combining shear and periodicity, we require the filament to be on a high order rational surface so that we can assume that the magnetic field line (on which our filament is positioned) is effectively infinitely long. This implies that the filament will vanish before it could overlap with itself, which is the next boundary condition:

$$\lim_{|l|\to\infty} \xi = 0 \tag{3.2}$$

where $l$ measures the distance along a magnetic field line.

In the next section, the variable $\chi$ described in Sect. 2.1.2 is mainly used instead of $l$. $\chi$ increases by $2\pi$ each time one has moved once around poloidally.

## 3.2. Regions along the magnetic field line

The magnetic field line can be divided into three regions to simplify the mathematical description of the displacement, see Fig. 3.1. Far along the magnetic field line when $l \sim \frac{v_A}{\gamma}$ or $\chi \sim \frac{v_A}{R\gamma}$ (where $\gamma$ is the linear growth, $R$ is a typical length scale, and $v_A$ is the Alfvén speed indicating that inertia cannot be neglected) the displacement is assumed to be small since we expect it to decay rapidly. Therefore the nonlinear terms are negligible, but the inertia cannot be treated as a perturbation – hence the name "inertial region"(see Section 3.2.1).

In the nonlinear region, where $|\chi| \ll \left|\frac{v_A}{R\gamma}\right|$, we can treat the inertia as small as we assume the equilibrium to be close to marginal stability. The derivation of these differential equations follows that of [3] and is described in Sect. 3.2.3. The final solution for the displacement of this region needs to match to the inertial region at the matching region.

The matching region is where $\chi$ satisfies $1 \ll |\chi| \ll \frac{v_A}{R\gamma}$. The two expressions for the displacement $\xi$ from the inertial and nonlinear region must match in this region. The matching procedure is described in Section 3.2.2.

### 3.2.1. Inertial region

This region is characterised by a small amplitude of the displacement so that the nonlinear effects can be assumed to be small but the inertia is expected to be large, hence the name for that region. This description is only needed to get a boundary condition via a matching procedure for the nonlinear main region.

#### Asymptotic Equations

In this section we discuss the differential equations for the displacement and for the Jacobian far along the field lines.

Analysing the Lagrangian MHD momentum equation (2.21) up to the third order yields the following three differential equations[1]:

$$\rho_0 \frac{|\boldsymbol{e}_\perp|^2}{B_0^2} \frac{\partial^2 y}{\partial t^2} = (\boldsymbol{B}_0 \cdot \boldsymbol{\nabla}_0) \left[ \frac{|\boldsymbol{e}_\perp|^2}{B_0^2} (\boldsymbol{B}_0 \cdot \boldsymbol{\nabla}_0) y \right] + \frac{2}{B_0^4} (\boldsymbol{e}_\perp \cdot \boldsymbol{\kappa}_0) (\boldsymbol{e}_\perp \cdot \boldsymbol{\nabla}_0 p_0) y + \frac{2\Gamma p_0}{B_0^3} (\boldsymbol{\kappa}_0 \cdot \boldsymbol{e}_\perp) \delta J \tag{3.3}$$

$$\rho_0 B_0^2 \frac{\partial^2 \xi_\parallel}{\partial t^2} = \Gamma p_0 (\boldsymbol{B}_0 \cdot \boldsymbol{\nabla}_0) \delta J \tag{3.4}$$

$$(\boldsymbol{B}_0 \cdot \boldsymbol{\nabla}_0) \xi_\parallel = \left( \frac{\Gamma p_0}{B_0^2} + 1 \right) \delta J + 2 \frac{\boldsymbol{\kappa}_0 \cdot \boldsymbol{e}_\perp}{B_0^3} y \tag{3.5}$$

where $\boldsymbol{\kappa}_0$ is the magnetic field curvature, $p_0$ is the equilibrium pressure, $\Gamma$ is the ratio of specific heats and we have defined $y \equiv \xi_\psi |B_0|$ and $\delta J \equiv J - 1$.

The variable $\chi$, which denotes the position along the equilibrium magnetic field line, can be divided into two variables, as there exists a periodic ($\theta$) and a nonperiodic ($v$) behaviour of all the quantities, see Fig. 3.2. All the equilibrium quantities only depend on the periodic variable $\theta$ which is due to the variation of these quantities along a field line from the low to the high field side of a tokamak. The nonperiodic part is caused by the perturbation. The derivative with respect to $\chi$ can be written as $\frac{\partial}{\partial \chi} = \frac{\partial}{\partial v} + \frac{\partial}{\partial \theta}$ since $df = \frac{\partial f}{\partial v} dv + \frac{\partial f}{\partial \theta} d\theta$. Therefore $(\boldsymbol{B}_0 \cdot \boldsymbol{\nabla}_0)$ can be written as:

$$(\boldsymbol{B}_0 \cdot \boldsymbol{\nabla}_0) = \frac{1}{\hat{\jmath}} \frac{\partial}{\partial \chi} = \frac{1}{\hat{\jmath}} \left( \frac{\partial}{\partial v} + \frac{\partial}{\partial \theta} \right).$$

[1] The derivation for this set of differential equations is not presented here since it is basically the same as for the nonlinear region. The difference is that the inertia enters in the parallel component in second order and the $\boldsymbol{e}_\perp$-component in third order, see Sect. 3.2.3 and Appendix C.1.1.

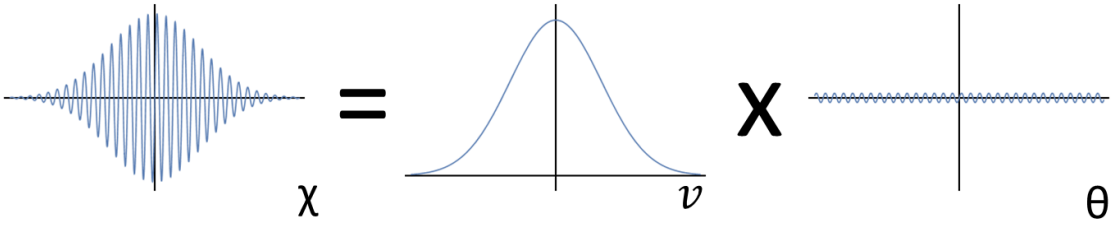


Figure 3.2.: *Here is a sketch of the nonperiodic and periodic behaviour together (on the left) and separated (on the right).*

All quantities which depend on $v$ can be written as inverse orders of $v$, i.e.,

$$\begin{aligned} A(\theta, v) &= \left( \tilde{A}_0(\theta) + \frac{\tilde{A}_1(\theta)}{v} + \frac{\tilde{A}_2(\theta)}{v^2} + \cdots \right) f(v) \\ &= A_0(\theta, v) + \frac{A_1(\theta, v)}{v} + \frac{A_2(\theta, v)}{v^2} + \cdots . \end{aligned}$$

By evaluating the components of the momentum equation (3.3), (3.4), and (3.5) and using the expressions (A.1), (A.2), (A.3) and (A.4) we can show that the lowest orders of $y$ and $\delta J$ do not depend on the periodic variable $\theta$. Additionally the lowest order of $\xi_\parallel$ can be written as a sum with one term independent of $\theta$ and a second part depending on $\theta$:

$$\begin{aligned} y(\theta, v, t) &= Y_0(v, t) + \frac{Y_1(\theta, v, t)}{v} + \cdots \\ \delta J(\theta, v, t) &= \mathcal{J}_0(v, t) + \frac{\mathcal{J}_1(\theta, v, t)}{v} + \cdots \\ \xi_\parallel(\theta, v, t) &= \Xi_{-1}(v, t) + q' I \left( \frac{1}{B_0^2} - \frac{V'}{\langle B_0^2 \rangle_\theta} \right) v Y_0(v, t) + \Xi_0(\theta, v, t) + \cdots \end{aligned}$$

where the angled brackets are defined as:

$$\langle A \rangle_\theta = \frac{1}{2\pi} \oint A \hat{J} \mathrm{d}\theta = \frac{1}{2\pi} \oint A \frac{\mathrm{d}l}{B_0}$$

where $l$ is defined in 2.1.1. Only the lowest order terms of $y$, $\delta J$ and $\xi_\parallel$ are needed since the other orders are small in comparison. These lowest orders ($Y_0, \Xi_{-1}$ and $\mathcal{J}_0$) only depend

on $v$ and are determined by the following differential equations:

$$A_0 v^2 \frac{\partial^2 Y_0}{\partial t^2} = \frac{\partial}{\partial v}\left[v^2 \frac{\partial Y_0}{\partial v}\right] + \tilde{D}_M \left[Y_0 + \frac{\Gamma p_0}{p_0'}\mathcal{J}_0\right] + A_1 v \frac{\partial \mathcal{J}_0}{\partial v} \tag{3.6}$$

$$\frac{\partial \Xi_{-1}}{\partial v} = A_2 \mathcal{J}_0 + A_3 Y_0 + A_4 \frac{\partial (v Y_0)}{\partial v} \tag{3.7}$$

$$A_6 \frac{\partial^2 \Xi_{-1}}{\partial t^2} = A_5 \frac{\partial \mathcal{J}_0}{\partial v} \tag{3.8}$$

with the coefficients defined as:

$$\begin{aligned}
A_0 &= \rho_0 \left\langle \frac{B_0^2}{|\boldsymbol{\nabla}\psi|^2} \right\rangle_\theta \left[ \left\langle R^2 \right\rangle_\theta - \frac{I^2 \left\langle 1 \right\rangle_\theta}{\left\langle B_0^2 \right\rangle_\theta} \right] \\
A_1 &= I \frac{\Gamma p_0}{q'} \left[ \left\langle \frac{1}{|\boldsymbol{\nabla}\psi|^2} \right\rangle_\theta - \left\langle \frac{B_0^2}{|\boldsymbol{\nabla}\psi|^2} \right\rangle_\theta \frac{\left\langle 1 \right\rangle_\theta}{\left\langle B_0^2 \right\rangle_\theta} \right] \\
A_2 &= \left\langle 1 + \frac{\Gamma p_0}{B_0^2} \right\rangle_\theta - I^2 \Gamma p_0 \left[ \left\langle \frac{B_0^2}{|\boldsymbol{\nabla}\psi|^2} \right\rangle_\theta^{-1} \left\langle \frac{1}{|\boldsymbol{\nabla}\psi|^2} \right\rangle_\theta^2 - \left\langle \frac{1}{B_0^2 |\boldsymbol{\nabla}\psi|^2} \right\rangle_\theta \right] \\
A_3 &= \frac{q'^2}{p_0'} \left\langle \frac{B_0^2}{|\boldsymbol{\nabla}\psi|^2} \right\rangle_\theta^{-1} \tilde{D}_M \\
A_4 &= -\frac{q'^2}{\Gamma p_0'} \left\langle \frac{B_0^2}{|\boldsymbol{\nabla}\psi|^2} \right\rangle_\theta^{-1} A_1 \\
A_5 &= -\frac{A_1}{A_4} \\
A_6 &= \frac{\rho_0}{q'^2} \left\langle \frac{B_0^2}{|\boldsymbol{\nabla}\psi|^2} \right\rangle_\theta \left\langle B_0^2 \right\rangle_\theta \\
\tilde{D}_M &= \frac{p_0'}{q'^2} \Bigg( f q' \left\langle \frac{1}{R^2 B_p^2} \right\rangle_\theta - p_0' f^2 \left\langle \frac{1}{R^2 B_p^2} \right\rangle_\theta^2 + \left\langle \frac{B_0^2}{R^2 B_p^2} \right\rangle_\theta \left[ p_0' f^2 \left\langle \frac{1}{R^2 B_p^2 B_0^2} \right\rangle_\theta \right. \\
&\quad \left. + 2 \left\langle \frac{1}{R^2 B_p^2 B_0^2} (\nabla\psi \cdot \nabla) \left( p_0 + \frac{B_0^2}{2} \right) \right\rangle_\theta - f \left\langle \frac{\nu'}{J B_0^2} \right\rangle_\theta \right] \Bigg)
\end{aligned} \tag{3.9}$$

where $\tilde{D}_M$ is the Mercier coefficient at marginal stability [65]. To solve the differential equations we need boundary conditions which can be determined by investigating the far inertial region.

### Far inertial region

To solve the set of differential equations in the inertial region, we must estimate their asymptotic behaviour. In the far inertial region we have:

$$|v| \gg \left|\frac{V_A}{R\gamma}\right|$$

When solving the differential equations (3.6) - (3.8), it is useful to replace $Y_0$ by $f$ defined as $f \equiv Y_0\, v$. If we take the second time derivative of Eq. (3.7) and a derivative with respect to $v$ of Eq. (3.8) we can eliminate the $\Xi_{-1}$ dependency:

$$A_0 \frac{\partial^2 f}{\partial t^2} = \frac{\partial^2 f}{\partial v^2} + \tilde{D}_M \left[\frac{f}{v^2} + \frac{\Gamma p_0}{p_0' v}\mathcal{J}_0\right] + A_1 \frac{\partial \mathcal{J}_0}{\partial v} \tag{3.10}$$

$$\frac{A_5}{A_6}\frac{\partial^2 \mathcal{J}_0}{\partial v^2} = A_2 \frac{\partial^2 \mathcal{J}_0}{\partial t^2} + \frac{A_3}{v}\frac{\partial^2 f}{\partial t^2} + A_4 \frac{\partial^3 f}{\partial v \partial t^2} \tag{3.11}$$

The solution of the homogeneous part of these differential equations is proportional to an exponential dependence of $v$: $\sim e^{\pm \tau v}$ (where $\tau$ is a constant). This means that the derivative with respect to $v$ is not changing the order of that term. Therefore the $\tilde{D}_M$ term and the $A_3$ term are of a lower order and can be neglected for high values of $v$. Additionally we can take the second derivative in Eq. (3.10) and another derivative with respect to $v$ of Eq. (3.11). This leads to a fourth order differential equation for $f = Y_0 v$ which is independent of $\mathcal{J}_0$:

$$\left(\tau_A^2 \frac{\partial^2}{\partial t^2} - \frac{\partial^2}{\partial v^2}\right)\left(\tau_s^2 \frac{\partial^2 f}{\partial t^2} - \frac{\partial^2 f}{\partial v^2}\right) = \tau^2 \frac{\partial^4 f}{\partial v^2 \partial t^2} \tag{3.12}$$

and for $\mathcal{J}_0$:

$$A_0 \frac{\partial^2 f}{\partial t^2} = \frac{\partial^2 f}{\partial v^2} + A_1 \frac{\partial}{\partial v}\mathcal{J}_0$$

with

$$\tau_a^2 = A_0 \qquad \tau_s^2 = \frac{A_2 A_6}{A_5} \qquad \tau^2 = -\frac{A_1 A_4 A_6}{A_5} \tag{3.13}$$

This differential equation (3.12) has four general solutions of which only two are decaying in $v$ and therefore fulfil our boundary conditions (3.2). So we are left with two general

solutions for $Y_0$.

#### Solutions of inertial region

We must find the solution of the inertial region in order to match it to the solution of the nonlinear region so that our final differential equation already includes the matching. One way to solve the set of differential equations (3.6), (3.7) and (3.8) is with a Laplace transform:

$$\tilde{Y}_0(v,p) \equiv \int_0^\infty e^{-pt} Y_0(v,t)\mathrm{d}t$$
$$\tilde{\mathcal{J}}_0(v,p) \equiv \int_0^\infty e^{-pt} \mathcal{J}_0(v,t)\mathrm{d}t$$
$$\tilde{\Xi}_{-1}(v,p) \equiv p\int_0^\infty e^{-pt} \Xi_{-1}(v,t)\mathrm{d}t$$

which leads to:

$$A_0 x^2 \tilde{Y}_0 = \frac{\partial}{\partial x}\left[x^2 \frac{\partial \tilde{Y}_0}{\partial x}\right] + \tilde{D}_M\left[\tilde{Y}_0 + \frac{\Gamma p_0}{p_0'}\tilde{\mathcal{J}}_0\right] + A_1 x \frac{\partial \tilde{\mathcal{J}}_0}{\partial x} \tag{3.14}$$

$$\frac{\partial \tilde{\Xi}_{-1}}{\partial x} = A_2\tilde{\mathcal{J}}_0 + A_3\tilde{Y}_0 + A_4\frac{\partial(x\tilde{Y}_0)}{\partial x} \tag{3.15}$$

$$A_6\tilde{\Xi}_{-1} = A_5\frac{\partial \tilde{\mathcal{J}}_0}{\partial x} \tag{3.16}$$

where $x$ is defined as:

$$x \equiv vp$$

Note that all equations (3.14), (3.15) and (3.16) only depend on $x$ and not on $v$ or $p$ separately. We expect a solution growing in time. Therefore the initial (time) values are set to 0 as they are negligible.

To solve the set of differential equations, the boundary condition in the far inertial region is needed. For that we can take the Laplace transform of equation (3.12). Then it is easy to see that the solution for $\tilde{Y}_0$ is:

$$\lim_{x\to\infty} \tilde{Y}_0 = \frac{A_{1+}}{x}e^{-\tau_1 x} + \frac{A_{2+}}{x}e^{-\tau_2 x} \tag{3.17}$$

with

$$\tau_1^2 \equiv \frac{1}{2}\left\{\left(\tau_a^2+\tau_s^2+\tau^2\right)+\sqrt{\left(\tau_a^2+\tau_s^2+\tau^2\right)^2-4\tau_a^2\tau_s^2}\right\}$$
$$\tau_2^2 \equiv \frac{1}{2}\left\{\left(\tau_a^2+\tau_s^2+\tau^2\right)-\sqrt{\left(\tau_a^2+\tau_s^2+\tau^2\right)^2-4\tau_a^2\tau_s^2}\right\}$$

where the $\tau$'s are defined in equations (3.13), and for $\mathcal{J}_0$:

$$\lim_{x\to\infty}\tilde{\mathcal{J}}_0 = A_{1+}\left(\frac{\tau_1^2-\frac{A_0}{A_1}}{\tau_1}\right)e^{-\tau_1 x}+A_{2+}\left(\frac{\tau_2^2-\frac{A_0}{A_1}}{\tau_2}\right)e^{-\tau_2 x} \tag{3.18}$$

We need the solutions (3.17) and (3.18) to calculate the solution of the differential equation numerically. Including the equations for $x<0$, we have four unknowns: $A_{1+}$, $A_{1-}$, $A_{2+}$ and $A_{2-}$. We also have three equations given by connection conditions for $Y_0$, $J_0$ and $\Xi_{-1}$ of the positive and negative regions. Therefore we can reduce the four constants to one unknown constant $a_0$ with the following relations: for $v>0$: $\tilde{Y}_0(v\,,p)=a_0(p)\tilde{Y}_{0+}(x)$ and for $v<0$: $\tilde{Y}_0(v\,,p)=a_0(p)\tilde{Y}_{0-}(x)$. We have equivalent expressions for $\tilde{\mathcal{J}}_0$ and $\tilde{\Xi}_{-1}$. We will show shortly that $a_0$ can be eliminated and therefore does not need to be determined. For the matching process to the nonlinear region, we can set the inertial terms of equation (3.15) equal zero ($A_0x^2\tilde{Y}_0$ and $A_6\tilde{\Xi}_{-1}$) since the inertial component is relatively small. The leading order solutions for $Y_0$ are then:

$$\tilde{Y}_{0+}(x) = -\frac{\Gamma p_0}{p_0'}\hat{J}+\left[\frac{Y_{S+}}{x^{\lambda_S}}+\frac{Y_{L+}}{x^{\lambda_L}}\right] \tag{3.19}$$
$$\tilde{Y}_{0-}(x) = -\frac{\Gamma p_0}{p_0'}\hat{J}+\left[\frac{Y_{S-}}{d_\pm x^{\lambda_S}}+\frac{Y_{L-}}{x^{\lambda_L}}\right] \tag{3.20}$$

To evaluate $\hat{J}$, $Y_{S+}$ and $Y_{L+}$ we must calculate the solution of the set of differential equations numerically and then solve for the three variables analytically.

### 3.2.2. Nonlinear limit of the inertial regions

Here we describe the solution of the inertial region in the limit of the matching region. This region is characterised by $1\ll|v|\ll\dfrac{V_A}{\gamma}$. In this limit the inertia terms are small and can be neglected when evaluating the differential equations. Therefore the lowest order

results become:

$$
\begin{aligned}
Y_0(v,t) &= -\frac{-\Gamma p_0}{p_0'}\overline{\mathcal{J}}(t) + \frac{y_S(t)}{v^{\lambda_S}} + \frac{y_L(t)}{v^{\lambda_L}} + \mathcal{O}(\frac{vR\gamma}{V_A}^2 Y_0) \qquad (3.21)\\
\mathcal{J}_0(v,t) &= \overline{\mathcal{J}}(t) + \mathcal{O}(v\left(\frac{R\gamma}{V_A}\right)^2 \overline{\Xi})\\
\Xi_{-1} &= \overline{\Xi}(t) + A_2 v\overline{\mathcal{J}}(t) + \frac{\lambda_S}{\tilde{D}_M}(A_3 + (1-\lambda_S)A_4)v\frac{y_S(t)}{v^{\lambda_S}}\\
&\quad + \frac{\lambda_L}{\tilde{D}_M}(A_3 + (1-\lambda_L)A_4)v\frac{y_L(t)}{v^{\lambda_L}} + \mathcal{O}(v\left(\frac{R\gamma}{V_A}\right)^2 v\frac{y_S(t)}{v^{\lambda_S}})
\end{aligned}
$$

where the bars indicate constants along $v$. $y_s$ and $y_l$ are the small and large solution for $Y_0(v,t)$ where the $\lambda_{S/L}$ are the small and large Mercier solutions which are defined with the Mercier coefficient $\tilde{D}_M$:

$$\lambda_{S/L} = \frac{1}{2} \pm \sqrt{\frac{1}{4} - \tilde{D}_M}. \qquad (3.22)$$

If we compare equation (3.19) and (3.20) with the nonlinear matching region equation (3.21) and recalling that the numerical solution differs by a factor $a_0$ we obtain:

$$
\begin{aligned}
\frac{a_0 Y_{S+}}{p^{\lambda_S}} &= \int_0^\infty e^{-pt'} y_{S+}(t')\mathrm{d}t'\\
\frac{a_0 Y_{L+}}{p^{\lambda_L}} &= \int_0^\infty e^{-pt'} y_{L+}(t')\mathrm{d}t'
\end{aligned}
$$

To eliminate the coefficient $a_0$ we can use the (Mellin's) inverse formula for Laplace transform, [112], which leads to:

$$y_{L+}(t) = \frac{Y_{L+}/Y_{S+}}{2\pi i}\int_0^\infty \mathrm{d}t' y_{S+}(t')\int_{-i\infty+p_0}^{i\infty+p_0} p^\lambda e^{p(t-t')}\mathrm{d}p$$

where

$$\lambda = \lambda_S - \lambda_L$$

with $\lambda_S$ and $\lambda_L$ given by equation (3.22). It is easy to show that this is equivalent to:

$$y_{L+}(t) = \frac{Y_{L+}/Y_{S+}}{2\pi i}\frac{\partial^2}{\partial t^2}\int_0^\infty \mathrm{d}t' y_{S+}(t')\int_{-i\infty+p_0}^{i\infty+p_0} p^{\lambda-2} e^{p(t-t')}\mathrm{d}p$$

The inverse Laplace transform from the right integral can be found in a table (see [113]).

It has the following form:

$$\begin{aligned} y_{L+}(t) &= \frac{Y_{L+}/Y_{S+}}{\kappa}\frac{\partial^2}{\partial t^2}\int_0^\infty \mathrm{d}t' \frac{y_{S+}(t')H(t-t')}{(t-t')^{1+\lambda-2}} \\ &= \frac{Y_{L+}/Y_{S+}}{\kappa}\frac{\partial^2}{\partial t^2}\int_0^t \mathrm{d}t' \frac{y_{S+}(t')}{(t-t')^{1+\lambda-2}} \end{aligned}$$

Here $\kappa \equiv \Gamma(2-\lambda)$ where $\Gamma$ is the gamma function and $H(t-t')$ is the Heaviside step function which can be absorbed into the limit of the integral. For a simplification of the equation, we can introduce the definition of the so called fractional derivative, [114]:

$$\frac{\partial^\lambda}{\partial t^\lambda} f(t) \equiv \frac{1}{\kappa}\frac{\partial^2}{\partial t^2}\int_0^t \mathrm{d}t' \frac{f(t')}{(t-t')^{\lambda-1}}$$

Therefore we obtain the shorter expressions:

$$\begin{aligned} \delta_+ &= \frac{y_{L+}(t)}{y_{S+}(t)} = \frac{Y_{L+}/Y_{S+}}{y_{S+}}\frac{\partial^\lambda y_{S+}}{\partial t^\lambda} \\ \delta_- &= \frac{y_{L-}(t)}{y_{S-}(t)} = \frac{Y_{L-}/Y_{S-}}{y_{S-}}\frac{\partial^\lambda y_{S-}}{\partial t^\lambda} \end{aligned} \tag{3.23}$$

In an up-down symmetric case we expect $\delta_+(t) = \delta_-(t) = \delta(t)$.
The results from here are used to match the small and large solutions to the solution of the nonlinear region which will now be derived.

### 3.2.3. Nonlinear region

In this subsection the derivation of the differential equations for the nonlinear region is outlined. The first three orders will lead us to the linear ballooning equation. With the fourth and fifth order we can finally obtain the nonlinear ballooning equation by matching the results of these orders with the inertial region.
For the nonlinear region we need to take again the components of the momentum equation (i.e. the Lagrangian form) (2.21):

$$\frac{\rho_0}{J}(\boldsymbol{\nabla}_0\boldsymbol{r})\cdot\frac{\partial^2\boldsymbol{\xi}}{\partial t^2} = -\boldsymbol{\nabla}_0\left[\frac{p_0}{J^\Gamma} + \frac{|(\boldsymbol{B}_0\cdot\boldsymbol{\nabla}_0\boldsymbol{r})|^2}{2J^2}\right] + (\boldsymbol{\nabla}_0\boldsymbol{r})\cdot\left[\frac{1}{J}(\boldsymbol{B}_0\cdot\boldsymbol{\nabla}_0)\left(\frac{1}{J}(\boldsymbol{B}_0\cdot\boldsymbol{\nabla}_0\boldsymbol{r})\right)\right]$$

where the viscosity and gravity are neglected.

We can re-write this equation to make the calculation more clear:

$$\frac{\rho_0}{J}(\boldsymbol{\nabla}_0\boldsymbol{r})\cdot\frac{\partial^2\boldsymbol{\xi}}{\partial t^2}=\boldsymbol{\nabla}_0 F+\frac{1}{J}\left(\boldsymbol{B}_0\cdot\boldsymbol{\nabla}_0\right)\left[\frac{\left(\boldsymbol{B}_0\cdot\boldsymbol{\nabla}_0\right)\boldsymbol{r}}{J}\right]-\boldsymbol{\nabla}_0\left[\frac{1}{J}\left(\boldsymbol{B}_0\cdot\boldsymbol{\nabla}_0\right)\left[\frac{\left(\boldsymbol{B}_0\cdot\boldsymbol{\nabla}_0\right)\boldsymbol{r}}{J}\right]\right]\cdot\boldsymbol{\xi} \tag{3.24}$$

with the scalar function $F$ defined as

$$F\equiv-\frac{p_0}{J^\Gamma}-\frac{1}{2J^2}\left|\left(\boldsymbol{B}_0\cdot\boldsymbol{\nabla}_0\right)\boldsymbol{r}\right|^2+\frac{1}{J}\boldsymbol{\xi}\cdot\left(\boldsymbol{B}_0\cdot\boldsymbol{\nabla}_0\right)\left[\frac{1}{J}\left(\boldsymbol{B}_0\cdot\boldsymbol{\nabla}_0\right)\boldsymbol{r}\right].$$

#### First Order: Incompressibility

The lowest order for the $\boldsymbol{e}_\perp$ component ($\mathcal{O}(\epsilon^0)$) and for the $\boldsymbol{e}_\wedge$ component ($\mathcal{O}(\epsilon^{-1})$) are given by:

$$\left(\boldsymbol{e}_\perp\cdot\boldsymbol{\nabla}_0\right)\left[\left(\Gamma p_0+B_0^2\right)J^{(1)}\right]=0$$
$$\left(\boldsymbol{e}_\wedge\cdot\boldsymbol{\nabla}_0\right)\left[\left(\Gamma p_0+B_0^2\right)J^{(1)}\right]=0$$

where the equilibrium relation (2.24) was used.

If these equations are integrated over a perpendicular variable to far away from the field line we find that $J^{(1)}$ has to be equal to a constant divided by $\Gamma p_0+B_0^2$. However, the chosen boundary condition, (3.1), implies that $J$ has to go to zero as well, which means:

$$J^{(1)}=0$$

This means that the lowest order of the parallel component of Eq. (3.24) is zero.

By using the ordering (2.20) we find that the lowest order of $\nabla\cdot\boldsymbol{\xi}$ is equal to zero which allows us to write:

$$\frac{\partial\xi_\wedge^{(3)}}{\partial\alpha}=-\frac{\partial\xi_\psi^{(2)}}{\partial\psi} \tag{3.25}$$

This relation is a lowest order incompressibility condition on the plasma. Averaging this expression with respect to $\alpha$ (in the range of $-\pi$ to $\pi$), we can see that $\overline{\xi_\psi^{(2)}}$ is constant

with respect to $\psi$ (as well as to $\alpha$). Using the boundary conditions leads to

$$\overline{\xi_\psi^{(2)}} = 0 \tag{3.26}$$

where the overbar is defined by

$$\overline{A} \equiv \frac{1}{2\pi}\int_{-\pi}^{\pi} A \mathrm{d}\alpha \tag{3.27}$$

which is an averaging with respect to $\alpha$.

#### Second order

The lowest relevant order of the parallel component of Eq. (3.24) is of order $\mathcal{O}(\epsilon^2)$ and given by:

$$(\boldsymbol{B}_0 \cdot \boldsymbol{\nabla}_0)\, J^{(2)} = 0$$

Therefore $J^{(2)}$ is constant along the magnetic field lines. The perpendicular components of order $\mathcal{O}(\epsilon)$ and $\mathcal{O}(\epsilon^0)$ are:

$$\begin{aligned} B_0 \left.\frac{\partial F^{(2)}}{\partial \psi}\right|_{\alpha,l} &= 0 \\ B_0 \left.\frac{\partial F^{(2)}}{\partial \alpha}\right|_{\psi,l} &= 0 \end{aligned} \tag{3.28}$$

where $F^{(2)}$ is:

$$F^{(2)} = (\Gamma p_0 + B_0^2) J^{(2)} - (\boldsymbol{B}_0 \cdot \boldsymbol{\nabla}_0)\,(B_0^2 \xi_\parallel^{(2)}) + 2\boldsymbol{\kappa}_0 \cdot \boldsymbol{\xi}^{(2)}$$

Note that the equations (3.28) contain higher order terms, which must be subtracted at the appropriate order.

Following a similar argument to that in the previous order, it follows that $F^{(2)} = 0$. This gives a relation between $\xi_\parallel^{(2)}$ and $\xi_\psi^{(2)}$:

$$(\boldsymbol{B}_0 \cdot \boldsymbol{\nabla}_0)\, \xi_\parallel^{(2)} - \frac{2\xi_\psi^{(2)} \boldsymbol{e}_\perp \cdot \boldsymbol{\kappa}_0}{B_0^2} = \frac{\Gamma p_0 + B_0^2}{B_0^2} J^{(2)} \tag{3.29}$$

We can average this equation with respect to $\alpha$ using $\overline{\xi_\psi^{(2)}} = 0$, then integrate with respect to the field-aligned variable. We use the fact that $J^{(2)}$ is constant along $\boldsymbol{B}_0$ and that $\xi_\parallel^{(2)}$

must vanish far along the field lines at the matching region. This yields $\overline{J^{(2)}} = 0$ and $\overline{\xi_{\parallel}^{(2)}} = 0$.

#### Third order: The ballooning equation

Since the derivation of the equations of this order is slightly longer, a summary of the results is given here, and a full derivation can be found in Appendix C.1.1.

With the terms of the third order we can show that $J^{(2)} = F^{(3)} = 0$. Additionally we can obtain a second order differential equation of $\xi_{\psi}^{(2)}$ with respect to $l$. Therefore a separation of variables is applicable. Since $\xi_{\parallel}^{(2)}$ is related to $\xi_{\psi}^{(2)}$ by an equation containing only derivatives along the magnetic field line (C.3), we can also use the separation approach for the parallel component of $\boldsymbol{\xi}^{(2)}$ which leads to:

$$\boldsymbol{\xi}^{(2)} = \hat{\xi}(\psi, \alpha; t) \left[ \frac{X}{B_0} \boldsymbol{e}_{\perp} + G \boldsymbol{B}_0 \right] = \hat{\xi}(\psi, \alpha; t) \boldsymbol{H} \tag{3.30}$$

where $\boldsymbol{H}$ is defined as: $\boldsymbol{H} \equiv \frac{X}{B_0} \boldsymbol{e}_{\perp} + G \boldsymbol{B}_0$. The ratio $\frac{X}{B_0}$ is independent of a fast variation of $\psi$, $\alpha$ and $t$ and is determined by the linear ballooning equation:

$$(\boldsymbol{B}_0 \cdot \boldsymbol{\nabla}_0) \left[ \frac{|\boldsymbol{e}_{\perp}|^2}{B_0^2} (\boldsymbol{B}_0 \cdot \boldsymbol{\nabla}_0) X \right] + \frac{2\mu}{B_0^4} \left( \boldsymbol{e}_{\perp} \cdot \boldsymbol{\kappa}_0 \right) \left( \boldsymbol{e}_{\perp} \cdot \boldsymbol{\nabla}_0 p_0 \right) X = 0 \tag{3.31}$$

where $\mu$ is the so called ballooning eigenvalue. Since we assume the plasma to be close to marginal stability, we set $1-\mu$ close to zero and of the order $\epsilon^2$. To introduce this eigenvalue, we added a term of a higher order ($\epsilon^4$) which will be subtracted in the appropriate order. The equation describing the parallel component of $\boldsymbol{\xi}^{(2)}$ is:

$$G = -\frac{1}{\mu p_0'} \frac{|\boldsymbol{e}_{\perp}|^2}{B_0^2} \left( \boldsymbol{B}_0 \cdot \boldsymbol{\nabla}_0 \right) X \tag{3.32}$$

By using the separation (3.30) we can also determine an expression for $\xi_{\wedge}^{(3)}$ by using equation (3.25) which leads to:

$$\xi_{\wedge}^{(3)} = -\frac{\partial u}{\partial \psi} \frac{X}{B_0} + \overline{\xi_{\wedge}^{(3)}}$$

where $u$ is defined as $u \equiv \dfrac{\partial \hat{\xi}}{\partial \alpha}$.

#### Fourth order

A summary of the results of the fourth order are given here, and the full derivation is found in Appendix C.1.2.

We can show that the third order of the Jacobian is independent of $\alpha$:

$$\frac{\partial J^{(3)}}{\partial \alpha} = 0$$

Note a shift of the $\alpha$ variable by a function $f = f(\psi)$ does not affect the equilibrium (i.e. the magnetic field $\boldsymbol{B}_0$), which means that the equilibrium is invariant under this transformation. However, by shifting the variable $\alpha$, the ballooning eigenfunction $\mu$, $\boldsymbol{e}_\perp$, and the function $X$ change. We can show that $\frac{\partial \boldsymbol{e}_\perp}{\partial f'} = -\boldsymbol{e}_\wedge$ where $f' \equiv \frac{\partial f}{\partial \psi}$. Additionally it is possible to show that

$$\frac{\partial \mu}{\partial f'} \approx 0$$

This means that we must calculate $\mu$ for each flux surface to find the most unstable one, which then will be used for this model.

The final main result is a representation of the third perpendicular order of the displacement:

$$\boldsymbol{\xi}_\perp^{(3)} = \frac{1}{B_0}\frac{\partial u}{\partial \psi}\frac{\partial \left(X \boldsymbol{e}_\perp\right)}{\partial f'} + \frac{B_0}{2} H^2 \frac{\partial \overline{\hat{\xi}^2}}{\partial \psi}\boldsymbol{e}_\perp + \overline{\xi_\wedge^{(3)}}\boldsymbol{e}_\wedge$$

where the second and third terms are the $\alpha$ independent parts of $\boldsymbol{\xi}_\perp^{(3)}$. This relation is used in the fifth order to achieve an equation only depending on $\hat{\xi}$.

#### Fifth Order: The nonlinear ballooning equation

This is the last order from the nonlinear region which will be used to calculate the ballooning envelope equation. After some algebra which is presented in the Appendix C.1.3

we can derive the following equation:

$$\begin{aligned}
&\boldsymbol{e}_\perp \cdot \mathcal{L}\left(\frac{\partial \boldsymbol{Z}_\perp^{(4)}}{\partial \alpha}\right) - \boldsymbol{e}_\wedge \cdot \mathcal{L}\left(\frac{\partial \boldsymbol{Z}_\perp^{(3)}}{\partial \psi}\right) + \frac{2}{B_0^2}(1-\mu)(\boldsymbol{e}_\perp \cdot \boldsymbol{\kappa}_0)(\boldsymbol{e}_\perp \cdot \boldsymbol{\nabla}_0 p_0)\frac{\partial \xi_\psi^{(2)}}{\partial \alpha} \\
&+ \left[\frac{(\boldsymbol{e}_\psi \cdot \boldsymbol{B}_0)}{B_0^2}(\boldsymbol{B}_0 \cdot \boldsymbol{\nabla}_0) + \frac{2}{B_0^2}(\boldsymbol{e}_\perp \cdot \boldsymbol{\kappa}_0)\right]\left[\frac{1}{B_0}\boldsymbol{e}_\wedge \cdot \mathcal{L}\left(\boldsymbol{\xi}_\perp^{(2)}\right)\right] + 2B_0\frac{\partial \xi_\psi^{(2)}}{\partial \psi}\boldsymbol{e}_\wedge \cdot \mathcal{L}\left(\frac{\partial \boldsymbol{\xi}_\perp^{(2)}}{\partial \psi}\right) \\
&+ B_0\left[\frac{\partial \xi_\wedge^{(3)}}{\partial \psi}\boldsymbol{e}_\wedge \cdot \mathcal{L}\left(\frac{\partial \boldsymbol{\xi}_\perp^{(2)}}{\partial \alpha}\right) - \frac{\partial \xi_\psi^{(2)}}{\partial \alpha}\boldsymbol{e}_\perp \cdot \mathcal{L}\left(\frac{\partial \boldsymbol{Z}_\perp^{(3)}}{\partial \psi}\right)\right] + P\frac{\partial \xi^2}{\partial \alpha} \\
&- \hat{\xi}B_0\left.\frac{\partial}{\partial \psi}\right|_{\alpha,l}\left[\frac{1}{B_0}\boldsymbol{e}_\wedge \cdot \mathcal{L}\left(\frac{X\boldsymbol{e}_\perp}{B_0}\right)\right] + 2J^{(3)}\left(\boldsymbol{e}_\perp \cdot \boldsymbol{\nabla}_0 \boldsymbol{\kappa}_0\right)\frac{\partial \boldsymbol{\xi}^{(2)}}{\partial \alpha} \\
&= \rho_0 |\boldsymbol{e}_\perp|^2 \frac{X}{B_0}\frac{\partial}{\partial \alpha}\frac{\partial^2 \hat{\xi}}{\partial t^2} + \frac{B_0 \Gamma p_0}{p_0'}\left(\boldsymbol{B}_0 \cdot \boldsymbol{\nabla}_0\right)\left[\frac{|\boldsymbol{e}_\perp|^2}{B_0^2}\left(\boldsymbol{B}_0 \cdot \boldsymbol{\nabla}_0\right)J^{(4)}\right] \\
&= \rho\left[|\boldsymbol{e}_\perp|^2\frac{X}{B_0} + \frac{B_0}{p_0'}\left(\boldsymbol{B}_0 \cdot \boldsymbol{\nabla}_0\right)\left[|\boldsymbol{e}_\perp|^2 G\right]\right]\frac{\partial}{\partial \alpha}\frac{\partial^2 \hat{\xi}}{\partial t^2}
\end{aligned} \tag{3.33}$$

where $\mathcal{L}$ is the linear operator which is defined acting on a perpendicular vector $\boldsymbol{W}_\perp$ (with only $\boldsymbol{e}_\perp$ and $\boldsymbol{e}_\wedge$ components) as:

$$\mathcal{L}\left(\boldsymbol{W}_\perp\right) \equiv \boldsymbol{B}_0 \cdot \boldsymbol{\nabla}_0\left[\boldsymbol{B}_0 \cdot \boldsymbol{\nabla}_0\left(\boldsymbol{W}_\perp\right)\right] - \left(\boldsymbol{\nabla}_0 \boldsymbol{\kappa}_0\right) \cdot \boldsymbol{W}_\perp + \left[\boldsymbol{B_0}\left(\boldsymbol{B}_0 \cdot \boldsymbol{\nabla}_0\right) + 2\boldsymbol{\kappa}_0\right]\left[\frac{2}{B_0^2}\left(\boldsymbol{\kappa}_0 \cdot \boldsymbol{W}_\perp\right)\right]$$

$\boldsymbol{Z}_\perp$ is defined as:

$$\boldsymbol{Z}_\perp^{(i)} = \boldsymbol{\xi}_\perp^{(i)} + \frac{\Gamma p_0}{p_0' B_0}J^{(i)}\boldsymbol{e}_\perp$$

where the third order of this quantity satisfies:

$$\frac{\boldsymbol{e}_\wedge}{B_0} \cdot \mathcal{L}\left(\overline{\boldsymbol{Z}_\perp^{(3)}}\right) = \frac{X}{B_0}\frac{\partial \overline{\hat{\xi}^2}}{\partial \psi}\boldsymbol{e}_\wedge \cdot \mathcal{L}\left(\boldsymbol{H}_\perp\right).$$

We separate the $\alpha$ derivative of $\boldsymbol{Z}_\perp^{(4)}$ into its $\boldsymbol{e}_\perp$ and $\boldsymbol{e}_\wedge$ components:

$$\frac{\partial \boldsymbol{Z}_\perp^{(4)}}{\partial \alpha} = \frac{1}{B_0}\frac{\partial Z}{\partial \alpha}\boldsymbol{e}_\perp + \frac{U}{B_0}\boldsymbol{e}_\wedge \tag{3.34}$$

The function $Z$ will be determined asymptotically and the quantity $U$ which is given by $U \equiv B_0 \frac{\partial \xi_\wedge^{(4)}}{\partial \alpha}$ is given by the following equation, where we used $J^{(2)} = 0$:

$$U = -B_0 \frac{\partial \xi_\psi^{(3)}}{\partial \psi} - \frac{(\boldsymbol{e}_\perp \cdot \boldsymbol{\nabla}_0 p_0)}{B_0^2} \xi_\psi^{(2)} - \frac{\hat{\xi}}{B_0} \boldsymbol{e}_\perp \cdot \boldsymbol{\nabla}_0 X + B_0^2 \left( \frac{\partial \xi_\psi^{(2)}}{\partial \alpha} \frac{\partial \xi_\wedge^{(3)}}{\partial \psi} - \frac{\partial \xi_\psi^{(2)}}{\partial \psi} \frac{\partial \xi_\wedge^{(3)}}{\partial \alpha} \right)$$
$$+ \frac{1}{2} (\boldsymbol{H} \cdot \boldsymbol{\nabla}_0 \boldsymbol{H}) \cdot \boldsymbol{\nabla}_0 \alpha \frac{\partial \hat{\xi}^2}{\partial \alpha} \tag{3.35}$$

Equation (3.33) is the last equation needed to determine the nonlinear ballooning envelope equation. To achieve it we must find a solution for the nonlinear solution as it approaches the inertial limit and match that with the solution in the inertial region as it approaches the nonlinear limit. These steps are presented in the next two subsections.

### 3.2.4. Inertial limit for the nonlinear region

In this section the solutions for the functions $X$, $G$ (and therefore $\boldsymbol{H}$) and $Z$ are presented for the limit $\chi \to \infty$. These solutions are needed to match the inertial solution to the nonlinear solution. To evaluate the nonlinear equations as the inertial region is approached the asymptotic forms ($|\chi| \gg 1$) for the functions $X$, $G$ and $Z$ are derived next, since these functions appear several times. We again use the separation of $\chi$ into $\theta$ and $v$ (see Sect. 3.2.1 for more detail).

#### Asymptotic form of $X$

Here we outline the steps of the derivation of the asymptotic form of $X$. The more detailed description can be found in Appendix C.2.1. The function $X$ is described by the linear ballooning mode equation (along field lines) at marginal stability (3.31). This equation can be exploited to determine the behaviour of $X$ for high values of $\chi$. Expanding $X$ with respect to $v$: $X = X_0 + \frac{X_1}{v} + \frac{X_2}{v^2} + \cdots$ and using the relations (A.1), (A.2), (A.3) and (A.4)

we obtain:

$$0 = \left(\frac{\partial}{\partial v} + \frac{\partial}{\partial \theta}\right)\left[\frac{1}{JR^2\boldsymbol{B}_p^2}\left[1 + \frac{R^4\boldsymbol{B}_p^4}{B^2}\left(q'v + Y'\right)^2\right]\left(\frac{\partial}{\partial v} + \frac{\partial}{\partial \theta}\right)\left(X_0 + \frac{X_1}{v} + \frac{X_2}{v^2} + \cdots\right)\right] +$$

$$+2\mu p'\left[\frac{J}{B^2R^2\boldsymbol{B}_p^2}\left(\boldsymbol{\nabla}\psi\cdot\nabla\right)\left(p + \frac{B^2}{2}\right) + \frac{I}{2}\frac{\partial}{\partial\theta}\left(\frac{1}{B^2}\right)\left(q'v + Y'\right)\right]\left(X_0 + \frac{X_1}{v} + \frac{X_2}{v^2} + \cdots\right) \tag{3.36}$$

The next step is to examine each order of equation (3.36). From the lowest order we can obtain that $X_0$ only depends on $v$: $X_0 = X_0(v)$.

Exploiting the next higher order we can obtain the expression for the $\theta$ derivative of the second lowest order of the displacement $X$:

$$\frac{\partial X_1}{\partial\theta} = \frac{J\mu I p'}{R^2B_p^2q'}\left[B^2\frac{\left\langle\frac{1}{R^2B_p^2}\right\rangle_\theta}{\left\langle\frac{B^2}{R^2B_p^2}\right\rangle_\theta} - 1\right]X_0 + \left[\frac{JB^2}{R^2B_p^2}\frac{1}{\left\langle\frac{B^2}{R^2B_p^2}\right\rangle_\theta} - 1\right]v\frac{\partial X_0}{\partial v} \tag{3.37}$$

where $\langle\cdots\rangle_\theta$ is the $\theta$ average. Determining the next order and using the expression for $\frac{\partial X_1}{\partial\theta}$ we can obtain, after some algebra, the differential equation for $X_0$:

$$\frac{\partial}{\partial v}\left[v^2\frac{\partial X_0}{\partial v}\right] + D_M X_0 = 0 \tag{3.38}$$

where $D_M$ defined by Eq. (C.15) is the Mercier coefficient including the ballooning eigenvalue, [65], where $D_M \approx \tilde{D}_M$ for $\mu \approx 1$. The general solution for equation (3.38) is:

$$X_0 = \frac{C_1}{|v|^{\lambda_+}} + \frac{C_2}{|v|^{\lambda_-}} \tag{3.39}$$

with

$$\lambda_\pm = \frac{1}{2} \pm \sqrt{\frac{1}{4} - D_M} \tag{3.40}$$

Since we assume our system to be close to marginal stability we will refer to the small and large solution $\lambda_S$ ($\approx \lambda_+$) and $\lambda_L$ ($\approx \lambda_-$) respectively.

**Asymptotic form of $G$**

The asymptotic form for the parallel component of the lowest order displacement is determined here. We can use equation (3.32) to evaluate the leading order of $G$. Using Eq. (A.4) and expanding $G$ into its orders we obtain:

$$G_0 + \frac{G_1}{v} + \cdots = -\frac{1}{R^2 B_p^2}\left[1 + \frac{R^2 B_p^2}{B_0^2}(q'v + Y')^2\right]\left(\frac{\partial X_0}{\partial v} + \frac{1}{v}\frac{\partial X_1}{\partial \theta} + \cdots\right)$$

where we can easily determine the lowest order of $G_0$ by using Eq. (3.37):

$$G_0 = -\frac{q'^2}{B_0^2}v^2\left[\frac{J\mu f p'}{R^2 B_p^2 q'}\left(B^2\frac{\left\langle\frac{1}{R^2B_p^2}\right\rangle_\theta}{\frac{B^2}{R^2B_p^2}} - 1\right)\frac{X_0}{v} + \frac{JB^2}{R^2B_p^2}\frac{1}{\left\langle\frac{B^2}{R^2B_p^2}\right\rangle_\theta}\frac{\partial X_0}{\partial v}\right] \tag{3.41}$$

**Asymptotic form of $Z$**

Here we determine the asymptotic behaviour of the function $Z$ given in Eq. (3.34). Starting with the final equation of the previous section (3.33), but including only the leading orders, we obtain:

$$\boldsymbol{e}_\perp \cdot \mathcal{L}\left(\frac{1}{B_0}\frac{\partial Z}{\partial \alpha}\boldsymbol{e}_\perp\right) + F(v,\theta) = \rho_0\left[\frac{|\boldsymbol{e}_\perp|^2}{B_0}X + \frac{B_0}{p_0'}\boldsymbol{B}_0\cdot\boldsymbol{\nabla}_0\left[|\boldsymbol{e}_\perp|^2 G\right]\right]\frac{\partial}{\partial\alpha}\frac{\partial^2\hat{\xi}}{\partial t^2}$$

where $F(v,\theta)$ represents the terms including $\boldsymbol{e}_\perp \cdot \mathcal{L}\left(\frac{U}{B_0}\boldsymbol{e}_\wedge\right)$. There are two larger contributions which makes this second order differential equation an inhomogeneous equation. First we consider the inertia term on the right hand side. If we ignore the inertia term, we can solve this differential equation with $Z_F$ as its special solution given by:

$$\frac{\partial Z_F}{\partial \alpha} = -\frac{1}{q'v}U_0.$$

where $U_0$ is the dominant term of $U$ containing only the last term of Eq. (3.35). By adding the $Z_F$ to our solution $Z_0$ we can eliminate $F(v,\theta)$ in the differential equation:

$$\boldsymbol{e}_\perp \cdot \mathcal{L}\left(\frac{1}{B_0}\frac{\partial Z}{\partial \alpha}\boldsymbol{e}_\perp\right) = \rho_0\left[\frac{|\boldsymbol{e}_\perp|^2}{B_0}X + \frac{B_0}{p_0'}\boldsymbol{B}_0\cdot\boldsymbol{\nabla}_0\left[|\boldsymbol{e}_\perp|^2 G\right]\right]\frac{\partial}{\partial\alpha}\frac{\partial^2\xi}{\partial t^2}$$

Note, that the homogeneous part of this differential equation is of the same form as the asymptotic equation for $X$, Eq. (3.31). Therefore we proceed in the same way and apply

our results for $X$ to the inertia term, which enters our calculation at order $\mathcal{O}(v)$. The highest order $\mathcal{O}(v^2)$ looks exactly like our equation for $X_0$:

$$q'^2 \frac{\partial}{\partial\theta}\left[\frac{R^2\boldsymbol{B}_p^2}{JB^2}\frac{\partial Z_0}{\partial\theta}\right] = 0$$

We find that $Z_0$ only depends on $v$: $Z_0 = Z_0(v)$. We can obtain an expression for the derivative $\frac{\partial Z_1}{\partial\theta}$ by investigating the next order:

$$\begin{aligned}\frac{\partial Z_1}{\partial\theta} =& \frac{JIp'}{R^2B_p^2q'}\left[B^2\frac{\left\langle\frac{1}{R^2B_p^2}\right\rangle_\theta}{\left\langle\frac{B^2}{R^2B_p^2}\right\rangle_\theta} - 1\right]Z_0 + \left[\frac{JB^2}{R^2B_p^2}\frac{1}{\left\langle\frac{B^2}{R^2B_p^2}\right\rangle_\theta} - 1\right]v\frac{\partial Z_0}{\partial v} \\ &+\frac{\rho_0}{p'}v\left[JB_0^2G_0 - \frac{\left\langle B_0^2G_0\right\rangle_\theta}{\left\langle\frac{B^2}{R^2B_p^2}\right\rangle_\theta}\frac{JB_0^2}{R^2B_p^2}\right]\frac{\partial^2\xi}{\partial t^2}\end{aligned} \tag{3.42}$$

The result for $\frac{\partial Z_1}{\partial\theta}$ has an additional term compared to $\frac{\partial X_1}{\partial\theta}$ which is due to the inertia. Using the next highest order and averaging over $\theta$ we obtain:

$$\begin{aligned}\frac{\partial}{\partial v}\left[v^2\frac{\partial Z_0}{\partial v}\right] + D_M Z_0 = \rho_0\Bigg\{&\left\langle\frac{B_0^2}{R^2B_p^2}\right\rangle_\theta\left\langle\frac{R^2B_p^2}{B_0^2}\right\rangle_\theta v^2X_0 + \frac{1}{p_0'}\frac{\partial}{\partial v}\left(v^2\left\langle B_0^2G_0\right\rangle_\theta\right) \\ &+\frac{f}{q'}v\left\langle G_0\right\rangle_\theta\left\langle\frac{B_0^2}{R^2B_p^2}\right\rangle_\theta - \frac{f}{q'}\left\langle\frac{1}{R^2B_p^2}\right\rangle_\theta v\left\langle B_0^2G_0\right\rangle_\theta\Bigg\}\frac{\partial^2\hat{\xi}}{\partial t^2}\end{aligned}$$

If we assume that $X_0$ only consists of the small solution (left term of Eq. (3.39)) which is discussed in the next section, we can write:

$$\frac{\partial}{\partial v}\left[v^2\frac{\partial Z_0}{\partial v}\right] + D_M Z_0 \equiv Q^{(z)}(\theta)\ v^{2-\lambda_S}.$$

where we defined the function $Q^{(z)}(\theta)$ such that it includes all the periodic quantities of the right hand side. The general solution of that differential equation is:

$$Z_0 = \frac{C_1^{(z)}}{v^{\lambda_S}} + \frac{C_2^{(z)}}{v^{\lambda_L}} + \frac{Q^{(z)}v^{2-\lambda_S}}{2(3-2\lambda_S)} \tag{3.43}$$

### 3.2.5. Matching of the nonlinear and inertial regions

In this section we merge the solutions of the inertial and nonlinear regions by using the solutions of the limits (Equations (3.21), and Equations (3.39), (3.41), (3.43)) which leads

to the final ballooning envelope equation for tokamak geometries.

$X_0$ and $Z_0$ can each consist of large ($\lambda_L$) and small ($\lambda_S$) solutions. However, we can choose them in such a way that the entire small solution only enters the displacement in $X_0$ and that the entire large solution only enters the displacement in $Z_0$. That choice is consistent since the coefficient of the small solution is assumed to be large – valid close to marginal stability. With that approach we obtain:

$$X_0 = \frac{C_1}{|v|^{\lambda_S}} \tag{3.44}$$

$$G_0 = q' \left( \frac{f}{B^2} + f_0 \right) v X_0 \tag{3.45}$$

with $f_0$ defined as:

$$f_0 \equiv \frac{\lambda_S q'}{\mu_0 p'} \frac{1}{\left\langle \frac{B_0^2}{R^2 B_p^2} \right\rangle_\theta} - f \frac{\left\langle \frac{1}{R^2 B_p^2} \right\rangle_\theta}{\left\langle \frac{B_0^2}{R^2 B_p^2} \right\rangle_\theta} \tag{3.46}$$

The constant $C_2^{(Z)}$ from Eq. (3.43) needs to be matched to the solution of the inertial region which means it is of this form $A_\pm \, \xi \, \delta$ where $\delta$ is given by Eq. (3.23) and assuming up-down symmetry. Therefore our complete solution for the lowest order of $Z$ is:

$$Z_0 = \frac{A_\pm \, \xi \, \delta}{v^{\lambda_L}} + \frac{Q v^{2-\lambda_S}}{2(3-2\lambda_S)} - \frac{1}{q' v} \int \mathrm{d}\alpha U_0 \tag{3.47}$$

Now using Equation (C.16), which is derived in the Appendix C.2.2, we can show that the following terms of equation (3.33) can be written as:

$$\begin{aligned}
&\left\langle \frac{X}{B_0} \boldsymbol{e}_\perp \cdot \mathcal{L} \left( \frac{1}{B_0} \frac{\partial Z}{\partial \alpha} \boldsymbol{e}_\perp \right) \right\rangle - \rho_0 \left[ \left\langle \frac{|\boldsymbol{e}_\perp|^2}{B_0} X^2 \right\rangle + \left\langle \frac{X}{p_0'} \left( \boldsymbol{B}_0 \cdot \boldsymbol{\nabla}_0 \right) \left( |\boldsymbol{e}_\perp|^2 G \right) \right\rangle \right] \frac{\partial}{\partial \alpha} \frac{\partial^2 \xi}{\partial t^2} \\
&+ \left\langle \frac{X}{B_0} \boldsymbol{e}_\perp \cdot \mathcal{L} \left( \frac{\partial \xi_\wedge^{(4)}}{\partial \alpha} \boldsymbol{e}_\wedge \right) \right\rangle \\
&= -C_0 \frac{\partial}{\partial \alpha} \frac{\partial^2 \xi}{\partial t^2} + (\lambda_S - \lambda_L) \, \delta \left( A_+^2 + A_-^2 \right) q'^2 \left\langle \frac{B_0^2}{|\nabla \psi|^2} \right\rangle_\theta^{-1} \frac{\partial \xi}{\partial \alpha} + \left\langle \frac{\partial \xi_\wedge^{(4)}}{\partial \alpha} \boldsymbol{e}_\wedge \cdot \mathcal{L} \left( \frac{X}{B_0} \boldsymbol{e}_\perp \right) \right\rangle
\end{aligned}$$

where $\langle \cdots \rangle$ is an integral along the magnetic field line. With this relation and equation (3.33) we obtain the final equation: the nonlinear ballooning mode envelope equation:

$$C_0 \frac{\partial}{\partial \alpha} \frac{\partial^2 \xi}{\partial t^2} + C_5 \frac{\partial}{\partial \alpha} \frac{\partial^n}{\partial t^n} \left[ \int_0^t \mathrm{d}t' \frac{\xi(t')}{(t-t')^{1+\lambda-n}} \right] = C_1 \left[ 2\,(1-\mu)\, \frac{\partial}{\partial \alpha} \xi - \frac{\partial^2 \mu}{\partial f'^2} \frac{\partial^2 u}{\partial \psi^2} \right] + C_2 \frac{\partial}{\partial \alpha} \xi^2 + C_3 \left[ \left( \frac{\partial \xi}{\partial \psi} \right)^2 - \frac{\partial^2 u}{\partial \psi^2} \frac{\partial}{\partial \alpha} \xi - \frac{1}{2} \frac{\partial^2 \overline{\xi^2}}{\partial \psi^2} \right] + C_4 \frac{\partial \xi}{\partial \alpha} \frac{\partial^2 \overline{\xi^2}}{\partial \psi^2} \tag{3.48}$$

The coefficients can be found in Chapter 5.1 where a method to calculate them is presented. The $C_0$, $C_3$ and $C_5$ coefficients are not always needed. The $C_0$ coefficient has to be used if $\lambda > 2$ otherwise it would not appear in the derivation. If $\lambda < 2$ we must evaluate and use $C_5$ instead, see Sect. 3.2.1. $C_3$ needs to be determined only if the geometry of the plasma is not up-down symmetric, otherwise it is close to zero and can be neglected[2].

## 3.3. Discussion

To obtain an initial intuitive interpretation of this model we will discuss the physical meaning of the relevant terms of the nonlinear ballooning envelope equation (3.48), [2, 67, 69]. The linear terms ($C_0$, $C_1$ and $C_5$) of this equation are discussed first. The $C_0$ and $C_5$ terms represent the inertia of the filaments. The first term in $C_1$ is the "linear drive term" which drives the filaments initially. Its physical origin is a balance between stabilising field line bending and the destabilising pressure gradient in the ballooning case (in Chapter 4 the pressure gradient drive is replaced by the Rayleigh-Taylor drive). The second term in $C_1$ is the so called "$1/n$-correction term" as it is a higher order linear term. It originates from filaments pushing surrounding field lines aside, which causes field line bending in the perpendicular directions. This is why we also call this term the "field line stability term". The two nonlinear terms are the $C_2$ and $C_4$ terms. The quadratic $C_2$ term is the "nonlinear drive term" (or "quadratic nonlinear term") which is the explosive drive in the nonlinear regime. It is mainly caused by a change of the field line bending force depending on the equilibrium structure. The sign of $C_2$ is responsible for the direction of the nonlinear drive. If $C_2$ is positive the field line bending force is nonlinearly weakened due to an expanding

[2] To obtain the equation calculated in the code Deton8 (see Sect. 2.5.1), we are using the Taylor-expansion of the quantity $\mu$ and calculating its values and the second derivative of $\mu$ with respect to $f'$ numerically. We can set $C_3 = 0$ since we only analyse up-down-symmetric cases. Furthermore we integrate with respect to $\alpha$ and exploit the fact that $\overline{\xi} = 0$ (see Eq. (3.26)).

flux tube as it moves radially outwards and therefore accelerates the filaments outwards. However, if the coefficient is negative the filament implodes instead. The cubic $C_4$ term is the "quasilinear nonlinearity term" which stabilises the filaments at the most unstable flux surface but drives them radially further away from this flux surface; therefore it causes the filaments to broaden in the $\psi$ direction and to narrow in the $\alpha$ direction as long as $C_4$ is positive. It is a physical mechanism which couples the flux surfaces in the $\psi$ direction such as the flattening of any steep pressure gradients.

In Chapter 5 we analyse each coefficient and discuss it in more detail so that we can calculate them for real equilibrium cases. But first in Chapter 4, we investigate how the nonlinear terms change the behaviour of interacting filaments.

# 4. Nonlinear interaction of filamentary eruptions

In this chapter the interaction of multiple filamentary plasma eruptions is investigated by modelling the nonlinear MHD ballooning mode envelope equation with a mixed Eulerian and Lagrangian characterisation of the boundary conditions. The study of multiple plasma filaments is performed in a specific slab equilibrium susceptible to Rayleigh-Taylor instabilities. We will argue that our main results are quite generic, independent of geometry and drive mechanism (within ideal MHD). We therefore demonstrate the essential physics with the relatively simple slab Rayleigh-Taylor-model, employed in [67]. We extend that calculation to derive the system with Eulerian boundary conditions, as employed in [4]. We shall find that if the unstable system is initiated with three equal sized filaments, they erupt at the same rate, independently of each other, even in the nonlinear regime. However, if one is initiated very slightly larger than the other two it causes a down-draft as it erupts upwards, which suppresses the smaller filaments. This suggests that those filaments which first enter the nonlinear regime will dominate the plasma eruption dynamics.

In section 4.1 the equilibrium is described with the boundary conditions and the derivation of the nonlinear ballooning model in slap geometry is outlined (a more detailed derivation can be found in Appendix D). In the next section (4.2) the influence of the included scalar viscosity is quantified. Section 4.3 is the main section of this chapter which shows how the so called "three filament system" is initialised and quantifies the interaction of the filaments. Section 4.4 provides two examples of experimental observations that potentially can be explained by our simulations. This chapter finishes with the conclusion in section 4.5.

Some parts of the viscosity section (4.2) have been reported in [4] and parts of section 4.3

have been published in [5, 6].

## 4.1. Theoretical model

### 4.1.1. Nonlinear equation with mixed Eulerian and Lagrangian boundary conditions

In this Section, we derive the nonlinear equation for the slab Rayleigh-Taylor model using mixed Eulerian and Lagrangian boundary conditions. Specifically, we employ boundary conditions with no vertical plasma displacement and no perturbed density or pressure at the walls.

We analyse a system with an equilibrium of a simple one dimensional line tied magnetised plasma atmosphere which is given by a magnetic field $\boldsymbol{B_0} = B_0(x)\,\hat{z}$, the pressure $p_0 = p_0(x)$, the density $\rho_0 = \rho_0(x)$ and the gravitational acceleration $\boldsymbol{g} = -g\,\hat{x}$ where the subscript "0" indicates equilibrium quantities, as shown in Fig. 4.1. Our starting point is

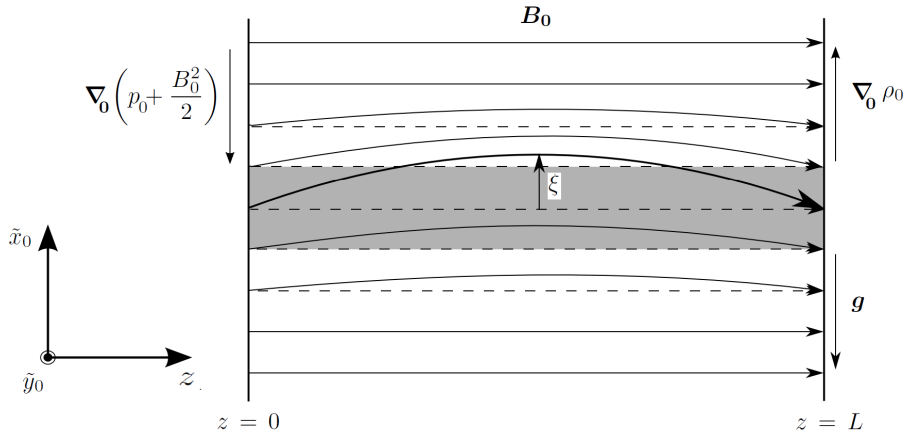


Figure 4.1.: *Slab geometry: Straight field lines represent the equilibrium. The curved field lines visualise a perturbed system. The displacement $\xi$ is a measure of how much the magnetic field lines or filaments have moved away from the equilibrium position. The gravity $g$ is pointing downwards and a density gradient is pointing upwards which results in a Rayleigh-Taylor drive. In the equilibrium case this drive is balanced by the pressure and magnetic field line gradient.*

the ideal MHD momentum equation considering gravity and with an additional kinematic, scalar viscosity term that is included to provide simple viscous dissipation [60]:

$$\rho\left(\frac{\partial \boldsymbol{v}}{\partial t} + \boldsymbol{v}\cdot\boldsymbol{\nabla}\boldsymbol{v}\right) = -\boldsymbol{\nabla}\left(p + \frac{B^2}{2}\right) + \boldsymbol{B}\cdot\boldsymbol{\nabla}\boldsymbol{B} - \rho g\hat{\boldsymbol{x}} + \nu\rho\,\triangle\boldsymbol{v}.$$

where $\boldsymbol{v} = \frac{\partial \boldsymbol{r}}{\partial t}$ is the velocity and $\nu$ is the scalar viscosity. We choose to perform the calculation in Lagrangian variables. In this approach all quantities can be expressed in terms of the displacement $\boldsymbol{\xi}$ of a fluid element. The position vector of a fluid element, $\boldsymbol{r}(t)$, is related to its initial position vector, $\boldsymbol{r}_0$, through $\boldsymbol{r}(t) = \boldsymbol{r}_0 + \boldsymbol{\xi}(\boldsymbol{r}_0, t)$, so that the components of the Jacobian matrix $J_{ij}$ are

$$J_{ij} = (\boldsymbol{\nabla}_0 \boldsymbol{r})_{ij} = \delta_{ij} + \frac{\partial \xi_j}{\partial x_{0i}},$$

where $x_{0i}$ are the components of $\boldsymbol{r}_0$ and $i, j$ run from 1 to 3 to label $x$,$y$ and $z$ coordinates of a Cartesian system. The Jacobian $J$ is the determinant of the Jacobian matrix $J_{ij}$. We choose the boundary conditions so that $\xi_x = 0$ and $J = 1$ at the walls where $z = 0$ and $z = L$, corresponding to unperturbed density $\rho$ and pressure $p$. We assume that gradients in the $\rho$ and $p$ profiles are in the $x$-direction and that the process is isothermal as the thermal conduction along the field lines is fast. This implies that the ratio of specific heat, $\Gamma$, is equal to one.

We measure the distance above marginal stability by a dummy large parameter $n$ where the growth rate of the most unstable perturbation $\Gamma$ is order $n^{-1/2}$. Thus

$$\frac{\partial}{\partial t} \sim \mathcal{O}\left(n^{-1/2}\right)$$

The order of the spatial derivatives as well as the order of the Lagrangian displacement is set by the localised geometry of the most unstable linear mode structure [67] which is similar to the ballooning mode structure [56]:

$$\frac{\partial}{\partial x_0} \sim \mathcal{O}\left(n^{+1/2}\right) \qquad k_y \sim \frac{\partial}{\partial y_0} \sim \mathcal{O}(n) \qquad \frac{\partial}{\partial z_0} \sim \mathcal{O}(1)\,. \tag{4.1}$$

Expanding the components of $\boldsymbol{\xi} = \xi_x \hat{\mathbf{x}} + \xi_z \hat{\mathbf{z}} + \xi_y \hat{\mathbf{y}}$ and the Jacobian $J$ in powers of $n^{-1/2}$ we anticipate:

$$\xi_x = \sum_{i=2}^{\infty} n^{-i/2} \xi_x^{(i/2)} \quad \xi_z = \sum_{i=2}^{\infty} n^{-i/2} \xi_z^{(i/2)} \quad \xi_y = \sum_{i=3}^{\infty} n^{-i/2} \xi_y^{(i/2)} \quad J = 1 + \sum_{i=1}^{\infty} n^{-i/2} J^{(i/2)}.$$

The viscosity is treated as small $\nu \sim \mathcal{O}(n^{-5/2})$ so that it only enters in our envelope equation for $\xi_x$.

Conservation of mass yields $\rho(\boldsymbol{r},t) = \rho_0(x_0)/J$ where the density at $\boldsymbol{r}$ at time $t$ is $\rho(\boldsymbol{r},t)$ and the equilibrium density at $\boldsymbol{r}_0$ is $\rho_0(x_0)$. Similarly pressure evolution is $p(\boldsymbol{r},t) = p_0(x_0)/J$ using $p(x,y,z,t) = \rho(x,y,z,t)T_0(x_0)$ and the assumption of an isothermal process which sets the ratio of specific heats to one: $\Gamma = 1$. The conservation of magnetic flux yields

$$\boldsymbol{B}(\boldsymbol{r},t) = \frac{\boldsymbol{B}_0(\boldsymbol{r}_0)\cdot\boldsymbol{\nabla}_0\boldsymbol{r}}{J} = \frac{B_0(x_0)}{J}\left[\hat{\mathbf{z}} + \frac{\partial\boldsymbol{\xi}}{\partial z_0}\right].$$

A full derivation can be found in [61].

With these relations the MHD momentum equation becomes:

$$\begin{aligned}\frac{\rho_0}{J}(\boldsymbol{\nabla}_0\boldsymbol{r})\cdot\frac{\partial^2\boldsymbol{\xi}}{\partial t^2} = &-\boldsymbol{\nabla}_0\left[\frac{p_0}{J} + \frac{|(\boldsymbol{B}_0\cdot\boldsymbol{\nabla}_0\boldsymbol{r})|^2}{2J^2}\right] \\ &+ (\boldsymbol{\nabla}_0\boldsymbol{r})\cdot\left[\frac{1}{J}(\boldsymbol{B}_0\cdot\boldsymbol{\nabla}_0)\left(\frac{1}{J}(\boldsymbol{B}_0\cdot\boldsymbol{\nabla}_0\boldsymbol{r})\right) + \frac{\rho_0}{J}\mathbf{g}\right] + \nu\nabla_0^2\frac{\partial\boldsymbol{\xi}}{\partial t}. \quad (4.2)\end{aligned}$$

Dotting Eq. (4.2) with $\boldsymbol{B}_0 = B_0\hat{\mathbf{z}}$ and multiplying by $J$ yields:

$$\rho_0 B_0(x_0)\left[\hat{\mathbf{z}} + \frac{\partial\boldsymbol{\xi}}{\partial z_0}\right]\cdot\frac{\partial^2\boldsymbol{\xi}}{\partial t^2} = B_0(x_0)\frac{\partial}{\partial z_0}\left[p_0\ln J - \rho_0 g\xi_x\right] + \nu B_0 J\nabla_0^2\frac{\partial\xi_z}{\partial t}.$$

Dropping terms $\mathcal{O}(n^{-3})$ and higher we can solve for $J$ using the boundary conditions:

$$J = \exp\left(\frac{\rho_0 g\xi_x}{p_0} + \frac{\rho_0}{p_0}\frac{\partial^2 s}{\partial t^2}\right) + \mathcal{O}\left(n^{-3}\right) \quad (4.3)$$

where $s = \int_0^{z_0}\xi_z dz_0$. The use of the Eulerian $z$ boundary condition distinguishes this calculation from previous derivations and simplifies the calculation as we have a specific form of the Jacobian. The steps include analysing the different orders of $n$ of the $x_0$-component and the $y_0$-component of Eq. (4.2). This derivation is a simplified version of the one summarised in Chapter 3 due to its boundary conditions and the simpler geometry and the full calculation is reported in Appendix D which derives the following equation for

the evolution of the filament in the direction perpendicular to the magnetic field lines:

$$\overbrace{\hat{C}_0\frac{\partial^2\xi}{\partial t^2}}^{\text{Inertia Term}} = \overbrace{\Gamma^2(x_0)\xi}^{\text{Linear Instability Drive}} - \overbrace{\hat{C}_2\frac{\partial^2 u}{\partial x_0^2}}^{\text{Field Line Stability Term}} + \overbrace{\nu\frac{\partial^2}{\partial y_0^2}\frac{\partial\xi}{\partial t}}^{\text{Viscosity Term}} + \underbrace{\hat{C}_3\xi\frac{\partial^2\overline{\xi^2}}{\partial x_0^2}}_{\text{Quasilinear Nonlinearity Term}} + \underbrace{\hat{C}_4\left(\xi^2-\overline{\xi^2}\right)}_{\text{Nonlinear Growth Drive}} \tag{4.4}$$

Here we have $\xi_x(x_0, y_0, z_0) = \xi(x_0, y_0, t)H(z)$ where the function $H(z)$ describes the vertical displacement along the field line and is given in Appendix D: $H(z) = \sin(\frac{\pi z}{L})$. We have also defined $\overline{\xi^2}$ is the $y_0$ average of the squared displacement, $\xi^2$ and $\frac{\partial^2 u}{\partial y_0^2} = \xi$. The local linear growth rate $\Gamma$, which is also derived in Appendix D, is given by, [71]:

$$\Gamma^2(x_0) = -\frac{B_0^2\pi^2}{\rho_0 L^2} + \frac{\rho_0 g^2}{p_0} + \frac{g}{\rho_0}\frac{d\rho_0}{dx_0}\,.$$

The first term describes the stabilising effect of field line bending, the second term is the Parker instability drive[1] and the third term is the Rayleigh-Taylor instability drive.
The coefficients $\hat{C}_0$, $\hat{C}_2$, $\hat{C}_3$ and $\hat{C}_4$ are given by:

$$\begin{aligned}
\hat{C}_0 &= \left(1+\frac{\rho_0^2 g^2 L^2}{p_0^2\pi^2}\right) & \hat{C}_2 &= -\left(\frac{B_0^2\pi^2}{\rho_0 L^2}\right)\\
\hat{C}_3 &= \left(\frac{B_0^2\pi^2}{8\rho_0 L^2}\right) & \hat{C}_4 &= \frac{4}{3\pi}\left(\frac{g}{\rho_0}\frac{d^2\rho_0}{dx_0^2} - \frac{\rho_0^2 g^3}{p_0^2}\right)
\end{aligned} \tag{4.5}$$

Notice that the Eq. (4.4) has the same form as the one derived in Chapter 3 except that it always has a second time derivative. Sect. 3.3 provides a discussion of the physical interpretation of this Eq. (4.4). Also, this is one reason why the results shown in this Chapter are generic and are considered to be relevant for tokamak geometry (especially for strong shaping where $\lambda_L - \lambda_S > 2$ [2]).

[1] The Parker instability is also known as "magnetic Rayleigh-Taylor" instability. A simplified explanation is that the supporting pressure gradient is replaced by a gradient in the *magnetic* pressure which can lead to an unfavourable density distribution [115, 116].

### 4.1.2. A model equilibrium

To obtain results for a specific situation we calculate coefficients for a simple model atmosphere in a slab geometry, which is an extension of that used in [71]. The equilibrium density and magnetic field are given by:

$$\rho(x_0) = \frac{\overline{\rho}}{cosh^2\left[\frac{x_0 - x_\rho}{L_\rho}\right]} \qquad B_0^2(x_0) = \overline{B}_1^2 - \frac{\overline{B}_2^2}{cosh^2\left[\frac{x_0 - x_B}{L_\rho}\right]}\,.$$

From the equilibrium equation $\frac{\partial}{\partial x}\left(p_0 + \frac{B_0^2}{2}\right) = -g\rho_0$ we obtain the following for the

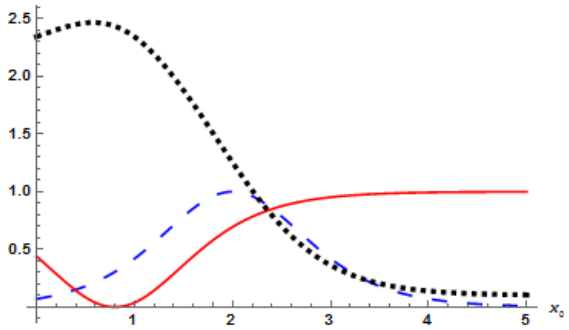


Figure 4.2.: *Sketch of the unperturbed density* $\rho(x_0) = \frac{\overline{\rho}}{cosh^2\left[\frac{x_0 - x_\rho}{L_\rho}\right]}$ *(blue, dashed), magnetic field* $B_0^2(x_0) = \overline{B}_1^2 - \frac{\overline{B}_2^2}{cosh^2\left[\frac{x_0 - x_B}{L_\rho}\right]}$ *(red, solid) and pressure* $p_0(x_0) = \overline{p}_0 - \frac{B_0^2}{2} - g\overline{\rho}_0 L_\rho \tanh\left[\frac{x_0 - x_\rho}{L_\rho}\right]$ *(black, dotted).*

equilibrium pressure profile:

$$p_0(x_0) = \overline{p}_0 - \frac{B_0^2}{2} - g\overline{\rho}_0 L_\rho \tanh\left[\frac{x_0 - x_\rho}{L_\rho}\right]\,.$$

Similar to [71], we define normalised variables and constants:

$$\tilde{x}_0 = \frac{x_0}{L_\rho}, \qquad \tilde{y}_0 = \frac{y_0}{L_\rho}, \qquad \tilde{t} = \sqrt{\frac{g}{L_\rho}}t, \qquad \tilde{B}_1^2 = \frac{\overline{B}_1^2}{2g\overline{\rho}_0 L_\rho}, \qquad \tilde{\xi} = \frac{\xi}{L_\rho},$$
$$\tilde{x}_B = \frac{x_B}{L_\rho}, \qquad \tilde{x}_\rho = \frac{x_\rho}{L_\rho}, \qquad A = \frac{L_\rho}{L}, \qquad \tilde{B}_2^2 = \frac{\overline{B}_2^2}{2g\overline{\rho}_0 L_\rho}.$$

With these normalised variables the form of Eq. (4.4) would change unless we make the following transformation:

$$\tilde{C}_0 = \hat{C}_0 \frac{\rho_0}{2\overline{\rho}} \qquad \tilde{C}_3 = \hat{C}_3 \frac{L_\rho \rho_0}{2g\overline{\rho}}$$
$$\tilde{\Gamma}^2 = \Gamma^2 \frac{L_\rho \rho_0}{2g\overline{\rho}} \qquad \tilde{C}_4 = \hat{C}_4 \frac{L_\rho^2 \rho_0}{2g\overline{\rho}}$$
$$\tilde{C}_2 = \hat{C}_2 \frac{L_\rho \rho_0}{2g\overline{\rho}} \qquad \tilde{\nu} = \nu \frac{\rho_0}{2\overline{\rho}\sqrt{gL_\rho^3}}$$

With these expressions we obtain:

$$\tilde{C}_0 \frac{\partial^2 \tilde{\xi}}{\partial \tilde{t}^2} = \tilde{\Gamma}^2(\tilde{x}_0)\tilde{\xi} - \tilde{C}_2 \frac{\partial^2 \tilde{u}}{\partial \tilde{x}_0^2} + \tilde{C}_3 \tilde{\xi} \frac{\partial^2 \overline{\tilde{\xi}^2}}{\partial \tilde{x}_0^2} + \tilde{C}_4(\tilde{\xi}^2 - \overline{\tilde{\xi}^2}) + \tilde{\nu} \frac{\partial^2}{\partial \tilde{y}_0^2} \frac{\partial \tilde{\xi}}{\partial \tilde{t}}$$

where $\frac{\partial^2 \tilde{u}}{\partial \tilde{y}_0^2} \equiv \tilde{\xi}$. To derive the normalised coefficients $\tilde{C}_i$ we use equations (4.5) and assume a large pressure to ensure that the Rayleigh-Taylor instability dominates over the Parker instability drive. We obtain:

$$\tilde{\Gamma}^2(\tilde{x}_0) = -\left( A^2 \tilde{B}_1^2 - \frac{A^2 \tilde{B}_2^2}{\cosh^2(\tilde{x}_0 - \tilde{x}_B)} \right) \pi^2 - \frac{\sinh(\tilde{x}_0 - \tilde{x}_\rho)}{\cosh^3(\tilde{x}_0 - \tilde{x}_\rho)}$$
$$\tilde{C}_0 = \frac{\rho_0}{2\overline{\rho}_0} = \frac{1}{2\,\cosh^2(\tilde{x}_0 - \tilde{x}_\rho)}$$
$$\tilde{C}_2 = -\frac{L_\rho}{2g\overline{\rho}_0} \left( \frac{B_0^2 \pi^2}{L^2} \right) = -\left( A^2 \tilde{B}_1^2 - \frac{A^2 \tilde{B}_2^2}{\cosh^2(\tilde{x}_0 - \tilde{x}_B)} \right) \pi^2$$
$$\tilde{C}_3 = \frac{L_\rho}{16g\overline{\rho}_0} \left( \frac{B_0^2 \pi^2}{L^2} \right) = \frac{1}{8} \left( A^2 \tilde{B}_1^2 - \frac{A^2 \tilde{B}_2^2}{\cosh^2(\tilde{x}_0 - \tilde{x}_B)} \right) \pi^2$$
$$\tilde{C}_4 = \frac{2L_\rho^2}{3\pi\overline{\rho}_0} \frac{d^2\rho_0}{dx_0^2} = \frac{8}{3\pi} \frac{3\tanh^2(\tilde{x}_0 - \tilde{x}_\rho) - 1}{\cosh^2(\tilde{x}_0 - \tilde{x}_\rho)}\,.$$

The linear drive coefficient $\tilde{\Gamma}^2(x_0)$ can be expanded about the position $x_{max}$ where the growth rate has a maximum:

$$\tilde{\Gamma}^2(x_0) \approx \tilde{\Gamma}^2(x_{max}) - \left| \frac{\mathrm{d}\tilde{\Gamma}^2}{\mathrm{d}x_0^2} \right|_{x_{max}} \left( \frac{(x_0 - x_{max})^2}{2} \right)$$
$$= \tilde{C}_1 \left( 1 - \frac{(\tilde{x}_0 - \tilde{x}_{max})^2}{\Delta^2} \right)$$

We adopt the same choice of variables as Ref. [71] to enable comparison: $\tilde{x}_\rho = 2$, $\tilde{x}_B = 0.8$, $A^2\overline{B}_1^2 = 0.07834$ and $A^2\overline{B}_2^2 = 0.04701$. With these parameters we obtain:

$$\tilde{C}_0 = 0.248 \qquad \tilde{C}_1 = 1.9 \times 10^{-4} \qquad \tilde{C}_2 = -0.352$$
$$\tilde{C}_3 = 0.044 \qquad \tilde{C}_4 = 0.216$$
$$\Delta = 0.017 \qquad \tilde{x}_{\max} = 1.1118$$

and we chose the viscosity to be $\tilde{\nu} = 10^{-10}$.

## 4.2. Scalar viscosity

In this section the influence of the small scalar viscosity on the system is analysed. For an investigation on how the viscosity changes the evolution of the filaments we perform a simple balancing of the nonlinear terms of the ballooning mode envelope equation (4.4) (i.e., inertia, viscosity, quasilinear nonlinearity and nonlinear growth drive term) which leads to the following relations:

$$\xi \propto (t_0 - t)^{-2} \qquad \frac{\Delta x^2}{\Delta y} \propto \xi \qquad \Delta y \propto (t_0 - t)^{0.5} \qquad \Delta x \propto (t_0 - t)^{-0.75} \tag{4.6}$$

where $\Delta y$ is the width of the filament in the $\nabla y$ direction and $\Delta x$ is the width of the filament in the $\nabla x$ direction; $t_0$ is a quantity that depends on initial conditions. The inclusion of viscosity allows for the derivation of the last two relations. We can define the widths $\Delta y$ and $\Delta x$ as follows to calculate these quantities from our simulations:

$$\Delta y = \frac{\int dy\ \xi(x_{max}, y, t)^2}{\xi(x_{max}, 0, t)^2} \tag{4.7}$$

$$\Delta x = \frac{\int dx \int dy\ (x - x_{max})\xi^2}{\int dx \int dy \xi^2} \tag{4.8}$$

where the $x$-integrals are over the whole regime of the simulation which should be a good estimate since $\xi$ decays to zero before the end of the numerical domain. The $y$-integrals are over one periodic interval. Using these definitions we can estimate the numerical results

to compare it with the indices of the relations (4.6):

$$\xi \propto (t_0-t)^{-2.52} \qquad \frac{\Delta x^2}{\Delta y} \propto (t_0-t)^{-2.5} \qquad \Delta y \propto (t_0-t)^{1.04} \qquad \Delta x \propto (t_0-t)^{-0.73} \tag{4.9}$$

To refer to the indices we introduce the indices $p$, for each of the asymptotic forms: $\xi \sim (t_0-t)^{p_\xi}$, $\Delta y \sim (t_0-t)^{p_y}$ and $\Delta x \sim (t_0-t)^{p_x}$. The predicted indices (see (4.6)) indicate that the width $\Delta y$ is shrinking and the width $\Delta x$ is growing as the finite time singularity, $t \to t_0$, is approached. Numerical simulations confirm this (Fig. 4.4 and (4.9)). The results always

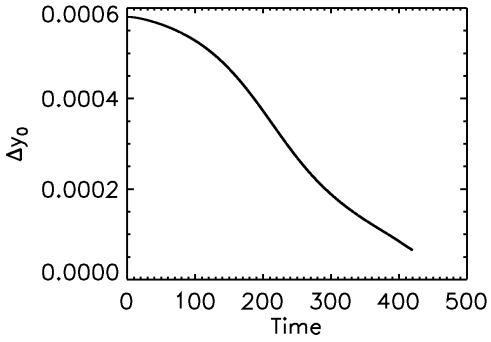


Figure 4.3.: *Evolution of the width $\Delta y$ defined by Eq.* (4.7)*. The process of narrowing, but not the rate of narrowing, agrees with the relation given in* (4.6)*.*

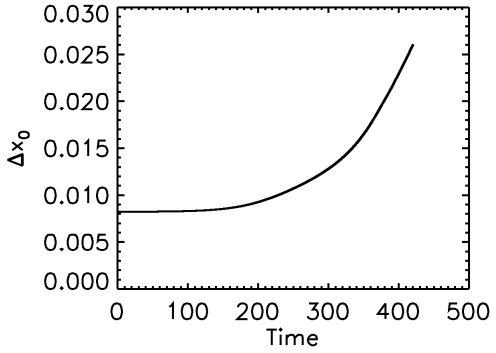


Figure 4.4.: *Evolution of the width $\Delta x$ defined by Eq.* (4.8)*. The broadening, but not the rate of narrowing, agrees with the relation given in* (4.6)*.*

exhibit an explosive behaviour of the filaments independent of whether or not viscosity is included. However, the simple balancing of terms does not give accurate quantitative results for the individual indices $p_\xi$, $p_y$ and $p_x$. This can be seen as a measure of how dominant the viscosity term is in the nonlinear regime because the predicted indices $p_y$ and $p_x$ are only valid if the influence of the viscosity is significant. Additionally numerical errors can be introduced in the simulation which can also affect the determined indices. This means that with the chosen values the viscosity term seems not as dominant as the other two nonlinear terms. This is in agreement with comparing the energy of each term to determine which terms are dominant. We can show that the energy of each term is described by this expression where the dissipated energy is equal to the viscosity term on

the right hand side:

$$2\frac{dE}{dt} = \frac{d}{dt}\int dV\left[C_0\left(\frac{\partial\xi}{\partial t}\right)^2 - \Gamma^2\xi^2 + C_2\left(\frac{\partial u}{\partial x_0}\right)^2 + \frac{1}{2}C_3\left(\frac{\partial\overline{\xi^2}}{\partial x_0}\right)^2 - \frac{2}{3}C_4\xi^3\right]$$
$$= -\nu\int dV\left(\frac{\partial^2\xi}{\partial t\partial y_0}\right)^2 \tag{4.10}$$

where $\int dV = \int dx_0\, dy_0 L_z$ is a volume integral. This relation enables us to quantify which terms dominate the evolution of the filaments at different times.

Fig. 4.5 shows the evolution of the energies of each term. The left side shows the time

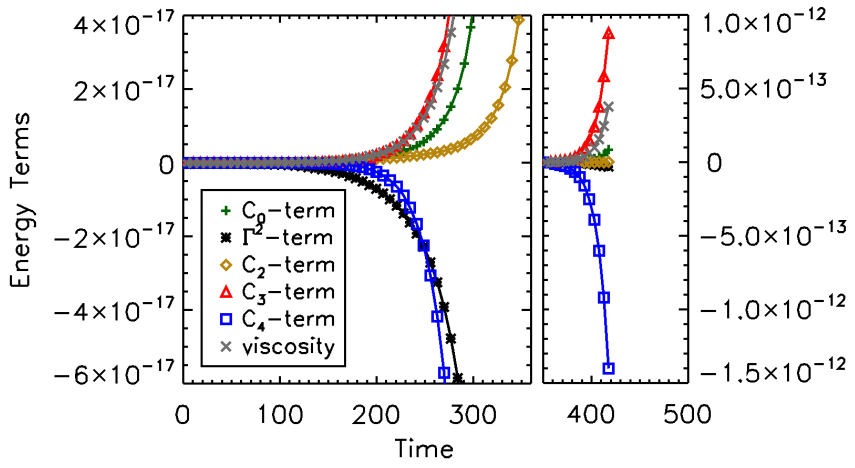


Figure 4.5.: *Evolution of the energies of each term (see Equation* (4.10)*). On the left: the change of linear to nonlinear regime; On the right: reaching the singularity in time in a very nonlinear regime.*

up to when the nonlinear drive overtakes the linear drive. The right hand side shows the energies deep in the nonlinear regime.

The relation $\frac{(2p_x - p_y)}{p_\xi} \approx 1$, which comes from balancing the nonlinear growth drive term and the quasilinear nonlinearity term, is very robust, agreeing well with simulations with and without viscosity. This indicates that these two terms are dominating the evolution close to the finite time singularity.

In summary the small viscosity influences the nonlinear evolution as it determines the behaviour of the widths $\Delta x$ and $\Delta y$ in the nonlinear regime. However, the viscosity chosen here has only a minor impact on this.

## 4.3. Interacting filaments

In this section the interaction of filaments with slightly different initial heights is investigated. Previous research [5] using this nonlinear ballooning model studied the evolution of single, isolated filaments in time and space. In a real plasma system it is more likely that several filaments will erupt, and interact - ELMs are a classic example [37]. This motivates our study to determine how the interaction of filaments affects their evolution, extending the studies of [69].

### 4.3.1. Initiation - linear solution

A linear stability analysis of Eq. (4.4) (neglecting the last two terms of Eq. (4.4)) provides an eigenmode structure of the displacement which can be used to initialise the simulations. To solve the linear differential equation, one can use a separation of variables:

$$\xi = X(x_0)\, Y(y_0)\, T(t)$$

Using the ansatz that $Y(y_0) = \cos(ny_0)$ and $T(t) = \exp(\gamma t)$, where $n$ is the mode number and $\gamma$ the linear growth rate, one obtains a Weber differential equation for the $x_0$ component [112]:

$$\frac{C_2}{n^2}\frac{\partial^2 X(x_0)}{\partial x_0^2} + \left[C_0\gamma^2 + n^2\nu\gamma - C_1\left(1 - \frac{(x_0 - x_{max})^2}{\Delta^2}\right)\right] X(x_0) = 0$$

Its solution is a Gaussian function: $X(x_0) = \exp(-\frac{x_0^2}{2\sigma^2})$. Combining, we initialise the displacement $\xi$ with $\xi(x_0, y_0, t = 0) = h\,\cos(ny_0)\exp(-\frac{x^2}{2\sigma^2})$ where the Gaussian width $\sigma^2(n) = \frac{4\Delta}{n}\sqrt{\frac{|C_2|}{C_1}}$ and a linear growth rate $\gamma(n) = -\frac{n^2\nu}{2C_0} + \sqrt{\frac{C_1}{C_0} - \frac{\sqrt{C_1|C_2|}}{C_0 n\Delta} + \frac{n^4\nu^2}{4C_0^2}}$, see Fig. 4.6. $h$ is an arbitrary constant which has to be chosen sufficiently small so that the linear terms of Eq. (4.4) are dominant. To explore the nonlinear evolution predicted by Eq. (4.4) we initialise the system at $t = 0$ with the linear eigenmode and evolve in time. We wish to explore how filaments of different heights evolve in time. We therefore initialise four distinct systems with

1. a superposition of two linear eigenmodes, with two mode numbers $n_1$, $n_2$ and two

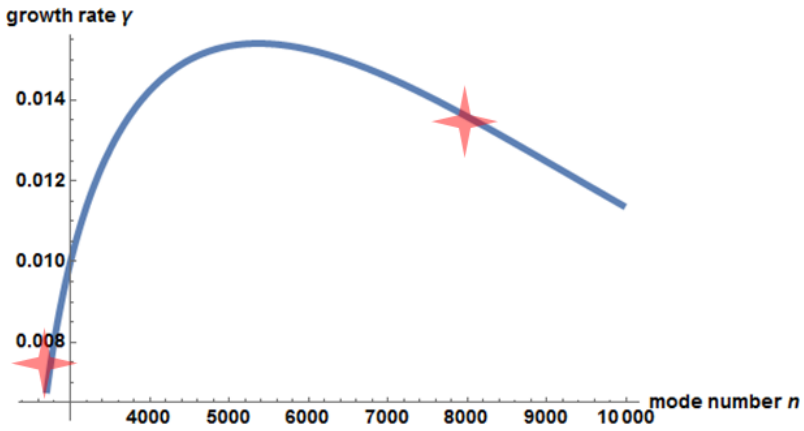


Figure 4.6.: *The linear growth rate $\gamma$ vs the mode number $n$. Highlighted are the growth rates for the mode numbers chosen in this section. Note that the three filament mode has a higher linear growth rate and therefore should be dominant if the linear drive is the full story.*

heights $h_1$ and $h_2$:

$$\xi_{\text{init}} = h_1 \cos(n_1 y_0)\, e^{(-\sigma_1 x_0^2 + \gamma_1 t)} + h_2 \cos(n_2 y_0)\, e^{(-\sigma_2 x_0^2 + \gamma_2 t)},$$

2. a single mode with the mode number $n_1$ and height $h_1$,

3. a single mode with the mode number $n_2$ and height $h_2$,

4. and a single mode with the mode number $n_2$ and the height $h = h_1 + h_2$.

Case 1 is the new case we are mainly interested in. Cases 2 and 3 are simulated to identify when the nonlinear regime is starting, and how the nonlinear interaction changes the behaviour. Case 4 is used to show how the interaction changes the behaviour compared to a case where the tallest filaments have the same heights, to exclude that as the reason why the main filament grows faster.

Case 1: A superposition of two linear eigenmodes:

If we select $n_2 = 3n_1$, this provides a perturbation which repeats every three oscillations in the $y_0$-direction. Thus, our simulation domain in this direction needs to contain only three oscillations, or filaments. If we take $h_1 = 0$, all three filaments will initially have the same amplitude (i.e. $h_2$). By introducing a small amount of $h_1$, we can enhance the initial amplitude of the central filament compared to the two side filaments. We select $n_1 = 2600$ and $n_2 = 7800$ which have linear growth rates $\gamma_1 = 0.0033$ and $\gamma_2 = 0.0136$, see Fig. 4.6.

This ensures that the linear evolution reinforces the three filaments, so any deviation from this must be a nonlinear effect.

We initiate our perturbation with $h_2 = 50\,h_1$ which ensures the filaments are initially very close in amplitude, but the central one penetrates slightly further than the two side filaments, see Fig. 4.7.

Case 2 and 3: two single mode initiations

All parameters are chosen as in the first case, but the two cases are simulated separately rather than superimposed. Therefore case 2 has $n = n_1$ and $h = h_1$, see the blue line in Fig 4.7 and case 3 has $n = n_2$ and $h = h_2$, see the black line in Fig. 4.7.

Case 4: another single mode

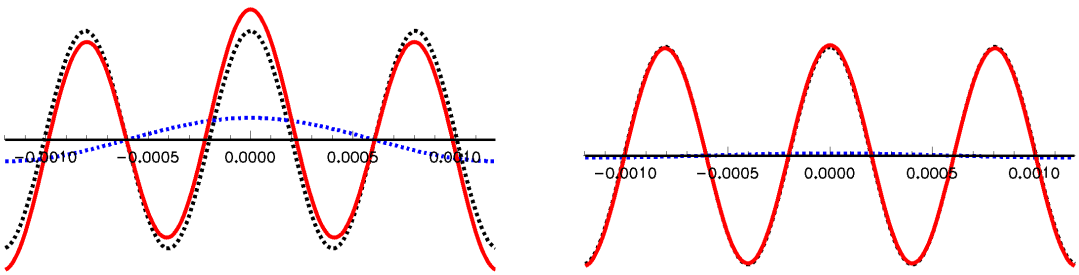


(a) *Superposition (red) of two modes with $n_2 = 3n_1$ and $h_2 = 5h_1$. Blue: $n_1$ and black $n_2$-mode. In the middle is the main central filament with two side filaments.*

(b) *Superposition (red) of two modes. This time with the actual heights $h_2 = 50h_1$ which produces a less than 2% larger main filament.*

Figure 4.7.: *Initiation of the filaments for two different choices of relative amplitude.*

This time we chose the mode number and the height so that the mode is the same as the dominant mode in case 1 but also the height is the same as the largest filament in case 1: $n = n_2$ and $h = h_1 + h_2$.

### 4.3.2. The evolution of multiple filaments

As the perturbation evolves, the energy is dissipated by the viscosity according to Eq. (4.10). The dominant terms are those involving $C_0$ and $C_4$ which arise from the inertia and the quadratic nonlinearity of Eq. (4.4), respectively. Figure 4.8 shows their evolution. We estimate that the nonlinear regime starts when the energy of the quadratic nonlinear drive term overtakes the energy of the linear drive term, which occurs at around $t = 260$. After this time, the behaviour of a filament approaches a finite time singularity $\xi \sim (t_0 - t)^{-\alpha}$,

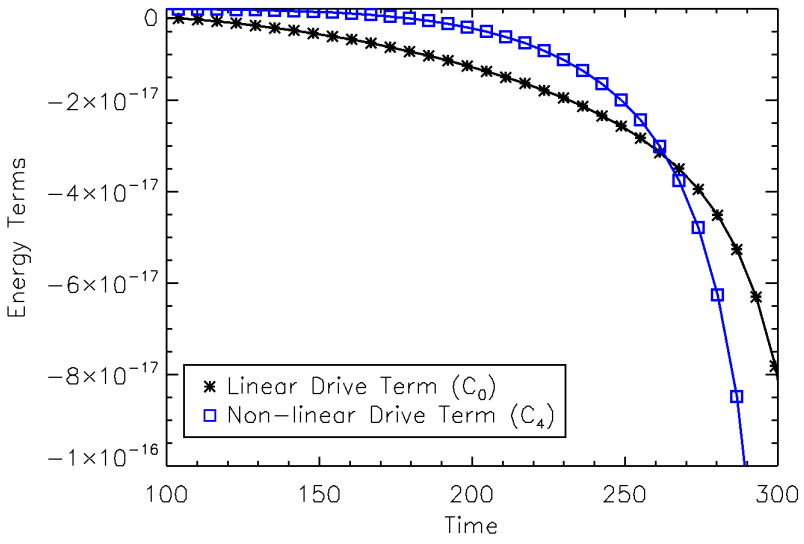


Figure 4.8.: *The two dominant drive terms of the energy Eq.* (4.10) *are shown. When the quadratic nonlinear drive term ($C_4$; blue, □-symbols) intersects with the linear drive term ($C_0$; black, ∗-symbols) we assume that the nonlinear dynamics start to dominate the evolution of the filaments*

where $\alpha$ is positive [67, 68]. We can fit this asymptotic form to the amplitude of the main central filament to determine $\xi_{mf} \sim (t_0 - t)^{-2.81}$. This is somewhat faster than our earlier simulations with a single, isolated filament where we found $\xi \sim (t_0 - t)^{-2.52}$ [71] (equivalent to taking $h_1 = 0$). Thus, simply enhancing one filament relative to the others by even a small amount has a significant impact on its subsequent nonlinear evolution. To explore this further, we plot in Fig. 4.9 the height of the main filament above the "ground level". We see that the main filament accelerates continuously throughout the simulation. To understand what we mean by the "ground level", we note that in the nonlinear regime, $\xi$ is negative and roughly constant over much of the region away from the three filaments along $x_0 = x_{max}$ [67]. This effectively reduces the "ground level" compared to the initial equilibrium. Thus we define $H_{mf}(t) = \xi(x_0 = x_{max}, y = 0.0, t) - min(\xi(x_{max}, y, t))$, see Fig. 4.10.

We now consider the height of the side filaments ($H_{sf}$ is defined in the same way) which, recall, were initiated with a height just 1.5% less than that of the main, central filament. While the side filaments grow with the main filament in the linear phase (at the linear growth rate) their growth rate reduces as they enter the nonlinear regime (at $t \approx 260$), and ultimately they are completely suppressed (beyond $t \approx 370$), see Fig. 4.9. Fig. 4.11

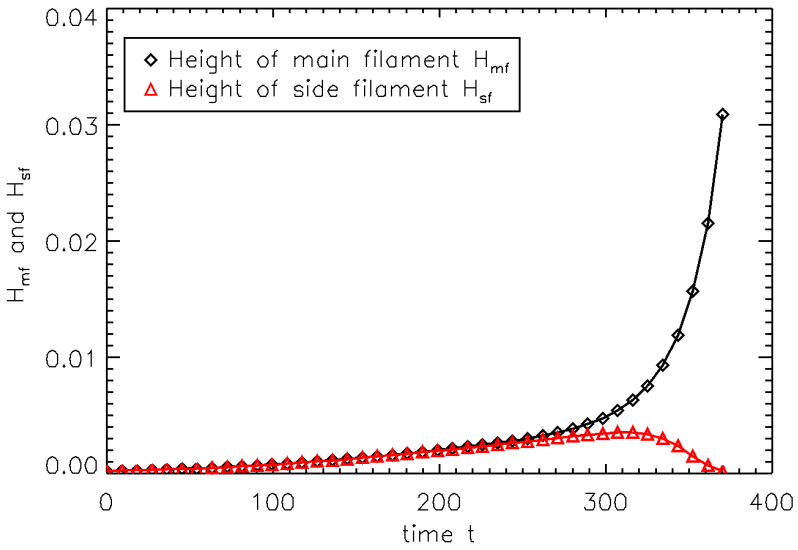


Figure 4.9.: *The normalised height at $x_0 = x_{max}$ of the main filament $H_{mf}$ (black, ◊-symbol) and the normalised height of the side filament $H_{sf}$ (red, △-symbol) vs time where the heights are shifted by the minimum value of $\xi$ at each time.*

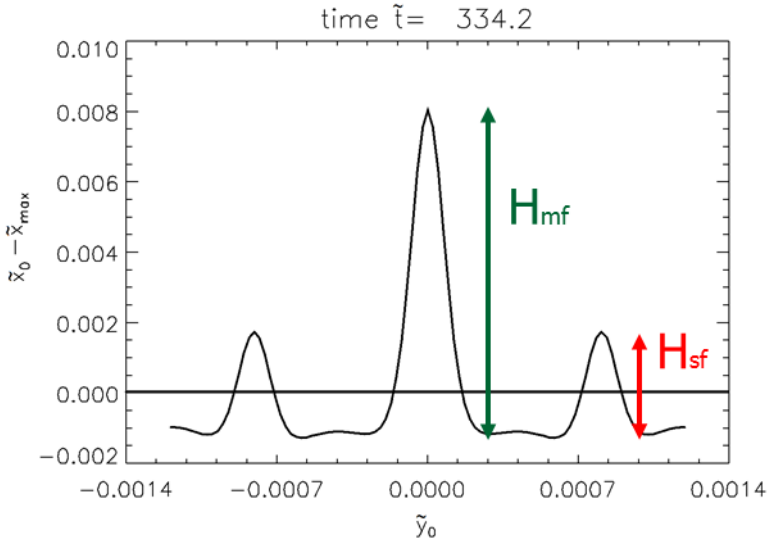


Figure 4.10.: *The main filament height $H_{mf}$ and the side filament height $H_{sf}$ on the most unstable flux line is plotted. Note how the "ground level" is reduced compared to zero – the starting point.*

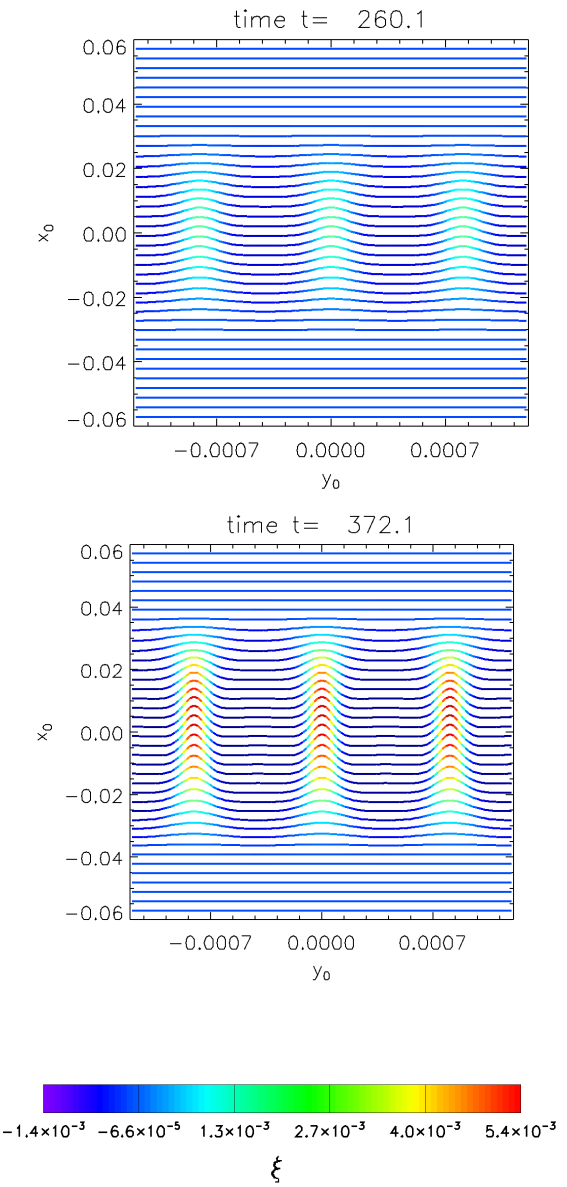


(a) *Initialised with three equal sized filaments (case 4).*

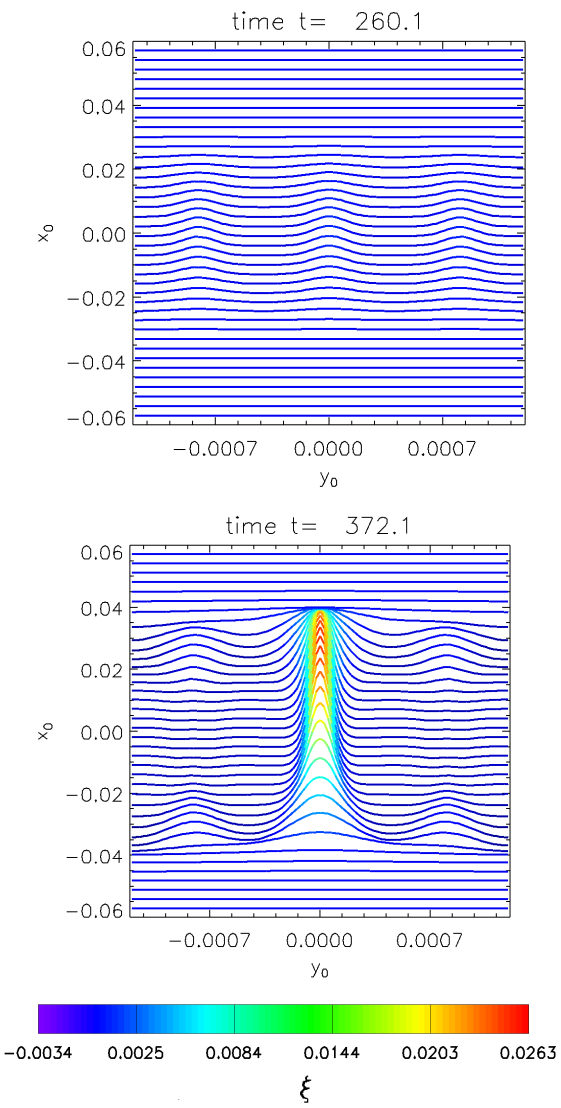


(b) *Central, main filament is initialised slightly larger (less than 2%) than the two side filaments (case 1). At the later time the two side filaments are much smaller than the main central filament and the amplitude of the main filament is approximately 5 times larger than in case 4.*

Figure 4.11.: *The flux surfaces in the x-y plane at $z = L/2$ (half way between the plates). The colour visualise additionally the displacement. The top is at the beginning of the nonlinear regime $t \approx 260$. The bottom shows the end of the simulation at a time $t = 370$, which is deep in the nonlinear regime, just as the perturbed flux surfaces of case 1 are about to overtake each other.*

shows a contour plot of the flux surfaces at a later time (i.e. $t = 370$). We see that the side filaments each form a double peak away from the most unstable $x_0 = x_{max}$ and are much smaller than the main one. Fig. 4.12 shows how this double peak structure develops through the nonlinear regime - the motion of the fluid element reverses direction at the

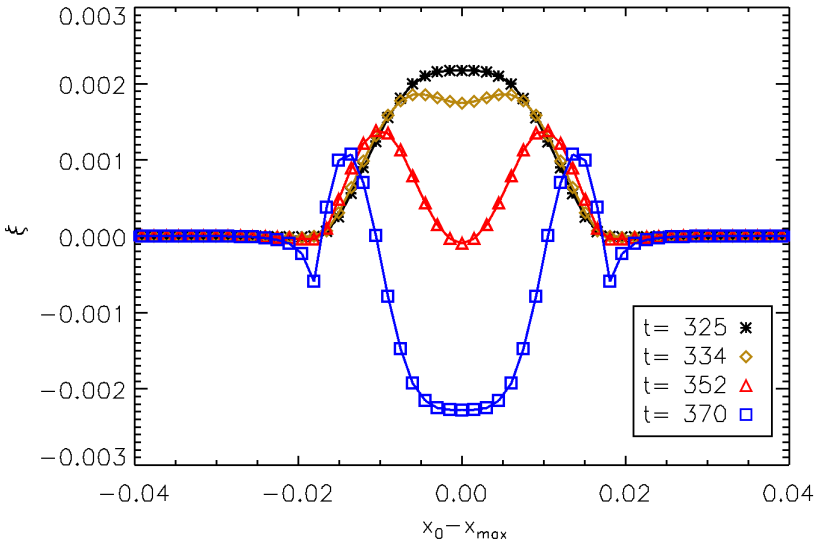


Figure 4.12.: *Evolution of a side filament vs $x_0$ in the nonlinear regime at $y_0 \approx \pm 0.0008$. The height is mainly reduced at the centre.*

position of maximum drive $x_0 = x_{max}$ leaving two peaks either side. The evolution of the ratio of the heights of the side and main filaments $p_H = \frac{H_{sf}}{H_{mf}}$ is shown in Fig. 4.13. During the linear phase this ratio is close to 1, as expected, but by the time overtaking occurs at $t \approx 370$ the side filaments have negligible amplitude. To compare the solution of the combined modes with the sum of the two individual mode solution, case 2 and 3, we define

$$\Delta\xi = \xi_{n_1+n_2} - (\xi_{n_1} + \xi_{n_2}).$$

Here $\xi_{n_1+n_2}$ is the displacement developed from the interaction of the two modes and $\xi_{n_1}$ and $\xi_{n_2}$ are the solutions from two separate nonlinear simulations for each $n = n_1$ and $n = n_2$. The plasma is in a linear regime at the beginning of the simulation as we start from close to marginal stability with a weak linear growth rate. Therefore we are expecting $\Delta\xi$ to be nearly zero at the beginning when the linear terms dominate as the modes evolve independently since they satisfy the superposition principle: $F(\sum_i x_i) = \sum_i F(x_i)$, where $F$ represents the solution of the differential equation and $x_i$ are different initiations. As the plasma enters the nonlinear regime the superposition of the modes will deviate from the sum of the two distinct solutions. We are interested in how the interaction between the two modes changes their evolution. To explore this we examine $\Delta\xi$, as shown in Fig. 4.14. Positive values of $\Delta\xi$ imply that the coupled filaments grow further than the sum of the

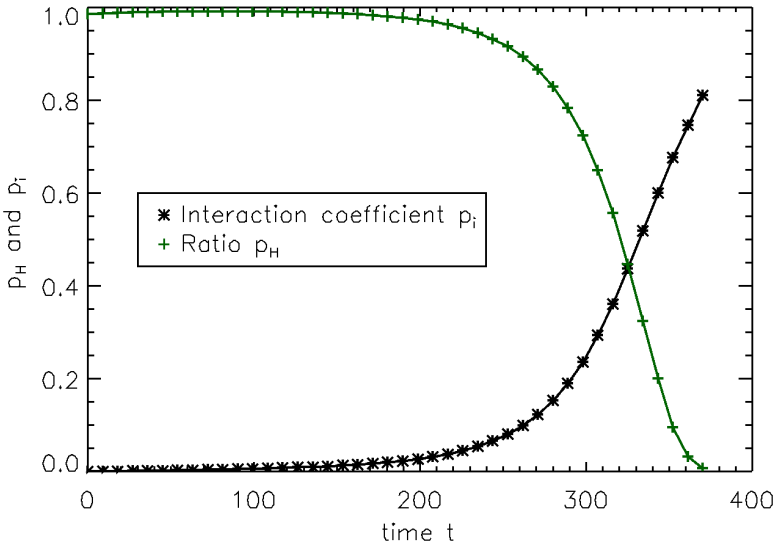


Figure 4.13.: *The ratio of the normalised height of the side filament to the main filament ($p_H = \frac{H_{sf}}{H_{mf}}$) vs time (green, +-Symbol) and the interaction-coefficient for the main filament vs time ($p_i = \frac{\Delta\xi}{\xi_{n_1+n_2}}$)(black, ∗-Symbol).*

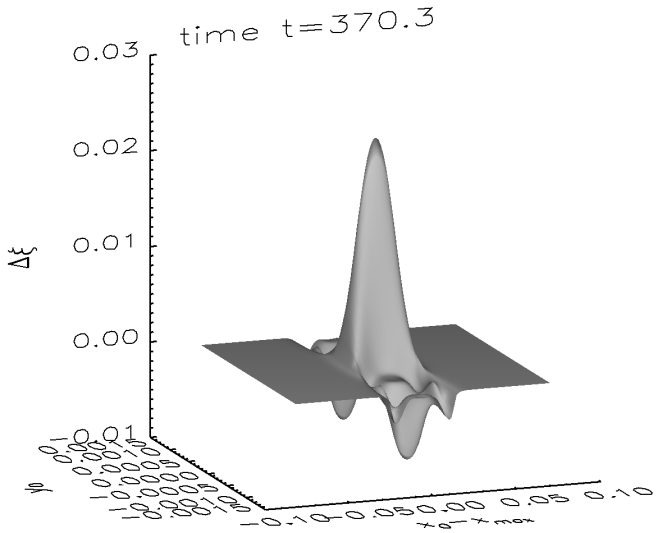


Figure 4.14.: *The spatial structure of $\Delta\xi$ deep in the nonlinear regime. Note the holes at the position of the side filaments which indicate that they get "eaten" by the main-filament.*

two individuals modes and negative values of $\Delta\xi$ mean that they grow slower. In Fig. 4.14 we show the spatial structure of $\Delta\xi$ deep inside the nonlinear phase. The main filament is indicated by the positive $\Delta\xi$ peak, and clearly grows stronger, suppressing the two side filaments for which $\Delta\xi < 0$. To quantify this effect further, we introduce the interaction coefficient $p_i = \dfrac{\Delta\xi}{\xi_{n_1+n_2}}$ for the main filament, which characterises the fraction of the main

filament height which is due to the coupling to the side filaments. In the linear phase $p_i$ is expected to be zero, as shown in Fig. 4.13. However, deep in the nonlinear regime, at $t = 370$, the height of the main filament is mostly (over 80 %) due to the interaction with the side filaments.

To understand this behaviour, let us return to Eq. (4.4). There are two key terms: the quasilinear nonlinearity term $C_3\xi\dfrac{\partial^2\overline{\xi^2}}{\partial x_0^2}$ and the nonlinear growth drive term $C_4\left(\xi^2-\overline{\xi^2}\right)$. Apart from the weak effect of viscosity, these are the only terms that couple in the $y$-direction, through the averaging of $\overline{\xi^2}$. This is therefore the dominant effect driving the interaction between the filaments. Later in time $\overline{\xi^2}$ is mainly dominated by the contribution from the main filament peak as it is the largest contribution and there is little contribution from the side filaments. Therefore, for values of $y_0$ in the vicinity of the main filament peak, where $\xi^2 > \overline{\xi^2}$, this provides a drive. Elsewhere, $\xi^2 < \overline{\xi^2}$ so the term is negative which explains the reduced “ground level" mentioned previously. It also serves to damp the side filaments. The quasilinear nonlinearity coefficient ($C_3$) is stabilising for both signs of $\xi$ when $x = x_{max}$ where the second derivative of $\overline{\xi^2}$ is negative. It does, however, drive the disturbed region to broaden in $x_0$ since the second derivative of $\overline{\xi^2}$ is positive and therefore destabilising at the edges of the disturbed region.

To understand the physics, we return to our earlier statement that the $\overline{\xi^2}$ averaging is a consequence of the incompressibility of the plasma. As the main filament pushes up into the background plasma above it, it must displace that plasma. This causes a down-draft of plasma (represented by $\overline{\xi^2}$) that pushes back to either side of the main filament. This downwards flow of plasma suppresses the two side-filaments, particularly around $x_0 = x_{max}$, where the main filament is situated.

## 4.4. Experimental observation

In this section, we want to present experimental observations which may be described by our simulations shown in the previous subsections. We present two selected examples: Type V ELMs in the NSTX tokamak [82] and ELMs in KSTAR [117]. The small, Type V ELMs in NSTX involve fine-scale filaments that one would typically associate with higher toroidal mode number $n$. However, these ELMs only consist of one or two filaments, see Fig. 4.15,

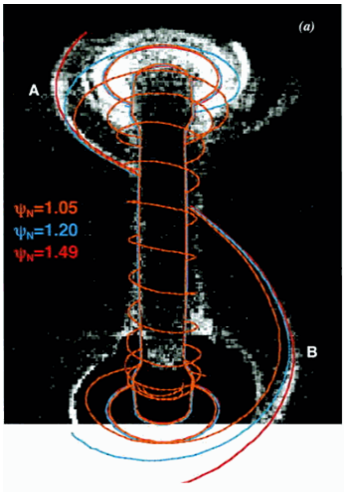


Figure 4.15.: *From [82]: "Visible camera pictures in unfiltered light of a single-filament Type V ELM with a wide-angle midplace view."*

which is in disagreement with what one would expect, $\sim n$ filaments, from linear theory. While their preliminary stability calculation indicates the dominant instability drive is current density rather than ballooning modes, it is possible that a similar mechanism to that identified here acts to limit the number of filaments.

Another example which might be described by the nonlinear ballooning mode with interacting filaments are ELMs in KSTAR [117]. They observe slowly growing "fingers" out of the plasma, see Fig. 4.16 which at some point suddenly transforms into a more irregular formation and then it seems that the filaments are being suppressed, which could be explained by the results presented here.

## 4.5. Conclusion

In summary, we have shown how the interaction between plasma filaments of slightly different amplitudes influences their evolution by solving the nonlinear ballooning mode envelope equation with a mixed Lagrangian-Eulerian boundary condition. We have quantified this effect for a three filament system by introducing the quantity $p_i$ which characterises the difference between the two-mode simulation and the two independent single mode simulations. We demonstrated that the larger filament gains amplitude from the interaction with the smaller filaments, which are suppressed. The larger filaments grow faster by devouring the smaller ones. It is expected therefore, that the filaments which first enter the nonlinear regime will dominate the physics of plasma eruptions. This is in agreement with Ref. [69],

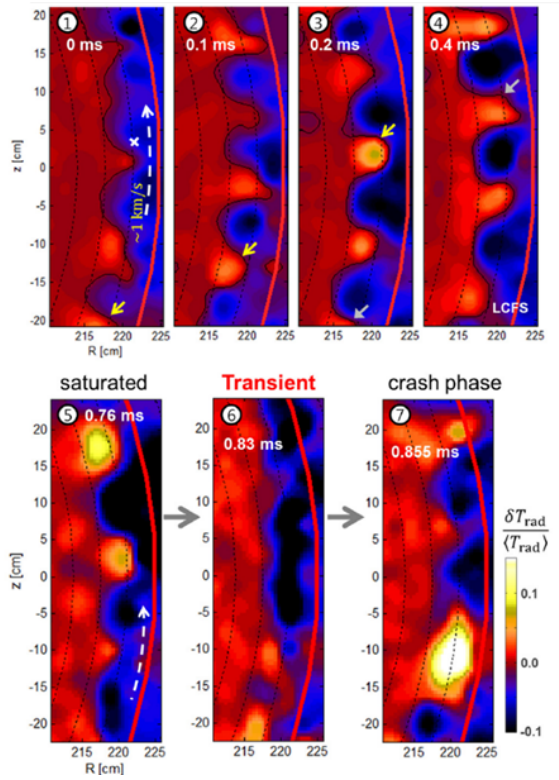


Figure 4.16.: *From [117]: First row:"Initial growth (frames 1-3) and saturation (frame 4) of multiple ELM filaments. The short arrows identifying individual filaments illustrate the apparent counterclockwise rotation of the filaments (also indicated by the long dashed arrow in frame 1)". Bottom row: "Changes of the filament structure through a short transient period. All frames are plotted in the same color scale."*
*In frame 5 one can see a single filament on the top, which is not in the next frame. It is possible that the single filament is still there, but out of the view and returns in frame 7.*

where it is shown that if one starts with random small fluctuations, the filament with the biggest amplitude at the transition from linear to nonlinear grows fastest, and suppresses the other filaments. The qualitative behaviour of the main filament is similar to the single mode calculation, but it does grow faster as the finite time singularity is approached.

Although our results are derived from a simple slab plasma model, it has the same features as more complex magnetic geometries, including tokamaks [2, 3]. We therefore believe the phenomenon of large filaments feeding off the smaller ones is a generic feature of ideal MHD. Supporting our model we presented two examples of experimental observations (Type V ELMs in NSTX and ELMs in KSTAR) which show dominant filaments where one would expect a higher mode number from linear theory.

We note that the theory is only valid in the early nonlinear stages of the evolution, and it requires that the dominant filaments will have time to have formed before the model

becomes invalid. It is therefore important to test these ideas in full, large scale simulations, close to marginal stability.

# 5. Simulation of ELMs in real tokamak equilibria

In this chapter we investigate whether the nonlinear ballooning model can capture quantitative features of Edge Localised Modes (ELMs) by applying this model to real tokamak equilibria. To exploit this model we must analyse the coefficients of the ballooning equation (3.48). The first part of this chapter (Sect. 5.1) presents the methods used to investigate the coefficients. Next, the coefficients of a MAST Type I ELMy H-mode equilibrium are calculated to verify the methods introduced previously (see Section 5.2). Finally, a JET-like Type II ELM case is studied in Section 5.3.

## 5.1. Coefficients of the nonlinear envelope equation

The coefficients of the nonlinear ballooning equation, derived in Chapter 3, are given by:

$$
\begin{aligned}
C_0 &= \rho_0 \left\langle \frac{|\boldsymbol{e}_\perp|^2}{B_0^2} X^2 + B_0^2 G^2 \right\rangle - \left[ \frac{\rho_0}{(3-2\lambda_s)} \left( q'^2 \left\langle \frac{|\nabla\psi|^2}{B_0^2} \right\rangle_\theta v^3 X_0^2 + v \left\langle B_0^2 G_0^2 \right\rangle_\theta \right) \right]_{-p_\chi}^{p_\chi} \\
C_1 &= \left\langle \frac{(\boldsymbol{e}_\perp \cdot \boldsymbol{\kappa}_0)}{B_0^4} (\boldsymbol{e}_\perp \cdot \nabla_0 p_0) X^2 \right\rangle \\
C_2 &= \left\langle \frac{X \widehat{P}}{B_0} \right\rangle \\
C_3 &= \left\langle \frac{X^2}{B_0^3} \boldsymbol{e}_\wedge \cdot \mathcal{L} \left( \frac{X}{B_0} \boldsymbol{e}_\perp \right) \right\rangle \\
C_4 &= 2 \left\langle X T_\wedge \boldsymbol{e}_\wedge \cdot \mathcal{L} \left( \frac{X}{B_0} \boldsymbol{e}_\perp \right) \right\rangle - \left\langle \frac{X^2}{B_0} \boldsymbol{e}_\perp \cdot \mathcal{L} \left( T_\perp \right) \right\rangle \\
C_5 &= -\frac{\lambda b_0}{\Gamma(2-\lambda)} \left( A_+^2 + A_-^2 \right) q'^2 \left\langle \frac{B_0^2}{|\nabla\psi|^2} \right\rangle_\theta^{-1}
\end{aligned}
$$

where the brackets $\langle \cdots \rangle$ denote integrals along the field aligned variable $\chi$, $\pm p_\chi$ are the limits of these integrals, and:

$$\begin{aligned}
\boldsymbol{T}_\perp &\equiv T_\psi \boldsymbol{e}_\perp + T_\wedge \boldsymbol{e}_\wedge \\
\boldsymbol{e}_\wedge \cdot \mathcal{L}\left(\boldsymbol{T}_\perp\right) &= X \boldsymbol{e}_\wedge \mathcal{L}\left(\frac{X \boldsymbol{e}_\perp}{B}\right) \\
T_\psi &= \frac{X^2}{2B} \\
b_0 &= \frac{Y_{L+}}{Y_{S+}} \\
\frac{X\widehat{P}}{B_0} &= H\left[(\boldsymbol{e}_\perp \cdot \nabla)\boldsymbol{H}\right] \cdot (\boldsymbol{B}_0 \cdot \nabla)\left[(\boldsymbol{B}_0 \cdot \nabla)\boldsymbol{H}\right] - 1/2H(\boldsymbol{e}_\perp \cdot \nabla)\left[\boldsymbol{H} \cdot (\boldsymbol{B}_0 \cdot \nabla)\left[(\boldsymbol{B}_0 \cdot \nabla)\boldsymbol{H}\right]\right] \\
&\quad + \frac{1}{2B_0}\left[(\boldsymbol{H} \cdot \nabla)\boldsymbol{H}\right] \cdot \nabla\alpha \boldsymbol{e}_\wedge \cdot \mathcal{L}\left(H \boldsymbol{e}_\perp\right) + 2(\boldsymbol{e}_\perp \cdot \boldsymbol{k}_0)\frac{Q_- H}{B^2}
\end{aligned}$$

with

$$\begin{aligned}
Q_\pm &\equiv \frac{1}{2}\left[\boldsymbol{H}(\boldsymbol{B}_0 \cdot \nabla)\left((\boldsymbol{B}_0 \cdot \nabla)\boldsymbol{H}\right) \pm \left|(\boldsymbol{B}_0 \cdot \nabla)\boldsymbol{H}\right|^2\right] \\
\boldsymbol{H} &\equiv \frac{X}{B_0}\boldsymbol{e}_\perp + G\boldsymbol{B}_0
\end{aligned}$$

with $\lambda = \lambda_S - \lambda_L$ ($\lambda_S$ and $\lambda_L$ defined by (3.40)) and where $Y_{L+}$ and $Y_{S+}$ are the large and small solutions of the set of differential equations (3.14), (3.15) and (3.16) of the inertial region.

Two coefficients ($C_0$ and $C_2$) have slowly converging integrands as their leading orders are proportional to $|\chi|^{(2-2\lambda_S)}$ and $|\chi|^{(2-3\lambda_S)}$ respectively, where $\lambda_S$ is between 1 and 2. To minimise the numerical calculations we divide the integrals into numerical evaluated parts and remaining integrals which can be evaluated analytically. This is described in the next section. For the coefficients $C_4$ and $C_5$ we must solve differential equations to calculate $\boldsymbol{T}_\perp$ and $b_0$ as presented in Section 5.1.6 and 5.1.7.

The $C_0$, $C_3$ and $C_5$ coefficients are only used under certain conditions. The $C_0$ coefficient must be used if $\lambda \geqq 2$. If $\lambda < 2$ we compute and use $C_5$ instead, see Sect. 3.2.1. $C_3$ must be determined only if the geometry of the plasma is not up-down symmetric, otherwise it is close to zero. Since we only evaluate up-down symmetric equilibria in this thesis, this coefficient and its corresponding term are neglected.

### 5.1.1. Dividing the integrals into numerical and analytic components

The integrands of the coefficients $C_0$ and $C_2$ converge slowly to zero with respect to the field aligned variable $\chi$ over which we integrate. Therefore we divide the integral at the points $\pm p_\chi$:

$$\int_{-\infty}^{\infty} I_{nd}\, d\chi = \int_{-\infty}^{-p_\chi} I_{nd}\, d\chi + \int_{-p_\chi}^{p_\chi} I_{nd}\, d\chi + \int_{p_\chi}^{\infty} I_{nd}\, d\chi \tag{5.1}$$

where $I_{nd}$ represents the integrand. For this estimation the point $p_\chi$ must satisfy $p_\chi \gg 1$ so that an asymptotic expansion of $I_{nd}$ can be used in the first and third integrals on the RHS of Eq. 5.1. If $p_\chi$ is too small the asymptotic approximation is invalid. For higher values, however, the calculation becomes increasingly more numerically expensive.

We separate the coordinate $\chi$, which labels the coordinate along the field line, into $v$ and $\theta$, where $\theta$ labels the periodic variation and $v$ labels the secular (asymptotic) variation (see Section 3.2 for more details).

The standard trapezoid rule is used for the numerical calculation of the integrals $\int_{-p_\chi}^{p_\chi} I_{nd}\, d\chi$ which will not be discussed [110]. Here we want to concentrate on how the asymptotic part (first and third term of the RHS of Eq. (5.1)) are determined. We expand the integrands in $\frac{1}{v} \ll 1$ and use the dominant, asymptotic expression of the integrand to find an analytic expression for its integral. The integrands of all coefficients can be expressed asymptotically ($v \gg 1$) in the form

$$I_{nd} = a\frac{Q(\theta)\, C_x^\alpha}{v^\beta} + \mathcal{O}\left(\frac{1}{v^{\beta+1}}\right) \tag{5.2}$$

where $C_x \equiv X_0|v|^{\lambda_s}$ (see Eq. (3.44)) with $X_0$ being the dominant order of $X$ in an expansion in $\frac{1}{v} \ll 1$. $a$, $\alpha$ and $\beta$ are constant and $Q$ is a periodic function which means that it only depends on $\theta$. Since we assume $p_\chi \gg 1$ we can exploit the expression (5.2) for the integrand of the coefficient for the first and third term of Eq. (5.1):

$$I_{nd} \approx a\frac{C_x^\alpha Q(\theta)}{v^\beta} \tag{5.3}$$

Furthermore the Reynolds decomposition states that every quantity can be divided into its mean $\overline{Q}$ and its fluctuating part $\tilde{Q}$: $Q = \overline{Q} + \tilde{Q}$ visualised in Fig. 5.1. In general, the fluctuation has an average of zero. By using the expression (5.3) and the Reynolds

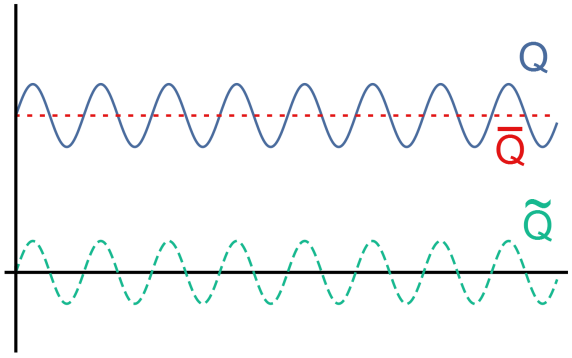


Figure 5.1.: *Reynolds decomposition of* $Q = \overline{Q} + \tilde{Q}$. *The fluctuating part is periodic because* $Q$ *itself is periodic.*

decomposition for the quantity $Q$ we obtain for the third term on the RHS of Eq. (5.1) (dropping the constants $C_x$ and $a$ for now to make the steps easier to follow):

$$\begin{aligned}\int_{p_\chi}^{\infty} \frac{Q(\theta)}{\chi^\beta} d\chi &= \int_{p_\chi}^{\infty} \frac{\overline{Q} + \tilde{Q}(\theta)}{\chi^\beta} d\chi \\ &= \int_{p_\chi}^{\infty} \frac{\overline{Q}}{\chi^\beta} d\chi + \int_{p_\chi}^{\infty} \frac{\tilde{Q}(\theta)}{\chi^\beta} d\chi \\ &= \frac{\overline{Q}}{(\beta-1)p_\chi^{\beta-1}} + \int_{p_\chi}^{\infty} \frac{\tilde{Q}(\theta)}{\chi^\beta} d\chi \end{aligned} \tag{5.4}$$

Here we have assumed that $(\beta - 1) > 0$ where $\beta$ is the power of $v$ in the integrand, see Eq. (5.2). If $(\beta - 1) < 0$ the integral would diverge and this method is not applicable since the nonlinear effects cannot be considered small for large values of $\chi$ [2] and our procedure becomes invalid.

Now we show that the second term of Eq. (5.4) is higher order than the first term which implies that it can be neglected. Using integration by parts for the second term on the right hand side of Eq. (5.4) we obtain:

$$\int_{p_\chi}^{\infty} \frac{\tilde{Q}(\theta)}{\chi^\beta} d\chi = \left[ \frac{\int \tilde{Q}(\theta) d\chi}{\chi^\beta} \right]_{p_\chi}^{\infty} - \int_{p_\chi}^{\infty} (-\beta) \frac{\int \tilde{Q}(\theta) d\chi}{\chi^{\beta+1}} d\chi \tag{5.5}$$

The second term on the right hand side is of the same form as the starting term but with a higher order in $p_\chi$. If we can show that the first term in (5.5) is also of a higher order than the first term of Eq. (5.4) we have proven that the second term of (5.4) can be neglected. The integral of the first term of Eq. (5.5) can be divided into its average and its fluctuating

part. The fluctuation is again periodic because the average of $\tilde{Q}(\theta)$ is zero, see Fig. 5.2.

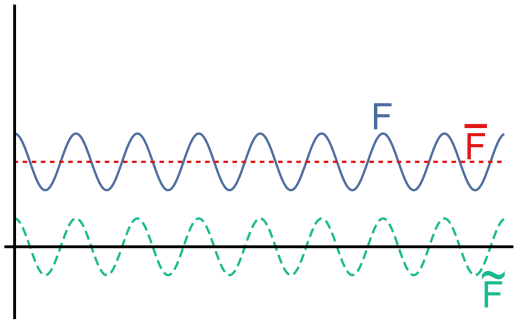


(a) *Reynolds decomposition of* $F \equiv \int \tilde{Q}(\theta)d\theta = \overline{F} + \tilde{F}(\theta)$ *where* $\overline{F}$ *represents the constant of integration. The fluctuation is again periodic because the average of* $\tilde{Q}(\theta)$ *is zero.*

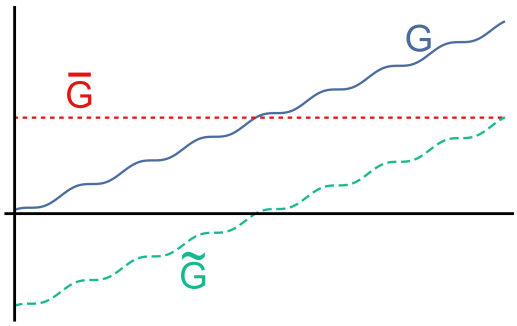


(b) *Reynolds decomposition of* $G \equiv \int Q(\theta)d\theta = \overline{G} + \tilde{G}$. *The fluctuation is not periodic because the average of* $Q$ *is not zero.*

Figure 5.2.: *Differences of the Reynolds decompositions of function with zero average and non-zero average.*

We can write $F \equiv \int \tilde{Q}(\theta)d\theta = \overline{F} + \tilde{F}(\theta)$. Therefore the first term on the RHS of Eq. (5.5) can be written as:

$$\left[\frac{\int \tilde{Q}d\chi}{\chi^\beta}\right]_{p_\chi}^{\infty} = -\frac{\tilde{F}(\theta)}{p_\chi^\beta} - \frac{\overline{F}}{p_\chi^\beta}$$

Both terms have a higher order with respect to $p_\chi$ than the first term of Eq. (5.4). Therefore we obtain the following expression for the third term on the RHS of Eq. (5.1):

$$a\int_{p_\chi}^{\infty} \frac{Q(\theta)C_x^\alpha}{\chi^\beta}d\chi = a\frac{\overline{Q}C_x^\alpha}{(\beta-1)p_\chi^{\beta-1}} + \mathcal{O}(p_\chi^{-\beta}) \tag{5.6}$$

with $\overline{Q}$ given by:

$$\overline{Q} \equiv \frac{1}{2\pi}\int_{-\pi}^{\pi} Q\, d\chi$$

The derivation of the first term of Eq. (5.1) is equivalent to the one shown here.

To utilise expression (5.6) for the evaluation of the integral of the coefficients, we must determine the asymptotic form $a\frac{Q}{\chi^\beta}$ of the coefficients.

### 5.1.2. Note on the implementation of the asymptotic function $X_0$

All the asymptotic quantities depend on the lowest order asymptotic term, $X_0$, of the function $X$ given by equation (3.31). However, it is not fully determined analytically as we must estimate the constant $C_x$ as

$$C_x \equiv X_0 |v|^{\lambda_s}.$$

$X$ itself is not fully defined as it has an arbitrary boundary condition which we usually choose to be $X(\chi = 0) = 1$. To obtain the constant $C_x$ such that $X_0$ is consistent with the function $X$, we exploit this numerically calculated function $X$.

One way would be to use the value of $X$ at the highest numerically available $\chi$: $\chi_{max}$. That approach would be sensible as the asymptotic expression $X_0$ becomes increasingly valid for larger values of $\chi$: $\lim_{\chi \to \infty} X = X_0$.

However, $X$ has a periodic behaviour which $X_0$ does not have, see Fig. 5.3. To account

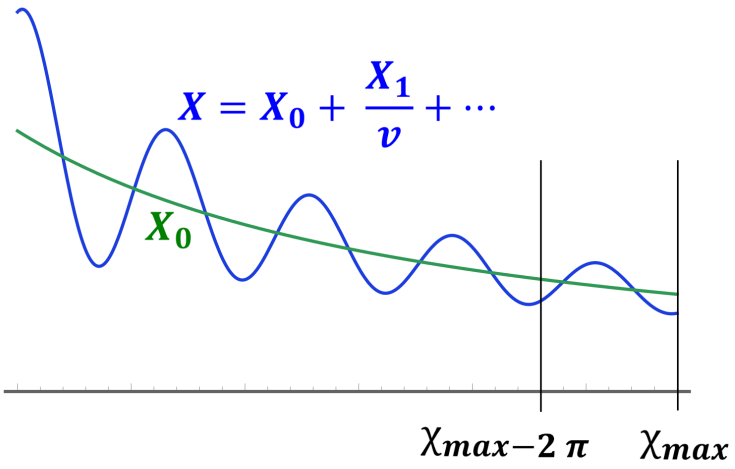


Figure 5.3.: *The functions $X$ and $X_0$ near the numerical maximum of $\chi$.*

for this we can use an averaged value of $X$ and $X_0$ for the last period in the numerically analysed range: $[\chi_{max} - 2\pi, \chi_{max}]$.

To implement this behaviour we average both $X$ and $\frac{1}{|\chi|^{\lambda_s}}$ with respect to $\chi$ over the last periodic range of the largest $\chi$ to obtain $\langle X \rangle_{\chi_{max}} \approx \langle X_0 \rangle$ and $\left\langle \frac{1}{|\chi|^{\lambda_s}} \right\rangle_{\chi_{max}}$. The ratio of $\langle X \rangle_{\chi_{max}}$ to $\left\langle \frac{1}{|\chi|^{\lambda_s}} \right\rangle_{\chi_{max}}$ gives the coefficient $C_x$. With this method we have a consistent asymptotic function $X_0$ for the numerically calculated function $X$. It is also clear that the

function $X$ is better approximated for higher values of $\chi_{max}$.
Another approach is to use higher orders of $X$ in the fitting procedure. This has been tested and did not lead to significantly better results.

Having shown we can split the terms into numerical and analytical components, we are now able to begin evaluating each coefficient.

### 5.1.3. Inertial coefficient $C_0$

In this section we discuss the inertial coefficient $C_0$ which only has to be calculated if $\lambda \geqq 2$. $C_0$ is defined as:

$$C_0 = \rho_0 \left\langle \frac{|\boldsymbol{e}_\perp|^2}{B_0^2} X^2 + B_0^2 G^2 \right\rangle - \left[ \frac{\rho_0}{(3-2\lambda_s)} \left( q'^2 \left\langle \frac{|\nabla\psi|^2}{B_0^2} \right\rangle_\theta v^3 X_0^2 + v \left\langle B_0^2 G_0^2 \right\rangle_\theta \right) \right]_{-p_\chi}^{p_\chi}$$

For $p_\chi \to \infty$ the boundary term (second term on the RHS) only diverges for $\lambda < 2$. Interestingly, investigating the dominant asymptotic part of the first term on the RHS[1] we find that it cancels the divergent boundary term. Therefore $C_0$ always has a finite value.

### 5.1.4. Linear coefficient $C_1$

The linear coefficient $C_1$ has the form:

$$C_1 = \left\langle \frac{(\boldsymbol{e}_\perp \cdot \boldsymbol{\kappa}_0)}{B_0^4} (\boldsymbol{e}_\perp \cdot \nabla_0 p_0) X^2 \right\rangle$$

The dominant asymptotic term of its integrand is of the order $\mathcal{O}(v^{-2(\lambda_S)+1})$ which means that it converges quickly and does not need an asymptotic treatment.
The linear ballooning equation (3.31) is used to obtain a second expression for $C_1$. The following expression can be derived by integration by parts:

$$C_1 = \left\langle \frac{(\boldsymbol{e}_\perp \cdot \boldsymbol{\kappa}_0)}{B_0^4} (\boldsymbol{e}_\perp \cdot \nabla_0 p_0) X^2 \right\rangle = \frac{1}{2\mu} \left\langle \frac{|\boldsymbol{e}_\perp|^2}{B^2} ((\boldsymbol{B}_0 \cdot \nabla) X)^2 \right\rangle$$

Therefore we have two expressions for $C_1$ which have both been used to verify the code.

[1] using the expressions for $|\boldsymbol{e}_\perp|^2$ (equation (A.1)), $X$ (equation (3.44)) and $G$ (equation (3.45)) and equation (5.6)

### 5.1.5. Quadratic nonlinear coefficient $C_2$

The quadratic, nonlinear coefficient $C_2$ is investigated here, which is given by:

$$C_2 = \left\langle \frac{X\widehat{P}}{B_0} \right\rangle \tag{5.7}$$

where $\frac{X\widehat{P}}{B_0} = H\widehat{P}$ is defined as:

$$H\widehat{P} = H\left[(\boldsymbol{e}_\perp \cdot \nabla)\boldsymbol{H}\right] \cdot (\boldsymbol{B}_0 \cdot \nabla)\left[(\boldsymbol{B}_0 \cdot \nabla)\boldsymbol{H}\right] - 1/2H(\boldsymbol{e}_\perp \cdot \nabla)\left[\boldsymbol{H} \cdot (\boldsymbol{B}_0 \cdot \nabla)\left[(\boldsymbol{B}_0 \cdot \nabla)\boldsymbol{H}\right]\right]$$

$$+ \frac{1}{2B_0}\left[(\boldsymbol{H} \cdot \nabla)\boldsymbol{H}\right] \cdot \nabla\alpha\boldsymbol{e}_\wedge \cdot \boldsymbol{\mathcal{L}}\left(H\boldsymbol{e}_\perp\right) + 2(\boldsymbol{e}_\perp \cdot \boldsymbol{\kappa}_0)\frac{Q_- H}{B^2}$$

with

$$\begin{aligned} Q_\pm &\equiv \frac{1}{2}\left[\boldsymbol{H}(\boldsymbol{B}_0 \cdot \nabla)\left((\boldsymbol{B}_0 \cdot \nabla)\boldsymbol{H}\right) \pm |(\boldsymbol{B}_0 \cdot \nabla)\boldsymbol{H}|^2\right] \\ \boldsymbol{H} &\equiv \frac{X}{B_0}\boldsymbol{e}_\perp + G\boldsymbol{B}_0 \end{aligned} \tag{5.8}$$

The lowest order of the asymptotic expression of the integrand of the nonlinear drive coefficient is proportional to $v^{2-3\lambda_S}$, which will be shown later. This means that the integral converges very slowly and therefore we need the analytic expression for the remaining integral beyond the numerical range $[-p_\chi, p_\chi]$. Since this coefficient consists of many terms it is sensible to divide the coefficient into a sum of terms called $\langle Q_i \rangle$ which makes the treatment clearer:

$$C_2 = \left\langle \frac{X\widehat{P}}{B_0} \right\rangle \equiv \sum_{i=1}^{6} \langle Q_i \rangle$$

where we define six terms:

$$\begin{aligned} Q_1 &\equiv -\left\langle \frac{f}{B^2} Q_- \boldsymbol{B}_0 \cdot \boldsymbol{\nabla}_0(X\Lambda) \right\rangle & Q_2 &\equiv \left\langle \left[\frac{\partial}{\partial\psi}\left(2p + B_0^2\right)\right] \frac{XQ_-}{B_0^2} \right\rangle \\ Q_3 &\equiv -\left\langle X\frac{\partial}{\partial\psi}Q_+ \right\rangle & Q_4 &\equiv \langle [\boldsymbol{B}_0 \cdot \boldsymbol{\nabla}_0 (X\Lambda)]\, S \rangle \\ Q_5 &\equiv -\left\langle \frac{X}{J}\frac{\partial}{\partial\psi}JT \right\rangle & &- \left\langle [\boldsymbol{B}_0 \cdot \boldsymbol{\nabla}_0 X]\, \frac{\partial}{\partial\psi}(\boldsymbol{H})\, [\boldsymbol{B}_0 \cdot \boldsymbol{\nabla}_0 \boldsymbol{H}] \right\rangle \\ Q_6 &\equiv \frac{1}{2}\left\langle \frac{1}{B} u\, \omega \right\rangle \end{aligned} \tag{5.9}$$

with $\Lambda \equiv q'(\chi - \chi_0) - Y'$ and the following definitions:

$$S \equiv \{[\boldsymbol{B}_0 \cdot \boldsymbol{\nabla}_0 \boldsymbol{H}]\,[R(\boldsymbol{e}_\phi \cdot \nabla)\boldsymbol{H}]\} \qquad T \equiv |\boldsymbol{B}_0 \cdot \boldsymbol{\nabla}_0 \boldsymbol{H}|^2$$

$$u \equiv \{[(\boldsymbol{H} \cdot \nabla)\,\boldsymbol{H}] \cdot \nabla\alpha\} \qquad \omega \equiv \boldsymbol{e}_\wedge \cdot \boldsymbol{\mathcal{L}}\,(H\boldsymbol{e}_\perp)$$

Appendix E presents the proof that the sum of these six terms is equivalent to the original equation, (5.7).

The next step is to evaluate the analytic expressions for the integrands of Eqs (5.9) at large $v$. The expressions for $X$ and $\boldsymbol{H}$ are derived in Chapter 3. The remaining task is to determine the analytic expressions for $Q_\pm$, $S$, $T$, $u$ and $\omega$. We start by determining $Q_\pm$, which appears in $Q_1$, $Q_2$ and $Q_3$ and is defined by equation (5.8). By investigating the orders of $Q_\pm$ we find that $Q_\pm \approx Q_{0\pm}(\theta)(vX_0)^2$ which means that the highest order is $\sim v^{(2-2\lambda_S)}$. $Q_{0\pm}$ is purely periodic and given by:

$$Q_{0\pm} = \frac{1}{2}q'^2\left[(f_0\boldsymbol{B_0} + R\boldsymbol{e}_\phi)\cdot[(f_0\boldsymbol{B_0} + R\boldsymbol{e}_\phi)\cdot\nabla\boldsymbol{\kappa}_0] \pm |\boldsymbol{B}_0\cdot\boldsymbol{\nabla}_0\,(f_0\boldsymbol{B_0} + R\boldsymbol{e}_\phi)\,|^2\right]$$

where $f_0$ is defined as (see Eq. (3.46)):

$$f_0 \equiv \frac{\lambda_S q'}{\mu_0 p'}\frac{1}{\left\langle \frac{B_0^2}{R^2 B_p^2}\right\rangle} - f\frac{\left\langle \frac{1}{R^2 B_p^2}\right\rangle}{\left\langle \frac{B_0^2}{R^2 B_p^2}\right\rangle}$$

By using equations (A.9), (A.10) and the fact that $f_0$ does not depend on $\chi$ we can re-write the expression of $Q_{0\pm}$ as:

$$\boxed{\begin{aligned} Q_{0+} &= \frac{q'^2}{2}\left\{Rk_R + \frac{f_0^2}{2}\boldsymbol{B}_0\cdot\boldsymbol{\nabla}_0\left[\boldsymbol{B}_0\cdot\boldsymbol{\nabla}_0 B^2\right] + B_R^2 + B_\phi^2\right\} \\ Q_{0-} &= \frac{q'^2}{2}\left\{(R + 4f_0 B_\phi)\,\kappa_R + \frac{f_0^2}{2}\boldsymbol{B}_0\cdot\boldsymbol{\nabla}_0\left[\boldsymbol{B}_0\cdot\boldsymbol{\nabla}_0 B^2\right] - 2f_0^2|\kappa_0|^2 - B_R^2 - B_\phi^2\right\} \end{aligned}}$$

where $B_R$ is defined as $B_R \equiv \boldsymbol{B}\cdot\nabla R$ and $\kappa_R$ is given by $\kappa_R \equiv \boldsymbol{\kappa}\cdot\nabla R$.

The variable $S$ is defined as $S \equiv R\,[\boldsymbol{B}_0\cdot\boldsymbol{\nabla}_0\boldsymbol{H}]\cdot[(\boldsymbol{e}_\phi\cdot\nabla)\,\boldsymbol{H}]$, which appears in $Q_4$, and can be expressed in the form $\lim_{\chi\to\infty} S = S_0(\theta)\,(vX_0)^2$ with $S_0$ given by:

$$\boxed{S_0 = q'^2\left\{f_0\left(-R\kappa_R + B_R^2 + B_\phi^2\right) + RB_\phi - f_0^2 B_\phi\kappa_R\right\}}$$

where we used the following expressions:

$$\begin{aligned}(\boldsymbol{e}_\phi \cdot \nabla)\,\boldsymbol{B} &= -\frac{B_\phi}{R}\hat{R} + \frac{B_R}{R}\boldsymbol{e}_\phi \\ (\boldsymbol{e}_\phi \cdot \nabla)\,\boldsymbol{e}_\phi &= -\frac{1}{R}\hat{R} \\ (\boldsymbol{B} \cdot \nabla)\,(\boldsymbol{e}_\phi R) &= -B_\phi \hat{R} + B_R \boldsymbol{e}_\phi\end{aligned}$$

These are derived by using the expression of the material derivative in the cylindrical coordinate system[2]. The variable $T$ is defined as $T \equiv |\boldsymbol{B}_0 \cdot \boldsymbol{\nabla}_0 \boldsymbol{H}|^2$. It appears in $Q_5$ and can be written in the same asymptotic form as the other quantities $\lim_{\chi\to\infty} T = T_0(\theta)\,(vX_0)^2$ with $T_0$:

$$\boxed{T_0 = q'^2\left[f_0^2|\boldsymbol{\kappa}_0|^2 - 2f_0 B_\phi \kappa_R + B_R^2 + B_\phi^2\right]}$$

The function $u \equiv [(\boldsymbol{H}\cdot\nabla)\boldsymbol{H}]\cdot\nabla\alpha$ (appearing in $Q_6$) is of a lower order compared to the previous quantities since its asymptotic expression is $\lim_{\chi\to\infty} u = u_0(\theta)\,v\,(vX_0)^2$, where we can show that:

$$\boxed{u_0 = q'^3\left[f_0^2 R^2 B_p^2 \frac{\partial}{\partial\psi}\left(p + B^2\right) + \left(R + 2f_0 B_\phi\right) R B_z\right]}$$

Here we have used $(\boldsymbol{e}_\phi\cdot\nabla)\,(R\boldsymbol{e}_\phi) = -\hat{R}$ and $\nabla R\cdot\nabla\psi = -RB_z$.

Finally, we need the asymptotic form of $\omega \equiv \frac{\boldsymbol{e}_\wedge}{B_0}\cdot\mathcal{L}\left(\frac{X}{B}\boldsymbol{e}_\perp\right)$ which requires more steps than for the previous terms[3].

Using Eq. (A.11) we can write $\omega$ as:

$$\frac{\boldsymbol{e}_\wedge}{B_0}\mathcal{L}\left(\frac{X}{B_0}\boldsymbol{e}_\perp\right) = \frac{1}{\mathcal{J}}\left(\frac{\partial}{\partial\theta}+\frac{\partial}{\partial v}\right)\Bigg[-\frac{R^2B_p^2}{JB^2}\left(q'v+Y'\right)\left(\frac{\partial}{\partial\theta}+\frac{\partial}{\partial v}\right)\left(X_0+\frac{X_1}{v}+\frac{X_2}{v^2}+\cdots\right)$$

$$+\,\sigma\left(X_0+\frac{X_1}{v}+\frac{X_2}{v^2}+\cdots\right)\Bigg] \tag{5.10}$$

[2]The material derivative in the cylindrical coordinates is given by
$\boldsymbol{A}\cdot\nabla\boldsymbol{B} = \left(A_R\frac{\partial B_R}{\partial R} + \frac{A_\phi}{R}\frac{\partial B_R}{\partial\phi} + A_z\frac{\partial B_R}{\partial z} - \frac{A_\phi B_\phi}{R}\right)\hat{R} + \left(A_R\frac{\partial B_\phi}{\partial R} + \frac{A_\phi}{R}\frac{\partial B_\phi}{\partial\phi} + A_z\frac{\partial B_\phi}{\partial z} + \frac{A_\phi B_R}{R}\right)\boldsymbol{e}_\phi + \left(A_R\frac{\partial B_z}{\partial R} + \frac{A_\phi}{R}\frac{\partial B_z}{\partial\phi} + A_z\frac{\partial B_z}{\partial z}\right)\hat{z}$

[3]The equation needed to derive the following expressions are: The expressions derived in Appendix B and Section C.2.1. From Appendix B we used Eq. (B.5) which is the $\boldsymbol{e}_\wedge$-component of the linear operator $\mathcal{L}$ used on $\boldsymbol{e}_\perp$-components. From Section C.2.1 we used the linear ballooning mode equation of order $\mathcal{O}(v)$ (Eq. (C.12)) and of order $\mathcal{O}(1)$ (Eq. (C.14)), and the relations (A.11), (B.6) and (A.12) derived in A

Eq. (5.10) is divided into its order of $v$ since we are seeking the leading order of $\omega$. The lowest order is equal to zero as $X_0$ is constant in $\theta$:

$$\frac{1}{\mathcal{J}}\frac{\partial}{\partial\theta}\left(-\frac{R^2B_p^2}{JB^2}q'v\frac{\partial}{\partial\theta}X_0\right)=0$$

and therefore we must investigate the next order $\mathcal{O}(1)$ which is:

$$\frac{\boldsymbol{e}_\wedge}{B_0}\mathcal{L}\left(\frac{X}{B_0}\boldsymbol{e}_\perp\right)=\frac{1}{\mathcal{J}}\frac{\partial}{\partial\theta}\left[\frac{R^2B_p^2}{JB^2}\left(q'v\frac{\partial}{\partial v}X_0+q'\frac{\partial}{\partial\theta}X_1\right)\right]+X_0\frac{\partial}{\partial\theta}\sigma+\mathcal{O}(v^{-1})$$

Exploiting Eq. (A.12) and Eq. (C.12) we find that this order is also zero. Therefore we must calculate the next order $\mathcal{O}(v^{-1})$:

$$\begin{aligned}\frac{\boldsymbol{e}_\wedge}{B_0}\mathcal{L}\left(\frac{X}{B_0}\boldsymbol{e}_\perp\right)=-\frac{1}{\mathcal{J}}\Bigg\{&\frac{\partial}{\partial\theta}\left[\frac{R^2B_p^2}{JB^2}q'v\frac{\partial}{\partial v}X_1-\frac{R^2B_p^2}{JB^2}q'v\frac{\partial}{\partial\theta}\left(\frac{X_2}{v^2}\right)-\frac{R^2B_p^2}{JB^2}Y'\frac{\partial}{\partial\theta}\left(\frac{X_1}{v}\right)\right.\\&\left.-\frac{R^2B_p^2}{JB^2}Y'\frac{\partial}{\partial v}X_0\right]+\frac{\partial}{\partial v}\left(-\frac{R^2B_p^2}{JB^2}q'\frac{\partial}{\partial\theta}X_1\right)+\frac{\partial}{\partial v}\left(-\frac{R^2B_p^2}{JB^2}q'v\frac{\partial}{\partial v}X_0\right)\\&+\frac{\partial}{\partial\theta}\left(\sigma\frac{X_1}{v}\right)+\sigma\frac{\partial}{\partial v}X_0\Bigg\}+\mathcal{O}\left(v^{-2}\right)\end{aligned}$$

We already have the analytic, asymptotic expressions for $X_0$ and $X_1$, but not for $X_2$. Using Eq. (C.14) and Eq. (C.12) we finally obtain:

$$\begin{aligned}\omega=\frac{\boldsymbol{e}_\wedge}{B_0}\mathcal{L}\left(\frac{X}{B_0}\boldsymbol{e}_\perp\right)\approx-\frac{1}{\mathcal{J}}\Bigg\{&\nu'\frac{R^2B_p^2}{JB^2}\left(\frac{1}{v}\frac{\partial X_1}{\partial\theta}-\frac{\lambda_S X_0}{v}\right)+\mu\sigma\left(\frac{1}{v}\frac{\partial X_1}{\partial\theta}-\frac{\lambda_S X_0}{v}\right)\\&+\frac{\mu p'J}{q'vB^2}\frac{\partial}{\partial\psi}\left(2p+B^2\right)X_0\Bigg\}\end{aligned}$$

Now that we have the asymptotic forms of all the quantities appearing in all the terms of $C_2$, we present the equations for the analytic parts of the integrals ($C_2^{asy}=\sum_i\langle Q_i\rangle^{asy}$)

given by equation (5.6):

$$\langle Q_1\rangle^{asy} = 2\frac{\overline{\left\{\frac{f}{B_0^2}Q_{0-}\left[\nu' + q'\left(-\lambda_S + \left(\frac{1}{X_0}\frac{\partial X_1}{\partial\theta}\right)\right)\right]\right\}}C_x^3}{6\pi(\lambda_S-1)p_\chi^{(3(\lambda_S-1))}}$$

$$\langle Q_2\rangle^{asy} = 2\frac{\overline{\left(\frac{\partial}{\partial\psi}\left(2p_0 + B_0^2\right)\frac{JQ_{0-}}{B_0^2}\right)}C_x^3}{6\pi(\lambda_S-1)p_\chi^{(3(\lambda_S-1))}}$$

$$\langle Q_3\rangle^{asy} = 2\frac{\overline{\left(J\left(\frac{\partial}{\partial\psi}Q_{0+} + \frac{Q_{0+}}{C_x}\frac{\partial}{\partial\psi}C_x\right)\right)}C_x^3}{6\pi(\lambda_S-1)p_\chi^{(3(\lambda_S-1))}} - 4\frac{\overline{JQ_{0+}}C_x^3\frac{\partial}{\partial\psi}l\left(1+3(\lambda_S-1)\log(p_\chi)\right)}{18\pi(\lambda_S-1)^2p_\chi^{(3(\lambda_S-1))}}$$

$$\langle Q_4\rangle^{asy} = 2\frac{\overline{\left(S_0\left[\nu' + q'\left(-\lambda_S + \left(\frac{1}{X_0}\frac{\partial X_1}{\partial\theta}\right)\right)\right]\right)}C_x^3}{6\pi(\lambda_S-1)p_\chi^{(3(\lambda_S-1))}}$$

$$\langle Q_5\rangle^{asy} = 2\frac{\overline{\left(T_0\frac{\partial}{\partial\psi}J\right)}C_x^3}{6\pi(\lambda_S-1)p_\chi^{(3(\lambda_S-1))}}$$

$$\langle Q_6\rangle^{asy} = 2\frac{\overline{(u_0\ \omega_0)}C_x^3}{6\pi(\lambda_S-1)p_\chi^{(3(\lambda_S-1))}}$$

We have made use of the fact that the equilibria are up-down symmetric and to evaluate $\langle Q_3\rangle^{asy}$ we have exploited the relation $\frac{d(b^{u(x)})}{dx} = b^u(\ln b)\frac{du(x)}{dx}$, and $\int x^a\log x dx = \frac{x^{1+a}(-1+(1_+a)\log x)}{(1+a)^2}$.

### 5.1.6. Quasilinear nonlinearity coefficient $C_4$

In this section the quasilinear nonlinearity coefficient is investigated:

$$C_4 = 2\left\langle XT_\wedge\boldsymbol{e}_\wedge\cdot\mathcal{L}\left(\frac{X}{B_0}\boldsymbol{e}_\perp\right)\right\rangle - \left\langle\frac{X^2}{B_0}\boldsymbol{e}_\perp\cdot\mathcal{L}\left(\boldsymbol{T}_\perp\right)\right\rangle$$

To be able to evaluate this coefficient we must determine the quantity $\boldsymbol{T}_\perp$ by evaluating its differential equation, which is described in the next section.

#### Determining $\boldsymbol{T}_\perp$

$\boldsymbol{T}_\perp$ is defined so that it satisfies the following two equations:

$$\boldsymbol{e}_\wedge \cdot \boldsymbol{\mathcal{L}}\left(\boldsymbol{T}_\perp\right) = X\boldsymbol{e}_\wedge \boldsymbol{\mathcal{L}}\left(\frac{X\boldsymbol{e}_\perp}{B}\right) \tag{5.11}$$

$$T_\psi = \frac{X^2}{2B} \tag{5.12}$$

with

$$\boldsymbol{T}_\perp = \frac{K}{B_0}\boldsymbol{e}_\wedge + T_\psi \boldsymbol{e}_\perp \tag{5.13}$$

where we defined $K \equiv T_\wedge |B_0|$ to simplify the subsequent calculation. By using these relations (equations (5.11), (5.12) and (5.13)) we obtain:

$$\frac{\boldsymbol{e}_\wedge}{B}\boldsymbol{\mathcal{L}}\left(\frac{K}{B_0}\boldsymbol{e}_\wedge\right) = \frac{X\boldsymbol{e}_\wedge}{B}\boldsymbol{\mathcal{L}}\left(\frac{X\boldsymbol{e}_\perp}{B}\right) - \frac{\boldsymbol{e}_\wedge}{B}\boldsymbol{\mathcal{L}}\left(\frac{X^2\boldsymbol{e}_\perp}{2B}\right) \tag{5.14}$$

Using the expressions for the $\boldsymbol{e}_\wedge$ components of the linear operator $\boldsymbol{\mathcal{L}}$ acting on vectors with either $\boldsymbol{e}_\wedge$ or $\boldsymbol{e}_\perp$ components (equations (B.2) and (B.5)), Eq. (5.14) can be re-written as:

$$J\boldsymbol{B}_0 \cdot \boldsymbol{\nabla}_0 \left\{ \frac{|\boldsymbol{e}_\wedge|^2}{JB^2} J\boldsymbol{B}_0 \cdot \boldsymbol{\nabla}_0 K \right\} = -\frac{\boldsymbol{e}_\perp \cdot \boldsymbol{e}_\wedge}{B^2 J} \left[J\boldsymbol{B}_0 \cdot \boldsymbol{\nabla}_0 X\right]^2 + \frac{X^2}{2} J\boldsymbol{B}_0 \cdot \boldsymbol{\nabla}_0 \sigma$$

We will show that only the derivative $\boldsymbol{B}_0 \cdot \boldsymbol{\nabla}_0 K$ is needed. To determine it numerically, we can integrate the right hand side along a field line and multiply the result by $\frac{JB^2}{|\boldsymbol{e}_\wedge|^2}$.

#### Determining the integrals

In this subsection the two terms of the quasilinear nonlinearity coefficient are simplified so that the coefficient can be easily implemented.

First term of the coefficient $C_4$

By dividing $C_4 = C_{4/1} + C_{4/2}$ the first term of the fourth coefficient can be written as:

$$\begin{aligned} C_{4/1} &\equiv 2\left\langle X\frac{K}{B_0}\boldsymbol{e}_\wedge \cdot \mathcal{L}\left(\frac{X}{B_0}\boldsymbol{e}_\perp\right)\right\rangle \\ &= 2\left\langle K\left[\frac{\boldsymbol{e}_\wedge}{B_0}\cdot\mathcal{L}\left(\frac{K}{B_0}\boldsymbol{e}_\wedge\right)+\frac{\boldsymbol{e}_\wedge}{B_0}\cdot\mathcal{L}\left(\frac{X^2}{2B_0}\boldsymbol{e}_\perp\right)\right]\right\rangle \\ &= 2\left\langle K\left\{\boldsymbol{B}_0\cdot\boldsymbol{\nabla}_0\left(\frac{|\boldsymbol{e}_\wedge|^2}{B_0^2}\boldsymbol{B}_0\cdot\boldsymbol{\nabla}_0 K\right)+\frac{1}{2}\boldsymbol{B}_0\cdot\boldsymbol{\nabla}_0\left[\frac{\boldsymbol{e}_\perp\cdot\boldsymbol{e}_\wedge}{B_0^2}\boldsymbol{B}_0\cdot\boldsymbol{\nabla}_0 X^2\right]+\frac{1}{2}\boldsymbol{B}_0\cdot\boldsymbol{\nabla}_0\left(\sigma X^2\right)\right\}\right\rangle \end{aligned}$$

using Eq.s (B.2), (B.5) and (5.11). It is evident that each term is of the form $\langle K\boldsymbol{B}_0\cdot\boldsymbol{\nabla}_0 F\rangle$ where $F$ is a place holder for any expression. This can be re-written in the following way:

$$\begin{aligned} \langle K\boldsymbol{B}_0\cdot\boldsymbol{\nabla}_0 F\rangle &= -\langle F\boldsymbol{B}_0\cdot\boldsymbol{\nabla}_0 K\rangle + \cancelto{0}{\langle \boldsymbol{B}_0\cdot\boldsymbol{\nabla}_0(KF)\rangle} \\ &\approx -\langle F\boldsymbol{B}_0\cdot\boldsymbol{\nabla}_0 K\rangle \end{aligned}$$

The term $\langle \boldsymbol{B}_0\cdot\boldsymbol{\nabla}_0(KF)\rangle$ can be neglected since the asymptotic parts of the variables go to zero at infinity. It follows that:

$$C_{4/1} = -2\left\langle\frac{|\boldsymbol{e}_\wedge|^2}{B_0^2}\left[\boldsymbol{B}_0\cdot\boldsymbol{\nabla}_0 K\right]^2+\frac{\boldsymbol{e}_\perp\cdot\boldsymbol{e}_\wedge}{B_0^2}\left[\boldsymbol{B}_0\cdot\boldsymbol{\nabla}_0 K\right]\left[X\boldsymbol{B}_0\cdot\boldsymbol{\nabla}_0 X\right]+\frac{1}{2}\left[\boldsymbol{B}_0\cdot\boldsymbol{\nabla}_0 K\right]\sigma X^2\right\rangle$$

Second term of the coefficient $C_4$

The second term of the fourth coefficient is:

$$\begin{aligned} C_{4/2} &\equiv -\left\langle\frac{X^2}{B_0}\boldsymbol{e}_\perp\cdot\mathcal{L}\left(\boldsymbol{T}_\perp\right)\right\rangle \\ &= -\left\langle\frac{X^2}{B_0}\left(\boldsymbol{e}_\perp\cdot\mathcal{L}\left(\frac{K}{B_0}\boldsymbol{e}_\wedge\right)+\boldsymbol{e}_\perp\cdot\mathcal{L}\left(\frac{X^2}{2B_0}\boldsymbol{e}_\perp\right)\right)\right\rangle \end{aligned}$$

Using the relations for $\mathcal{L}$ of the basis vectors (B.4), (B.3) and integration by parts leads to:

$$\begin{aligned} C_{4/2} = 2\left\langle\frac{\boldsymbol{e}_\perp\cdot\boldsymbol{e}_\wedge}{B_0^2}\left[\boldsymbol{B}_0\cdot\boldsymbol{\nabla}_0 K\right]\left[X\boldsymbol{B}_0\cdot\boldsymbol{\nabla}_0 X\right]\right\rangle + \left\langle\left[\boldsymbol{B}_0\cdot\boldsymbol{\nabla}_0 K\right]\sigma X^2\right\rangle \\ + \left\langle 2X^2\left[\left(\boldsymbol{B}_0\cdot\boldsymbol{\nabla}_0\right)X\right]^2\frac{\boldsymbol{e}_\perp^2}{B^2}\right\rangle - \left\langle\frac{2}{B_0^4}\left(\boldsymbol{e}_\perp\cdot\boldsymbol{\kappa}_0\right)\left(\boldsymbol{e}_\perp\cdot\nabla p_0\right)\frac{X^4}{2}\right\rangle \end{aligned}$$

Combining the two terms of $C_4$ and using Eq.s (A.2) and (A.3) leads to the full expression for this coefficient:

$$C_4 = -2\left\langle \frac{|\boldsymbol{e}_\wedge|^2}{B_0^2}\left[\boldsymbol{B}_0\cdot\boldsymbol{\nabla}_0 K\right]^2\right\rangle + \left\langle \frac{X^4\Lambda f p'}{2JB^4}\frac{\partial B^2}{\partial\theta}\right\rangle + \left\langle \frac{2\boldsymbol{e}_\perp^2 X^2}{B^2}\left(\boldsymbol{B}_0\cdot\boldsymbol{\nabla}_0 X\right)^2\right\rangle - \left\langle \frac{X^4 p'}{B^2}\left(p' + \frac{1}{2}\frac{\partial B^2}{\partial\psi}\right)\right\rangle$$

### 5.1.7. Fractional derivative coefficient $C_5$

The final coefficient $C_5$, which is the fractional derivative coefficient, is given by:

$$C_5 = -\frac{\lambda b_0}{\Gamma(2-\lambda)}\left(A_+^2 + A_-^2\right) q'^2 \left\langle \frac{B_0^2}{|\nabla\psi|^2}\right\rangle_\theta^{-1}$$

with $\lambda \equiv \lambda_S - \lambda_L$. To obtain $b_0 = \frac{Y_{L+}}{Y_{S+}}$ we must evaluate $Y_{L+}$ and $Y_{S+}$ which can be found by solving the set of differential equations (3.14), (3.15) and (3.16) of the inertial region. To solve this set of differential equations we reduce it by using Eq. (3.16) to eliminate the $\tilde{\Xi}_{-1}$ dependency in Eq. (3.15). The remaining set of two differential equations is given by:

$$A_0 x^2 \tilde{Y}_0 = \frac{\partial}{\partial x}\left[x^2\frac{\partial\tilde{Y}_0}{\partial x}\right] + D_M\left[\tilde{Y}_0 + \frac{\Gamma p_0}{p_0'}\tilde{\mathcal{J}}_0\right] + A_1 x\frac{\partial\tilde{\mathcal{J}}_0}{\partial x}$$

$$A_5\frac{\partial^2\tilde{\mathcal{J}}_0}{\partial x^2} = A_2\tilde{\mathcal{J}}_0 + A_3\tilde{Y}_0 + A_4\frac{\partial(x\tilde{Y}_0)}{\partial x}$$

This can be solved numerically by exploiting a coupled Runge-Kutta-Nyström method [110] combined with the shooting method [111], see Sect. 2.5.3. We must use the shooting method since the boundary conditions (3.17) and (3.18) are used which gives asymptotic relations for $\tilde{Y}_0$ and $\tilde{J}_0$.

To obtain $b_0$ we must evaluate the ratio $\dfrac{Y_{L+}}{Y_{S+}}$ using the numerical solutions. We define three of these numerical solutions $y_i$ for small $x_i$ which have the form of equation (3.19):

$$y_i = -A + \left(\frac{Y_{S+}^n}{x_i^{\lambda_S}} + \frac{Y_{L+}^n}{x_i^{\lambda_L}}\right)$$

where $A$, $Y_{S+}^n$ and $Y_{L+}^n$ are constant. Defining $a_i \equiv x_i^{-\lambda_s}$ and $b_i \equiv x_i^{-\lambda_L}$ we obtain for the ratio:

$$b_0 = \frac{Y_{L+}}{Y_{S+}} \approx \frac{a_3(y_1-y_2) + a_1(y_2-y_3) + a_2(y_3-y_1)}{b_3(y_2-y_1) + b_2(y_1-y_3) + b_1(y_3-y_2)} \tag{5.15}$$

Therefore, we must determine the function $\tilde{Y}_0$ numerically and calculate three solutions at points with $x_i \ll 1$ to then evaluate $b_0$ using equation (5.15).

### 5.1.8. Conclusion

A method for the calculation of each coefficient has been presented which includes a division into numerically and analytically treated parts of the integrals for the coefficients. The next step is to verify that the asymptotic expressions are correct and that each of the coefficient converges with respect to the cut off $p_\chi$. These tests are performed using the Type I ELMy MAST equilibrium case presented in the next section. After these verifications the coefficients are investigated for Type I ELMs in MAST and Type II ELMs in a JET-like equilibria.

## 5.2. Type I ELMs in a MAST equilibrium

In this section a MAST Type I ELMy H-mode equilibrium is investigated (shot 24763). The fits of the profiles were produced by the standard equilibrium reconstruction code EFIT [118] and the equilibrium was calculated with the fixed boundary equilibrium solver HELENA which solves the Grad-Shafranov equation [119, 120]. We start by examining the asymptotic expressions and the convergence of the coefficients with respect to the value $p_\chi$ in Sect. 5.2.1. Then we investigate the coefficients of this MAST equilibrium in Sect. 5.2.3 and study how they depend on the local pressure gradient (Sect. 5.2.4). Lastly we present methods for comparing our results with experiments in Sect. 5.2.5.

### 5.2.1. Convergence verifications

In this subsection the implementation of the methods derived in Sect. 5.1 are tested. In the first part we compare the asymptotic versus the numerical integrands derived in Section 5.1.1. The method is found to be correct because the asymptotic integrands match the numerical integrands for higher values of $\chi$.

The second verification is that of the convergence with respect to the value $p_\chi$. As indicated in the previous section, when $p_\chi$ goes to infinity the integrals should become exact.

**Comparison: Asymptotic vs Numerical Integrands**

In this subsection we compare the integrands (and not the integrals) of the asymptotic and numerical quantities to verify that the asymptotic expressions derived in 5.1.3 and 5.1.5 are accurate. If they are correct they should match for sufficiently high values of $\chi$. The asymptotic treatment has only to be implemented for the inertial and the quadratic nonlinear coefficients ($C_0$ and $C_2$), therefore only these integrands are investigated.

Inertial coefficient, $C_0$

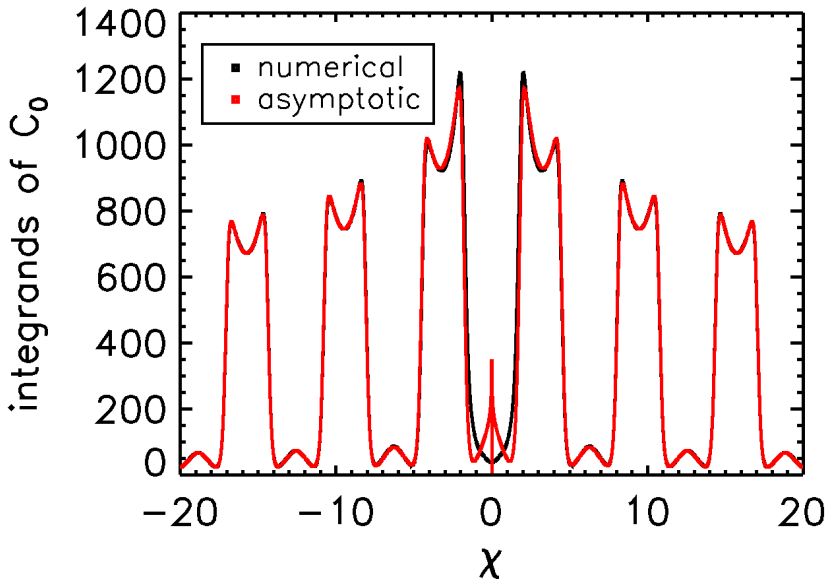


Figure 5.4.: *The integrands of the inertial coefficient. Black: integrand calculated with the numerical functions. Red: integrand calculated with the dominant order of the analytic, asymptotic functions. After half a period ($\chi = \pi$) the relative error is only* 1.2%.

The integrand of the inertial coefficient presented in Section 5.1.3 is displayed here to verify the calculations. We found that the asymptotic description of the integrand coincides with the numerical integrand well, figure 5.4. We can define the relative error as:

$$E_{rel} = \left| 1 - \frac{C_0^{asy}}{C_0^{num}} \right|$$

where $C_0^{asy}$ represents the asymptotic integrand and $C_0^{num}$ represents the numerical integrand. After only half a period (half way around the poloidal circumference) the relative error of the asymptotic integrand is $E_{rel} \approx 1.2\%$. After 80 periods the relative error is

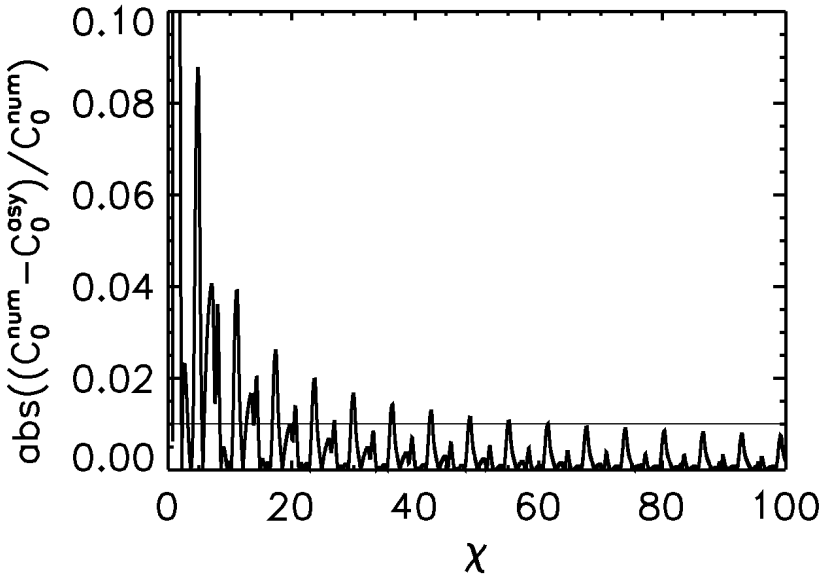


Figure 5.5.: *The relative error of the asymptotic form of the integrand relative to the numerical form. Note that after around* $\chi = 60$ *the relative error is throughout smaller than* 1%*. Since the integrand of the* $C_0$ *coefficient is an even function, only the positive values of* $\chi$ *are shown.*

$\approx 0.28\%$. This is evidence that our method is sufficient.

Quadratic nonlinear coefficient, $C_2$

The integrand of the quadratic nonlinear coefficient presented in Section 5.1.5 is displayed here to verify the calculations. Since this coefficient was divided into six components labelled as $Q_i$, we display each to ensure that all of these integrands are in agreement with their asymptotic form.

The relative error is not useful here since the numerical form of the integrand of $Q_i$ is zero periodically which means the relative error is not defined at these locations. Therefore the absolute error is evaluated instead:

$$E_{abs} = Q_i^{asy} - Q_i^{num}$$

The absolute error converges to zero quickly for all $Q_i$, see Fig.5.6.

Fig. 5.4, 5.5 and 5.6 suggest that the analytical forms of the integrands are correct. However, we still must verify that the asymptotic form is accurate enough so that the total

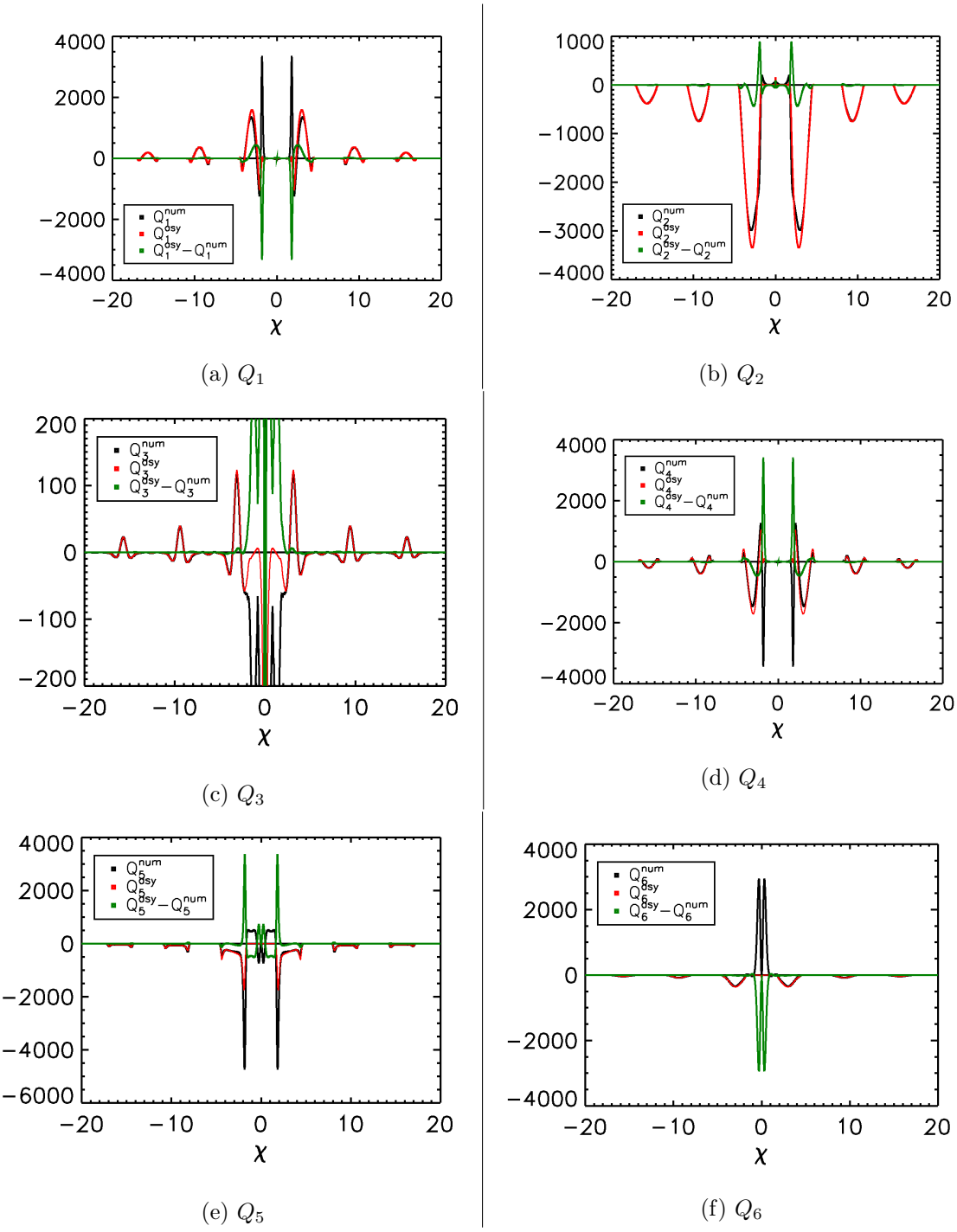


(a) $Q_1$ (b) $Q_2$

(c) $Q_3$ (d) $Q_4$

(e) $Q_5$ (f) $Q_6$

Figure 5.6.: *The numerical (in black) and analytical (in red) form of each $Q_i$ integrand, and the difference between them in green. We can see that the two forms agree quite well as the difference converges to zero quickly*

value calculated for the coefficient (i.e., by evaluating the integrals) converges.

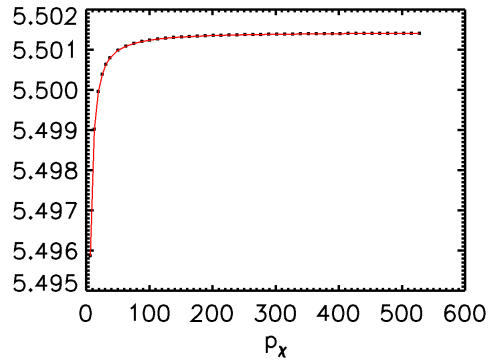


(a) *The calculated value of the linear coefficient. By fitting we estimate the limit of the real value to be* 5.50144 *and that it converges slowly with* $\sim \frac{1}{p_\chi^{1.21}}$. *The approximate value of* 5.5 *is reached for a* $p_\chi$ *around* 10 *which is equivalent to two to three turns around the torus.*

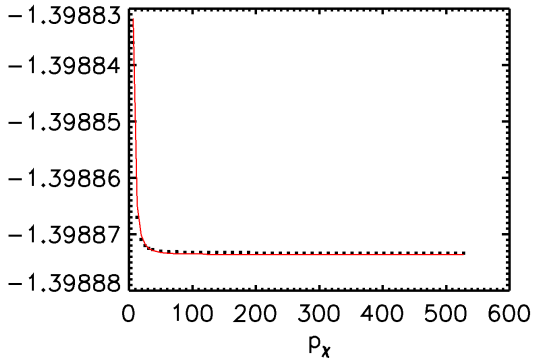


(b) *The calculated value of the quasilinear nonlinearity coefficient. We can see that the approximate value is* $-1.4$ *and we can use a fitting to estimate its convergence to be* $\sim \frac{0.003}{p_\chi^{2.26}}$ *which indicates that it converges quickly to its value.*

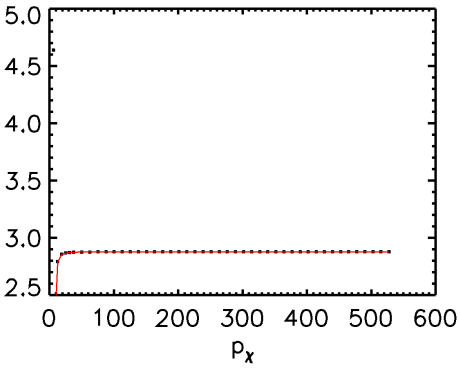


(c) *The calculated value of the fractional derivative coefficient. This coefficient does not depend on the cut-off of* $p_\chi$ *since it is calculated with a differential equation. However, its results improve as well if the function* $X$ *is evaluated further along the magnetic field lines. It converges to* 2.878.

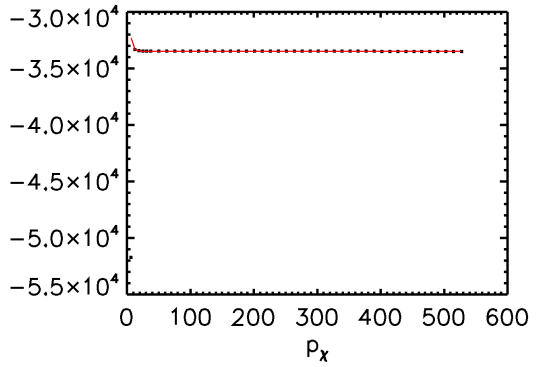


(d) *The calculated value of the nonlinear drive coefficient. It converges very quickly to its value of* $-33474$ *because of the asymptotic treatment.*

Figure 5.7.: *Coefficients vs the cut off value* $p_\chi$.

### Convergence test of the coefficients

Here we present the convergence of all coefficients as a function of the integration range. Only the inertial and the quadratic nonlinear coefficients have additional asymptotic parts. We show that the other coefficients converge as well and therefore do not require an extension for the numerical integration.

We find that all coefficients converge, as shown in Figs. 5.7 and 5.8. By using a fitting method we determine the values of the coefficients as $p_\chi \to \infty$. We estimate the limit of

the real value of the linear coefficient $C_0$ to be 5.50144 and it converges slowly with $\sim \frac{1}{p_\chi^{1.21}}$. The approximate value of 5.5 is reached for a $p_\chi$ around 10 which is equivalent to two to three turns around the torus.

The approximate value of the quasilinear nonlinearity coefficient $C_4$ is $-1.4$ and we can use a fitting to estimate its convergence to be $\sim \frac{0.003}{p_\chi^{2.26}}$ which indicates that this coefficient converges quickly.

The fractional derivative coefficient $C_5$ does not need the asymptotic treatment. Nevertheless it depends on the cut-off of $p_\chi$ since its results depend on the function $X$ which becomes more accurate if it is evaluated further along the magnetic field lines. The fractional derivative coefficient converges to 2.878.

The nonlinear drive coefficient $C_2$ converges very quickly to its value of $-33474$ because of the asymptotic treatment.

In summary the values for each coefficient are:

$$C_1 \approx 5.501 \qquad C_4 \approx -1.4$$

$$C_5 \approx 2.878 \qquad C_2 \approx -33474$$

### 5.2.2. Note on the order of coefficients

A careful reader might notice that the nonlinear explosive coefficient $C_2$ has a larger magnitude than the other coefficients. However, this depends on the chosen boundary condition of the function $X$ and can be changed by scaling this function. Since the displacement $\xi$ is given by $\xi = \hat{\xi}\frac{X}{B_0}$, the real displacement stays the same if $\hat{\xi}$ is scaled inversely to $X$. Therefore the scaling of $X$ does not change the physics if $\hat{\xi}$ is changed with the inverse scaling factor. Thus we can choose the boundary condition of the function $X$ for $\chi = 0$, since the initial displacement is freely chosen under the constraint that it has to be small. The values presented are for the boundary condition $X(\chi = 0) = 1$.

All the terms of the nonlinear differential equation determining $\hat{\xi}$ are of the form

$$\langle F(\chi)X(\chi)^\alpha \rangle \boldsymbol{A}\hat{\xi}^\alpha$$

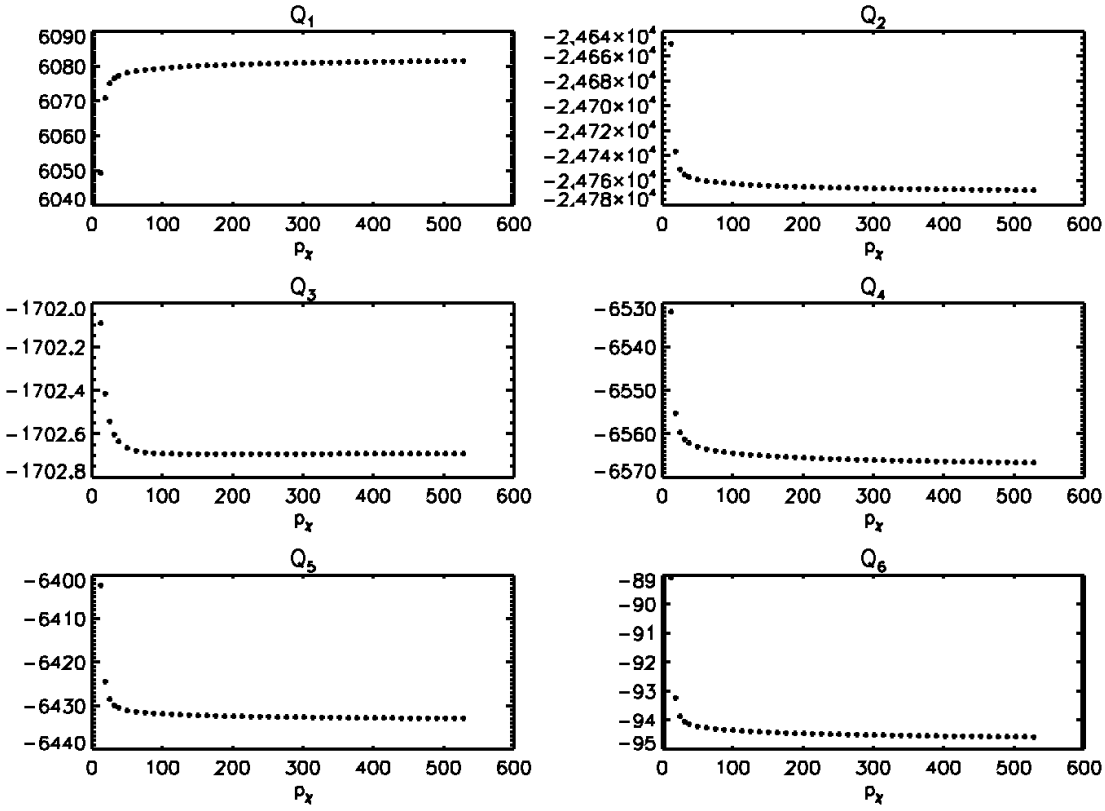


Figure 5.8.: *The convergence of each $Q_i$ of the nonlinear drive coefficient.*

where $F(\chi)$ is a function and $\boldsymbol{A}$ is an operator. The averaged term $\langle F(\chi)X(\chi)^{\alpha}\rangle$ represents the coefficient. One can see that changing $X$ and inversely changing $\hat{\xi}$ does not change the equation. However scaling $X$ will influence the coefficients. This effect is larger for nonlinear terms when one deviates away from 1 since $\alpha > 1$.

If for instance we change it to be $X(\chi = 0) = 10^{-4}$ and multiply the whole equation by a scaling factor $10^8$, we obtain the equivalent coefficients:

$$C_1 \approx 5.501 \qquad C_4 \approx -1.4 \cdot 10^{-8}$$

$$C_5 \approx 2.878 \qquad C_2 \approx -3.3474$$

If we use these coefficients the final displacement at $\chi = 0$ would be $\hat{\xi}$ multiplied by $X = 10^4$ with this treatment. We see that the nonlinear explosive coefficient is of the same order as the linear coefficients, but we also notice that the second nonlinear coefficient $C_4$ is very small after this treatment.

For the following results we have used the original boundary condition $X(\chi = 0) = 1$.

### 5.2.3. Simulation with original coefficients

Here we discuss the results of the coefficients of the original MAST Type I ELMy equilibrium and we present the results of the simulations with these coefficients which are:

$$C_1 \approx 5.501 \qquad C_4 \approx -1.4$$
$$C_5 \approx 2.878 \qquad C_2 \approx -33474$$
$$\mu \approx 0.74 \qquad \lambda \approx 1.252$$

We notice that both nonlinear coefficients are negative. If only the nonlinear drive coefficient were negative, the behaviour of the filaments would be the same as shown in previous work [67, 68] but with the explosive drive inwards instead of outwards. To show this let's start with the nonlinear ballooning equation implemented in Deton8[4], equation (2.28):

$$D_0\kappa\frac{\partial^\lambda}{\partial t^\lambda}\xi = \left(D_1 - \frac{(\psi-\psi_0)^2}{\Delta^2}\right)\xi - D_2\frac{\partial^2 u}{\partial\psi^2} + D_3\left(\xi^2 - \overline{\xi^2}\right) + D_4\xi\frac{\partial^2\overline{\xi^2}}{\partial\psi^2}$$

If we transform: $\alpha \to a\alpha$, $t \to \tau t$, $\psi \to p\psi$ and $\xi \to x\xi$ with

$$a = \frac{D_1}{D_2}\sqrt{\frac{D_4}{D_2}} \qquad \tau = \sqrt[\kappa]{\frac{D_0\kappa}{D_1}}$$
$$p = \frac{\sqrt{D_1 D_4}}{D_3} \qquad x = \frac{D_1}{D_3}$$

and

$$\Delta \to \sqrt{x}p\Delta$$

we obtain a generic equation where $\Delta$ is the only parameter. This generic equation was used previously [67, 68] and with it the qualitative results of filaments are similar. If $D_3$ reverses its sign, the filaments move in the opposite direction, which can be seen by replacing $\xi \to -\xi$. The only term that changes sign by this transformation is the nonlinear drive term. When the sign of the nonlinear drive coefficient is negative, the filament implodes rather than explodes.

[4]The nonlinear coefficients of deton8 are related to the nonlinear coefficients of the nonlinear envelope equation as follows: $D_3 = C_2$ and $D_4 = C_4$.

However, if the quasilinear nonlinearity coefficient is also negative this leads to an imaginary transformation in the generic equation. This means that the change of this sign leads to a new generic equation. If the quasilinear nonlinearity coefficient is positive it leads to a broadening in the radial ($\psi$) direction and a narrowing in the periodic ($\alpha$) direction. This can be seen by plotting $\frac{\partial^2 \overline{\xi^2}}{\partial \psi^2}$ vs $\psi$, see Fig. 5.9b. It is negative at the most unstable flux

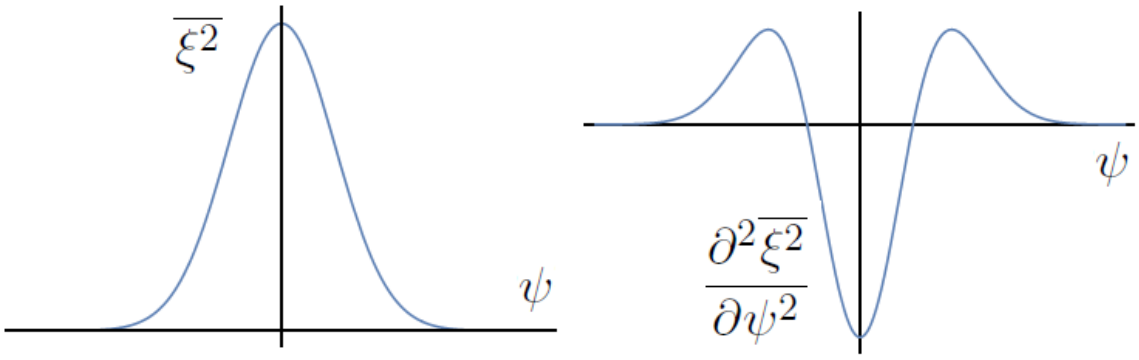


(a) *A sketch of $\overline{\xi^2}$ versus $\psi$ which has a similar shape to a Gaussian.*

(b) *A sketch of $\frac{\partial^2 \overline{\xi^2}}{\partial \psi^2}$ which is of a similar form of the second derivative of a Gaussian.*

Figure 5.9.: *Sketches of quantities appearing in the nonlinear terms (nonlinear drive term and quasilinear nonlinearity term)*

surface (displayed at the middle). It then changes sign radially further away from the most unstable flux surface, labelled with $\psi_0$. Multiplying by a positive $\xi$ leads to a negative sign at the most unstable flux surface which means the filament is damped and further away it leads to a positive sign which means the filament is driven. Therefore the filament becomes broader in $\psi$ which reduces the value of the quasilinear nonlinearity term as the second derivative with respect to $\psi$ becomes smaller.

However, if this quasilinear nonlinearity coefficient is negative then it drives (instead of damps) the filament at the most unstable flux surface and damps the filaments at other flux surfaces. This means that the filament becomes very narrow in the $\psi$-direction which therefore increases the quasilinear nonlinearity term as the second $\psi$-derivative becomes large, see Fig. 5.10. Therefore the cubic term is the most dominant term (and not the cubic together with the nonlinear drive term). This mechanism causes the model to break almost as soon as the filament enters the cubic-drive regime since it leads to overlapping flux surfaces which are not allowed in ideal MHD. As a result we cannot simulate the filaments with this model in this cubic nonlinear regime if the quasilinear nonlinearity coefficient is negative. Therefore this chapter concentrates more on the analysis of the

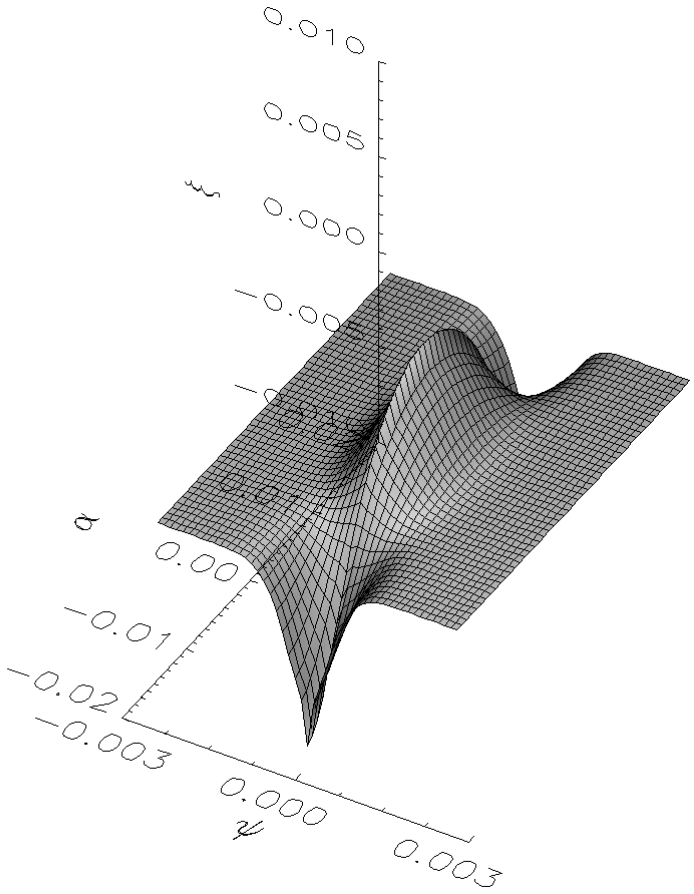


Figure 5.10.: *The quasilinear nonlinearity effect: the profile becomes sharply peaked due to the negative sign of the quasilinear nonlinearity coefficient.*

coefficients than on the simulation of these filaments.

To show that the negative quasilinear nonlinearity does indeed dominate the evolution of the filaments at some time, we discuss the results of the simulation briefly. Since $\lambda$ is close to 1 we choose to use the first order derivative instead, to reduce the run time. The energy of each of the terms is given by:

$$2\frac{dE}{dt} = \frac{d}{dt}\int \mathrm{d}\alpha\mathrm{d}\psi\left[D_0\left(\frac{\partial\xi}{\partial t}\right)^2 - \Gamma^2\xi^2 + D_2\left(\frac{\partial u}{\partial\psi}\right)^2 + \frac{1}{2}D_4\left(\frac{\partial\overline{\xi^2}}{\partial\psi}\right)^2 - \frac{2}{3}D_3\xi^3\right]$$

This relation enables us to quantify which terms dominate the evolution of the filaments at different times.

Fig. 5.11a shows how the cubic nonlinear term overtakes the nonlinear drive term; thus the cubic regime starts from about $t \approx 0.006$. Fig. 5.11b shows how the cubic nonlinear

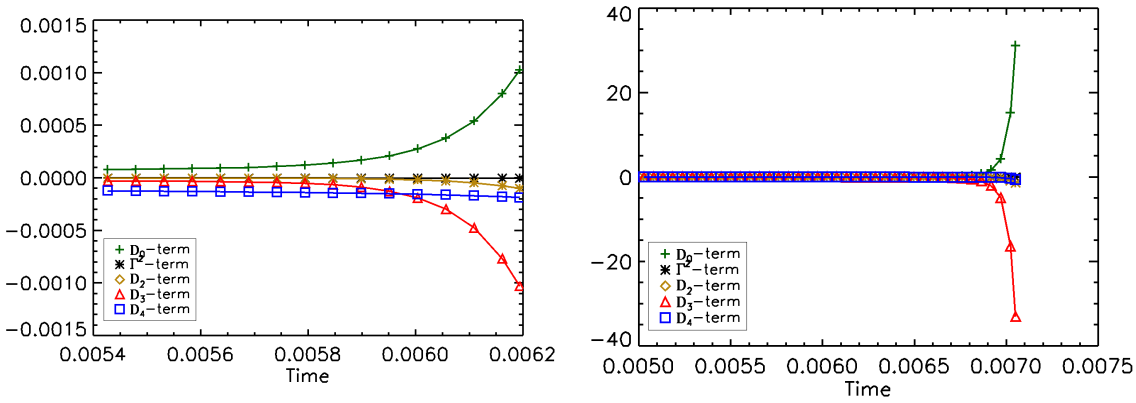


(a) *The energy terms vs time. The cubic quasi-linear nonlinearity term overtakes the non-linear drive term.*

(b) *The energy terms vs time. The cubic quasi-linear nonlinearity term dominates the fila-ment's behaviour at the end.*

Figure 5.11.: *Energy evolution of each term of the nonlinear ballooning envelope equation, given by Eq.* (5.16).

term balances the inertial term which means that it dominates the behaviour entirely. This change of regime can also be seen in the evolution of the displacement, Fig. 5.12, where the beginning of the evolution is dominated by the quadratic nonlinear drive coefficient, which forces the filaments inwards since it has a negative coefficient. Were we to display a

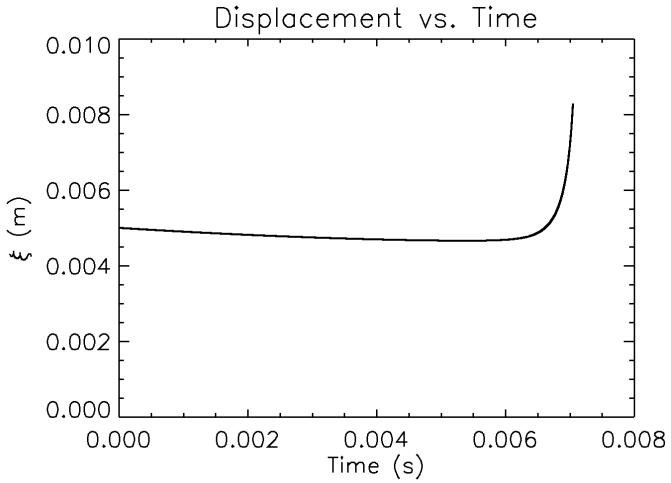


Figure 5.12.: *The displacement vs time. The beginning of the evolution is dominated by the quadratic nonlinear drive coefficient. It forces the filaments inwards because it has a negative coefficient. When the cubic term starts to dominate it drives the filaments outwards.*

position of an initial minimum of $\xi$ instead, we would see a larger (negative) growth. When the cubic term starts to dominate it drives the filaments outwards which is in agreement with Fig. 5.9b.

To analyse why this quasi-linear nonlinearity coefficient ($C_4$) is negative we investigate the values of each of its terms:

$$
\begin{aligned}
-2\left\langle \frac{R^2 B_p^2}{B^2}\left[\boldsymbol{B}_0\cdot\boldsymbol{\nabla}_0 K\right]^2\right\rangle &= -1.344 && < 0 \text{ always} \\
2\left\langle X^2\left[\boldsymbol{B}_0\cdot\boldsymbol{\nabla}_0 X\right]^2\left[\frac{1}{R^2B_p^2}+\frac{R^2B_p^2\Lambda^2}{B^2}\right]\right\rangle &= 3.99 && > 0 \text{ always} \\
-\left\langle \frac{fp'}{2J}\left(\frac{\partial}{\partial\theta}\frac{1}{B^2}\right)\Lambda\frac{X^4}{2}\right\rangle &= 0.184 && \\
-\left\langle \frac{p'^2X^4}{B^2}\right\rangle &= -6.98 && < 0 \text{ always} \\
-\left\langle \frac{p'X^4}{B^2}\frac{\partial}{\partial\psi}\frac{B^2}{2}\right\rangle &= 2.75 &&
\end{aligned}
\tag{5.16}
$$

Comparing the last two terms we can see that the pressure gradient is larger than the magnetic pressure gradient $\left(\frac{\partial}{\partial\psi}\frac{B^2}{2}\right)$ which leads to a large negative contribution from the second to last term.

We have presented why a negative quasilinear nonlinearity coefficient breaks the model as soon as the filament enters the cubic regime. Additionally we have shown that a negative nonlinear drive coefficient describes an imploding filament. Next we investigate if we can find a positive nonlinear drive coefficient to compare this model with ELMs as we know that these have an explosive nature.

### 5.2.4. Coefficient profiles

The nonlinear coefficients are negative for the current Type I ELM MAST case. Therefore the profiles of each coefficient relative to the flux surfaces are investigated to determine if they are negative on all relevant flux surfaces. Additionally we investigate the effects of changing the local pressure gradient on the radial profiles of the coefficients.

The nonlinear ballooning model is valid if the ballooning eigenvalue $\mu$ is close to but smaller than 1 and if $\frac{\partial\mu}{\partial\psi}\approx 0$. $\mu \lesssim 1$ indicates that the plasma is ballooning unstable. $\frac{\partial\mu}{\partial\psi}\approx 0$ means that $\mu$ must be a minimum, see Chapter 3. This means that the values calculated for the coefficients are less precise further away from the extreme of the ballooning eigenvalue. We evaluated the profiles for the coefficients with $p_\chi \approx 250$. The quantity $\lambda$ remains between 1 and 1.5, Fig. 5.13a. The ballooning eigenvalue has a broad minimum and

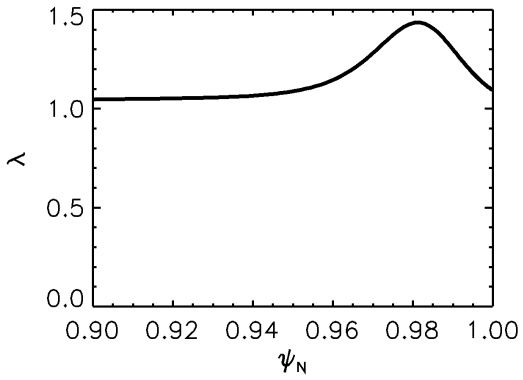


(a) $\lambda = \lambda_S - \lambda_L$ *which determines the order of the fractional derivative.*

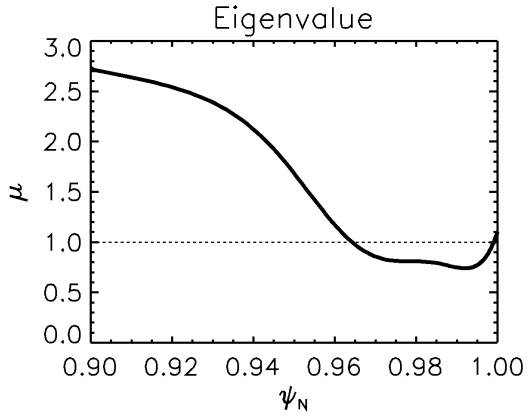


(b) *The ballooning eigenvalue* $\mu$*. If this value is below* 1 *the plasma is ballooning unstable.*

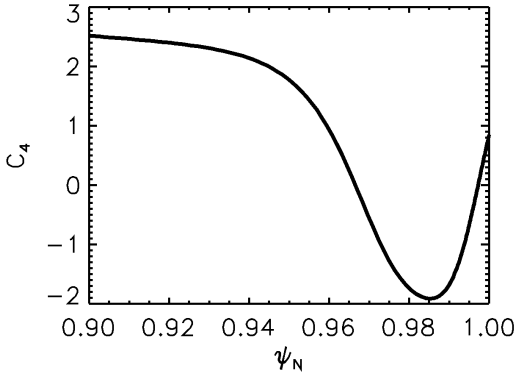


(c) *The quasilinear nonlinearity coefficient, which is negative where the plasma is ballooning unstable.*

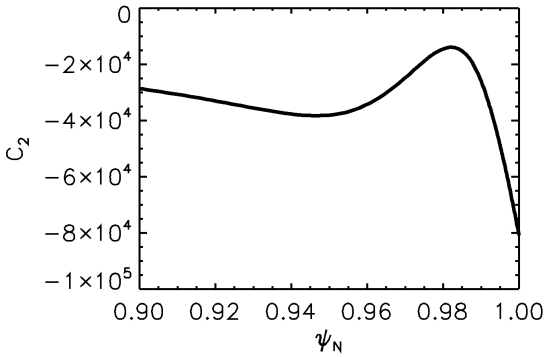


(d) *The explosive nonlinear drive coefficient* $C_2$*. It continues to be negative.*

Figure 5.13.: *Profiles of the coefficients with the original equilibrium.*

differs by around 20% from 1, Fig. 5.13b. Additionally we observe that the nonlinear drive coefficient continues to be negative on all flux-surfaces, but has a local maximum where the plasma is ballooning unstable.

The profiles obtained by increasing the local pressure gradient no longer represent an equilibrium, but help to understand the dependencies of the coefficients. The nonlinear drive coefficient changes if the pressure gradient is adjusted, as illustrated in Fig. 5.14. Specifically, as the pressure gradient is increased the nonlinear drive coefficient is also increased. Additionally $\lambda$ exceeds 2 (Fig. 5.14a) which means that the normal inertial coefficient can be used, see Chapter 3. However, the quasilinear nonlinearity term remains negative and its minimum decreases, see Fig. 5.14c.

Note that for this case there are flux surfaces which are ballooning unstable and have a positive nonlinear ballooning drive, see Fig. 5.15. However, recall that the local pressure

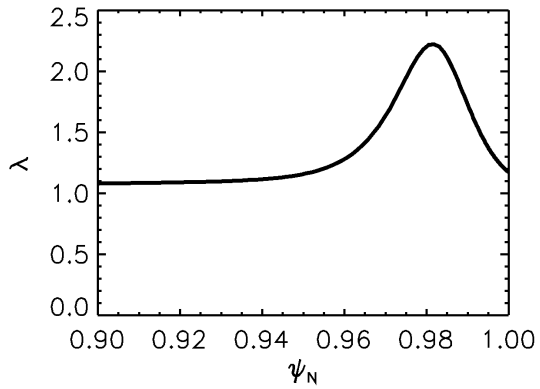


(a) $\lambda = \lambda_S - \lambda_L$ *which determines the order of the fractional derivative.*

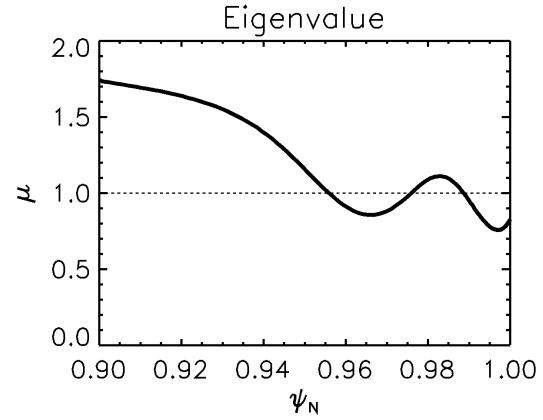


(b) *The ballooning eigenvalue* $\mu$*. If this value is below* 1 *the plasma is ballooning unstable.*

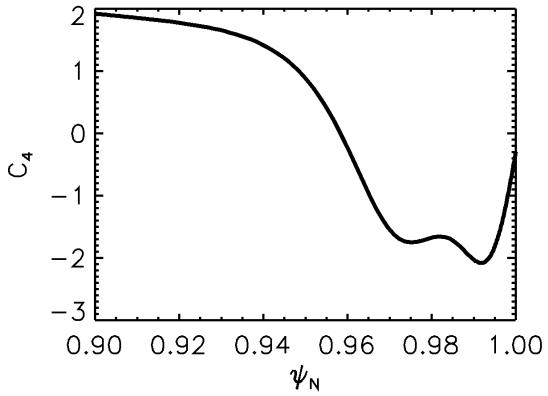


(c) *The quasilinear nonlinearity coefficient, which is negative where the plasma is ballooning unstable.*

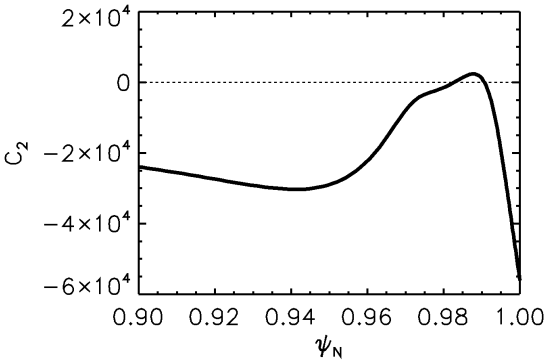


(d) *The explosive nonlinear drive coefficient* $C_2$*. It now has a small but positive value near* $\psi_N = 0.987$*.*

Figure 5.14.: *Profiles of the coefficients with an altered equilibrium where the local pressure gradient is increased by* 60%*.*

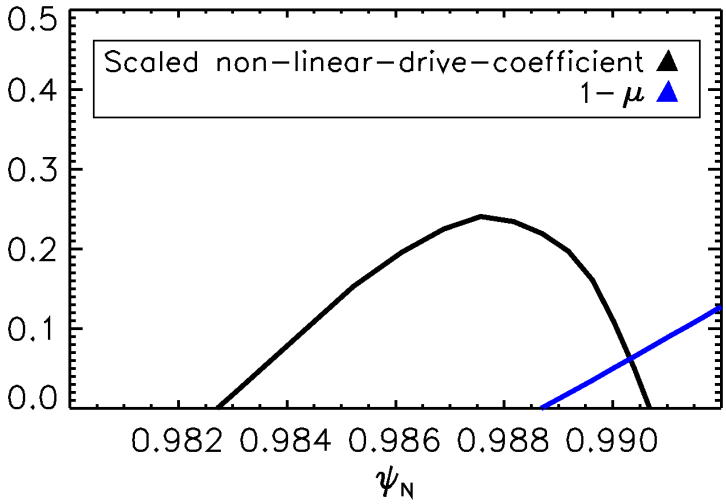


Figure 5.15.: *Scaled nonlinear drive coefficient and* $1-\mu$ *vs normalised flux surfaces for a local pressure gradient which is increased by* 60%*. The plasma is ballooning unstable which means that the linear drive term is initially driving the filaments. Also the nonlinear drive coefficient is positive, which means that it drives the filaments outwards.*

gradient must be changed by 60% in this case. This is larger than we would expect from experimental errors of the pressure gradient measurements which are around 20% [80].

### 5.2.5. Methods for experimental comparison

To compare our results with experimental measurements we must first determine a suitable method. The most obvious one is to visualise the results of the simulations and compare these structures with observed structures in experiments. Here we present a method for direct comparison with MAST high speed camera measurements. This method is insufficient for quantitative comparison, therefore a heuristic energy model is presented. It is used to calculate the energy released in an ELM from the simulated plasma. This energy can be easily compared with energies released in experiments.

We use the coefficients obtained from the case of the increased local pressure gradient, as it is a case which is ballooning unstable with a positive nonlinear drive. However, the reader should keep in mind that the equilibrium pressure gradient is increased by 60% which makes the comparison to experiments qualitative, at best. Nevertheless these methods are presented to show that comparison between simulations and experiments is in principle possible.

### 3D visualisation of filamentary structures

To visualise the perpendicular displacement of the filaments in Cartesian coordinates we first superimpose the solutions of the separated function $\frac{X}{B_0}$ and $\hat{\xi}$ given in equation (3.30), which are the solutions of the linear ballooning equation (3.31) and the nonlinear ballooning equation (3.48). The $\psi$ meshes vary between the two codes (evaluating the linear and nonlinear ballooning equations), but we only display the displacement from the most unstable flux surface.

The next step is to switch from the Clebsch coordinate system to a Cartesian system. We know that the cylindrical coordinate $\phi$ is related to the Clebsch coordinate $\alpha$ by the following equation:

$$\alpha = q\,(\chi - \chi_0) + Y - \phi$$

With this relation we calculate the toroidal angle $\phi$ for each given $\alpha$ and $\chi$. Furthermore we know the $Z$ and $R$ values for each given $\chi$ as these values are given in the input files for the coefficient code (in the MAST case produced by HELENA). We then exploit the transformation relations for cylindrical coordinates to Cartesian coordinates:

$$x = R\cos(\phi)$$

$$y = R\sin(\phi)$$

$$Z = Z$$

A typical result of displaying the filaments in 3 dimensions with an adjusted mode number[5] is shown in Fig. 5.16 where the data are visualised on top of a high speed camera image of an H-mode plasma in MAST. The brighter parts are regions with higher values of the displacement.

Using this method, we could in principle compare simulations with fast camera observations, as long as the equilibrium used provided suitable coefficients for the nonlinear ballooning mode envelope equation.

[5] The original mode number is reduced by a factor of approximately 20. This high mode number compared to experiments is probably due to the Taylor expansion of the ballooning eigenvalue $\mu$. This could be investigated in the future.

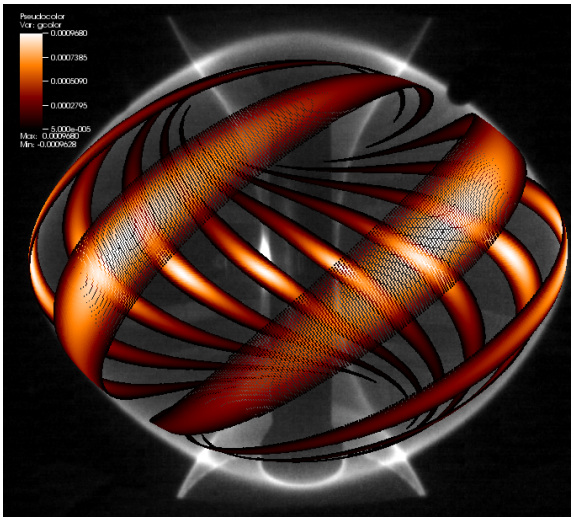


Figure 5.16.: *3D visualisation of the filamentary displacement with an enforced mode number of* $n = 10$.

### Heuristic energy model

This model was continued from work presented in Reference [7].

We know that the linear drive in tokamaks is caused by the pressure gradient. The linear drive in our nonlinear ballooning envelope equation (3.48) is proportional to the ballooning eigenvalue, described by the following equation:

$$1 - \mu = \frac{p' - p'_c}{p'}$$

where $p'$ is the pressure gradient in the plasma and $p'_c$ is the critical pressure gradient which cannot be exceeded [121]. In our heuristic energy model we use observations from experiments:

- The region of the steep pressure gradient (called pedestal) is increasing before an ELM crash.
- We also know that the pressure gradient collapses during an ELM crash [121].

Therefore we introduce a pedestal that grows linearly with time in our model. It increases until the nonlinear terms are of the same order as the linear terms. Then we make the pressure gradient crash until the instantaneous force on the filaments is approximately

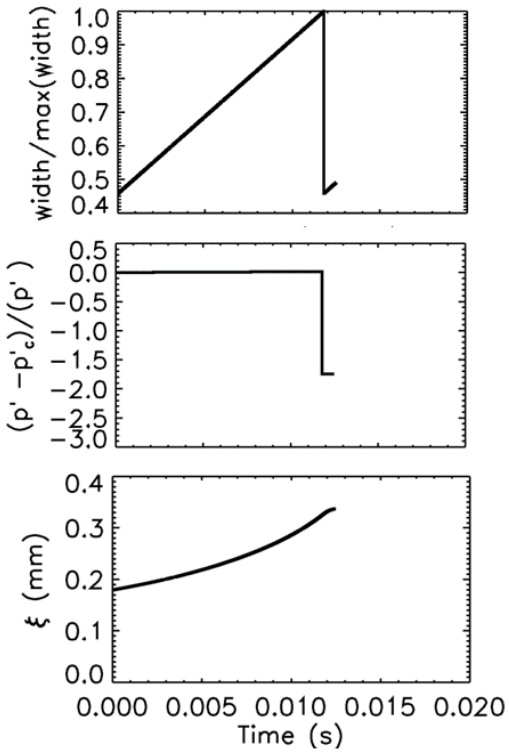


Figure 5.17.: *Evolution of the normalised width* $\frac{\Delta}{\Delta_{max}}$ *of the pedestal (top figure), the evolution of the normalised pressure gradient where the drop of it is seen (middle figure), and the evolution of the displacement (bottom figure). Note, that it is the very beginning of the nonlinear regime where the crash of the pressure gradient is initialised.*

zero, see Fig. 5.17.

To implement this model we must translate it into the correct form to input into our codes. The $1-\mu$ is replaced by the Taylor expansion: $1-\mu(\psi(0))-\frac{\partial^2\mu}{\partial\psi^2}\left(\psi-\psi_0\right)^2 = D_1-\frac{(\psi-\psi_0)^2}{\Delta^2}$, which allows us to represent the width of the pedestal by $\Delta$. To estimate the energy released during the drop in the pressure gradient we make the approximation that the released energy is proportional to the drop in pressure gradient, the pedestal width, and the volume of the pedestal. With that we obtain from this heuristic model the energy released in one ELM cycle of $\sim$ 0.65kJ. Typical energy released during one Type I ELM cycle in MAST are between 0.5-1.7kJ [45, 122].

At this point these values are not predictive. One has to compare several of the calculated energies with experiments since we can adjust several quantities in the model. However, it is already promising that it is possible to reach sensible values for the energy released, especially if we consider that there is no kink-drive in our model. This could explain why we had to increase the pressure gradient to find appropriate coefficients. A purely pressure

driven ELM is typically a Type II ELM [80, 96] which exists in a high collisionality regimes and reduced bootstrap current. Type II ELMs typically release less energy during one ELM cycle, which could explain why the obtained energy is at the lower range of the energies released in MAST.

To evaluate if the missing kink-drive is the explanation for the negative coefficients we investigate Type II ELMs on JET next.

## 5.3. JET-like equilibrium: Type II ELMs

In this section the coefficients for a JET-like equilibrium with Type II ELMs are investigated to examine if the missing kink drive in the nonlinear ballooning model is responsible for the negative nonlinear coefficients. This is the motivation for investigating equilibria susceptible to Type II ELMs, since they are considered to be purely ballooning driven [80, 96]. The coefficient code was constructed to analyse up-down symmetric equilibria, however, JET is not up-down symmetric. Fortunately the Type II case we are investigating (#70500) is close to a double null configuration and is therefore close to being up-down symmetric [80, 123, 124].

### 5.3.1. Obtaining up-down symmetric JET-like equilibrium

To obtain an up-down symmetric equilibrium to use for the coefficient code, we exploit the code SCENE [8] which is a self-consistent equilibrium code including neoclassical effects. As the input we have used an equilibrium created with HELENA and EFIT from shot number 70500.

To symmetrise the original equilibrium we perform the following steps: We find the maximum and minimum radius and their corresponding indices $i$, where $i$ is the label of each original point of the boundary, see Fig. 5.18. To simplify the description here we assume that $i = 1$ labels the point with the maximum radius $R_{max}$ and the subsequent labels follow anticlockwise along the boundary. We can always shift the index such that this is true, and the method is equivalent if the labels increase clockwise. Defining a new radial grid with $N$ points and an equidistant mesh spacing of $\frac{(R_{max}-R_{min})}{N}$ where the new radii are $R_{sym}(j) = R_{sym}(\frac{N}{2}+1-j)$ for $j\epsilon[0, \frac{N}{2}]$ where $j$ is the new label of the points. For each

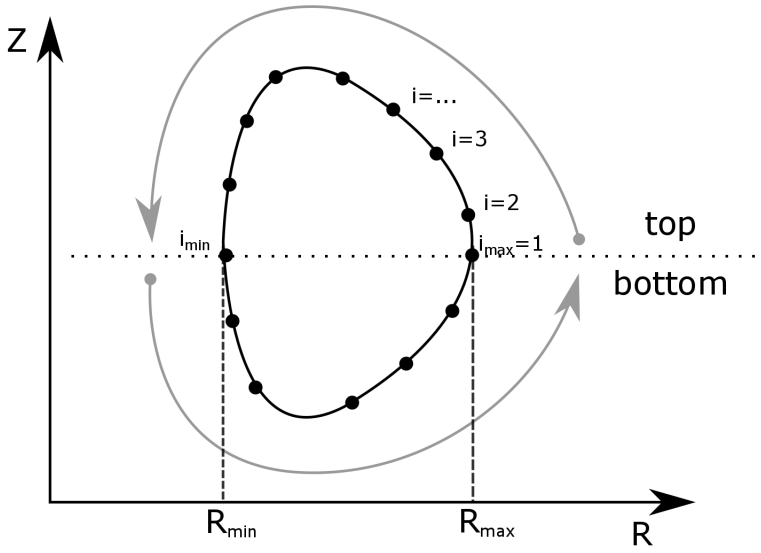


Figure 5.18.: *Sketch of grid of the plasma boundary.*

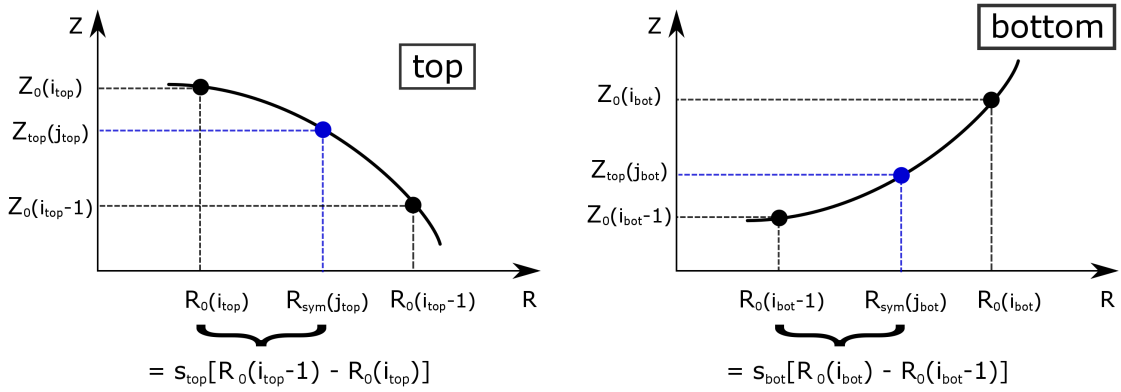


(a) *New radius $R_{sym}$ between two original radii $R_0$ and the corresponding new vertical height $Z_{top}$.*

(b) *New radius $R_{sym}$ between two original radii $R_0$ and the corresponding new vertical height $Z_{bot}$.*

Figure 5.19.: *Sketch of old and new radii and vertical heights.*

new radius $R_{sym}$ we can find two original radii such that $R_0(i) < R_{sym}(j_{top}) < R_0(i-1)$ in the top half and $R_0(i-1) < R_{sym}(j_{bottom}) < R_0(i)$ in the bottom half, see Fig. 5.19. We can then define a scaling parameter $s_{top}$:

$$s_{top} = \frac{R_{sym}(j_{top}) - R_0(i_{top})}{R_0(i_{top}-1) - R_0(i_{top})}$$

and an equivalent scaling factor $s_{bot}$ for the bottom part of the boundary. We can now estimate the vertical positions $Z_{top}$ of the new point as:

$$Z_{top} = s_{top}\left(Z_0(i_{top}-1) - Z_0(i_{top})\right)$$

and equivalently for the bottom vertical position $Z_{bot}$. The new symmetrical position is the average of these two values:

$$Z_{sym} = \frac{Z_{top} - Z_{bot}}{2}$$

The original and new boundaries for the equilibrium are shown in Fig. 5.20. To verify

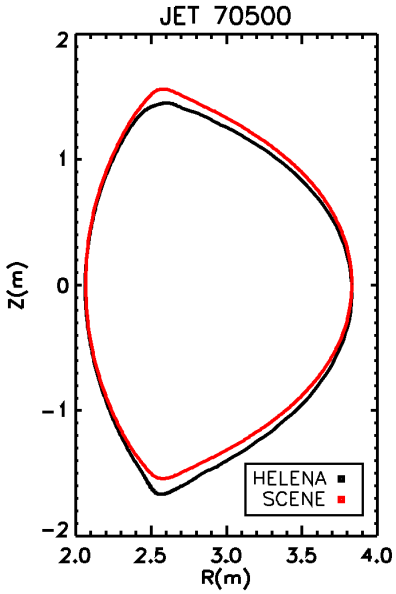


Figure 5.20.: *The original boundary from HELENA in black with the new up-down symmetric boundary produced with SCENE in red.*

that the modified equilibrium is indeed similar to the unmodified equilibrium, we display all the equilibrium quantities in Fig. 5.21, which also lead to a very similar ballooning eigenvalue profile, Fig. 5.22. Closer to the edge the differences become very small, which is preferable as the most unstable flux surface is in this region. Therefore we can produce up-down symmetric JET-like plasma equilibria (or for any other tokamak device) with SCENE. Additionally we can change certain parameters like the pressure gradient or the density to determine how these changes affect the coefficients.

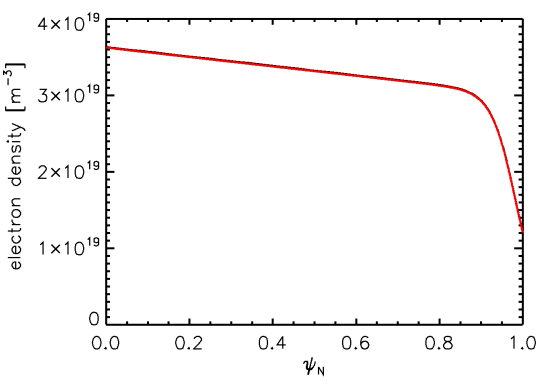


(a) *Electron density $n_e$ profile*

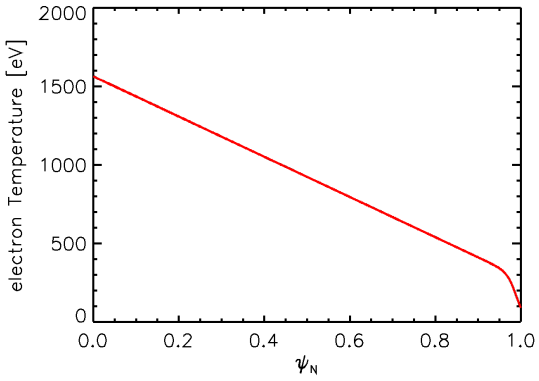


(b) *Electron temperature $T_e$ profile*

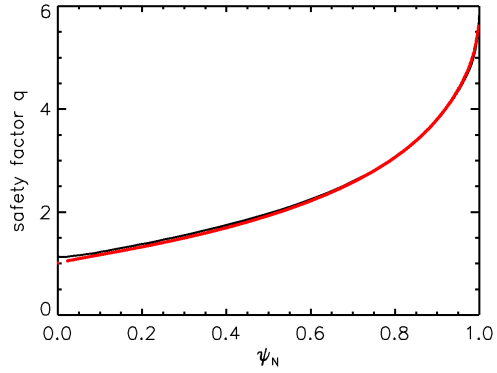


(c) *Safety factor q profile*

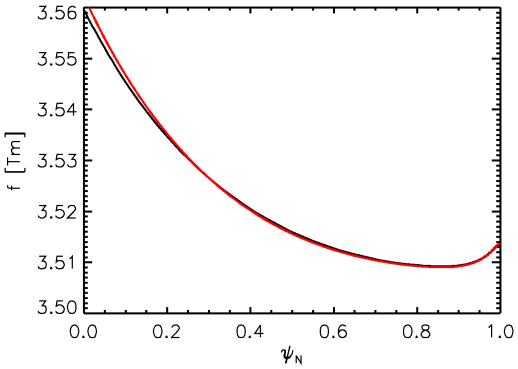


(d) *The flux function $f$ defined as a product of the toroidal magnetic field and the major radius $f \equiv B_\phi R$*

Figure 5.21.: *Comparison between non-up-down symmetric profiles in black (created with HELENA) versus up-down symmetric profiles in red (created with SCENE).*

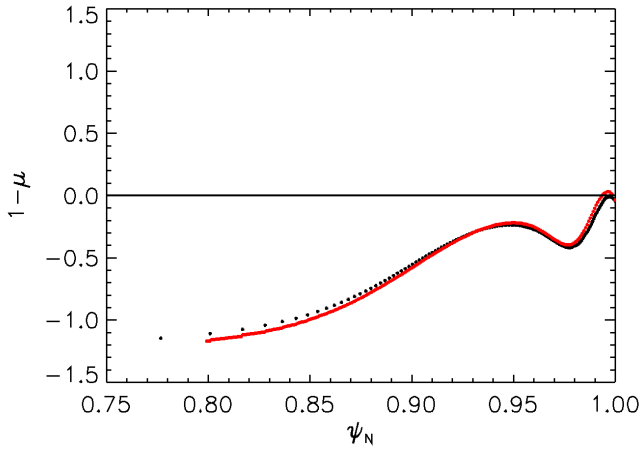


Figure 5.22.: *The ballooning eigenvalue vs the normalised flux surfaces. When $1-\mu$ is positive, the plasma is ballooning unstable which generates the initial linear drive.*

### 5.3.2. Results for the coefficients for JET-like equilibrium

For the up-down symmetric case we obtain the following coefficients:

$$C_1 \approx 0.38 \qquad C_4 \approx -0.0098$$
$$C_5 \approx 0.5 \qquad C_2 \approx -940$$
$$\mu \approx 0.975 \qquad \lambda \approx 1.08$$

We find that the JET-like equilibrium again has two negative nonlinear coefficients. Since we investigate Type II ELMs which are considered to be purely ballooning driven, we can conclude that these negative coefficients are not (only) caused by the missing kink drive. Furthermore we investigate how changing the density with either constant temperature or with constant pressure influences the nonlinear coefficients. Since the first case is similar to the change in the local pressure gradient we want to examine if it can also change the coefficients similar to the MAST case. The second case is to evaluate how the coefficient change with the same pressure gradient but with a modified bootstrap current. The original density at the magnetic axis is $n_e \approx 0.36 \times 10^{20}\mathrm{m}^{-3}$, see Fig. 5.21a. We change the density and and use SCENE to create a new equilibrium.

First, we increase the density with a constant temperature. The nonlinear drive coefficient increases and the quasilinear nonlinearity decreases with increasing density, see Figures 5.23 and 5.24. Note that the most unstable flux surface varies depending on the density. This change in the location of the most unstable flux surface also affects the coefficients.

Secondly, we change the density at a constant pressure. The nonlinear drive coefficient decreases and the quasilinear nonlinearity coefficient increases by increasing density, see Figures 5.25 and 5.26. There exists positive quasilinear nonlinearity coefficients for which the nonlinear ballooning model can describe the evolution of the filaments for longer. However, the change of the most unstable flux surface affects the quasilinear nonlinearity coefficient stronger than the change in density.

This study is limited by the equilibrium profile, see Fig. 5.22. When the density is increased further, the location of the $1-\mu$ maximum moves outwards ($\psi_N > 1$).

In the first case, shown in Fig. 5.23 and 5.24, the bootstrap current increases with increasing density and in the second case, presented in Fig. 5.25 and 5.26, the bootstrap current

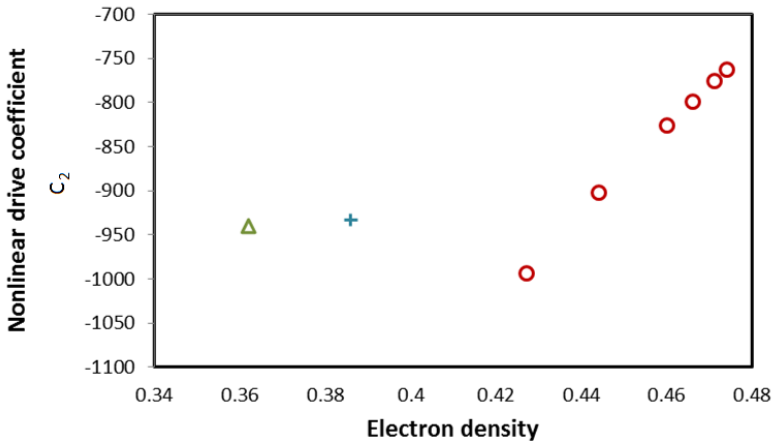


Figure 5.23.: *The nonlinear drive coefficient vs the electron density* $[10^{20}m^{-3}]$ *with constant temperature. The green* $\triangle$ *has its most unstable flux surface at* $\psi_N \approx 0.9958$*; the blue* $+$ *has its most unstable flux surfaces at* $\psi_N \approx 0.9966$ *and the red* $\circ$ *symbol indicates the most unstable flux surface at* $\psi_N \approx 0.99827$*.*

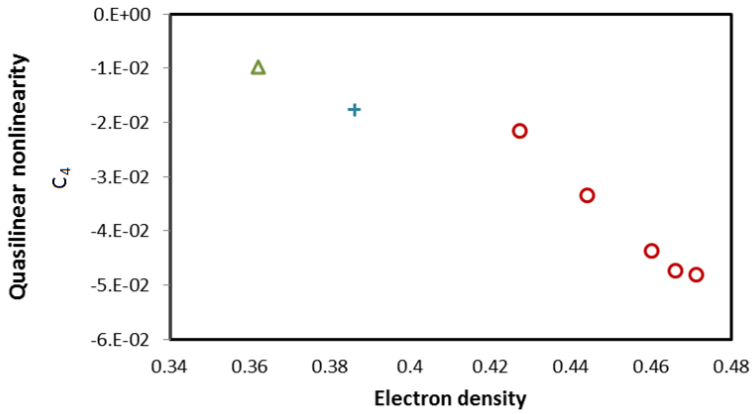


Figure 5.24.: *The quasilinear nonlinearity coefficient vs the electron density* $[10^{20}m^{-3}]$ *with constant temperature. The green* $\triangle$ *has its most unstable flux surface at* $\psi_N \approx 0.9958$*; the blue* $+$ *has its most unstable flux surfaces at* $\psi_N \approx 0.9966$ *and the red* $\circ$ *symbol indicates the most unstable flux surface at* $\psi_N \approx 0.99827$*.*

increases with decreasing density. Therefore we detect an increasing nonlinear drive coefficient with an increasing bootstrap current. This means the inwards drive of the nonlinear drive term reduces when the equilibrium is changed towards an equilibrium which is more likely to have Type I ELMs.

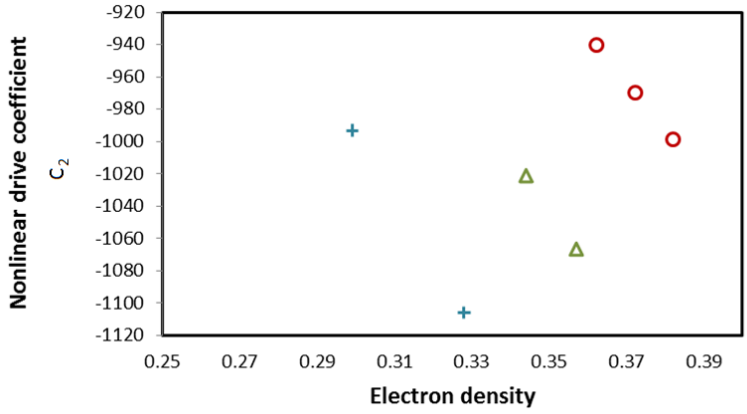


Figure 5.25.: *The nonlinear drive coefficient vs the electron density* $[10^{20}m^{-3}]$ *with constant pressure. The green* $\triangle$ *has its most unstable flux surface at* $\psi_N \approx 0.9966$*; the blue* $+$ *has its most unstable flux surfaces at* $\psi_N \approx 0.997$ *and the red* $\circ$ *symbol indicates the most unstable flux surface at* $\psi_N \approx 0.9958$*.*

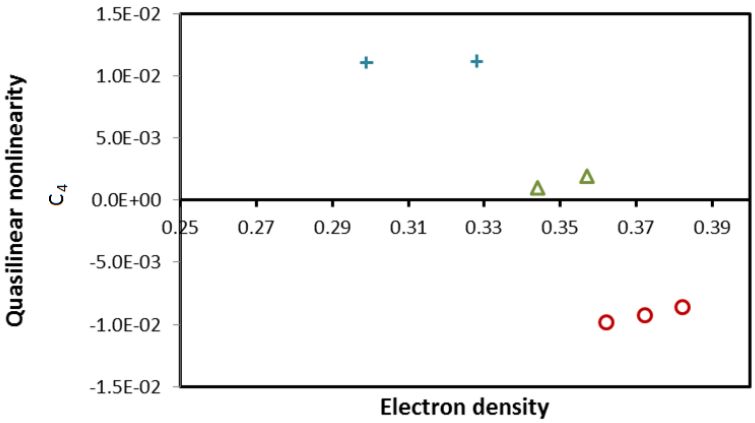


Figure 5.26.: *The quasilinear nonlinearity coefficient vs the electron density* $[10^{20}m^{-3}]$ *with constant pressure. The green* $\triangle$ *has its most unstable flux surface at* $\psi_N \approx 0.9966$*; the blue* $+$ *has its most unstable flux surfaces at* $\psi_N \approx 0.997$ *and the red* $\circ$ *symbol indicates the most unstable flux surface at* $\psi_N \approx 0.9958$*.*

## 5.4. Conclusion

We have presented the methods to calculate the coefficients of the nonlinear ballooning envelope equation and the results for these coefficients for Type I ELMs equilibria in MAST and for Type II ELMs equilibria in JET.

We described the method used to calculate slowly converging integrals for the $C_2$ coefficient in an efficient way. Additionally we confirmed that the methods for the calculation of coefficients were successfully implemented and worked as predicted.

We presented methods to compare simulations with experiments in two different ways:

visualisation of the filaments to compare filament width and growth rates and a semi-heuristic energy model to compare the energies released during ELMs. However, the current results suggest that the nonlinear ballooning model on its own cannot sufficiently describe Type I nor Type II ELMs in a quantitative manner.

# 6. Conclusion and future work

## 6.1. Conclusion

As ELMs are predicted to have detrimental effects on the plasma facing components in future tokamak devices, obtaining a deeper understanding of this type of instability would increase the feasibility of fusion energy produced by magnetically confined plasmas in tokamaks.

A promising candidate to describe ELMs quantitatively is the nonlinear ballooning model since its qualitative characterisation of explosive filaments are in agreement with experimental observations of ELMs. This model is derived from ideal MHD assuming close proximity to marginal stability, and consists of two differential equations to describe the evolution of the displacement: one differential equation describes the spatial distribution of the displacement along the field aligned variable and the second, two-dimensional, nonlinear equation describes the perpendicular evolution of the filaments and can involve fractional temporal-derivatives, but is often second-order in time and space. In a tokamak geometry the first differential equation is the linear second-order ballooning mode equation [56] and the second differential equation describing the perpendicular evolution is referred to as the nonlinear ballooning envelope equation in this thesis and was derived by Wilson and Cowley [2].

In this thesis two main questions regarding the description of ELMs with the explosive filaments characterised by the non-linear ballooning model are investigated:

- Does the nonlinear interaction of explosive multiple filaments influence their evolution?
- Can the nonlinear ballooning model describe Type I and II ELMs quantitatively?

The second topic is of special interest because the model, once derived, is quite simple to analyse because one only has to solve two differential equations. Additionally it is easy to modify this model to investigate the effects of other physical impacts, e.g., nonscalar viscosity, in a way similar to what we have done by addressing the first question investigated in the first part of this thesis. Therefore this model has the potential to increase our understanding of ELMs significantly.

In the first part of this thesis we have investigated the interaction of multiple explosive filaments with varying amplitudes in the linear and nonlinear regime by exploiting the nonlinear ballooning model in slab geometry with an added scalar viscosity. We presented the derivation of the ballooning model in the slab geometry with a mixed Lagrangian and Eulerian boundary conditions [71]. This set of boundary conditions allows the flow to pass through the boundaries and simplifies the differential equation describing the displacement along the field aligned variable. To implement filaments with different initial amplitudes we changed the initialisation in the code Deton8, which is exploited to solve the nonlinear ballooning envelope equation. Specifically, we adopted a superposition of the analytical solutions of the linear terms of the nonlinear ballooning envelope equation.

We have shown that the multiple filaments interact as soon as they enter the nonlinear regime, where we could demonstrate that the filaments which are able to enter the nonlinear regime first suppress the other, smaller filaments and additionally gain amplitude from the suppressed filaments. We have quantified this effect in two ways for a three filament system by comparing four different cases; by introducing the quantity $p_i$ which characterises the difference between the two-mode simulation and the two independent single mode simulations, and by taking the ratio of the superimposed simulation with the sum of two single mode simulations. With the latter method we could show in the superimposed case that 80% of the amplitude of the larger filament at the final time was due to the interaction with the smaller filaments.

We identified the non-linear suppression mechanisms to be the down-draft caused by the dominant central filament as it erupts pushing down plasma which suppresses the subdominant smaller filaments.

Our results are qualitatively consistent with Ref. [69], which investigated the evolution of

random small fluctuations. The filament with the biggest amplitude at the transition from the linear to nonlinear regime grows fastest and suppresses the other filaments, but the interactions were not quantified previously.

Although our results are derived from a simple slab plasma model, it has the same features as more complex magnetic geometries, including tokamaks [2, 3], because the form of the nonlinear ballooning envelope equation is the same as for certain tokamak geometries. We therefore believe the phenomenon of large filaments feeding off the smaller ones is a generic feature of MHD. To support our model we presented two examples of experimental observations (Type V ELMs in NSTX and ELMs in KSTAR) which show single dominant filaments where one would expect a higher mode number from linear theory. These effects could be potentially described by the methods shown in this thesis.

This theory is only valid in the early nonlinear stages of the evolution since it is derived assuming a slow time derivative. Hence it requires that the dominant filaments will have time to have formed before the model becomes invalid. It is therefore sensible to test these ideas in large scale simulations with less reduced models, close to marginal stability, e.g., with a reduced MHD model similar to [101].

In the second part of this thesis we have studied whether or not the nonlinear ballooning model can describe Type I ELMs in MAST and Type II ELMs in JET-like equilibria quantitatively. To this end, we have presented a method to calculate the required coefficients of the nonlinear ballooning envelope equation to accomplish the comparison between the model and experimental observations.

The coefficients of the nonlinear ballooning envelope equation are complicated, field line averaged equilibrium quantities and two of their integrands decay slowly. Therefore we presented a method to reduce the numerical domain of the field aligned variable by calculating the asymptotic form of the remaining integral analytically.

We examined whether the analytic description of the equilibrium quantities is appropriate by comparing the numerical with the analytical integrands and found that they were in agreement. Furthermore we successfully performed convergence tests on our code to examine if the method for the slowly converging integrals functions properly.

We determined the coefficients for a Type I ELMy H-mode MAST equilibrium where we

found both nonlinear coefficients to be negative. We showed that this implies that the filaments implode due to the negative nonlinear drive term and that the filaments do not radially broaden which more quickly causes the model to enter a regime where the model is invalid. By changing the local pressure gradient we obtained flux-surfaces with a positive nonlinear drive coefficient, i.e. exploding filaments. We presented methods to compare simulations with experiments in two different ways: visualisation of the filaments to compare filament width and growth rates and a semi-heuristic energy model to compare the energies released during ELMs.

Furthermore we investigated the coefficients for Type II ELMs in a JET-like equilibrium since we know that Type II ELMs are considered to be purely ballooning unstable and therefore could be captured more completely by the nonlinear ballooning model. We changed the equilibrium so that it is up-down-symmetric and obtained again two negative nonlinear coefficients.

In summary, we obtained imploding filaments for which the description by the nonlinear ballooning model breaks down faster than expected due to the second nonlinear coefficient, but by changing the equilibria we were able to invert the signs. Therefore the results for the ELM equilibria indicate that either the nonlinear ballooning model is not sufficient to describe the explosive nature of the filaments or that the coefficients themselves are too sensitive to the equilibria, since we can show that they can switch signs depending on the input parameters. Either way the current results suggest that the nonlinear ballooning model alone is insufficient to describe Type I or Type II ELMs quantitatively.

## 6.2. Future work

While the work presented in this thesis has shown that Type I and Type II ELMs cannot be described quantitatively with the nonlinear ballooning model, there are several other types of ELMs which are worthy of investigation with this model. Promising candidates for future research are Type V ELMs from NSTX and the ELMs in KSTAR which both show the interacting behaviour featured by the nonlinear ballooning model. Since they show characteristics which only the nonlinear terms could describe, it would be more likely that this model can capture their evolution quantitatively.

Another possible application would be to investigate the equilibria of the ballooning precursors of disruptions which were found in the Tokamak Fusion Test Reactor (TFTR) [125]. Since disruptions can be very detrimental to tokamaks and can limit the operating regimes, improving the understanding of disruptions is essential.

In addition to investigating more equilibria it would also be of interest to examine how the neglected non-up-down-symmetric term would change the behaviour of the filaments. For example we know that Type II ELMs can be reached in JET by creating a quasi-double null configuration [80]. This could be explained by turning the non-up-down-symmetric term on or off. Additionally one could investigate non-up-down symmetric equilibria in general.

Lastly, the interacting filaments could be investigated with full, large scale simulations near marginal stability, for example with BOUT++ [126]. This would address two purposes: First one could then compare how much the evolution differs due to the neglected terms in the analytic nonlinear ballooning model. This would help us to understand what effects the different terms have on the plasma behaviour. Second one could determine how the filaments behave, not only at the early evolution, but also throughout an entire ELM cycle.

# A. Common coordinate systems - useful relations

The following relations are derived here:

$$\frac{|\boldsymbol{e}_\perp|^2}{B_0^2} = \frac{1}{R^2\boldsymbol{B}_p^2}\left[1 + \frac{R^4\boldsymbol{B}_p^4}{B_0^2}\left(q'v + Y'\right)^2\right] \tag{A.1}$$

$$\boldsymbol{e}_\perp \cdot \boldsymbol{\kappa}_0 = \frac{B_0}{R^2\boldsymbol{B}_p^2}(\boldsymbol{\nabla}\psi\cdot\nabla)(p_0 + \frac{B_0^2}{2}) - \frac{I}{2JB_0}\frac{\partial B_0^2}{\partial\theta}\left(q'v + Y'\right) \tag{A.2}$$

$$\boldsymbol{e}_\perp \cdot \boldsymbol{\nabla} p_0 = Bp_0' \tag{A.3}$$

$$\frac{1}{B_0^4}\frac{\partial B_0^2}{\partial\theta} = -\frac{\partial}{\partial\theta}\left(\frac{1}{B_0^2}\right) \tag{A.4}$$

$$\left(\boldsymbol{e}_\phi\cdot\nabla\right)\boldsymbol{B} = -\frac{B_\phi}{R}\hat{R} + \frac{B_R}{R}\boldsymbol{e}_\phi \tag{A.5}$$

$$\left(\boldsymbol{e}_\phi\cdot\nabla\right)\boldsymbol{e}_\phi = -\frac{1}{R}\hat{R} \tag{A.6}$$

$$\left(\boldsymbol{B}\cdot\nabla\right)\left(\boldsymbol{e}_\phi R\right) = -B_\phi\hat{R} + B_R\boldsymbol{e}_\phi \tag{A.7}$$

$$\boldsymbol{B}_0\cdot\boldsymbol{\nabla}_0\boldsymbol{e}_\phi = -\frac{B_\phi}{R}\hat{R} \tag{A.8}$$

$$\boldsymbol{e}_\phi\cdot\boldsymbol{B}_0\cdot\boldsymbol{\nabla}_0\boldsymbol{\kappa}_0 = \frac{\kappa_R B_\phi}{R} \tag{A.9}$$

$$\boldsymbol{e}_\phi\boldsymbol{B}_0\cdot\boldsymbol{\nabla}_0 R = B_r\boldsymbol{e}_\phi \tag{A.10}$$

$$\frac{\boldsymbol{e}_\perp\cdot\boldsymbol{e}_\wedge}{B^2} = -\frac{R^2B_p^2}{B^2}\Lambda \tag{A.11}$$

$$\boldsymbol{B}_0\cdot\boldsymbol{\nabla}_0\sigma = -fp_0'\boldsymbol{B}_0\cdot\boldsymbol{\nabla}_0\left(\frac{1}{B^2}\right) \tag{A.12}$$

where $v = \chi - \chi_0$. The derivation of equation (A.4) is straight forward. To obtain expression (A.3) one can use $\boldsymbol{e}_\perp = \frac{B_0}{R^2B_p^2}\nabla\psi - \Lambda\boldsymbol{e}_\wedge$ and that $p_0$ only depends on the flux coordinate $\psi$.

Now we will derive Eq. (A.1). Using the Eq. (2.6) which is the representation of the operator $\nabla$ in the $\psi$-$\chi$-$\phi$ coordinate system and the expression for $\alpha$ (Eq. (2.10)) it follows that:

$$\nabla\alpha = v\nabla\chi - \nabla\phi + \nabla\psi\left[q'v + Y'\right] \tag{A.13}$$

where the primes denote derivatives with respect to $\psi$. Now we use the values for $|\nabla\chi| = \frac{1}{JB_p}$, $|\nabla\phi| = \frac{1}{R}$ and $|\nabla\psi| = RB_p$ (equations (2.7), (2.8), and (2.9)) to calculate the square of $\nabla\alpha$:

$$(\nabla\alpha)^2 = \frac{B_0^2}{R^2B_p^2} + R^2B_p^2\left[q'v + Y'\right]^2 \tag{A.14}$$

With Eq. (A.14) and Eq. (2.13) we obtain the Eq. (A.1).

Now Eq. (A.2) is derived. To derive it we use the representation of the magnetic field: $\boldsymbol{B}_0 = f\nabla\phi + \nabla\phi\times\nabla\psi$ (see Sect. 2.1.3). By using the definition of $\boldsymbol{e}_\perp = \frac{\nabla\alpha\times\boldsymbol{B}_0}{B_0}$ (Eq. (2.11)) and by using Eq. (A.13) we obtain:

$$\boldsymbol{e}_\perp = \frac{1}{B_0}\left[\left(\frac{f}{R^2}\frac{1}{R^2B_p^2} + \frac{1}{R^2}\right)\nabla\psi + A\,\nabla\phi - f\left(q'v + Y'\right)\boldsymbol{B}_0\right],$$

where we do not need to specify the quantity $A$ as we will multiply this equation with $\boldsymbol{\kappa}_0$. $\boldsymbol{\kappa}_0$ can be written as $\nabla(p_0 + \frac{B_0^2}{2})$ and we exploit that all derivatives with respect to $\phi$ of equilibrium quantities are equal to zero.

Using $\nabla\psi\times\nabla\phi = -JB_p^2\nabla\chi$ and $\nabla\chi\times\nabla\phi = \frac{1}{JR^2Bp^2}\nabla\psi$ we obtain:

$$\boldsymbol{e}_\perp\cdot\boldsymbol{k_0} = \frac{1}{B_0}\left[\frac{B_0^2}{R^2B_p^2}\left(\nabla\psi\cdot\nabla\right) - \frac{f}{J}\left(q'v + Y'\right)\left(\frac{\partial}{\partial\theta} + \frac{\partial}{\partial v}\right)\right]\left(p_0 + \frac{B_0^2}{2}\right)$$

Using $\left(\frac{\partial}{\partial\theta} + \frac{\partial}{\partial v}\right)(p_0 + \frac{B_0^2}{2}) = \frac{1}{2}\frac{\partial}{\partial\theta}B_0^2$ it follows Eq. (A.2). To derive the equations (A.5), (A.6), (A.7) and (A.8) we only need to use the material derivative in cylindrical coordinate

system:

$$\begin{aligned}\boldsymbol{A}\cdot\nabla\boldsymbol{B} = &\left(A_R\frac{\partial B_R}{\partial R}+\frac{A_\phi}{R}\frac{\partial B_R}{\partial\phi}+A_z\frac{\partial B_R}{\partial z}-\frac{A_\phi B_\phi}{R}\right)\hat{R}\\ &+\left(A_R\frac{\partial B_\phi}{\partial R}+\frac{A_\phi}{R}\frac{\partial B_\phi}{\partial\phi}+A_z\frac{\partial B_\phi}{\partial z}+\frac{A_\phi B_R}{R}\right)\boldsymbol{e}_\phi\\ &+\left(A_R\frac{\partial B_z}{\partial R}+\frac{A_\phi}{R}\frac{\partial B_z}{\partial\phi}+A_z\frac{\partial B_z}{\partial z}\right)\hat{z}\end{aligned}$$

To derive Eq. (A.9) we can exploit that $\boldsymbol{e}_\phi\cdot\boldsymbol{\kappa}_0=0$ because of symmetry and we can use Eq. (A.8):

$$\begin{aligned}\boldsymbol{e}_\phi\cdot\boldsymbol{B}_0\cdot\boldsymbol{\nabla}_0\boldsymbol{\kappa}_0 &= -\boldsymbol{\kappa}_0\cdot\boldsymbol{B}_0\cdot\boldsymbol{\nabla}_0\boldsymbol{e}_\phi\\ &= \frac{\nabla R}{R}\cdot\boldsymbol{\kappa}_0\\ &= \frac{\kappa_R}{R}\end{aligned}$$

To derive Eq. (A.10) we only need to exploit Eq.s (A.6) and (A.8). Using the relation $\boldsymbol{e}_\perp=\frac{B_0}{R^2B_p^2}\nabla\psi-\Lambda\boldsymbol{e}_\wedge$ and that $\boldsymbol{e}_\wedge$ is perpendicular to $\nabla\psi$ by definition we obtain Eq. (A.11). The last Eq. (A.12) can be derived by using $\sigma$'s definition (B.6): $\sigma=-\frac{fp_0'}{B_0^2}-f'$ and the fact that the quantities $f$ and $p_0$ only depend on the flux coordinate $\psi$.

# B. Components of linear operator $\mathcal{L}$

## B.1. Properties

It is useful to find relations for each component of the linear operator acting on each component. In this appendix we present the different expressions and the derivations of the expressions.

The linear operator acting on a perpendicular vector $\boldsymbol{W}_\perp$ (with only $\boldsymbol{e}_\perp$ and $\boldsymbol{e}_\wedge$ components) is defined as:

$$\mathcal{L}\left(\boldsymbol{W}_\perp\right) \equiv \boldsymbol{B}_0 \cdot \boldsymbol{\nabla}_0 \left[\boldsymbol{B}_0 \cdot \boldsymbol{\nabla}_0 \left(\boldsymbol{W}_\perp\right)\right] - \left(\boldsymbol{\nabla}_0 \boldsymbol{\kappa}_0\right) \cdot \boldsymbol{W}_\perp + \left[\boldsymbol{B_0}\left(\boldsymbol{B}_0 \cdot \boldsymbol{\nabla}_0\right) + 2\boldsymbol{\kappa}_0\right] \left[\frac{2}{B_0^2}\left(\boldsymbol{\kappa}_0 \cdot \boldsymbol{W}_\perp\right)\right] \tag{B.1}$$

One useful property of $\mathcal{L}$ is:

$$\boldsymbol{B}_0 \cdot \mathcal{L}\left(\boldsymbol{W}_\perp\right) = 0$$

Another useful property of the linear operator is that it is self-adjoint, [63]:

$$\langle \boldsymbol{A}_\perp \cdot \mathcal{L}(\boldsymbol{C}_\perp) \rangle = \langle \boldsymbol{C}_\perp \cdot \mathcal{L}(\boldsymbol{A}_\perp) \rangle$$

where $\boldsymbol{A}_\perp$ and $\boldsymbol{C}_\perp$ are perpendicular vectors and $\langle \cdots \rangle$ is defined as:

$$\langle \cdots \rangle \equiv \int_{-\infty}^{\infty} \cdots \frac{\mathrm{d}l}{B_0}$$

where $l$ measures the distance along the magnetic field line.

By expanding the linear operator of the basis vectors $\boldsymbol{e}_\perp$ and $\boldsymbol{e}_\wedge$ we obtain:

$$\frac{\boldsymbol{e}_\wedge}{B_0}\cdot\mathcal{L}\left(\frac{W}{B_0}\boldsymbol{e}_\wedge\right)=(\boldsymbol{B}_0\cdot\boldsymbol{\nabla}_0)\left[\frac{|\boldsymbol{e}_\wedge|^2}{B_0^2}(\boldsymbol{B}_0\cdot\boldsymbol{\nabla}_0)W\right] \tag{B.2}$$

$$\frac{\boldsymbol{e}_\perp}{B_0}\cdot\mathcal{L}\left(\frac{W}{B_0}\boldsymbol{e}_\perp\right)=(\boldsymbol{B}_0\cdot\boldsymbol{\nabla}_0)\left[\frac{|\boldsymbol{e}_\perp|^2}{B_0^2}(\boldsymbol{B}_0\cdot\boldsymbol{\nabla}_0)W\right]+\frac{2}{B_0^4}(\boldsymbol{e}_\perp\cdot\boldsymbol{\kappa}_0)(\boldsymbol{e}_\perp\cdot\boldsymbol{\nabla}_0 p_0)W \tag{B.3}$$

$$\frac{\boldsymbol{e}_\perp}{B_0}\cdot\mathcal{L}\left(\frac{W}{B_0}\boldsymbol{e}_\wedge\right)=(\boldsymbol{B}_0\cdot\boldsymbol{\nabla}_0)\left[\frac{(\boldsymbol{e}_\perp\cdot\boldsymbol{e}_\wedge)}{B_0^2}(\boldsymbol{B}_0\cdot\boldsymbol{\nabla}_0)W\right]-\sigma(\boldsymbol{B}_0\cdot\boldsymbol{\nabla}_0)W \tag{B.4}$$

$$\frac{\boldsymbol{e}_\wedge}{B_0}\cdot\mathcal{L}\left(\frac{W}{B_0}\boldsymbol{e}_\perp\right)=(\boldsymbol{B}_0\cdot\boldsymbol{\nabla}_0)\left[\frac{(\boldsymbol{e}_\perp\cdot\boldsymbol{e}_\wedge)}{B_0^2}(\boldsymbol{B}_0\cdot\boldsymbol{\nabla}_0)W+\sigma W\right] \tag{B.5}$$

where $\sigma$ is the parallel current given by:

$$\sigma=\frac{\boldsymbol{J}\cdot\boldsymbol{B_0}}{B_0^2}=-\frac{f\,p_0'}{B_0^2}-f' \tag{B.6}$$

## B.2. Description of derivations

Firstly, we derive some useful relations which simplify the derivation of the components of the linear operator.

#### Deriving relation for $\frac{\boldsymbol{e}_\wedge}{B_0}\cdot\mathcal{L}\left(\frac{W}{B_0}\boldsymbol{e}_\perp\right)$

The derivation of Eq. (B.5) is very similar to the one for (B.4). However, one more relation is needed to derive this equation:

$$\begin{aligned}\frac{2}{B_0^4}(\boldsymbol{e}_\wedge\cdot\boldsymbol{\kappa}_0)(\boldsymbol{e}_\perp\cdot\boldsymbol{\nabla}_0 p)&=-fp_0'(\boldsymbol{B}_0\cdot\boldsymbol{\nabla}_0)\left(\frac{1}{B_0^2}\right)\\&=(\boldsymbol{B}_0\cdot\boldsymbol{\nabla}_0)\sigma\end{aligned}$$

#### Deriving relation for $\nabla\cdot\boldsymbol{e}$

Deriving: $\nabla\cdot\boldsymbol{e}=-\frac{2}{B_0^2}(\boldsymbol{e}\cdot\boldsymbol{\kappa}_0)+\frac{1}{B_0^2}\boldsymbol{e}\cdot\nabla p_0$ where $\boldsymbol{e}=\frac{\boldsymbol{e}_\perp}{B_0}$ OR $\boldsymbol{e}=\frac{\boldsymbol{e}_\wedge}{B_0}$.

1st $\frac{\boldsymbol{e}_\perp}{B_0}$:

We use the definition of $\boldsymbol{e}_\perp$, Eq. (2.11):

$$\begin{aligned}\nabla\cdot\left(\frac{\boldsymbol{e}_\perp}{B_0}\right) &= \nabla\cdot\left(\frac{\nabla\alpha\times\boldsymbol{B}_0}{B_0^2}\right)\\ &= -\frac{\nabla\alpha\times\boldsymbol{B}_0}{B_0^4}\cdot\nabla B_0^2+\frac{1}{B_0^2}\nabla\cdot(\nabla\alpha\times\boldsymbol{B}_0)\\ &= -\frac{1}{B_0^3}\left(\boldsymbol{e}_\perp\cdot\nabla\right)B_0^2-\frac{1}{B_0^2}\boldsymbol{J}\cdot\nabla\alpha\end{aligned}\tag{B.7}$$

where the following vector identity $\nabla\cdot(\boldsymbol{A}\times\boldsymbol{B}_0)=\boldsymbol{B}_0\cdot(\nabla\times\boldsymbol{A})-\boldsymbol{A}\cdot(\nabla\times\boldsymbol{B}_0)$ was used twice. To get an expression for $\boldsymbol{J}$ we use the equilibrium relation Eq. (2.23):

$$\begin{aligned}\nabla p_0\times\nabla\alpha &= (\boldsymbol{J}\times\boldsymbol{B_0})\times\nabla\alpha\\ &= (\boldsymbol{J}\cdot\nabla\alpha)\,\boldsymbol{B_0}\\ \Rightarrow(\boldsymbol{J}\cdot\nabla\alpha)\,B_0^2 &= \nabla p_0\cdot(\nabla\alpha\times\boldsymbol{B_0})\\ &= B_0\boldsymbol{e}_\perp\cdot\nabla p_0\end{aligned}$$

Using this relation for $\boldsymbol{J}$ in equation (B.7) we obtain:

$$\begin{aligned}\nabla\cdot\left(\frac{\boldsymbol{e}_\perp}{B_0}\right) &= -\frac{1}{B_0^3}\boldsymbol{e}_\perp\cdot\nabla\left(p_0+B_0^2\right)\\ &= -\frac{2}{B_0^3}\boldsymbol{e}_\perp\cdot\boldsymbol{\kappa}_0+\frac{1}{B_0^3}\boldsymbol{e}_\perp\cdot\nabla p_0\end{aligned}$$

2nd $\frac{\boldsymbol{e}_\wedge}{B_0}$:

Here we use the definition for $\boldsymbol{e}_\wedge$ (Eq. (2.12)) and the same vector identity as above:

$$\begin{aligned}\nabla\cdot\left(\frac{\boldsymbol{e}_\wedge}{B_0}\right) &= \nabla\cdot\left(\frac{\boldsymbol{B}_0\times\nabla\psi}{B_0^2}\right)\\ &= -\frac{\boldsymbol{B}_0\times\nabla\psi}{B_0^4}\cdot\nabla B_0^2+\frac{1}{B_0^2}\nabla\cdot(\boldsymbol{B}_0\times\nabla\psi)\\ \nabla\cdot(\boldsymbol{B}_0\times\nabla\psi) &= \nabla\psi\cdot(\nabla\times\boldsymbol{B_0})-0\\ &= \nabla\psi\cdot J(\psi)\\ &= 0\\ \Rightarrow\nabla\cdot\left(\frac{\boldsymbol{e}_\wedge}{B_0}\right) &= -\frac{1}{B_0^3}\left(\boldsymbol{e}_\wedge\cdot\nabla\right)B_0^2\end{aligned}$$

To get the more general relation for $\nabla\cdot\boldsymbol{e}$ we must show that $\boldsymbol{e}_\wedge\cdot\nabla p_0=0$ by using

Eq. (2.12):

$$\begin{aligned} \boldsymbol{e}_{\wedge} \cdot \nabla p_0 &= \left(\boldsymbol{B_0} - R^2 B_0^2 \nabla\phi\right) \cdot \nabla p_0 \\ &= 0 \end{aligned}$$

Therefore it follows:

$$\nabla \cdot \boldsymbol{e} = -\frac{2}{B_0^2}\left(\boldsymbol{e} \cdot \boldsymbol{\kappa}_0\right) + \frac{1}{B_0^2}\boldsymbol{e} \cdot \nabla p_0 \tag{B.8}$$

**Deriving a relation for $(\boldsymbol{B}_0 \cdot \boldsymbol{\nabla}_0)\boldsymbol{e}$**

In this subsection the derivation of the following relation is described:

$$\left(\boldsymbol{B}_0 \cdot \boldsymbol{\nabla}_0\right)\boldsymbol{e} = -\boldsymbol{B}_0\left[\frac{2\boldsymbol{e} \cdot \boldsymbol{\kappa}_0}{B_0^2}\right] + \boldsymbol{B}_0\frac{\boldsymbol{e} \cdot \nabla p_0}{B_0^2} + \left(\frac{\boldsymbol{e}}{B_0} \cdot \boldsymbol{\nabla}_0\right)\boldsymbol{B}_0 \tag{B.9}$$

To derive this expression we only need to use the vector identity:

$$\nabla \times (A \times B) = A\left(\nabla \cdot B\right) - B\left(\nabla \cdot A\right) + \left(B \cdot \nabla\right)A - \left(A \cdot \nabla\right)B$$

where the third term on the right hand side is equivalent to the left hand side of Eq. (B.9):

$$\left(\boldsymbol{B}_0 \cdot \boldsymbol{\nabla}_0\right)\frac{\boldsymbol{e}}{B_0} = \nabla \times \left(\frac{\boldsymbol{e}}{B_0} \times \boldsymbol{B}_0\right) - \frac{\boldsymbol{e}}{B_0}(\boldsymbol{\nabla}_0 \cdot \boldsymbol{B}_0) + \boldsymbol{B}_0\left(\boldsymbol{\nabla}_0 \cdot \frac{\boldsymbol{e}}{B_0}\right) + \left(\frac{\boldsymbol{e}}{B_0} \cdot \boldsymbol{\nabla}_0\right)\boldsymbol{B}_0$$

Then we can use the fact that the divergence of the magnetic field is equal to zero: $\nabla \cdot \boldsymbol{B}_0 = 0$, which eliminates the second term on the right hand side. By using the identity $\boldsymbol{e}_{\wedge} = \frac{\boldsymbol{B}_0 \times \nabla\psi}{B_0}$ or $\boldsymbol{e}_{\perp} = \frac{\nabla\alpha \times \boldsymbol{B}_0}{B_0}$ and that $\nabla\psi$ or $\nabla\alpha$ is perpendicular to the magnetic field $\boldsymbol{B}_0 \cdot \nabla\psi = 0$, we can show that the first term on the right hand side is equal zero. By exploiting the expression (B.8) derived in the previous section we can transform the third term on the right hand side to $-2\boldsymbol{B}_0\frac{\boldsymbol{e}\cdot\boldsymbol{\kappa}_0}{B_0^2} + \boldsymbol{B}_0\frac{\boldsymbol{e}\cdot\nabla p_0}{B_0^2}$, which means we are left with the desired expression (B.9).

**Deriving relation for $\frac{\boldsymbol{e}_\wedge}{B_0} \cdot \mathcal{L}\left(\frac{W}{B_0}\boldsymbol{e}_\wedge\right)$ and $\frac{\boldsymbol{e}_\perp}{B_0} \cdot \mathcal{L}\left(\frac{W}{B_0}\boldsymbol{e}_\perp\right)$**

To derive the relation (B.2) and (B.3) we can use Eq. (B.9), $\boldsymbol{e} \cdot \boldsymbol{B}_0 = 0$ and the following relation, which can be easily shown:

$$\begin{aligned}(\boldsymbol{B}_0 \cdot \boldsymbol{\nabla}_0)\left[\left(\frac{\boldsymbol{e}}{B_0} \cdot \boldsymbol{\nabla}_0\right)\boldsymbol{B}_0\right] &= \left[(\boldsymbol{B}_0 \cdot \boldsymbol{\nabla}_0)\frac{\boldsymbol{e}}{B_0}\right] \cdot \boldsymbol{\nabla}_0 \boldsymbol{B}_0 + \left(\frac{\boldsymbol{e}}{B_0} \cdot \boldsymbol{\nabla}_0\right)\boldsymbol{\kappa}_0 \\ &\quad - \left[\left(\frac{\boldsymbol{e}}{B_0} \cdot \boldsymbol{\nabla}_0\right)\boldsymbol{B}_0\right] \cdot \boldsymbol{\nabla}_0 \boldsymbol{B}_0 \\ &= -2\boldsymbol{\kappa}_0 \frac{\boldsymbol{e} \cdot \boldsymbol{\kappa}_0}{B_0^2} + \boldsymbol{\kappa}_0 \frac{\boldsymbol{e} \cdot \boldsymbol{\nabla}_0 p_0}{B_0^2} + \left(\frac{\boldsymbol{e}}{B_0} \cdot \boldsymbol{\nabla}_0\right)\boldsymbol{\kappa}_0 \quad \text{(B.10)}\end{aligned}$$

**Deriving relation for $\frac{\boldsymbol{e}_\perp}{B_0} \cdot \mathcal{L}\left(\frac{W}{B_0}\boldsymbol{e}_\wedge\right)$**

To derive the relation (B.4) we can exploit Eq. (B.9), (B.10), $\boldsymbol{e}_\wedge = \frac{f}{B_0}\boldsymbol{B}_0 - R^2 B_0 \boldsymbol{\nabla}_0 \phi$ (Eq. (2.12)) , $\boldsymbol{e}_\perp = \frac{B_0}{R^2 B_p^2}\boldsymbol{\nabla}_0 \psi - \Lambda \boldsymbol{e}_\wedge$ (Eq. (2.11)) and $\boldsymbol{B}_0 = f\boldsymbol{\nabla}_0\phi + \boldsymbol{\nabla}_0\phi \times \boldsymbol{\nabla}_0\psi$ (Eq. (2.15)). Additionally we can use the following equations, which can be easily derived:

$$A \cdot (B \cdot \nabla)\boldsymbol{\kappa}_0 = B \cdot (A \cdot \nabla)\boldsymbol{\kappa}_0$$

$$\boldsymbol{\nabla}_0\psi \cdot (\boldsymbol{\nabla}_0\phi \cdot \boldsymbol{\nabla}_0)\boldsymbol{B}_0 = 0$$

$$\boldsymbol{\nabla}_0\phi \cdot (\boldsymbol{\nabla}_0\psi \cdot \boldsymbol{\nabla}_0)\boldsymbol{B}_0 = B_p^2 f'$$

# C. Derivation of the nonlinear ballooning model for tokamak geometries - Regions along the magnetic field line

## C.1. Nonlinear orders of the momentum equation in the nonlinear region

In this Appendix the more detailed steps of the third, fourth and fifth order of the derivation of the nonlinear ballooning equation are presented. Most of these steps follow the derivation of Hurricane et al. [3].

### C.1.1. Third order

In this section a more detailed discussion of deriving the terms of the third order of the nonlinear region is presented. Starting as in the previous order with the parallel component:

#### parallel component ($\epsilon^3$)

The equation for the parallel component looks identical to the previous order:

$$\boldsymbol{B}_0 \cdot \boldsymbol{\nabla}_0 \delta J^{(3)} = 0$$

Therefore $\delta J^{(3)}$ is also constant along the magnetic field line.

#### $\boldsymbol{e}_\wedge$-component ($\epsilon$)

This order for the $\boldsymbol{e}_\wedge$-component of the momentum equation takes the form:

$$\boldsymbol{e}_\wedge \cdot \boldsymbol{\nabla}_0 F^{(3)} = 0$$

which means that $F^{(3)}$ is constant along $\alpha$:

$$F^{(3)} = \overline{F^{(3)}}$$

#### $\boldsymbol{e}_\perp$-component ($\epsilon^2$)

This order has more terms than the previous orders:

$$-\boldsymbol{e}_\perp \cdot \boldsymbol{\nabla}_0 F^{(3)} + \boldsymbol{e}_\perp \cdot \left[\boldsymbol{B}_0 \cdot \boldsymbol{\nabla}_0 \left(\boldsymbol{B}_0 \cdot \boldsymbol{\nabla}_0 \boldsymbol{\xi}^{(2)}\right) - 2\delta J^{(2)} \boldsymbol{\kappa}_0\right] - \boldsymbol{\xi}^{(2)} \cdot \left(\boldsymbol{e}_\perp \cdot \boldsymbol{\nabla}_0\right) \boldsymbol{\kappa}_0 = \frac{2(1-\mu)}{B_0^2} \left(\boldsymbol{e}_\perp \cdot \boldsymbol{\kappa}_0\right) \left(\boldsymbol{e}_\perp \cdot \boldsymbol{\nabla}_0 p_0\right) \xi_\psi \quad \text{(C.1)}$$

The term on the right hand side has been added so that we can find solutions for $\boldsymbol{\xi}^{(2)}$ which satisfy the boundary conditions. Since we are close to marginal stability the ballooning eigenvalue $\mu$ is close to 1, therefore we can estimate $(1-\mu)$ to be of order $\epsilon^2$. By adding this term, we obtain an eigenvalue problem.
By averaging equation (C.1) with respect to $\alpha$ and using $\overline{\boldsymbol{\xi}^{(2)}} = 0$, $\overline{\delta J^{(2)}} = 0$ and $\overline{F^{(3)}} = F^{(3)}$ which we have shown previously, we obtain:

$$\left.\frac{\partial F^{(3)}}{\partial \psi}\right|_{\alpha,l} = 0$$

Integrating along $\psi$ and using the boundary conditions leads to $F^{(3)} = 0$ which is equivalent to

$$\left(\boldsymbol{B}_0 \cdot \boldsymbol{\nabla}_0\right) \xi_\parallel^{(3)} - \frac{2\boldsymbol{\xi}_\perp^{(3)} \cdot \boldsymbol{\kappa}_0}{B_0^2} = \left[\frac{\Gamma p_0 + B_0^2}{B_0^2}\right] \delta J^{(3)} \quad \text{(C.2)}$$

Using that $F^{(3)} = 0$ and equation (3.29) we can obtain:

$$\boldsymbol{e}_\perp \cdot \mathcal{L}(\boldsymbol{\xi}_\perp^{(2)}) = \frac{2(1-\mu)}{B_0^2} \left(\boldsymbol{e}_\perp \cdot \boldsymbol{\kappa}_0\right) \left(\boldsymbol{e}_\perp \cdot \boldsymbol{\nabla}_0 p_0\right) \xi_\psi^{(2)} - 2\Gamma \frac{p_0}{B_0^2} \left(\boldsymbol{\kappa}_0 \cdot \boldsymbol{e}_\perp\right) \delta J^{(2)}$$

with the linear operate $\mathcal{L}$ defined as in (B.1). By using expression (B.3) we obtain a second order differential equation for $B_0\xi_\psi^{(2)}$:

$$\boldsymbol{B}_0\cdot\boldsymbol{\nabla}_0\left[\frac{|\boldsymbol{e}_\perp|^2}{B_0^2}\boldsymbol{B}_0\cdot\boldsymbol{\nabla}_0\left(B_0\xi_\psi^{(2)}\right)\right]+\frac{2\mu}{B_0^3}\left(\boldsymbol{e}_\perp\cdot\boldsymbol{\kappa}_0\right)\left(\boldsymbol{e}_\perp\cdot\boldsymbol{\nabla}_0 p_0\right)\xi_\psi^{(2)}=-2\frac{\Gamma p_0}{B_0^3}\left(\boldsymbol{\kappa}_0\cdot\boldsymbol{e}_\perp\right)\delta J^{(2)}$$

By using equation (3.29) to replace $\frac{(\boldsymbol{e}_\perp\cdot\boldsymbol{\kappa}_0)\xi_\psi^{(2)}}{B_0^2}$ we obtain:

$$\begin{aligned}\mu\left(\boldsymbol{e}_\perp\cdot\boldsymbol{\nabla}_0 p_0\right)\left(\boldsymbol{B}_0\cdot\boldsymbol{\nabla}_0\right)\xi_\parallel^{(2)}+\boldsymbol{B}_0\cdot\boldsymbol{\nabla}_0\left[\frac{|\boldsymbol{e}_\perp|^2}{B_0^2}\boldsymbol{B}_0\cdot\boldsymbol{\nabla}_0\left(B_0\xi_\psi^{(2)}\right)\right]\\=\left[\frac{\Gamma p_0+B_0^2}{B_0^2}\mu\left(\boldsymbol{e}_\perp\cdot\boldsymbol{\nabla}_0 p_0\right)-2\frac{\Gamma p_0}{B_0^3}\boldsymbol{\kappa}_0\cdot\boldsymbol{e}_\perp\right]\delta J^{(2)}\end{aligned}\tag{C.3}$$

By integrating along the magnetic field line and using the fact that the displacement at this order must go to zero, we obtain that $\delta J^{(2)}=0$.

### C.1.2. Fourth order

The steps in the derivation of the fourth order in the nonlinear region are discussed here.

#### parallel coponent ($\epsilon^4$)

The fourth order, and also the last order used, of the parallel component has the following form:

$$\frac{\rho_0 B_0^2}{p_0\Gamma}\frac{\partial^2\xi_\parallel^{(2)}}{\partial t^2}=\left(\boldsymbol{B}_0\cdot\boldsymbol{\nabla}_0\right)\delta J^{(4)}$$

which means that $\delta J^{(4)}$ is not constant along the magnetic field lines.

#### $\epsilon^2$ of $\boldsymbol{e}_\wedge$-component

After some algebra we can show that this order takes the form:

$$\frac{\partial\hat{F}^{(4)}}{\partial\alpha}+\frac{\boldsymbol{e}_\wedge}{B_0}\cdot\mathcal{L}\left(\boldsymbol{\xi}_\perp^{(2)}\right)=0\tag{C.4}$$

where $\hat{F}^{(4)}$ is defined as:

$$\begin{aligned}\hat{F}^{(4)} &\equiv F(4) - \frac{1}{2}\boldsymbol{\xi}^{(2)} \cdot \left[ (\boldsymbol{B}_0 \cdot \boldsymbol{\nabla}_0)(\boldsymbol{B}_0 \cdot \boldsymbol{\nabla}_0)\boldsymbol{\xi}^{(2)} \right] \\ &= \left(\Gamma p_0 + B_0^2\right)\delta J^{(4)} + \frac{1}{2}\left[ \boldsymbol{\xi}^{(2)} \cdot (\boldsymbol{B}_0 \cdot \boldsymbol{\nabla}_0)(\boldsymbol{B}_0 \cdot \boldsymbol{\nabla}_0)\boldsymbol{\xi}^{(2)} - |(\boldsymbol{B}_0 \cdot \boldsymbol{\nabla}_0)\boldsymbol{\xi}^{(2)}|^2 \right] \\ &- \boldsymbol{B}_0 (\boldsymbol{B}_0 \cdot \boldsymbol{\nabla}_0)\boldsymbol{\xi}^{(4)} + \boldsymbol{\kappa}_0 \cdot \boldsymbol{\xi}^{(4)}\end{aligned}$$

To obtain equation (C.4) it is useful to exploit the following relation which can be derived with some straightforward algebra:

$$\boldsymbol{e} \cdot (\boldsymbol{B}_0 \cdot \boldsymbol{\nabla}_0)(\boldsymbol{B}_0 \cdot \boldsymbol{\nabla}_0)\boldsymbol{\xi}_\parallel - \boldsymbol{\xi}_\parallel \cdot (\boldsymbol{e} \cdot \boldsymbol{\nabla}_0)\boldsymbol{\kappa}_0 = 2\boldsymbol{e} \cdot \boldsymbol{\kappa}_0 (\boldsymbol{B}_0 \cdot \boldsymbol{\nabla}_0)\xi_\parallel$$

where $\boldsymbol{e}$ can be either $\boldsymbol{e}_\perp$ or $\boldsymbol{e}_\wedge$ and $\boldsymbol{\xi}_\parallel = \xi_\parallel \boldsymbol{B}_0$. This relation is valid for each order of $\boldsymbol{\xi}_\parallel$. By using equation (3.29) and $\delta J^{(2)} = 0$ we obtain for the second order:

$$\boldsymbol{e} \cdot (\boldsymbol{B}_0 \cdot \boldsymbol{\nabla}_0)(\boldsymbol{B}_0 \cdot \boldsymbol{\nabla}_0)\boldsymbol{\xi}_\parallel - \boldsymbol{\xi}_\parallel \cdot (\boldsymbol{e} \cdot \boldsymbol{\nabla}_0)\boldsymbol{\kappa}_0 = 4\frac{\xi_\psi^{(2)} \boldsymbol{e}_\perp \cdot \boldsymbol{\kappa}_0}{B_0^2}\, \boldsymbol{e} \cdot \boldsymbol{\kappa}_0 \tag{C.5}$$

The other important relation which was used is:

$$\frac{\partial \boldsymbol{\xi}^{(2)}}{\partial x} \mathrm{A}\, \boldsymbol{\xi}^{(2)} = \frac{1}{2}\frac{\partial}{\partial x}\left[ \boldsymbol{\xi}^{(2)} \mathrm{A}\, \boldsymbol{\xi}^{(2)} \right] + HOT \tag{C.6}$$

where $HOT$ stands for "higher order terms", $x$ for either $\alpha$ or $\psi$ and A for a linear, equilibrium dependent operator. To derive this equation we can exploit the separation of $\boldsymbol{\xi}^{(2)} = \hat{\xi}(\alpha, \psi, t)\boldsymbol{H}(\alpha, l)$. The higher order terms which are neglected must be retained at the appropriate higher order. However, in this current case these terms are of order $\epsilon^4$ and therefore smaller than we are going to evaluate.

To determine an expression for $\boldsymbol{B}_0 \cdot \boldsymbol{\nabla}_0 \xi_\parallel^{(4)}$ we can integrate equation (C.4) with respect to $\alpha$ where a constant $\overline{\hat{F}^{(4)}}$ appears:

$$\boldsymbol{B}_0 \cdot \boldsymbol{\nabla}_0 \xi_\parallel^{(4)} - \frac{2\boldsymbol{\kappa}_0 \cdot \boldsymbol{\xi}_\perp^{(4)}}{B_0^2} = (\Gamma\beta + 1)\,\delta J^{(4)} + \frac{Q}{B_0^2}\hat{\xi}^2 + \frac{u}{B_0^3}\boldsymbol{e}_\wedge \mathcal{L}(\boldsymbol{H}_\perp) - \overline{\hat{F}^{(4)}} \tag{C.7}$$

where

$$Q \equiv \frac{1}{2}\left[\boldsymbol{H}\left(\boldsymbol{B}_0\cdot\boldsymbol{\nabla}_0\right)\left(\boldsymbol{B}_0\cdot\boldsymbol{\nabla}_0\right)\boldsymbol{H}-\left|\left(\boldsymbol{B}_0\cdot\boldsymbol{\nabla}_0\right)\boldsymbol{H}\right|^2\right]$$

#### $\epsilon^3$ of $\boldsymbol{e}_\perp$-component

By using equation (C.6), (C.5) and (C.2) we obtain:

$$\frac{\partial\hat{F}^{(4)}}{\partial\psi}+\frac{\boldsymbol{e}_\perp}{B_0}\cdot\mathcal{L}\left(\boldsymbol{\xi}_\perp^{(3)}\right)+\frac{2}{B_0}\boldsymbol{e}_\perp\cdot\boldsymbol{\kappa}_0\Gamma\beta\delta J^{(3)}=0$$

where $\beta\equiv\frac{2\mu_0 p_0}{B_0^2}$. We again neglect higher order terms by using equation (C.6). These are of order $\epsilon^4$ which is a relevant order for the $\boldsymbol{e}_\perp$-component. The neglected terms are:

$$B_0\hat{\xi}^2\frac{\partial\boldsymbol{H}}{\partial\alpha}\left[\left(\boldsymbol{B}_0\cdot\boldsymbol{\nabla}_0\right)\left(\boldsymbol{B}_0\cdot\boldsymbol{\nabla}_0\right)\boldsymbol{H}\right]-B_0\frac{\hat{\xi}^2}{2}\frac{\partial}{\partial\alpha}\left[\boldsymbol{H}\left(\boldsymbol{B}_0\cdot\boldsymbol{\nabla}_0\right)\left(\boldsymbol{B}_0\cdot\boldsymbol{\nabla}_0\right)\boldsymbol{H}\right]$$

These terms must be carried into the fifth order.

To evaluate the results from the two perpendicular components and to eliminate the $\hat{F}^{(4)}$, we can differentiate the $\boldsymbol{e}_\wedge$-component with respect to $\psi$ and subtract the $\alpha$-derivative of the $\boldsymbol{e}_\perp$-component, which leads to:

$$\frac{\partial}{\partial\psi}\left[\frac{\boldsymbol{e}_\wedge}{B_0}\cdot\mathcal{L}\left(\boldsymbol{\xi}_\perp^{(2)}\right)\right]-\frac{\partial}{\partial\alpha}\left[\frac{\boldsymbol{e}_\perp}{B_0}\cdot\mathcal{L}\left(\boldsymbol{\xi}_\perp^{(3)}\right)\right]-\frac{\partial}{\partial\alpha}\left[\frac{2}{B_0}\boldsymbol{e}_\perp\cdot\boldsymbol{\kappa}_0\Gamma\beta\delta J^{(3)}\right]=0$$

Consider that the first term can be written in the form:

$$\frac{\partial}{\partial\psi}\left[\hat{\xi}\frac{\boldsymbol{e}_\wedge}{B_0}\cdot\mathcal{L}\left(\boldsymbol{H}_\perp\right)\right]=\underbrace{\frac{\partial\hat{\xi}}{\partial\psi}\frac{\boldsymbol{e}_\wedge}{B_0}\cdot\mathcal{L}\left(\boldsymbol{H}_\perp\right)}_{\sim\epsilon}+\underbrace{\hat{\xi}\frac{\partial}{\partial\psi}\left[\frac{\boldsymbol{e}_\wedge}{B_0}\cdot\mathcal{L}\left(\boldsymbol{H}_\perp\right)\right]}_{\sim\epsilon^2}$$

Note that the second term on the right hand side is of a higher order and therefore can be neglected here but must be added at the higher order. Therefore:

$$\frac{\partial\hat{\xi}}{\partial\psi}\frac{\boldsymbol{e}_\wedge}{B_0}\cdot\mathcal{L}\left(\boldsymbol{H}_\perp\right)=\frac{\partial}{\partial\alpha}\left[\frac{\boldsymbol{e}_\perp}{B_0}\cdot\mathcal{L}\left(\boldsymbol{\xi}_\perp^{(3)}\right)\right]+\frac{\partial}{\partial\alpha}\left[\frac{2}{B_0}\boldsymbol{e}_\perp\cdot\boldsymbol{\kappa}_0\Gamma\beta\delta J^{(3)}\right]\tag{C.8}$$

By integrating along the magnetic field line up to the matching region, which is indicated by angled brackets $\langle \cdots \rangle$, and by differentiating with respect to $\alpha$ we can obtain:

$$\frac{\partial}{\partial \alpha} \left\langle \frac{2}{B_0^2} \boldsymbol{\xi}_\perp^{(3)} \cdot \boldsymbol{\kappa}_0 p_0' \right\rangle + \left\langle \frac{2\Gamma p_0}{B_0^3} \left( \boldsymbol{\kappa}_0 \cdot \boldsymbol{e}_\perp \right) \right\rangle \frac{\partial \delta J^{(3)}}{\partial \alpha} = 0$$

where the term $\delta J^{(3)} \frac{\partial}{\partial \alpha} \left\langle \frac{2\Gamma p_0}{B_0^3} \left( \boldsymbol{\kappa}_0 \cdot \boldsymbol{e}_\perp \right) \right\rangle$ is neglected. We can obtain a similar equation by using equation (C.2) and integrating along the field line, multiplying by $p_0'$:

$$\left\langle \frac{2}{B_0^2} \boldsymbol{\xi}_\perp^{(3)} \cdot \boldsymbol{\kappa}_0 p_0' \right\rangle + \left\langle p_0' + p_0' \Gamma \beta \right\rangle \delta J^{(3)} = 0$$

By comparing the last two equations it follows that:

$$\frac{\partial \delta J^{(3)}}{\partial \alpha} = 0$$

We can exploit this result in equation (C.8) to obtain an equation to determine $\boldsymbol{\xi}^{(3)}$:

$$\frac{\partial \hat{\xi}}{\partial \psi} \frac{\boldsymbol{e}_\wedge}{B_0} \cdot \mathcal{L} \left( \boldsymbol{H}_\perp \right) = \frac{\partial}{\partial \alpha} \left[ \frac{\boldsymbol{e}_\perp}{B_0} \cdot \mathcal{L} \left( \boldsymbol{\xi}_\perp^{(3)} \right) \right] \tag{C.9}$$

We use the ansatz $\boldsymbol{\xi}_\perp^{(3)} = \frac{\partial u}{\partial \psi} \boldsymbol{H}_\perp^{(3)} + \overline{\boldsymbol{\xi}_\perp^{(3)}}$ and neglecting higher order terms again. Note that these are not relevant for the next order since they appear to be two orders higher. We obtain:

$$\frac{\partial \hat{\xi}}{\partial \psi} \frac{\boldsymbol{e}_\wedge}{B_0} \cdot \mathcal{L} \left( \boldsymbol{H}_\perp \right) = \frac{\boldsymbol{e}_\perp}{B_0} \cdot \mathcal{L} \left( \frac{\partial^2 u}{\partial \psi \partial \alpha} \boldsymbol{H}_\perp^{(3)} \right)$$

where $\hat{\xi} = \frac{\partial u}{\partial \alpha}$ and $\boldsymbol{H}_\perp = \frac{X}{B_0} \boldsymbol{e}_\perp$:

$$\frac{\boldsymbol{e}_\wedge}{B_0} \cdot \mathcal{L} \left( \frac{X}{B_0} \boldsymbol{e}_\perp \right) = \frac{\boldsymbol{e}_\perp}{B_0} \cdot \mathcal{L} \left( \boldsymbol{H}_\perp^{(3)} \right)$$

By using the results from the first order (3.25) we can derive the $\boldsymbol{e}_\wedge$-component of $\boldsymbol{\xi}_\perp^{(3)}$:

$$\boldsymbol{H}_\perp^{(3)} = H^{(3)} \boldsymbol{e}_\perp - \frac{X}{B_0} \boldsymbol{e}_\wedge$$

To investigate the third order of the displacement we can exploit the fact that the equilibrium is invariant under the transformation: $\alpha \to \alpha + f(\psi)$ since the magnetic field is

given by $\boldsymbol{B}_0 = \nabla\psi \times \nabla\alpha$. However, $\boldsymbol{e}_\perp$,$\mu$ and $X$ depend on the choice of $f$ where we can show that $\frac{d\boldsymbol{e}_\perp}{df'} = -\boldsymbol{e}_\wedge$ where $f'$ is given by $f' = \frac{\partial f}{\partial \psi}$. Starting with the linear ballooning equation (3.31) and differentiate it with respect to $f'$ we obtain:

$$-\boldsymbol{e}_\wedge \cdot \mathcal{L}(\boldsymbol{\xi}_\perp^{(2)}) + \boldsymbol{e}_\perp \cdot \mathcal{L}\left(\frac{1}{B_0}\frac{\partial}{\partial f'}\left[X\boldsymbol{e}_\perp\right]\right) = -\frac{2}{B_0^2}\frac{\partial \mu}{\partial f'}\left(\boldsymbol{e}_\perp \cdot \boldsymbol{\kappa}_0\right)\left(\boldsymbol{e}_\perp \cdot \boldsymbol{\nabla}_0 p_0\right)\xi_\psi^{(2)}$$

Note that terms with $(1-\mu)$ are of a higher order and therefore can be neglected. By combining the last three equations we can obtain:

$$\frac{\boldsymbol{e}_\perp}{B_0}\mathcal{L}\left(\left(H^{(3)} - \frac{\partial X}{\partial f'}\right)\boldsymbol{e}_\perp\right) = -\frac{2}{B_0^2}\frac{\partial \mu}{\partial f'}\left(\boldsymbol{e}_\perp \cdot \boldsymbol{\kappa}_0\right)\left(\boldsymbol{e}_\perp \cdot \boldsymbol{\nabla}_0 p_0\right)\xi_\psi^{(2)}$$

By integrating along the magnetic field line we can show that

$$\frac{\partial \mu}{\partial f'} \approx 0$$

Therefore we must calculate $\mu$ for each flux surface to find the most unstable surface on which to apply the model presented in this thesis. Since $\frac{\partial \mu}{\partial f'} \approx 0$, $\boldsymbol{\xi}_\perp^{(3)}$ is:

$$\boldsymbol{\xi}_\perp^{(3)} = \frac{1}{B_0}\frac{\partial u}{\partial \psi}\frac{\partial\left(X\boldsymbol{e}_\perp\right)}{\partial f'} + \overline{\boldsymbol{\xi}_\perp^{(3)}}$$

To determine the $\alpha$-independent part of $\boldsymbol{\xi}_\perp^{(3)}$ (second term on the right hand side) we can examine the fact that $\delta J^{(2)} = 0$:

$$\begin{aligned}\delta J^{(2)} = {} & B_0\left(\frac{\partial \xi_\psi^{(3)}}{\partial \psi} + \frac{\partial \xi_\wedge^{(4)}}{\partial \alpha}\right) + \left(\boldsymbol{B}_0 \cdot \boldsymbol{\nabla}_0\right)\xi_\parallel^{(2)} + \hat{\xi}\boldsymbol{\nabla}_0 \cdot \left(\frac{X}{B_0}\boldsymbol{e}_\perp\right) \\ & - B_0^2\left(\frac{\partial \xi_\psi^{(2)}}{\partial \alpha}\frac{\partial \xi_\wedge^{(3)}}{\partial \psi} - \frac{\partial \xi_\psi^{(2)}}{\partial \psi}\frac{\partial \xi_\wedge^{(3)}}{\partial \alpha}\right) - \frac{1}{2}\left[\left(\boldsymbol{H} \cdot \boldsymbol{\nabla}_0\right)\boldsymbol{H}\right] \cdot \nabla\alpha\frac{\partial \hat{\xi}^2}{\partial \alpha}\end{aligned}$$

which can be shown by evaluating equation (2.20). Averaging over $\alpha$ and using that $\overline{\xi_\parallel^{(2)}} = 0$ and $\overline{\xi_\psi^{(2)}} = 0$ leads to the final results of this order:

$$\overline{\boldsymbol{\xi}_\perp^{(3)}} = \frac{B_0}{2}\frac{\partial \overline{\left(\xi_\psi^{(2)}\right)^2}}{\partial \psi}$$

### C.1.3. Fifth order

The derivation of the final order is presented in this section. Only the perpendicular components are needed here.

#### $\epsilon^3$ of $\boldsymbol{e}_\wedge$-component

The $\boldsymbol{e}_\wedge$ component at this order has the following form:

$$\begin{aligned} 0 = B_0 \frac{\partial}{\partial \alpha} \hat{F}^{(5)} + \left[ \left( \boldsymbol{e}_\wedge \cdot \boldsymbol{\nabla}_0 \right) \boldsymbol{\xi}^{(2)} \right] \left[ -2\delta J^{(3)} \boldsymbol{\kappa}_0 + \boldsymbol{B}_0 \cdot \boldsymbol{\nabla}_0 \boldsymbol{B}_0 \cdot \boldsymbol{\nabla}_0 \boldsymbol{\xi}^{(3)} \right] \\ + \left[ \left( \boldsymbol{e}_\wedge \cdot \boldsymbol{\nabla}_0 \right) \boldsymbol{\xi}^{(3)} \right] \left[ \boldsymbol{B}_0 \cdot \boldsymbol{\nabla}_0 \boldsymbol{B}_0 \cdot \boldsymbol{\nabla}_0 \boldsymbol{\xi}^{(2)} \right] + \boldsymbol{e}_\wedge \cdot \mathcal{L} \left( \boldsymbol{\xi}_\perp^{(3)} \right) + 2 \left( \boldsymbol{e}_\wedge \cdot \boldsymbol{\kappa}_0 \right) \Gamma \beta \delta J^{(3)} \end{aligned} \tag{C.10}$$

where $\hat{F}^{(5)}$ is defined as:

$$\hat{F}^{(5)} \equiv F^{(5)} + \delta J^{(3)} \boldsymbol{\xi}^{(2)} \cdot \boldsymbol{\kappa}_0 + \boldsymbol{\xi}^{(2)} \boldsymbol{B}_0 \cdot \boldsymbol{\nabla}_0 \delta J^{(3)} \boldsymbol{B}_0 - \boldsymbol{\xi}^{(2)} \boldsymbol{B}_0 \cdot \boldsymbol{\nabla}_0 \boldsymbol{B}_0 \cdot \boldsymbol{\nabla}_0 \boldsymbol{\xi}^{(3)} + \boldsymbol{\xi}^{(3)} \boldsymbol{B}_0 \cdot \boldsymbol{\nabla}_0 \boldsymbol{B}_0 \cdot \boldsymbol{\nabla}_0 \boldsymbol{\xi}^{(2)}$$

From equation (C.10) we can derive a relation between $\boldsymbol{\xi}_\perp^{(3)}$, $\delta J^{(3)}$, $\hat{\xi}$ and $X$ which must be satisfied. To derive this relation we must take the integral with respect to the fast varying part of $\alpha$, which eliminates the $F^{(5)}$ term:

$$\begin{aligned} \frac{\boldsymbol{e}_\wedge}{B_0} \cdot \mathcal{L} \left( \overline{\boldsymbol{\xi}_\perp^{(3)}} \right) + \overline{\left[ \frac{\partial}{\partial \alpha} \boldsymbol{\xi}^{(2)} \right] \left[ \mathcal{L} \left( \boldsymbol{\xi}_\perp^{(3)} \right) + \left( \boldsymbol{\nabla}_0 \boldsymbol{\kappa}_0 \right) \boldsymbol{\xi}^{(3)} \right]} + \overline{\left[ \frac{\partial}{\partial \alpha} \boldsymbol{\xi}^{(3)} \right] \left[ \mathcal{L} \left( \boldsymbol{\xi}_\perp^{(2)} \right) + \left( \boldsymbol{\nabla}_0 \boldsymbol{\kappa}_0 \right) \boldsymbol{\xi}^{(2)} \right]} \\ + \frac{2 \boldsymbol{e}_\wedge \cdot \boldsymbol{\kappa}_0}{B_0} \Gamma \beta \delta J^{(3)} = 0 \end{aligned}$$

where we have used that $\delta J^{(3)}$ is independent of $l$ and where the overbar is defined by Eq. (3.27). We can combine the second parts of the second and third terms:

$$\frac{\partial \boldsymbol{\xi}^{(2)}}{\partial \alpha} \left[ \left( \boldsymbol{\nabla}_0 \boldsymbol{\kappa}_0 \right) \boldsymbol{\xi}^{(3)} \right] + \frac{\partial \boldsymbol{\xi}^{(3)}}{\partial \alpha} \left[ \left( \boldsymbol{\nabla}_0 \boldsymbol{\kappa}_0 \right) \boldsymbol{\xi}^{(2)} \right] = \frac{\partial}{\partial \alpha} \left( \boldsymbol{\xi}^{(2)} \left( \boldsymbol{\nabla}_0 \boldsymbol{\kappa}_0 \right) \boldsymbol{\xi}^{(3)} \right)$$

The $\alpha$ average of the combination is zero, which leads to:

$$\frac{\boldsymbol{e}_\wedge}{B_0} \cdot \mathcal{L} \left( \overline{\boldsymbol{\xi}_\perp^{(3)}} \right) + \overline{\left( \frac{\partial}{\partial \alpha} \boldsymbol{\xi}^{(2)} \right) \mathcal{L} \left( \boldsymbol{\xi}_\perp^{(3)} \right)} + \overline{\left( \frac{\partial}{\partial \alpha} \boldsymbol{\xi}^{(3)} \right) \mathcal{L} \left( \boldsymbol{\xi}_\perp^{(2)} \right)} + \frac{2 \boldsymbol{e}_\wedge \cdot \boldsymbol{\kappa}_0}{B_0} \Gamma \beta \delta J^{(3)} = 0$$

By exploiting equations (3.25), (C.9) and (3.31) we obtain:

$$\frac{\boldsymbol{e}_\wedge}{B_0}\cdot\mathcal{L}\left(\overline{\boldsymbol{\xi}_\perp^{(3)}}\right)=\frac{X}{B_0}\frac{\partial\overline{\hat{\xi}^2}}{\partial\psi}\boldsymbol{e}_\wedge\cdot\mathcal{L}\left(\boldsymbol{H}_\perp\right)-2\frac{\boldsymbol{e}_\wedge\cdot\boldsymbol{\kappa}_0}{B_0}\Gamma\beta\delta J^{(3)}$$

We can simplify this equation by introducing a shifted displacement defined as:

$$\boldsymbol{Z}^{(3)}=\boldsymbol{\xi}_\perp^{(3)}+\frac{\Gamma p_0}{p_0' B_0}\delta J^{(3)}\boldsymbol{e}_\perp$$

which leads to:

$$\frac{\boldsymbol{e}_\wedge}{B_0}\cdot\mathcal{L}\left(\overline{\boldsymbol{Z}_\perp^{(3)}}\right)=\frac{X}{B_0}\frac{\partial\overline{\hat{\xi}^2}}{\partial\psi}\boldsymbol{e}_\wedge\cdot\mathcal{L}\left(\boldsymbol{H}_\perp\right)$$

#### $\epsilon^4$ of $\boldsymbol{e}_\perp$-component

The $\boldsymbol{e}_\perp$ component of order $\epsilon^4$ is:

$$\begin{aligned}\rho_0|\boldsymbol{e}_\perp|^2\frac{\partial^2\xi_\psi}{\partial t^2}=&B_0\frac{\partial\hat{F}^{(5)}}{\partial\psi}-\frac{\boldsymbol{e}_\psi\cdot\boldsymbol{B}_0}{B_0^2}\boldsymbol{B}_0\cdot\boldsymbol{\nabla}_0\hat{F}^{(4)}\\&+\left[\left(\boldsymbol{e}_\wedge\cdot\boldsymbol{\nabla}_0\right)\boldsymbol{\xi}^{(2)}\right]\left[-2\delta J^{(3)}\boldsymbol{\kappa}_0+\boldsymbol{B}_0\cdot\boldsymbol{\nabla}_0\boldsymbol{B}_0\cdot\boldsymbol{\nabla}_0\boldsymbol{\xi}^{(3)}\right]\\&+\left[\left(\boldsymbol{e}_\wedge\cdot\boldsymbol{\nabla}_0\right)\boldsymbol{\xi}^{(3)}\right]\left[\boldsymbol{B}_0\cdot\boldsymbol{\nabla}_0\boldsymbol{B}_0\cdot\boldsymbol{\nabla}_0\boldsymbol{\xi}^{(2)}\right]-2\delta J^{(4)}\boldsymbol{e}_\perp\cdot\boldsymbol{\kappa}_0+\boldsymbol{e}_\perp\cdot\mathcal{L}\left(\boldsymbol{\xi}_\perp^{(4)}\right)\\&+2\boldsymbol{e}_\perp\cdot\boldsymbol{\kappa}_0\left[\boldsymbol{B}_0\cdot\boldsymbol{\nabla}_0\xi_\parallel^{(4)}-\frac{2}{B_0^2}\boldsymbol{\kappa}_0\cdot\boldsymbol{\xi}_\perp^{(4)}\right]-\delta J^{(3)}\boldsymbol{e}_\perp\left(\boldsymbol{B}_0\cdot\boldsymbol{\nabla}_0\right)\left(\boldsymbol{B}_0\cdot\boldsymbol{\nabla}_0\right)\boldsymbol{\xi}^{(2)}\\&-\boldsymbol{e}_\perp\left(\boldsymbol{B}_0\cdot\boldsymbol{\nabla}_0\right)\left(\boldsymbol{B}_0\cdot\boldsymbol{\nabla}_0\right)\left(\delta J^{(3)}\boldsymbol{\xi}^{(2)}\right)+\frac{2}{B_0^2}(1-\mu)\boldsymbol{e}_\perp\cdot\boldsymbol{\kappa}_0\boldsymbol{e}_\perp\cdot\boldsymbol{\nabla}_0 p_0\xi_\psi^{(2)}\\&+B_0\hat{\xi}^2\frac{\partial\boldsymbol{H}}{\partial\alpha}\left[\left(\boldsymbol{B}_0\cdot\boldsymbol{\nabla}_0\right)\left(\boldsymbol{B}_0\cdot\boldsymbol{\nabla}_0\right)\boldsymbol{H}\right]-B_0\frac{\hat{\xi}^2}{2}\frac{\partial}{\partial\alpha}\left[\boldsymbol{H}\left(\boldsymbol{B}_0\cdot\boldsymbol{\nabla}_0\right)\left(\boldsymbol{B}_0\cdot\boldsymbol{\nabla}_0\right)\boldsymbol{H}\right]\end{aligned}\tag{C.11}$$

The terms which were neglected at lower orders have been added to equation (C.11). We can show that:

$$\left(\boldsymbol{B}_0\cdot\boldsymbol{\nabla}_0\right)\left(\boldsymbol{B}_0\cdot\boldsymbol{\nabla}_0\right)\boldsymbol{\xi}=\mathcal{L}\left(\boldsymbol{\xi}_\perp\right)+\left(\boldsymbol{\nabla}_0\boldsymbol{\kappa}_0\right)\boldsymbol{\xi}+\left[2\boldsymbol{\kappa}_0+\boldsymbol{B}_0\boldsymbol{B}_0\cdot\boldsymbol{\nabla}_0\right]\left(\Gamma\beta+1\right)\delta J$$

where all $\boldsymbol{\xi}$ (and $\delta J$) are either $\boldsymbol{\xi}^{(2)}$ ($\delta J^{(2)}$) or $\boldsymbol{\xi}^{(2)}$ ($\delta J^{(3)}$). Using the last equation and equation (C.7) to replace $\boldsymbol{B}_0\cdot\boldsymbol{\nabla}_0\xi_\parallel^{(4)}$ and taking the derivative with respect to $\alpha$ we obtain:

$$\begin{aligned}
\rho_0\frac{\partial}{\partial\alpha}\frac{\partial^2}{\partial t^2}\left(\boldsymbol{e}_\perp\cdot\boldsymbol{\xi}^{(2)}\right) &= B_0\frac{\partial^2 F^{(5)}}{\partial\alpha\partial\psi} - \frac{\boldsymbol{e}_\psi\cdot\boldsymbol{B}_0}{B_0^2}\left(\boldsymbol{B}_0\cdot\boldsymbol{\nabla}_0\right)\frac{\partial F^{(4)}}{\partial\alpha} + \boldsymbol{e}_\perp\cdot\mathcal{L}\left(\frac{\partial\boldsymbol{\xi}_\perp^{(4)}}{\partial\alpha}\right)\\
&+ 2\Gamma\beta\left(\boldsymbol{e}_\perp\cdot\boldsymbol{\kappa}_0\right) + \frac{2}{B_0^3}\left(\boldsymbol{e}_\perp\cdot\boldsymbol{\kappa}_0\right)\boldsymbol{e}_\wedge\cdot\mathcal{L}\left(\boldsymbol{\xi}_\perp^{(2)}\right)\\
&+ \frac{2}{B_0^2}(1-\mu)\left(\boldsymbol{e}_\perp\cdot\boldsymbol{\kappa}_0\right)\left(\boldsymbol{e}_\perp\cdot\boldsymbol{\nabla}_0 p_0\right)\frac{\partial\xi_\psi^{(2)}}{\partial\alpha}\\
&+ \frac{\partial}{\partial\alpha}\Bigg\{\left[\left(\boldsymbol{e}_\perp\cdot\boldsymbol{\nabla}_0\right)\boldsymbol{\xi}^{(2)}\right]\cdot\left[\mathcal{L}\left(\boldsymbol{\xi}_\perp^{(3)}\right) + \left(\boldsymbol{\nabla}_0\kappa_0\right)\cdot\boldsymbol{\xi}_\perp^{(3)}\right]\\
&+ \left[\left(\boldsymbol{e}_\perp\cdot\boldsymbol{\nabla}_0\right)\boldsymbol{\xi}^{(3)}\right]\cdot\left[\mathcal{L}\left(\boldsymbol{\xi}_\perp^{(2)}\right) + \left(\boldsymbol{\nabla}_0\kappa_0\right)\cdot\boldsymbol{\xi}_\perp^{(2)}\right]\Bigg\}\\
&+ \frac{\partial\hat{\xi}^2}{\partial\alpha}P + \Gamma\beta\left[\left(\boldsymbol{e}_\perp\cdot\boldsymbol{\nabla}_0\right)\frac{\partial\boldsymbol{\xi}^{(2)}}{\partial\alpha}\right]\cdot\left[2\boldsymbol{\kappa}_0 - \frac{1}{B_0^2}\left[\left(\boldsymbol{B}_0\cdot\boldsymbol{\nabla}_0\right)B_0^2\right]\boldsymbol{B}_0\right]J^{(3)}\\
&- \hat{\xi}B_0\frac{\partial}{\partial\psi}\left[\frac{1}{B_0}\boldsymbol{e}_\perp\cdot\mathcal{L}\left(\frac{X}{B_0}\boldsymbol{e}_\perp\right)\right]
\end{aligned}$$

Similar to the previous order we subtract the $\alpha$ derivative of the $\boldsymbol{e}_\perp$-component from the $\psi$-derivative of the $\boldsymbol{e}_\wedge$ component. We define the $\boldsymbol{Z}^{(4)}$ the same way as for the third order and find:

$$\boldsymbol{e}_\perp\cdot\mathcal{L}\left(\boldsymbol{\xi}_\perp^{(4)}\right) + 2\boldsymbol{e}_\perp\cdot\boldsymbol{\kappa}_0\Gamma\beta\delta J^{(4)} = \boldsymbol{e}_\perp\cdot\mathcal{L}\left(\boldsymbol{Z}^{(4)}\right) - \rho_0\left[\left(\boldsymbol{B}_0\cdot\boldsymbol{\nabla}_0\right)\left(\frac{\boldsymbol{e}_\perp^2 B_0}{p_0'}G\right)\right]\frac{\partial^2\hat{\xi}}{\partial t^2}$$

with some algebra (using equation (3.25) and (C.9) again and equation (C.4)) we obtain the final equation of this order before the matching procedure (equation (3.33)).

## C.2. Matching region

### C.2.1. Asymptotic form of the parallel component of the displacement

The equation (4.1) can be separated with respect to its different orders. The highest order of (4.1) is $\mathcal{O}(v^2)$:

$$\frac{\partial}{\partial\theta}\left[\frac{R^2\boldsymbol{B}_p^2}{JB_0^2}\frac{\partial X_0}{\partial\theta}\right] = 0$$

Evaluating this equation we can show that $X_0$ only depends on $v$: $X_0 = X_0(v)$. The next order has the following form:

$$\frac{\partial}{\partial\theta}\left[\frac{R^2\boldsymbol{B}_p^2}{JB_0^2}q'^2v^2\left(\frac{\partial X_0}{\partial v}+\frac{1}{v}\frac{\partial X_1}{\partial\theta}\right)\right]+\mu p_0' f\frac{\partial}{\partial\theta}\left(\frac{1}{B_0^2}\right)q'vX_0=0 \tag{C.12}$$

The last term of this order can be expressed as: $\mu p_0' f\frac{\partial}{\partial\theta}\left(\frac{1}{B_0^2}\right)q'vX_0=\frac{\partial}{\partial\theta}\left(\mu p_0' f\left(\frac{1}{B_0^2}\right)q'vX_0\right)$. Integrating over $\theta$ introduces a constant which depends on $v$:

$$\frac{\partial X_1}{\partial\theta}=\frac{JB_0^2}{R^2\boldsymbol{B}_p^2q'^2v}*C(v)-\frac{f\mu p_0' J}{R^2\boldsymbol{B}_p^2q'}X_0-v\frac{\partial X_0}{\partial v} \tag{C.13}$$

To determine $C(v)$ we calculate the integral of the last equation: $\int d\theta$, where we use the definition: $\langle\cdots\rangle_\theta=\frac{1}{2\pi}\oint\cdots Jd\theta$. Using the fact that $X_0$, $p_0$ and $f$ are periodic and $q(\psi)$ is independent of $\chi$ we find that the constant is given by:

$$C(v)=\frac{q'^2v}{\left\langle\frac{B_0^2}{R^2B_p^2}\right\rangle_\theta}\cdot\left[\frac{\mu f p_0'}{q'}\left\langle\frac{1}{R^2B_p^2}\right\rangle_\theta X_0+v\frac{\partial X_0}{\partial v}\right]$$

Combining this relation with Eq. (C.13) we obtain the expression for $\frac{\partial X_1}{\partial\theta}$, Eq. (3.37):

$$\frac{\partial X_1}{\partial\theta}=\frac{J\mu f p_0'}{R^2B_p^2q'}\left[B_0^2\frac{\left\langle\frac{1}{R^2B_p^2}\right\rangle_\theta}{\left\langle\frac{B_0^2}{R^2B_p^2}\right\rangle_\theta}-1\right]X_0+\left[\frac{JB_0^2}{R^2B_p^2}\frac{1}{\left\langle\frac{B_0^2}{R^2B_p^2}\right\rangle_\theta}-1\right]v\frac{\partial X_0}{\partial v}$$

The next step is to calculate another order so that we can derive an equation for $X_1$ so that we can obtain a differential equation with only $X_0$ and no $X_1$, as we are only interested in the highest order approximation for the asymptotic behaviour.

The next order has the following form:

$$\begin{aligned}0=&\frac{\partial}{\partial\theta}\left\{\frac{R^2B_p^2}{JB_0^2}q'^2v^2\left(\frac{\partial}{\partial\theta}\frac{X_2}{v^2}+\frac{\partial}{\partial v}\frac{X_1}{v}\right)+2\frac{R^2B_p^2}{JB_0^2}q'Y'v\left[\frac{\partial}{\partial\theta}\frac{X_1}{v}+\frac{\partial}{\partial v}X_0\right]\right\}\\&+\frac{\partial}{\partial v}\left[\frac{R^2B_p^2}{JB_0^2}q'^2v\left(\frac{\partial}{\partial\theta}X_1\right)\right]+\mu p_0' f\frac{\partial}{\partial\theta}\left(\frac{1}{B_0^2}\right)q'X_1\\&+\frac{\partial}{\partial v}\left[\frac{R^2B_p^2}{JB_0^2}q'^2v^2\left(\frac{\partial}{\partial v}X_0\right)\right]+2\mu p_0'\left[\frac{J}{B_0^2R^2B_p^2}\left(\nabla\psi\cdot\nabla\right)\left(p_0+\frac{B_0^2}{2}\right)+\frac{1}{2}\frac{\partial}{\partial\theta}\left(\frac{1}{B_0^2}\right)Y'\right]X_0\end{aligned} \tag{C.14}$$

We again calculate the integral with respect to $\theta$ and notice that the first term of the right hand side disappears:

$$\begin{aligned}0 = &\frac{1}{2\pi}\oint \mathrm{d}\theta \left[\frac{\partial}{\partial v}\left[\frac{R^2B_p^2}{JB_0^2}q'^2 v\left(\frac{\partial}{\partial v}X_1\right)\right] + \mu p_0' f \frac{\partial}{\partial\theta}\left(\frac{1}{B_0^2}\right) q' X_1\right] \\ &+ \frac{1}{2\pi}\oint \mathrm{d}\theta \left[\frac{\partial}{\partial v}\left[\frac{R^2B_p^2}{JB_0^2}q'^2 v^2\left(\frac{\partial}{\partial v}X_0\right)\right]\right. \\ &\left. + 2\mu p_0' \left[\frac{J}{B_0^2R^2B_p^2}\left(\nabla\psi\cdot\nabla\right)\left(p_0 + \frac{B_0^2}{2}\right) + \frac{1}{2}\frac{\partial}{\partial\theta}\left(\frac{1}{B_0^2}\right)Y'\right] X_0\right]\end{aligned}$$

By using Eq. (3.37) to eliminate $X_1$, the relation

$$\frac{1}{2\pi}\oint \mathrm{d}\theta \frac{\partial}{\partial\theta}\left(\frac{1}{B_0^2}\right) f = -\frac{1}{2\pi}\oint \mathrm{d}\theta \left(\frac{1}{B_0^2}\frac{\partial}{\partial\theta}f\right)$$

and the equation $\dfrac{\partial}{\partial\theta}Y' = Y'' = \nu' - q'$, we get the following equation (3.38):

$$\frac{\partial}{\partial v}\left[v^2\frac{\partial X_0}{\partial v}\right] + D_M X_0 = 0,$$

where $D_M$ is the Mercier coefficient, [65], which has the following form:

$$\begin{aligned}D_M = \frac{\mu p_0'}{q'^2}\Bigg(&fq'\left\langle\frac{1}{R^2B_p^2}\right\rangle_\theta - \mu p_0' f^2\left\langle\frac{1}{R^2B_p^2}\right\rangle_\theta^2 + \left\langle\frac{B_0^2}{R^2B_p^2}\right\rangle_\theta\left[\mu p_0' f^2\left\langle\frac{1}{R^2B_p^2B_0^2}\right\rangle_\theta\right. \\ &\left.\left. + 2\left\langle\frac{1}{R^2B_p^2B_0^2}(\nabla\psi\cdot\nabla)\left(p_0 + \frac{B_0^2}{2}\right)\right\rangle_\theta - f\left\langle\frac{\nu'}{JB_0^2}\right\rangle_\theta\right]\Bigg)\end{aligned} \tag{C.15}$$

With the ansatz that $X_0 = \frac{C}{|v|^\lambda}$ we obtain a general solution for $X_0$:

$$X_0 = \frac{C_1}{|v|^{\lambda_+}} + \frac{C_2}{|v|^{\lambda_-}}$$

with $\lambda_\pm = \frac{1}{2} \pm \sqrt{\frac{1}{4} - D_M}$ where we will refer to the small $\lambda_S$ and large solution $\lambda_L$.

### C.2.2. Useful equation for the matching region

The following expression will be derived here as it is needed for the matching region:

$$\left\langle \frac{X}{B_0}\boldsymbol{e}_\perp \cdot \mathcal{L}\left(\frac{Z}{B_0}\boldsymbol{e}_\perp\right)\right\rangle - \frac{\rho_0}{p_0'}\left[|\boldsymbol{e}_\perp|^2 XG\right]_{-l_0}^{l_0} = \left[q'^2\left\langle\frac{B_0^2}{R^2B_p^2}\right\rangle_\theta^{-1}(\lambda_S-\lambda_L)\delta X_0^2 v|v|^{2\lambda_S}\xi\right.$$
$$\left. + \frac{\rho_0}{(3-2\lambda_S)}\left(q'^2\left\langle\frac{R^2B_p^2}{B_0^2}\right\rangle_\theta v^3X_0^2 + v\left\langle B_0^2G_0^2\right\rangle\right)\frac{\partial^2\xi}{\partial t^2} + q'v\frac{R^2B_p^2}{JB_0^2}X_0\int d\alpha\frac{\partial U_0}{\partial\theta}\right]_{-l_0}^{l_0} \quad \text{(C.16)}$$

where $l_0$ sets the limits of the integral $\langle\cdots\rangle$ and it is determined by the matching of the non-linear and inertia regions. By integrating by parts we obtain:

$$\left\langle \frac{X}{B_0}\boldsymbol{e}_\perp \cdot \mathcal{L}\left(\frac{Z}{B_0}\boldsymbol{e}_\perp\right)\right\rangle - \frac{\rho_0}{p_0'}\left[|\boldsymbol{e}_\perp|^2 XG\right]_{-l_0}^{l_0} =$$
$$\left[\frac{|\boldsymbol{e}_\perp|^2}{B_0^2}\left(X\boldsymbol{B}_0\cdot\boldsymbol{\nabla}_0 Z - Z\boldsymbol{B}_0\cdot\boldsymbol{\nabla}_0 X\right) - \frac{\rho_0}{p_0'}|\boldsymbol{e}_\perp|^2 XG\right]$$

where the relation $\boldsymbol{e}_\perp\cdot\mathcal{L}\left(\frac{X}{B_0}\boldsymbol{e}_\perp\right)=0$ was used. These limits are non-zero for only the highest order of the right hand side as $l_0\to\infty$. Therefore lower orders can be neglected and we obtain:

$$\left\langle \frac{X}{B_0}\boldsymbol{e}_\perp \cdot \mathcal{L}\left(\frac{Z}{B_0}\boldsymbol{e}_\perp\right)\right\rangle - \frac{\rho_0}{p_0'}\left[|\boldsymbol{e}_\perp|^2 XG\right]_{-l_0}^{l_0} = \left[q'^2v^2\frac{R^2B_p^2}{JB_0^2}\left\{X_0\left(\frac{\partial Z_0}{\partial v}+\frac{1}{v}\frac{\partial Z_1}{\partial\theta}\right)\right.\right.$$
$$\left.\left. - Z_0\left(\frac{\partial X_0}{\partial v}+\frac{1}{v}\frac{\partial X_1}{\partial\theta}\right)\right\} - \frac{\rho_0}{p_0'}q'^2v^2R^2B_p^2X_0G_0\right]$$
$$+\left[q'^2v^2\frac{R^2B_p^2}{JB_0^2}X_0\frac{\partial}{\partial\theta}\left(-\frac{1}{q'v}\int d\alpha U_0\right)\right]$$

Using the expression (3.42) for $\frac{\partial Z_1}{\partial\theta}$ and equation (3.37) $\frac{\partial X_1}{\partial\theta}$ leads to:

$$\left\langle \frac{X}{B_0}\boldsymbol{e}_\perp \cdot \mathcal{L}\left(\frac{Z}{B_0}\boldsymbol{e}_\perp\right)\right\rangle - \frac{\rho_0}{p_0'}\left[|\boldsymbol{e}_\perp|^2 XG\right]_{-l_0}^{l_0} =$$
$$\left[q'^2v^2\left\langle\frac{JB_0^2}{R^2B_p^2}\right\rangle_\theta^{-1}\left(X_0\frac{\partial Z_0}{\partial v} - Z_0\frac{\partial X_0}{\partial v} - \frac{\rho_0X_0}{p_0'}\left\langle B_0^2G_0\right\rangle\frac{\partial^2\xi}{\partial t^2}\right)\right]$$
$$+\left[q'^2v^2\frac{R^2B_p^2}{JB_0^2}X_0\frac{\partial}{\partial\theta}\left(-\frac{1}{q'v}\int d\alpha U_0\right)\right]$$

Using the expressions (3.47) and (3.44) for $Z_0$ and $X_0$ we can derive the desired expression:

$$\left\langle \frac{X}{B_0}\boldsymbol{e}_\perp \cdot \mathcal{L}\left(\frac{Z}{B_0}\boldsymbol{e}_\perp\right)\right\rangle - \frac{\rho_0}{p_0'}\left[|\boldsymbol{e}_\perp|^2 XG\right]_{-l_0}^{l_0} = \Bigg[q'^2\left\langle \frac{JB_0^2}{R^2B_p^2}\right\rangle_\theta^{-1}(\lambda_S-\lambda_L)\delta X_0^2|v|^{2\lambda_S}$$
$$+\frac{\hat{\rho}_0 v X_0}{3-2\lambda_S}\left\{q'^2\left\langle \frac{JR^2B_p^2}{B_0^2}\right\rangle_\theta v^3X_0^2 + v\left\langle B_0^2G_0^2\right\rangle\right\} + q'^2v^2\frac{R^2B_p^2}{JB_0^2}X_0\frac{\partial}{\partial\theta}\left(-\frac{1}{q'v}\int d\alpha U_0\right)\Bigg],$$

where we additionally used the following relation which is easy to show by using the expression of $G_0$ once:

$$\left\langle B_0^2G_0^2\right\rangle = \left\{\frac{\lambda_S}{p_0'}\left\langle \frac{JB_0^2}{R^2B_p^2}\right\rangle_\theta^{-1} v\left\langle B_0^2G_0\right\rangle - \frac{fv}{q'}\left\langle \frac{JB_0^2}{R^2B_p^2}\right\rangle_\theta^{-1}\left\langle \frac{1}{R^2B_p^2}\right\rangle_\theta\left\langle B_0^2G_0\right\rangle + \frac{vf}{q'}\left\langle G_0\right\rangle\right\}X_0q'^2$$

# D. Deriving the non-linear ballooning model in slab geometry

Here we derive the ballooning mode envelope equation (4.4) and its coefficients (4.5) with the Eulerian boundary condition. We start from the Lagrangian MHD momentum equation (4.2). To derive these relations we must calculate the different orders of the $x_0$ and $y_0$ components of (4.2).

The $x_0$ component of Eq. (4.2) to $\mathcal{O}(n^{-2})$ becomes

$$\begin{aligned}\rho_0\frac{\partial^2\xi_x}{\partial t^2} = &-\frac{\partial F}{\partial x_0} + \left(B_0^2\frac{\partial^2\xi_x}{\partial z_0^2} + \frac{\rho_0^2 g^2}{p_0}\xi_x + \rho_0' g\xi_x\right) - B_0^2\left(2(J-1)\frac{\partial^2\xi_x}{\partial z_0^2} + \frac{\partial J}{\partial z_0}\frac{\partial \xi_x}{\partial z_0}\right)\\ &+ \frac{\partial\xi_x}{\partial x_0}\left(B_0^2\frac{\partial^2\xi_x}{\partial z_0^2} + \frac{\rho_0^2 g^2}{p_0}\xi_x + \rho_0' g\xi_x\right) + \frac{1}{2}\rho_0'' g\xi_x^2 - \frac{\rho_0^3 g^3}{2p_0^2}\xi_x^2\\ &+ B_0^2\frac{\partial\xi_z}{\partial x_0}\left[\frac{\partial}{\partial z_0}\left(1 - J + \frac{\partial\xi_z}{\partial z_0}\right)\right] + \frac{\rho_0^2 g}{p_0}\frac{\partial^2 s}{\partial t^2} + \nu\frac{\partial^2}{\partial y_0^2}\frac{\partial\xi_x}{\partial t}.\end{aligned} \tag{D.1}$$

Similarly the $y_0$ component to $\mathcal{O}(n^{-3/2})$ becomes:

$$\begin{aligned}0 = &-\frac{\partial F}{\partial y_0} + \left(B_0^2\frac{\partial^2\xi_y}{\partial z_0^2}\right) + \frac{\partial\xi_x}{\partial y_0}\left(B_0^2\frac{\partial^2\xi_x}{\partial z_0^2} + \frac{\rho_0^2 g^2}{p_0}\xi_x + \rho_0' g\xi_x\right)\\ &+ B_0^2\frac{\partial\xi_z}{\partial y_0}\left[\frac{\partial}{\partial z_0}\left(1 - J + \frac{\partial\xi_z}{\partial z_0}\right)\right]\end{aligned} \tag{D.2}$$

where we have defined $F$ as

$$F \equiv \left[\frac{p_0}{J} + \frac{B_0^2}{2J^2}\left(1 + 2\frac{\partial\xi_z}{\partial z_0} + \left(\frac{\partial\xi_z}{\partial z_0}\right)^2 + \left(\frac{\partial\xi_x}{\partial z_0}\right)^2\right) + \rho_0 g\xi_x + \frac{1}{2}\rho_0' g\xi_x^2\right].$$

## Lowest Order: Incompressibility

We now analyse the lowest order of $F$. It is given by: $F^{(1/2)} = -(p_0 + B_0^2)\,J^{(1/2)}$ where the superfix $(i)$ indicates an order $n^{-i}$ term. From Eq. (4.3), we see that $J^{(1/2)} = 0$. Therefore

we can write

$$J^{(1/2)} = \frac{\partial \xi_y^{(3/2)}}{\partial y_0} + \frac{\partial \xi_x^{(1)}}{\partial x_0} = 0 \tag{D.3}$$

where we have used the relation $J = |\boldsymbol{\nabla}_0 \mathbf{r}|$ and the ordering shown in Eq. (4.1). With these relations we see that Eq. (D.2) is $\mathcal{O}(1)$ and Eq. (D.1) is $\mathcal{O}(n^{-1/2})$.

## $y_0$ component to $\mathcal{O}(1)$ and $x_0$ component to $\mathcal{O}(n^{-1/2})$

Integrating Eqs. (D.1) and (D.2) we deduce:

$$(p_0 + B_0^2)J^{(1)} - B_0^2 \frac{\partial \xi_z^{(1)}}{\partial z_0} - \rho_0 g \xi_x^{(1)} = -F^{(1)}(z_0, t)$$

and from Eq. (4.3):

$$J^{(1)} = \frac{\rho_0 g}{p_0} \xi_x^{(1)}.$$

The boundary condition that $J$ and $\boldsymbol{\xi}$ must vanish as $x_0 \to \pm\infty$ forces $F^{(1)}(z_0, t) = 0$ which then provides

$$\frac{\partial \xi_z^{(1)}}{\partial z_0} = J^{(1)} = \frac{\rho_0 g}{p_0} \xi_x^{(1)}\,. \tag{D.4}$$

Using the expression for $J^{(1)}$ obtained from $J = |\boldsymbol{\nabla}_0 \mathbf{r}|$ we find:

$$\Rightarrow 0 = \frac{\partial \xi_y^{(2)}}{\partial y_0} + \frac{\partial \xi_x^{(3/2)}}{\partial x_0} + \frac{\partial \xi_y^{(3/2)}}{\partial y_0}\frac{\partial \xi_x^{(1)}}{\partial x_0} - \frac{\partial \xi_y^{(3/2)}}{\partial x_0}\frac{\partial \xi_x^{(1)}}{\partial y_0}\,. \tag{D.5}$$

We now average Eq. (D.5) over $y_0$, using the notation: $\bar{A} = \lim_{Y\to\infty} \frac{1}{L_Y} \int_{-Y}^{Y} A\, dy_0$. Noting from Eqs. (D.3) and (D.4) that $\overline{\xi_x^{(1)}} = \overline{\xi_z^{(1)}} = \overline{J^{(1)}} = 0$ we obtain:

$$\overline{\xi_x^{(3/2)}} = \frac{1}{2} \frac{\partial \overline{\left(\xi_x^{(1)}\right)^2}}{\partial x_0} \tag{D.6}$$

and from Eq. (4.3):

$$\overline{J^{(3/2)}} = \frac{\rho_0 g}{p_0} \overline{\xi_x^{(3/2)}}\,.$$

### $y_0$ component to $\mathcal{O}(n^{-1/2})$ and $x_0$ component to $\mathcal{O}(n^{-1})$

These orders provide the equations:

$$\frac{\partial}{\partial y_0}\left((p_0+B_0^2)J^{(3/2)}-B_0^2\frac{\partial \xi_z^{(3/2)}}{\partial z_0}-\rho_0 g\xi_x^{(3/2)}\right)=-\frac{\partial F^{(3/2)}}{\partial y_0}=0 \tag{D.7}$$

$$\frac{\partial}{\partial x_0}\left(F^{(3/2)}\right)=B_0^2\frac{\partial^2\xi_x^{(1)}}{\partial z_0^2}+\frac{\rho_0^2 g^2}{p_0}\xi_x^{(1)}+\rho_0' g\xi_x^{(1)}\,. \tag{D.8}$$

From Eq. (D.7) we deduce $F^{(3/2)}=\overline{F^{(3/2)}}$. Averaging Eq. (D.8) over $y_0$ and observing that $\xi_x^{(1)}$ must vanish as $x_0\to\pm\infty$, we find that $F^{(3/2)}=\overline{F^{(3/2)}}=0$. In order to satisfy the boundary conditions at the walls we introduce a small eigenvalue $\Gamma^2(x_0)\sim\mathcal{O}(n^{-1})\frac{\pi^2B_0^2}{L^2\rho_0}$ into Eq. (D.8). The same term is then subtracted at higher order so the procedure is consistent. This provides an equation for the vertical displacement of the filament:

$$\rho_0\Gamma^2(x_0)\xi_x^{(1)}=B_0^2\frac{\partial^2\xi_x^{(1)}}{\partial z_0^2}+\frac{\rho_0^2 g^2}{p_0}\xi_x^{(1)}+\rho_0' g\xi_x^{(1)}\,. \tag{D.9}$$

We must solve Eq. (D.9) subject to the boundary condition $\xi_x=0$ at $z=0,L$ (with $z=z_0+\xi_z$) corresponding to field lines frozen to the wall. A solution is:

$$\xi_x^{(1)}=\sin\left(\frac{\pi z}{L}\right)\xi(x_0,y_0,t) \tag{D.10}$$

where $\xi(x_0,y_0,t)$ is a function to be found from the higher order equations. While Eq. (D.10) satisfies the boundary conditions exactly it is not quite a solution of Eq. (D.9) since:

$$\frac{\partial}{\partial z_0}=\frac{\partial z}{\partial z_0}\frac{\partial}{\partial z}=\left[\left(1+\frac{\partial\xi_z}{\partial z_0}\right)\frac{\partial}{\partial z}\right].$$

Our solution, Eq. (D.10) requires the second term, which is $\mathcal{O}(n^{-1})$, to be moved to higher order. Specifically, Eq. (D.9) can be written in the form:

$$\begin{aligned}\rho_0\Gamma^2(x_0)\xi_x^{(1)}=&B_0^2\frac{\partial^2\xi_x^{(1)}}{\partial z^2}+\frac{\rho_0^2 g^2}{p_0}\xi_x^{(1)}+\rho_0' g\xi_x^{(1)}\\&+B_0^2\left(2J^{(1)}\frac{\partial^2\xi_x^{(1)}}{\partial z_0^2}+\frac{\partial J^{(1)}}{\partial z_0}\frac{\partial\xi_x^{(1)}}{\partial z_0}\right)+\mathcal{O}(n^{-5/2})\,.\end{aligned} \tag{D.11}$$

The extra $\mathcal{O}(n^{-2})$ term will cancel with the second term on the second line of Eq. (D.1) at the final order of interest. We therefore drop it here and reintroduce it at $\mathcal{O}(n^{-2})$ - see Eq. (D.14) below. Finally using Eq. (D.10) we obtain the eigenvalue.

$$\Gamma^2(x_0) = -\frac{B_0^2\pi^2}{\rho_0 L^2} + \frac{\rho_0 g^2}{p_0} + \frac{\rho_0' g}{\rho_0}\,.$$

Our procedure is only valid for equilibria close to marginal stability, such that $\Gamma^2 = \mathcal{O}(n^{-1})$.

## $y_0$ component to $\mathcal{O}(n^{-1})$ and $x_0$ component to $\mathcal{O}(n^{-3/2})$

Some straigthforward algebra yields:

$$F^{(2)} = -\left((p_0 + B_0^2)J^{(2)} - B_0^2\frac{\partial\xi_z^{(2)}}{\partial z_0} - \rho_0 g\xi_x^{(2)} - \frac{B_0^2}{2}\left(\frac{\partial\xi_z^{(1)}}{\partial z_0}\right)^2 - \frac{B_0^2}{2}\left(\frac{\partial\xi_x^{(1)}}{\partial z_0}\right)^2 - \rho_0' g\frac{(\xi_x^{(1)})^2}{2}\right).$$

This allows us to write Eq. (D.2) at $\mathcal{O}(n^{-1})$ in the form:

$$\frac{\partial F^{(2)}}{\partial y_0} = 0$$

and Eq. (D.1) at $\mathcal{O}(n^{-3/2})$ becomes:

$$\frac{\partial F^{(2)}}{\partial x_0} + B_0^2\frac{\partial^2\xi_x^{(3/2)}}{\partial z_0^2} + \frac{\rho_0^2 g^2}{p_0}\xi_x^{(3/2)} + \rho_0' g\xi_x^{(3/2)} = 0\,. \tag{D.12}$$

Writing $\xi_x^{(3/2)} = \overline{\xi_x^{(3/2)}} + \tilde{\xi}_x^{(3/2)}$ where $\overline{\xi_x^{(3/2)}}$ (the $y_0$ average) is given in Eq. (D.6). The fluctuating part must satisfy:

$$B_0^2\frac{\partial^2\tilde{\xi}_x^{(3/2)}}{\partial z_0^2} + \frac{\rho_0^2 g^2}{p_0}\tilde{\xi}_x^{(3/2)} + \rho_0' g\tilde{\xi}_x^{(3/2)} = 0.$$

Thus $\tilde{\xi}_x^{(3/2)}$ obeys the same equation as $\xi_x^{(1)}$ to the order of interest (to this order $\Gamma$ and the difference between $z$ and $z_0$ are not important)– thus we can absorb it into $\xi_x^{(1)}$ and simply set $\tilde{\xi}_x^{(3/2)} = 0$. We could then solve Eq. (D.12) by integrating in $x_0$ – but we don't need to.

### $y_0$ component to $\mathcal{O}(n^{-3/2})$ and $x_0$ component to $\mathcal{O}(n^{-2})$

To $\mathcal{O}(n^{-3/2})$ Eq. (D.2) becomes:

$$-\frac{\partial F^{(5/2)}}{\partial y_0} + B_0^2 \frac{\partial^2 \xi_y^{(3/2)}}{\partial z_0^2} + \alpha \frac{\partial \xi}{\partial y_0} \frac{\partial \overline{\xi^2}}{\partial x_0} = 0 \tag{D.13}$$

where the $\alpha$ term comes from substituting for $\overline{\xi_x^{(3/2)}}$ in the second bracket of the second line of Eq. (D.2) and we have introduced

$$\alpha = \frac{B_0^2 \pi^2}{2L^2} \left[ 2\cos^2\left(\frac{\pi z}{L}\right) \sin\left(\frac{\pi z}{L}\right) - \sin^3\left(\frac{\pi z}{L}\right) \right] .$$

To $\mathcal{O}(n^{-2})$ Eq. (D.1) becomes:

$$\begin{aligned} \rho_0 \sin\left(\frac{\pi z}{L}\right) \frac{\partial^2 \xi}{\partial t^2} = & -\frac{\partial F^{(5/2)}}{\partial x_0} + \rho_0 \Gamma^2(x_0) \sin\left(\frac{\pi z}{L}\right) \xi \\ & + B_0^2 \frac{\partial^2 \xi_x^{(2)}}{\partial z^2} + \frac{\rho_0^2 g^2}{p_0} \xi_x^{(2)} + \rho_0' g \xi_x^{(2)} \\ & + \alpha \frac{\partial \xi}{\partial x_0} \frac{\partial \overline{\xi^2}}{\partial x_0} + \frac{1}{2} \left( \rho_0'' g - \frac{\rho_0^3 g^3}{p_0^2} \right) \sin^2\left(\frac{\pi z}{L}\right) \xi^2 \\ & - \frac{L^2 \rho_0^2 g^2}{\pi^2 p_0^2} \rho_0 \sin\left(\frac{\pi z}{L}\right) \frac{\partial^2 \xi}{\partial t^2} + \nu \frac{\partial^2}{\partial y_0^2} \frac{\partial \xi}{\partial t} \end{aligned} \tag{D.14}$$

where we have included the eigenvalue term $\rho_0 \Gamma^2(x_0) \sin(\frac{\pi z}{L}) \xi$ which was added to the left hand side at $\mathcal{O}(n^{-1})$ in Eq. (D.11) and the higher order non-linear terms that we dropped from Eq. (D.11) have been included in Eq. (D.14) (where they cancel the second term in the second line of Eq. (D.1)). From Eq. (D.3), setting $\xi = \frac{\partial^2 u}{\partial y_0^2}$, we have $\xi_y^{(3/2)} = -\sin(\frac{\pi z}{L}) \frac{\partial^2 u}{\partial y_0 \partial x_0}$, so Eq. (D.13) provides:

$$F^{(5/2)} = \overline{F^{(5/2)}} + \frac{B_0^2 \pi^2}{L^2} \sin\left(\frac{\pi z}{L}\right) \frac{\partial u}{\partial x_0} + \alpha \xi \frac{\partial \overline{\xi^2}}{\partial x_0} .$$

From the $y_0$ average of Eq. (D.14) we obtain

$$\frac{\partial \overline{F^{(5/2)}}}{\partial x_0} = \frac{1}{2} \left( \rho_0'' g - \frac{\rho_0^3 g^3}{p_0^2} \right) \sin^2\left(\frac{\pi z}{L}\right) \overline{\xi^2} .$$

Thus combining these expression for $F^{(5/2)}$ in Eq. (D.14) and annihilating the $\xi_x^{(2)}$ terms by multiplying by $\sin(\frac{\pi z}{L})$ and integrating over $z$ we obtain the final non-linear equation:

$$C_0\frac{\partial^2\xi}{\partial t^2} = \Gamma^2(x_0)\xi + C_2\frac{\partial^2 u}{\partial x_0^2} + C_3\xi\frac{\partial^2\overline{\xi^2}}{\partial x_0^2} + C_4\left(\xi^2 - \overline{\xi^2}\right) + \nu\frac{\partial^2}{\partial y_0^2}\frac{\partial\xi}{\partial t}.$$

To reiterate, $\overline{\xi}^2$ is the $y_0$ average of the squared displacement, $\xi^2$, and $\frac{\partial^2 u}{\partial y_0^2} = \xi$. The local linear growth rate $\Gamma_0$ is given by:

$$\Gamma_0^2(x_0) = -\frac{B_0^2\pi^2}{\rho_0 L^2} + \frac{\rho_0 g^2}{p_0} + \frac{g}{\rho_0}\frac{d\rho_0}{dx_0}\,.$$

The coefficients $C_0$, $C_2$, $C_3$ and $C_4$ are given by:

$$C_0 = \left(1 + \frac{\rho_0^2 g^2 L^2}{p_0^2\pi^2}\right) \qquad C_2 = -\left(\frac{B_0^2\pi^2}{\rho_0 L^2}\right)$$
$$C_3 = \left(\frac{B_0^2\pi^2}{8\rho_0 L^2}\right) \qquad C_4 = \frac{4}{3\pi}\left(\frac{g}{\rho_0}\frac{d^2\rho_0}{dx_0^2} - \frac{\rho_0^2 g^3}{p_0^2}\right).$$

# E. Expanding the nonlinear drive coefficient

In this appendix it is shown that the coefficient $C_2 = \left\langle \frac{X\widehat{P}}{B_0} \right\rangle$ can be divided into a sum of functions: $C_2 \equiv \sum_{i=1}^{6} \langle Q_i \rangle$ which has been done to simplify the treatment of the numerical and analytical calculations. We can determine the six terms as:

$$
\begin{aligned}
Q_1 &\equiv -\left\langle \frac{f}{B_0^2} Q_- \boldsymbol{B}_0 \cdot \boldsymbol{\nabla}_0 (X\Lambda) \right\rangle \\
Q_2 &\equiv \left\langle \left[ \frac{\partial}{\partial \psi} \left( 2p_0 + B_0^2 \right) \right] \frac{XQ_-}{B_0^2} \right\rangle \\
Q_3 &\equiv -\left\langle X \frac{\partial}{\partial \psi} Q_+ \right\rangle \\
Q_4 &\equiv \langle [\boldsymbol{B}_0 \cdot \boldsymbol{\nabla}_0 (X\Lambda)] \, S \rangle \\
Q_5 &\equiv -\left\langle \frac{X}{J} \frac{\partial}{\partial \psi} JT \right\rangle - \left\langle [\boldsymbol{B}_0 \cdot \boldsymbol{\nabla}_0 X] \frac{\partial}{\partial \psi} (\boldsymbol{H}) \, [\boldsymbol{B}_0 \cdot \boldsymbol{\nabla}_0 \boldsymbol{H}] \right\rangle \\
Q_6 &\equiv \frac{1}{2} \left\langle \frac{1}{B_0} u \, \omega \right\rangle
\end{aligned}
$$

with the defined variables:

$$
\begin{aligned}
S &\equiv \{ [\boldsymbol{B}_0 \cdot \boldsymbol{\nabla}_0 \boldsymbol{H}] \, [R(\boldsymbol{e}_\phi \cdot \nabla) \boldsymbol{H}] \} & T &\equiv |\boldsymbol{B}_0 \cdot \boldsymbol{\nabla}_0 \boldsymbol{H}|^2 \\
U &\equiv \{ [(\boldsymbol{H} \cdot \nabla) \, \boldsymbol{H}] \cdot \nabla \alpha \} & \omega &\equiv \boldsymbol{e}_\wedge \cdot \mathcal{L}(H \boldsymbol{e}_\perp)
\end{aligned}
$$

The coefficient is defined as $C_2 = \left\langle \frac{X\widehat{P}}{B_0} \right\rangle$ where $H\widehat{P}$ is given by:

$$
\begin{aligned}
H\widehat{P} =& H \, [(\mathbf{e}_\perp \cdot \nabla) \mathbf{H}] \cdot (\boldsymbol{B}_0 \cdot \nabla) \, [(\boldsymbol{B}_0 \cdot \nabla) \mathbf{H}] - \frac{1}{2} H (\mathbf{e}_\perp \cdot \nabla) \, [\mathbf{H} \cdot (\boldsymbol{B}_0 \cdot \nabla) \, [(\boldsymbol{B}_0 \cdot \nabla) \mathbf{H}]] \\
&+ \frac{1}{2B_0} \, [(\mathbf{H} \cdot \nabla) \mathbf{H}] \cdot \nabla \alpha \mathbf{e}_\wedge \cdot \mathcal{L}(H \mathbf{e}_\perp) + 2(\mathbf{e}_\perp \cdot \mathbf{k}_0) \frac{Q_- H}{B_0^2}
\end{aligned} \tag{E.1}
$$

with

$$
Q_\pm = \frac{1}{2} \left[ \mathbf{H} (\boldsymbol{B}_0 \cdot \nabla) \, ((\boldsymbol{B}_0 \cdot \nabla) \mathbf{H}) \pm |(\boldsymbol{B}_0 \cdot \nabla) \mathbf{H}|^2 \right]
$$

We can use this definition to re-write the second term on the right hand side of Eq. (E.1):

$$-\frac{1}{2}H(\mathbf{e}_\perp\cdot\nabla)\left[\mathbf{H}\cdot(\boldsymbol{B}_0\cdot\nabla)\left[(\boldsymbol{B}_0\cdot\nabla)\mathbf{H}\right]\right]=(\mathbf{e}_\perp\cdot\nabla)Q_-+\frac{1}{2}(\mathbf{e}_\perp\cdot\nabla)|\left(\boldsymbol{B}_0\cdot\boldsymbol{\nabla}_0\right)\boldsymbol{H}|^2$$

The next step is to expand $\boldsymbol{e}_\perp$ into its components: $\boldsymbol{e}_\perp=\frac{B_0}{R^2B_p^2}\boldsymbol{\nabla}_0\psi-\frac{\Lambda f}{B_0}\boldsymbol{B}_0+\Lambda RB_0\boldsymbol{e}_\phi$ in the terms of $H\widehat{P}$, where it appears as $\boldsymbol{e}_\perp\cdot\boldsymbol{\nabla}_0$ in the first and second term of Eq. (E.1):

$$\begin{aligned}
&H\left[(\mathbf{e}_\perp\cdot\nabla)\mathbf{H}\right]\cdot(\boldsymbol{B}_0\cdot\nabla)\left[(\boldsymbol{B}_0\cdot\nabla)\mathbf{H}\right]+(\mathbf{e}_\perp\cdot\nabla)Q_-+\frac{1}{2}(\mathbf{e}_\perp\cdot\nabla)|\left(\boldsymbol{B}_0\cdot\boldsymbol{\nabla}_0\right)\boldsymbol{H}|^2\\
&=\frac{B_0}{R^2B_p^2}\left[(\nabla\psi\cdot\nabla)\,\boldsymbol{H}\right]\cdot\left(\boldsymbol{B}_0\cdot\boldsymbol{\nabla}_0\right)\left[\left(\boldsymbol{B}_0\cdot\boldsymbol{\nabla}_0\right)\boldsymbol{H}\right]-\frac{B_0}{2R^2B_p^2}\left(\nabla\psi\cdot\boldsymbol{\nabla}_0\right)|\left(\boldsymbol{B}_0\cdot\boldsymbol{\nabla}_0\right)\boldsymbol{H}|^2 \quad \text{(E.2)}\\
&+\Lambda RB_0\left[\left[\left(\boldsymbol{e}_\phi\cdot\boldsymbol{\nabla}_0\right)\boldsymbol{H}\right]\cdot\left(\boldsymbol{B}_0\cdot\boldsymbol{\nabla}_0\right)\left[\left(\boldsymbol{B}_0\cdot\boldsymbol{\nabla}_0\right)\boldsymbol{H}\right]\right]+\frac{B_0}{R^2B_p^2}\left(\boldsymbol{\nabla}_0\psi\cdot\nabla\right)Q_--\frac{\Lambda f}{B_0}\left(\boldsymbol{B}_0\cdot\boldsymbol{\nabla}_0\right)Q_-
\end{aligned}$$

Here we used the cancellation of the terms with the resulting $\boldsymbol{B}_0\cdot\boldsymbol{\nabla}_0$ - derivative and the derivative with respect to $\phi$ vanishes because of symmetry.
By using:

$$R\left(\boldsymbol{e}_\phi\cdot\nabla\right)\left[\left(\boldsymbol{B}_0\cdot\boldsymbol{\nabla}_0\right)\boldsymbol{H}\right]=\left(\boldsymbol{B}_0\cdot\boldsymbol{\nabla}_0\right)\left[R\left(\boldsymbol{e}_\phi\cdot\nabla\right)\boldsymbol{H}\right]$$

we can show that:

$$R\left[\left(\boldsymbol{e}_\phi\cdot\nabla\right)\boldsymbol{H}\right]\cdot\left(\boldsymbol{B}_0\cdot\boldsymbol{\nabla}_0\right)\left[\left(\boldsymbol{B}_0\cdot\boldsymbol{\nabla}_0\right)\boldsymbol{H}\right]=\left(\boldsymbol{B}_0\cdot\boldsymbol{\nabla}_0\right)\left\{R\left[\left(\boldsymbol{e}_\phi\cdot\nabla\right)\boldsymbol{H}\right]\cdot\left[\left(\boldsymbol{B}_0\cdot\boldsymbol{\nabla}_0\right)\boldsymbol{H}\right]\right\}$$

which can be used for the last term of Eq. (E.2). To calculate the coefficient $C_2$ we must apply $<\cdots>$ to Eq. (E.1).The remaining steps to derive the terms (5.9) are integrating by parts and using the relations: $\left(\boldsymbol{B}_0\cdot\boldsymbol{\nabla}_0\right)\dfrac{\partial\boldsymbol{H}}{\partial\psi}=\dfrac{\partial}{\partial\psi}\left(\boldsymbol{B}_0\cdot\boldsymbol{\nabla}_0\boldsymbol{H}\right)+\dfrac{J'}{J}\boldsymbol{B}_0\cdot\boldsymbol{\nabla}_0\boldsymbol{H}$ and $Q_--|\boldsymbol{B}_0\cdot\boldsymbol{\nabla}_0\boldsymbol{H}|^2=Q_+$.

# Bibliography


[1] S. Cowley, M. Artun, and B. Albright. "Detonation: A mechanism for the explosive release of energy in a plasma". In: *Physics of Plasmas* 3.5 (1996), pp. 1848–1852.

[2] H. R. Wilson and S. C. Cowley. "Theory for Explosive Ideal Magnetohydrodynamic Instabilities in Plasmas". In: *Physical Review Letters* 92.17 (2004), p. 175006.

[3] O. Hurricane, B. Fong, and S. Cowley. "Nonlinear magnetohydrodynamic detonation: Part I". In: *Physics of Plasmas* 4.10 (1997), pp. 3565–3580.

[4] S. Cowley et al. "Explosive instability and erupting flux tubes in a magnetized plasma". In: 471.2180 (2015), p. 20140913.

[5] S. Henneberg, S. Cowley, and H. Wilson. "Interacting filamentary eruptions in magnetised plasmas". In: *Plasma Physics and Controlled Fusion* 57.12 (2015), p. 125010.

[6] S. A. Henneberg, S. C. Cowley, and H. R. Wilson. "Explosive Ballooning Mode Instability inTokamaks: Modelling the ELM Cycle". In: in 41st EPS Conference on Plasma Physics. (European Physical Society, Germany, 2014), 2014.

[7] S. A. Henneberg, S. C. Cowley, and H. R. Wilson. "Interaction of explosive multiple filaments in magnetised plasmas". In: in 42nd EPS Conference on Plasma Physics. (European Physical Society, Portugal, 2015), 2015.

[8] H. Wilson. *SCENE Simulation of Self-Consistent Equilibria with Neoclassical Effects, Rep*. Tech. rep. UKAEA-FUS-271, UKAEA Govt. Division, Fusion, Culham, UK, 1994.

[9] NOAA. *Carbon Dioxide - PROXY (INDIRECT) MEASUREMENTS - Reconstruction from Ice cores*. URL: http://climate.nasa.gov/vital-signs/carbon-dioxide/.

[10] E. Dlugokencky, P. Tans, and NOAA/ESRL. *Trends in Atmospheric Carbon Dioxide*. URL: www.esrl.noaa.gov/gmd/ccgg/trends/.

[11] J. Hansen et al. "Global surface temperature change". In: *Reviews of Geophysics* 48.4 (2010).

[12] GISTEMP Team and NASA Goddard Institute for Space Studies. *GISS Surface Temperature Analysis (GISTEMP)*. 2016. URL: http://data.giss.nasa.gov/gistemp/.

[13] *"CLIMATE CHANGE 2014: Synthesis Report. Summary for Policymakers"*. 2015. URL: http://www.ipcc.ch/pdf/assessment-report/ar5/syr/AR5_SYR_FINAL_SPM.pdf.

[14] C. L. Quéré et al. "The global carbon budget 1959–2011". In: *Earth System Science Data* 5.1 (2013), pp. 165–185.

[15] International Energy Agency. *World Energy Outlook 2015 - Press Release*. International Energy Agency, 2015.

[16] D. MacKay. *Sustainable Energy-without the hot air*. UIT Cambridge, 2008. ISBN: 978-0954452933.

[17] O. Edenhofer et al. *Renewable energy sources and climate change mitigation: Special report of the intergovernmental panel on climate change*. Cambridge University Press, 2011.

[18] I. Cook et al. "Safety and environmental impact of fusion". In: *EUR (01) CCE-FU/FTC* 8.5 (2001).

[19] J. P. Freidberg. *Plasma physics and fusion energy*. Cambridge university press, 2008.

[20] H.-S. Bosch and G. Hale. "Improved formulas for fusion cross-sections and thermal reactivities". In: *Nuclear Fusion* 32.4 (1992), p. 611.

[21] J. Wesson. *Tokamaks 3rd Edition by John Wesson*. 2004.

[22] J. D. Lawson. "Some Criteria for a Power Producing Thermonuclear Reactor". In: *Proceedings of the Physical Society. Section B* 70.1 (1957), p. 6.

[23] F. F. Chen. "Introduction to Plasma Physics and Controlled Fusion". In: *Plasma Physics* (1984).

[24] G Hommen et al. "Optical boundary reconstruction of tokamak plasmas for feedback control of plasma position and shape". In: *Review of Scientific Instruments* 81.11 (2010), p. 113504.

[25] F Wagner et al. "Regime of improved confinement and high beta in neutral-beam-heated divertor discharges of the ASDEX tokamak". In: *Physical Review Letters* 49.19 (1982), p. 1408.

[26] ASDEX Team. "The H-Mode of ASDEX". In: *Nuclear Fusion* 29.11 (1989), p. 1959.

[27] F Wagner. "A quarter-century of H-mode studies". In: *Plasma Physics and Controlled Fusion* 49.12B (2007), B1.

[28] R. Groebner. "An emerging understanding of H-mode discharges in tokamaks*". In: *Physics of Fluids B: Plasma Physics (1989-1993)* 5.7 (1993), pp. 2343–2354.

[29] K. Burrell. "Effects of E× B velocity shear and magnetic shear on turbulence and transport in magnetic confinement devices". In: *Physics of Plasmas (1994-present)* 4.5 (1997), pp. 1499–1518.

[30] H. Wilson. "Edge Localized Modes in Tokamaks". In: *Fusion Science and Technology* 61.2T (2012), pp. 122–130.

[31] A Loarte et al. "Characteristics of type I ELM energy and particle losses in existing devices and their extrapolation to ITER". In: *Plasma Physics and Controlled Fusion* 45.9 (2003), p. 1549.

[32] F Ryter et al. "H-mode results in ASDEX Upgrade". In: *Plasma Physics and Controlled Fusion* 36.7A (1994), A99.

[33] H Urano et al. "Energy and particle losses during type-I ELMy H-mode in ASDEX Upgrade". In: *Plasma Physics and Controlled Fusion* 45.9 (2003), p. 1571.

[34] T. H. Osborne et al. "H-mode pedestal characteristics, ELMs, and energy confinement in ITER shape discharges on DIII-D". In: *Plasma Physics and Controlled Fusion* 40.5 (1998), p. 845.

[35] R. Maingi et al. "H-mode pedestal, ELM and power threshold studies in NSTX". In: *Nuclear Fusion* 45.9 (2005), p. 1066.

[36] R Maingi et al. "ELMs and the H-mode pedestal in NSTX". In: *Journal of nuclear materials* 337 (2005), pp. 727–731.

[37] A Kirk et al. "Evolution of filament structures during edge-localized modes in the MAST tokamak". In: *Phys. Rev. Lett.* 96.18 (2006), p. 185001.

[38] J. Pamela, J. Ongena, and J. E. Contributors. "Overview of JET results". In: *Nuclear Fusion* 45.10 (2005), S63.

[39] M. Cox, MAST Team, et al. "The mega amp spherical tokamak". In: *Fusion engineering and design* 46.2 (1999), pp. 397–404.

[40] B. Lloyd et al. "Overview of physics results from MAST". In: *Nuclear Fusion* 47.10 (2007), S658.

[41] G. Counsell et al. "Overview of MAST results". In: *Nuclear Fusion* 45.10 (2005), S157.

[42] J. Milnes et al. "MAST Upgrade - Construction Status". In: *Fusion Engineering and Design* 96-97 (2015). Proceedings of the 28th Symposium On Fusion Technology (SOFT-28), pp. 42 –47. ISSN: 0920-3796.

[43] M. Ono et al. "Exploration of spherical torus physics in the NSTX device". In: *Nuclear Fusion* 40.3Y (2000), p. 557.

[44] D. Gates et al. "Overview of results from the National Spherical Torus Experiment (NSTX)". In: *Nuclear Fusion* 49.10 (2009), p. 104016.

[45] A Kirk et al. "Structure of ELMs in MAST and the implications for energy deposition". In: *Plasma physics and controlled fusion* 47.2 (2005), p. 315.

[46] F. Romanelli and on behalf of JET Contributors. "Overview of the JET results". In: *Nuclear Fusion* 55.10 (2015), p. 104001.

[47] P. Rebut, R. Bickerton, and B. Keen. "The Joint European Torus: installation, first results and prospects". In: *Nuclear Fusion* 25.9 (1985), p. 1011.

[48] P.-H. Rebut. "The JET preliminary tritium experiment". In: *Plasma Physics and Controlled Fusion* 34.13 (1992), p. 1749.

[49] A. Gibson, JET Team, et al. "Deuterium–tritium plasmas in the Joint European Torus (JET): Behavior and implications". In: *Physics of Plasmas (1994-present)* 5.5 (1998), pp. 1839–1847.

[50] J. Jacquinot et al. "Overview of ITER physics deuterium-tritium experiments in JET". In: *Nuclear Fusion* 39.2 (1999), p. 235.

[51] E Bertolini et al. "JET with a pumped divertor: design, construction, commissioning and first operation". In: *Fusion engineering and design* 30.1 (1995), pp. 53–66.

[52] J. P. Coad et al. "Overview of JET post-mortem results following the 2007–9 operational period, and comparisons with previous campaigns". In: *Physica Scripta* 2011.T145 (2011), p. 014003.

[53] R Aymar, P Barabaschi, and Y Shimomura. "The ITER design". In: *Plasma Physics and Controlled Fusion* 44.5 (2002), p. 519.

[54] J. Stober et al. "Type II ELMy H modes on ASDEX Upgrade with good confinement at high density". In: *Nuclear Fusion* 41.9 (2001), p. 1123.

[55] W. D. D'haeseleer et al. *Flux coordinates and magnetic field structure: a guide to a fundamental tool of plasma theory*. Springer Science & Business Media, 2012.

[56] J. W. Connor, R. J. Hastie, and J. B. Taylor. "High Mode Number Stability of an Axisymmetric Toroidal Plasma". In: *Proc. Roy. Soc.* A.365 (1979), p. 1.

[57] J. P. Freidberg. *Ideal magnetohydrodynamics*. Cambridge University Press, 2014.

[58] D. Biskamp. *Nonlinear magnetohydrodynamics*. Vol. 1. Cambridge University Press, 1997.

[59] J. P. Goedbloed, R. Keppens, and S. Poedts. *Advanced magnetohydrodynamics: with applications to laboratory and astrophysical plasmas*. Cambridge University Press, 2010.

[60] L. D. Landau and E. Lifshitz. *Fluid Mechanics*. 2nd ed. Elsevier Ldt, 2010.

[61] D Pfirsch and R. Sudan. "Nonlinear ideal magnetohydrodynamics instabilities". In: *Physics of Fluids B: Plasma Physics (1989-1993)* 5.7 (1993), pp. 2052–2061.

[62] H Grad and H Rubin. "Hydromagnetic Equilbiria and Force-Free Fields". In: *Peaceful Uses of Atomic Energy–Proc. 2nd Int. Conf.(Geneva, 1958)* 31 (1958).

[63] I. B. Bernstein et al. "An energy principle for hydromagnetic stability problems". In: *Proceedings of the Royal Society of London A: Mathematical, Physical and Engineering Sciences* 244.1236 (1958), pp. 17–40.

[64] U. Stroth. "Plasmaphysik". In: *Vieweg+ Teubner: Wiesbaden, Germany* (2011).

[65] C. Mercier. "Un critere necessaire de stabilite hydromagnetique pour un plasma en symetrie de revolution". In: *Nuclear Fusion* 1.1 (1960), p. 47.

[66] B. Suydam. "Stability of a linear pinch". In: *Conf. on Peaceful uses of Atomic Energy* 31 (1958), p. 157.

[67] S. C. Cowley and M. Artun. "Explosive instabilities and detonation in magnetohydrodynamics". In: *Physics Reports* 283 (1997), pp. 185–211.

[68] B. H. Fong, S. C. Cowley, and O. A. Hurricane. "Metastability in Magnetically Confined Plasmas". In: *Physical Review Letters* 82.23 (1999), pp. 4651–4654.

[69] B. H. Fong. "Metastable and Explosive Properties of Ballooning Modes in Laboratory and Space Plasmas". PhD thesis. Princeton Unviersity, 2000.

[70] S. Cowley et al. "Explosive instabilities: from solar flares to edge localized modes in tokamaks". In: *Control. Fusions* 45 (2003), A31.

[71] S. C. Cowley et al. "Explosive Instability and Erupting Flux Tubes in a Magnetised Plasma Atmosphere". In: *arXiv:1411.7797v1 [physics.plasm-ph]* (submitted to Proc. Roy. Soc. A).

[72] J. Connor, R. Hastie, and J. Taylor. "Shear, periodicity, and plasma ballooning modes". In: *Physical Review Letters* 40.6 (1978), p. 396.

[73] H. Wilson et al. "ELM crash theory: relaxation, filamentation, explosions and implosions". In: *paper TH/4-1Rb* (2006).

[74] A Kirk et al. "The spatial structure of type-I ELMs at the mid-plane in ASDEX Upgrade and a comparison with data from MAST". In: *Plasma physics and controlled fusion* 47.7 (2005), p. 995.

[75] A. Kirk et al. "Spatial and Temporal Structure of Edge-Localized Modes". In: *Phys. Rev. Lett.* 92 (2004), p. 245002.

[76] A. W. Leonard. "Edge-localized-modes in tokamaks". In: *Phys. Plasmas* 21 (2014), p. 090501.

[77] A Loarte et al. "Characteristics and scaling of energy and particle losses during Type I ELMs in JET H-modes". In: *Plasma Physics and Controlled Fusion* 44.9 (2002), p. 1815.

[78] I Nunes and the JET Contributors. "Plasma confinement at JET". In: *Plasma Physics and Controlled Fusion* 58.1 (2016), p. 014034.

[79] J. Stober et al. "Small ELM regimes with good confinement on JET and comparison to those on ASDEX Upgrade, Alcator C-mod and JT-60U". In: *Nuclear Fusion* 45.11 (2005), p. 1213.

[80] S. Saarelma et al. "MHD stability analysis of small ELM regimes in JET". In: *Plasma physics and controlled fusion* 51.3 (2009), p. 035001.

[81] R Sartori et al. "Study of Type III ELMs in JET". In: *Plasma Physics and Controlled Fusion* 46.5 (2004), p. 723.

[82] R. Maingi et al. "Characterization of small, Type V edge-localized modes in the National Spherical Torus Experiment)". In: *Physics of Plasmas (1994-present)* 13.9 (2006), p. 092510.

[83] H Zohm. "Edge localized modes (ELMs)". In: *Plasma Physics and Controlled Fusion* 38.2 (1996), p. 105.

[84] J. Connor. "Edge-localized modes-physics and theory". In: *Plasma physics and controlled fusion* 40.5 (1998), p. 531.

[85] N Oyama et al. "Pedestal conditions for small ELM regimes in tokamaks". In: *Plasma Physics and Controlled Fusion* 48.5A (2006), A171.

[86] N Oyama. "Progress and issues in understanding the physics of ELM dynamics, ELM mitigation, and ELM control". In: *Journal of Physics: Conference Series* 123.1 (2008), p. 012002.

[87] P. Lang et al. "ELM control strategies and tools: status and potential for ITER". In: *Nuclear Fusion* 53.4 (2013), p. 043004.

[88] P. Lang et al. "Investigation of pellet-triggered MHD events in ASDEX Upgrade and JET". In: *Nuclear Fusion* 48.9 (2008), p. 095007.

[89] A. W. Degeling et al. "Magnetic triggering of ELMs in TCV". In: *Plasma Physics and Controlled Fusion* 45.9 (2003), p. 1637.

[90] P. T. Lang et al. "Frequency control of type-I ELMs by magnetic triggering in ASDEX Upgrade". In: *Plasma Physics and Controlled Fusion* 46.11 (2004), p. L31.

[91] T. Evans et al. "Suppression of Large Edge-Localized Modes in High-Confinement DIII-D Plasmas with a Stochastic Magnetic Boundary". In: *Physical Review Letters* 92 (2004), p. 23.

[92] M. Fenstermacher et al. "Effect of island overlap on edge localized mode suppression by resonant magnetic perturbations in DIII-D)". In: *Physics of Plasmas (1994-present)* 15.5 (2008), p. 056122.

[93] A. Kirk et al. "Effect of resonant magnetic perturbations on low collisionality discharges in MAST and a comparison with ASDEX Upgrade". In: *Nuclear Fusion* 55.4 (2015), p. 043011.

[94] J. Connor et al. "Magnetohydrodynamic stability of tokamak edge plasmas". In: *Phys. Plasmas* 5 (1998), p. 2687.

[95] J. Connor. "A review of models for ELMs". In: *Plasma physics and controlled fusion* 40.2 (1998), p. 191.

[96] P. Snyder et al. "ELMs and constraints on the H-mode pedestal: peeling–ballooning stability calculation and comparison with experiment". In: *Nuclear fusion* 44.2 (2004), p. 320.

[97] H. Wilson et al. "Numerical studies of edge localized instabilities in tokamaks". In: *Physics of Plasmas (1994-present)* 9.4 (2002), pp. 1277–1286.

[98] P. Snyder et al. "Edge localized modes and the pedestal: a model based on coupled peeling–ballooning modes". In: *Physics of Plasmas (1994-present)* 9.5 (2002), pp. 2037–2043.

[99] X. Xu et al. "Nonlinear Simulations of Peeling-Ballooning Modes with Anomalous Electron Viscosity and their Role in Edge Localized Mode Crashes". In: *Physical review letters* 105.17 (2010), p. 175005.

[100] X. Xu et al. "Nonlinear ELM simulations based on a nonideal peeling-ballooning model using the BOUT++ code". In: *Nuclear Fusion* 51.10 (2011), p. 103040.

[101] B. Dudson et al. "Simulation of edge localized modes using BOUT++". In: *Plasma Physics and Controlled Fusion* 53.5 (2011), p. 054005.

[102] P. Snyder, H. Wilson, and X. Xu. "Progress in the peeling-ballooning model of edge localized modes: Numerical studies of nonlinear dynamicsa)". In: *Physics of Plasmas (1994-present)* 12.5 (2005), p. 056115.

[103] G. T. A. Huysmans et al. "Non-linear MHD simulations of edge localized modes (ELMs)". In: *Plasma Physics and Controlled Fusion* 51.12 (2009), p. 124012.

[104] B. Burke et al. "Edge localized linear ideal magnetohydrodynamic instability studies in an extended-magnetohydrodynamic code". In: *Physics of Plasmas (1994-present)* 17.3 (2010), p. 032103.

[105] A Kirk et al. "Current understanding of the processes underlying the triggering of and energy loss associated with type I ELMs". In: *arXiv preprint arXiv:1312.4300* (2013).

[106] J. Leddy. "Nonlinear Modelling of Ballooning Theory: A Search for ELMs". MA thesis. University of York, 2012.

[107] J. Jim Douglas and B. F. Jones. "On Predictor-Corrector Methods for Nonlinear Parabolic Differential". In: *Journal of the Society for Industrial and Applied Mathematics* 11.1 (1963), pp. 195–204.

[108] H Luc et al. "Helicoidal approximation for general non-symmetric closed plasma configurations". In: *Plasma Physics* 16.5 (1974), p. 455.

[109] R. Miller et al. "Noncircular, finite aspect ratio, local equilibrium model". In: *Physics of Plasmas (1994-present)* 5.4 (1998), pp. 973–978.

[110] E. Kreyszig. *Advanced engineering mathematics*. John Wiley & Sons, 2010.

[111] W. H. Press et al. *Numerical Recipes in FORTRAN*. Cambridge University Press, 2nd edition. 1992.

[112] I. Bronstein et al. "Taschenbuch der Mathematik, 7. vollständig überarbeitete und ergänzte Auflage". In: *Verlag Harri Deutsch* 1 (2008).

[113] C. B. Lang and N. Pucker. *Mathematische Methoden in der Physik*. Spektrum, Akad. Verlag, 2. Auflage 2005, korrigierter Nachdruck 2010.

[114] R. Herrmann. "Fraktionale Infinitesimalrechnung". In: *Books on Demand GmbH* (2008).

[115] E. J. Alfaro, E. Pérez, and J. Franco, eds. *How does the galaxy work?* Vol. 315 2005. Springer Astrophysics and Space Science Library, 2005.

[116] E. G. Zweibel and D. L. Bruhwiler. "The effect of line tying on parker's instability". In: *The Astrophysical Journal* 399 (1992), p. 318.

[117] G. Yun et al. "Two-dimensional imaging of edge-localized modes in KSTAR plasmas unperturbed and perturbed by n= 1 external magnetic fields". In: *Physics of Plasmas (1994-present)* 19.5 (2012), p. 056114.

[118] L. Lao et al. "Reconstruction of current profile parameters and plasma shapes in tokamaks". In: *Nuclear Fusion* 25.11 (1985), p. 1611.

[119] G. Huysmans, J. Goedbloed, and W Kerner. "Isoparametric bicubic Hermite elements for solution of the Grad-Shafranov equation". In: *Proc. Europhysics 2nd Intern. Conf. on Compputational Physics, 10-14 Sept. 1990* (1991), pp. 371–376.

[120] C. Konz and R. Zille. *HELENA - Fixed boundary equilibrium solver*. Max-Planck-Institut für Plasmaphysik. Garching, 2007.

[121] D Dickinson et al. "Towards the construction of a model to describe the inter-ELM evolution of the pedestal on MAST". In: *Plasma physics and controlled fusion* 53.11 (2011), p. 115010.

[122] A Kirk et al. "Evolution of the pedestal on MAST and the implications for ELM power loadings". In: *Plasma Physics and Controlled Fusion* 49.8 (2007), p. 1259.

[123] I Nunes et al. "Small ELMs in quasi-double null plasmas at JET". In: *Proc. 34th EPS Conf. on Plasma Physics (Warsaw, Poland, 2007)* 31 (2007).

[124] G. Saibene et al. "Characterization of small ELM experiments in highly shaped single null and quasi-double-null plasmas in JET". In: *Nuclear Fusion* 45.5 (2005), p. 297.

[125] E. Fredrickson et al. "Ballooning instability precursors to high $\beta$ disruptions on the Tokamak Fusion Test Reactor". In: *Physics of Plasmas (1994-present)* 3.7 (1996), pp. 2620–2625.

[126] B. Dudson et al. "BOUT++: A framework for parallel plasma fluid simulations". In: *Computer Physics Communications* 180.9 (2009), pp. 1467–1480.